RĪGAS TEHNISKĀ UNIVERSITĀTE

Ilijana Kovrlija

OCTACALCIUM PHOSPHATE BIOMATERIALS: FORMATION PROCESS, MODIFICATION AND APPLICATION

Doctoral Thesis

BIOMATERIĀLI UZ OKTAKALCIJA FOSFĀTA BĀZES: IEGŪŠANA, MODIFIKĀCIJA UN PIELIETOJUMS

Promocijas darbs

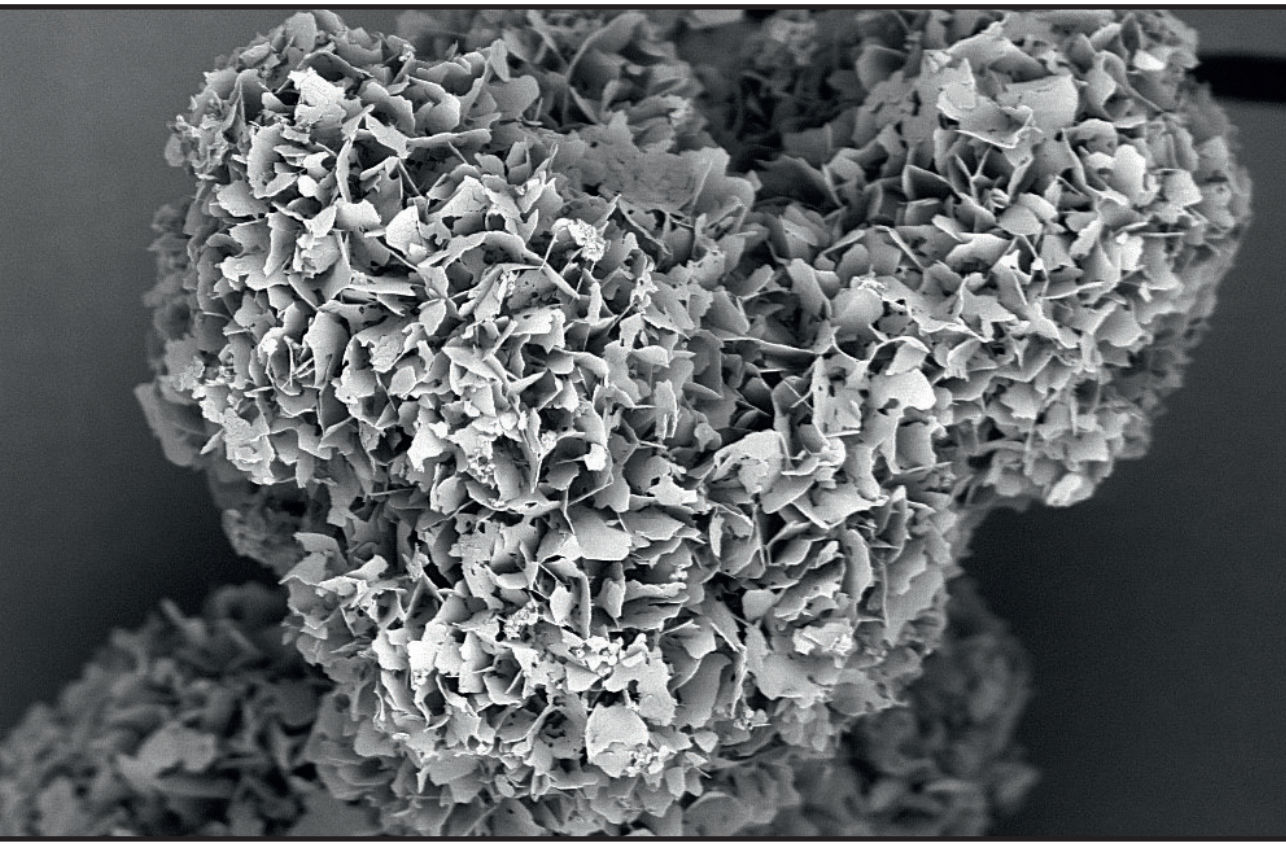

RTU Press
RTU Izdevniecība
Rīga 2024

RIGA TECHNICAL UNIVERSITY
Faculty of Natural Sciences and Technology
Institute of Biomaterials and Bioengineering

RĪGAS TEHNISKĀ UNIVERSITĀTE
Dabaszinātņu un tehnoloģiju fakultāte
Biomateriālu un bioinženierijas institūts

ILIJANA KOVRLIJA
Doctoral Student of the Study Programme "Chemistry, Materials Science and Engineering"
Doktora studiju programmas "Ķīmija, materiālzinātne un tehnoloģijas" doktorante

OCTACALCIUM PHOSPHATE BIOMATERIALS: FORMATION PROCESS, MODIFICATION AND APPLICATION

Doctoral Thesis

BIOMATERIĀLI UZ OKTAKALCIJA FOSFĀTA BĀZES: IEGŪŠANA, MODIFIKĀCIJA UN PIELIETOJUMS

Promocijas darbs

Scientific supervisors / Zinātniskie vadītāji
Professor *Dr.sc.ing* / profesore *Dr.sc.ing.*
DAGNIJA LOČA
Professor *Dr.sc.ing* / profesors *Dr.sc.ing.*
JĀNIS LOČS

RTU Press / RTU Izdevniecība
Riga 2024 / Rīga 2024

Kovrlija, I. Octacalcium Phosphate Biomaterials: Formation Process, Modification and Application. Doctoral Thesis. Riga: RTU Press, 2024. 173 p.

Kovrlija, I. Biomateriāli uz oktakalcija fosfāta bāzes: iegūšana, modifikācija un pielietojums. Promocijas darbs. Rīga: RTU Izdevniecība, 2024. 173 lpp.

Publicēts saskaņā ar promocijas padomes "RTU P-02" 2024. gada 3. jūnija lēmumu, protokols Nr. 04030-9.2.2/4.

Published in accordance with the decision of the Promotion Council "RTU P-02", June 03, 2024, Minutes No 04030-9.2.2/4.

This work has been supported by the European Union's Horizon 2020 research and innovation programmes "Precision medicine for musculoskeletal regeneration, prosthetics, and active ageing" [No.860462, PREMUROSA], "Baltic Biomaterials Centre of Excellence" [No. 857287, BBCE] and "Rising competitiveness of early-stage researchers and research management in Latvia" [No. 952347, RISEus2].

Šis darbs izstrādāts Eiropas Savienības Apvārsnis 2020 projekta "Precīzijas medicīna muskuloskeletālai reģenerācijai, protezēšanai un aktīvām vecumdienām" [Nr. 860462, PREMUROSA], "Baltijas Biomateriālu Ekselences centrs" [Nr. 857287, BBCE] un "Jauno pētnieku un pētniecības pārvaldības konkurētspējas paaugstināšana Latvijā" [Nr. 952347, RISEus2] ietvaros.

DOCTORAL THESIS PROPOSED TO RIGA TECHNICAL UNIVERSITY FOR THE PROMOTION TO THE SCIENTIFIC DEGREE OF DOCTOR OF SCIENCE

To be granted the scientific degree of Doctor of Science (Ph. D.), the present Doctoral Thesis has been submitted for the defense at the open meeting of the RTU Promotion Council on September 6, 2024, at 14:00, at the Faculty of Natural Sciences and Technology of Riga Technical University, 3 Paula Valdena Street, Room 272.

OFFICIAL REVIEWERS

Assistant Professor *Dr. sc. ing*. Agnese Brangule
Riga Stradins University, Latvia

Professor *Dr. chem*. Maris Turks
Riga Technical University, Latvia

Associate Professor *Dr.* Sabine van Rijt
Institute for Technology-Inspired Regenerative Medicine (MERLN), The Netherlands

DECLARATION OF ACADEMIC INTEGRITY

I hereby declare that the Doctoral Thesis submitted for review to Riga Technical University for the promotion to the scientific degree of Doctor of Science (Ph. D.) is my own. I confirm that this Doctoral Thesis has not been submitted to any other university for the promotion to a scientific degree.

Ilijana Kovrlija ……. (signature)
Date: 06.09.2024

The Doctoral Thesis has been written as a collection of articles. It consists of a summary in English and Latvian and five SCI publications. The publications have been written in English and have a total volume of 84 pages.

ANNOTATION

Within the present work, the synthesis methodology and upscaling of octacalcium phosphate (OCP) production from low-temperature α-tricalcium phosphate (α-TCP) have been optimized, and a comprehensive analysis profile of the obtained OCP has been established. To ultimately utilize the data from the physicochemical analysis, an *in silico* model capable of identifying the production stage of OCP has been designed. The developed OCP has been applied in two approaches: as a doxorubicin hydrochloride (DOX) drug delivery system for the treatment of osteosarcoma and as a protective coating against corrosion for titanium implants. The doxorubicin-octacalcium phosphate (DOX-OCP) drug delivery system was characterized, and the *in vitro* drug release and biological effects on MG63 (cancer cells) and MC3T3-E1 (normal cells) were studied. Sodium alginate/octacalcium phosphate (Alg/OCP) composite coatings were developed, and their electrochemical behavior on titanium alloys in inflammatory conditions was assessed.

The Doctoral Thesis has been written as a collection of articles. It consists of a summary in Latvian and English and five SCI publications. Each summary contains 15 figures and 1 table, followed by 5 appendices, totaling in 173 pages, including electronically available supplementary information.

TABLE OF CONTENTS

ACKNOWLEDGEMENT

Firstly, I would like to acknowledge the PREMUROSA, BBCE, and RISEus2 projects that financed my PhD and made it possible to visit all the incredible institutes, scientific conferences, and networking events.

There were many details and experiences that were important for me during the last four years, however I will mention only several of the most important ones.

First and foremost, I would like to thank my professors – Dagnija and Janis, who were there for me, not only as supervisors, but as friends and as a support system, whenever it was needed. I would like to thank you for millions of "fast questions", for numerous newly learned scientific facts, for a chance to show what I can achieve, for trusting me, for many parties and, the most important one, for showing me how to be a true mentor!

Also, I would like to thank my family – mom, dad, Danka, Sava, uncle, Dana and Vasilije. For your unconditional support to enroll in a PhD programme and for everything before and during my studies, without which none of this would be possible! To my best friends – Maja, Isidora, Maja and Daka – who were always there for me with their support and understanding! To Milica, for many hours of conversation on all the new things, cultures and work challenges! To Una and Kića, for the best and most important company that I was extremely lucky to have! To Aert, for all the support, love and laughter that made everything easier! And lastly, I would like to thank all of the people whom I met during this journey, who taught me many things and who I can now call my friends (you will recognize yourselves!)!

A special thank you goes to Jana and Līga, without whose help I would not have been able to submit my Thesis on time!

ZAHVALNICA

Postoje mnogi detalji i događaji koji su bili ključni tokom zadnjih četiri godine, ali ću da naglasim samo nekoliko najbitnijih.

Prije svega, htjela bih da se zahvalim mojim profesorima – Dagniji i Janisu, koji su bili uz mene, ne samo kao mentori, već kao i prijatelji i podrška kad god je to bilo potrebno. Htjela bih da Vam se zahvalim za milion „brzinskih pitanja", za mnogo novih naučenih činjenica, za šansu da pokažem šta mogu da postignem, za povjerenje, za mnoge žurke i kao najbitnije, za savršen primjer kako biti pravi mentor!!

Takođe, htjela bih da se zahvalim svojoj porodici – mami, tati, Danki, Savi, ujki, Dani i Vasiliju. Za vašu bezuslovnu podršku da upišem doktorat i za sve prije i tokom studija, bez čega ništa od ovoga ne bi bilo moguće! Mojim najboljim prijateljicama – Maji, Isidori, Maji i Daki, koje su uvijek bile tu za mene sa svojom podrškom i razumjevanjem! Milici, za mnoge sate razgovora oko novih stvari, kultura i poslovnih izazova! Uni i Kići, za najbolje i najvažnije društvo koje sam imala ogromnu sreću da ostvarim! Aertu, za svu podršku, ljubav i osmjehe koji su sve olakšali! I na kraju, željela bih da se zahvalim svim osobama koje sam upoznala na ovom putovanju, koje su me naučile mnogim stvarima i koje mogu sad da nazovem prijateljima (vi ćete se lako prepoznati!)!

Posebno se želim zahvaliti Jani i Ligi, bez čije pomoći ne bih mogla da predam tezu na vrijeme!

ABBREVIATIONS

ACP	amorphous calcium phosphate
Alg	sodium alginate
Alg/OCP	alginate/octacalcium phosphate
BET	Brunauer–Emmett–Teller method
CaP(s)	calcium phosphate(s)
CDHAp	calcium deficient hydroxyapatite
CPE	constant phase element
CPE_{dl}	interface between a substrate and a solution
DCPD/Brushite	dicalcium phosphate dihydrate
DDS(s)	drug delivery system(s)
DLC	drug loading capacity
DOX	doxorubicin hydrochloride
DOX-OCP	doxorubicin-loaded octacalcium phosphate
nDOX-OCP	n wt% of active substance (from the initial low temperature-α-tricalcium phosphate amount)
EIS	electrochemical impedance spectroscopy
Fer-1	ferrostatin-1
FTIR	Fourier transform infrared spectroscopy
HAp	hydroxyapatite
hBMSC	human bone mesenchymal stem cells
I	inflammatory medium
ICDD	International Centre for Diffraction Data
LT-α-TCP	low temperature-α-tricalcium phosphate
ML	Machine learning
N	normal medium
NMR	nuclear magnetic resonance
OCP	octacalcium phosphate
OS	osteosarcoma cells
PARP	poly (ADP-ribose) polymerase
PBS	phosphate buffered saline
PBT	polybutylene terephthalate
PCD	programmed cell death
PEGT	polyethylene glyco terephthalate
Rc	resistance
Rct	resistance to charge transfer
SEM	scanning electron microscopy
SI	severe inflammatory medium
SSA	specific surface area
TCP (α, β)	tricalcium phosphate (α, β)
TEM	transmission electron microscopy

TGA	thermogravimetric analysis
Ti Gr2	99.3 wt% titanium balance
Ti Gr23	Al 5.4 wt %, V 3.8 wt%, Fe 0.2 wt%, C 0.009 wt% of titanium balance
XRD	X-ray diffraction

GENERAL OVERVIEW OF THE THESIS

Introduction and Literature Review

Due to an increasing number of people having musculoskeletal diseases (322.75 million incident cases in 2019) [1], bone cancers (by 2040, global cancer cases will reach 26 million [2]) or incomplete regeneration of bones, it is detrimental to guide the research in the direction of finding the most effective solutions, which are able to help in the treatment of bone defects and bone tissue regeneration. Regenerative medicine's main endeavor is to mimic the properties of the native bone as closely as possible so the entire regeneration process can be faster and easier for the patients. Considering that using different drugs is also necessary to battle certain diseases, an additional goal is to minimize the aftermath of the systemic distribution that can have a lethal outcome. Nevertheless, irrespective of the end application, a suitable material needs to closely align to the golden standard: be biocompatible, biodegradable and exhibit osteoinductive properties (engagement and stimulation of cells to differentiate into preosteoblasts [3]).

Calcium phosphates (CaPs) are highly effective and reliable materials [4], biocompatible, osteoconductive, have the ability to incorporate different drugs/ions, and they are also the main constituents of bone's and teeth's inorganic part [5–8]. CaPs can be classified by their Ca/P molar ratio, solubility, crystallinity, particle size, morphology and specific surface area (SSA), but also based on their final form (nanoparticles, scaffolds, coatings, etc.). Hydroxyapatite (HAp, $Ca_{10}(PO_4)_6(OH)_2$), the most commonly used phase, is also naturally present in hard tissues (in non-stoichiometric form). Even though HAp is the most stable phase under physiological conditions, the disadvantage to using it could be slow resorption kinetics [9,10]. The second most often used CaP is tricalcium phosphate (TCP, $Ca_3(PO_4)_2$). The two polymorphs of TCP are α and β, and they are mostly used for bone regeneration [11], for example, α-TCP is extensively used in bone cements and other bone substitutes, as it has excellent biocompatibility and it showed positive results in *in vivo* [8]. Conversely, α-TCP has too high degradation rate when compared to the new bone growth rate [12,13]. Three out of all CaPs are presumed to be the precursors of bone apatite – amorphous calcium phosphate (ACP, $Ca_3(PO_4)_2 \cdot nH_2O$), dicalcium phosphate dihydrate (brushite or DCPD, $CaHPO_4 \cdot 2H_2O$), and octacalcium phosphate (OCP, $Ca_8(HPO_4)_2(PO_4)_4 \cdot 5H_2O$) [8,14]. ACP exhibits higher solubility and resorption rates, facilitated by lack of crystallinity, the presence of a hydrated layer, and the existence of defects, which ultimately contribute to the improved bioactivity [15,16]. DCPD has layers (sheets of CaO and PO_4^{3-}) that are parallel to the c-axis and are held together by hydrogen bonds from the water molecules within the structure [17,18]. DCPD forms in acidic aqueous solutions at pH 2–6, and one of the major DCPD's advantages is the strong inclination to transform to OCP or calcium deficient hydroxyapatite (CDHAp), which is why it is often used in self-setting CaP cements.

The third precursor, i.e., OCP, is the most similar one to HAp. The similarity lies in its structure – apatite layers being parallel to the (100) plane with hydrated layers in between [19,20]. This particular arrangement of apatite crystallographic planes (~ 1.1 nm thickness) and

a relatively empty hydrated layer (~ 0.8 nm thickness) [21], enables OCP to transform itself to the thermodynamically more stable phase, CDHAp, both *in vitro* and *in vivo* [21,22]. The presence of water molecules in the hydrated layer influences the level of the similarity of OCP structure to the one of HAp. Comparable conversion of OCP to apatite transpires in the process of bone formation [8]. Moreover, due to the presence of the hydrated layer, the incorporation of different ions and molecules is significantly more attainable [23]. From the biological point of view, the release of the HPO_4^{2-} ions from OCP [24] facilitates the stimulation of main bone cells (e.g., osteoblasts, osteocytes, osteoclasts [25]) and helps in enhancing macrophage migration to the implantation site [21]. Several studies showed that OCP can decrease the secretion of proinflammatory cytokines (necrosis factor-alpha and Interleukin-1), which show anti-inflammatory properties [26,27]. Also, multiple groups showed evidence of OCP's osteoinductivity – OCP-coated titanium [28] and OCP-coated polyethylene glyco-terephthalate/polybutylene terephthalate (PEGT/PBT) [29].

There are two main pathways for synthesizing OCP: the precipitation [20,30] and the hydrolysis [17,31]. The starting sources of calcium (Ca^{2+}) and phosphate (PO_4^{3-}) ions vary, and usually, in precipitation, they are combinations of calcium acetate, calcium carbonate, sodium acid phosphate and phosphoric acid, whereas in hydrolysis, the most common precursors are DCPD or α-TCP. Both processes are quite complex, and they depend on the intertwined effects of the pH, temperature, stir rate, ionic strength, etc. [23,32]. For example, if the temperature in the system is higher, the time until OCP materializes is shorter due to the more kinetically conducive conditions, which favor the formation of this phase. Alternatively, if the pH increases, it could lead to the precipitation of another phase (e.g., CDHAp). The aforementioned factors can also influence the size and morphology of the crystals (precipitation can result in thin elongated and lamellar particles, whereas hydrolysis can exhibit thin plate-like particles mixed with finer whisker-like particles) and the biological effect it will have [20,33]. Owing to this, the appropriate synthesis conditions must be chosen, depending on not only phase purity but also final morphology and the application of OCP.

To determine the CaP phase, its characteristic markings and morphology, a multi-technique characterization approach is necessary. To confirm the presence of a specific phase, X-ray diffraction (XRD), Fourier transform infrared spectroscopy (FTIR), Raman spectroscopy, scanning electron microscopy (SEM), nuclear magnetic resonance (NMR), thermogravimetric analysis (TGA), transmission electron microscopy (TEM), Brunauer–Emmett–Teller method (BET), Laser granulometry, etc. are being used. However, the downside of OCP (a very high similarity to CDHAp [23]) creates difficulty in claiming the phase purity quantitatively (overlap of XRD maxima with CDHAp can disrupt the Rietveld analysis). Other obstacles detected during the course of the literature review were relatively small yields of the obtained pure product (~ 100 mg – 2 g), a narrow region of pH (5.0–7.0 pH), temperatures favorable for the synthesis of OCP, and the inability to process it under high temperatures (> 80 °C) [23].

As the ongoing research progresses, innovative ways to employ OCP in regenerative medicine are being explored. OCP has been used as a bone cement [34] and as a composite scaffold with polymers (alginate, gelatin, collagen, PEGT, etc.) for the reconstruction of bone defects [35–37]. Also, as a coating on titanium alloy implants to enhance the biological

performance of the metal surfaces [29,38]. Considering the additional objective of regenerative medicine is to address systemic conditions like osteoporosis and minimize drug intake frequency and toxicity in cancer patients, the integration of bioactive ions and drugs into the CaPs has gained considerable popularity. When it comes to OCP, several ion substitutions (carbonate (CO_3^{2-}), magnesium (Mg^{2+}), zinc (Zn^{2+}), and strontium (Sr^{2+})) have been done to tune the bioactive effects [23]. Moreover, OCP has been used as a drug delivery system (DDS) to improve the biodistribution of therapeutics (bisphosphonates, ibuprofen, methotrexate) via local delivery pathways [23]. The conventional systemic drug delivery route operates through the circulatory system, potentially resulting in various side effects, systemic toxicity, and suboptimal delivery to the targeted site [39]. To mitigate these drawbacks, local agent delivery aims to reduce the burst release and to establish a tailored drug release profile, specific to the defect site. As malignant skeletal tumors (osteosarcoma (OS) standing out as a prominent representative), make up roughly 40 % of all bone tumors [2], some of the efforts on employing OCP as a carrier were directed to testing the effect of methotrexate-loaded OCP on OS cell lines [40], however research on OCP drug loading was mostly focused on bisphosphonates. Thus, it is crucial to devise a new DDS that effectively controls the localized administration and short/long-term effects of the anticancer drugs. It also enhances the applicability and mitigates the development of chemoresistance and dosage-dependent toxicity. It has been hypothesized that, if the drug loading is achieved *in situ* during the initial stages of OCP synthesis, it can lead to ultrahigh drug loading capacity (DLC) [41]. However, even though OCP has shown a high potential as a biologically active ion/molecule delivery system, there is scarce data on how the drug release mechanism from OCP works and how the process of drug/ion loading affects the formation of the OCP phase.

The rationale behind the proposed research

After a thorough review and bearing in mind the demonstrated importance of OCP, the Thesis focused on delivering systematic studies on OCP formation and utilization that were lacking in the literature, therefore filling the identified knowledge gap to some extent. Thus, within the Thesis, the optimization of the synthesis methodology and scale-up method of OCP synthesis was elaborated, anticancer drug-loaded OCP delivery systems were developed, and OCP applicability in composite coatings was tested. The comprehensive strategy of the PhD research is shown in Fig. 1.

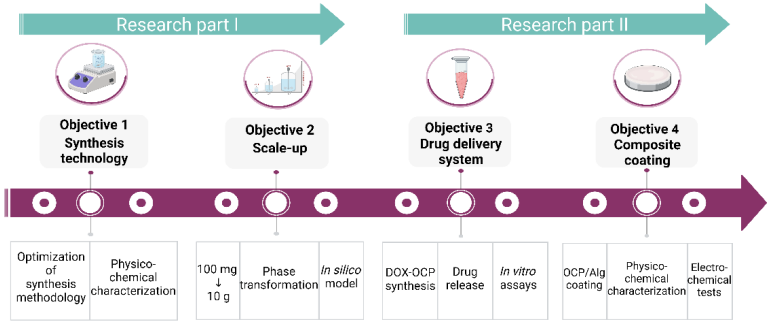

Fig. 1. PhD project roadmap. OCP – octacalcium phosphate; Alg – alginate; DOX – doxorubicin; DOX-OCP – doxorubicin loaded octacalcium phosphate.

Aim and Objectives

The aim of the Thesis was to optimize the synthesis technology to obtain a stable OCP with high phase purity and to explore its application as a drug delivery vehicle as well as a protective composite coating. To fulfil the aim, the following objectives were set:

1. To optimize the synthesis methodology of OCP via the hydrolysis of low-temperature α-tricalcium phosphate (LT-α-TCP) and study the physicochemical properties of the obtained OCP.
2. To optimize the scale-up of the synthesis technology, determine the formation pathway of OCP, and develop an *in silico* model for the determination of the OCP synthesis termination based on the XRD and FTIR results.
3. To develop a drug delivery system for cancer treatment by combining OCP with an anti-neoplastic agent – doxorubicin hydrochloride (DOX-OCP).
4. To develop the OCP-embedded hydrogel coatings for metallic implants able to enhance corrosion resistance.

Thesis to Defend

1. Hundredfold upscaling of OCP synthesis via the hydrolysis of LT-α-TCP at room temperature does not affect the physicochemical properties of the final product (phase composition, molecular structure and morphology).
2. Doxorubicin can be incorporated into the octacalcium phosphate particles up to 10 wt% of the initial OCP precursor amount, while higher amounts of doxorubicin inhibit the OCP phase formation. The as-synthesized product can serve as a prolonged-release anticancer drug delivery system.
3. If used in coatings for 3D printed Tibased metallic implants, OCP affects electrical charge transfer resistance at the substrate and coating interface.

Scientific Novelty

The scientific novelty was recognized in the following aspects:

1. By following the phase transformations from LT-α-TCP to OCP, it was established and described through chemical equations that the progressive shift from LT-α-TCP phase to the OCP phase transpired through DCPD as an intermediary point.
2. Maximum loading of doxorubicin hydrochloride during the *in situ* synthesis of OCP was 10 wt% (of the initial LT-α-TCP amount), whereas everything above inhibited the OCP formation. Furthermore, doxorubicin-loaded OCP caused apoptosis as the main cell death pathway.

Practical Significance

OCP's simple and straightforward synthesis methodology was optimized by choosing LT-α-TCP as a single precursor that required less energy consumption to produce, which aligned with the set goals of the European Green Deal. The synthesis methodology was further utilized to obtain high yields of OCP, which could be used on an industrial scale. The applicability of as-synthesized OCP is twofold:

1) in the development of a novel DDS for the local treatment of osteosarcoma, and
2) in the development of OCP-embedded hydrogel coatings for the enhancement of corrosion resistance of 3D-printed titanium alloys.

Publications and Approbation of the Thesis

The results of the Thesis were published in five SCI scientific publications.

1. **Kovrlija I**., Locs, J., Loca, D. Octacalcium phosphate: Innovative vehicle for the local biologically active substance delivery in bone regeneration, *Acta Biomaterialia*, 135, 2021, pp. 27–47. doi: 10.1016/j.actbio.2021.08.021 (Scopus, Open Access, IF 9.4, Q1, CiteScore 16.8).
    - Kovrlija, I. contributed to the publication by writing the original draft, reviewing and editing, and visualization (in total 85/100 %).
2. **Kovrlija, I.,** Menshikh, K., Marsan, O., Rey, C., Combes, C., Locs, J., Loca, D. Exploring the Formation Kinetics of Octacalcium Phosphate from Alpha-Tricalcium Phosphate: Synthesis Scale-Up, Determination of Transient Phases, Their Morphology and Biocompatibility, *Biomolecules*, 13, 2023, 462. doi:10.3390/biom13030462 (Scopus, Open Access, IF 4.8, Q1, CiteScore 9.4).
    - Kovrlija, I. contributed to the publication by writing the original draft, reviewing and editing, conceptualization, visualization, formal analysis, and investigation (in total 80/100 %).
3. Nascimben, M., **Kovrlija, I.,** Locs, J., Loca, D., Rimondini, L. Fusion and classification algorithm of octacalcium phosphate production based on XRD and FTIR data, *Scientific Reports*, 14:1489, 2024, 1–11. doi: 10.1038/s41598-024-51795-0 (Scopus, Open Access, IF 3.8, Q1, CiteScore 6.9).
    - Kovrlija, I. contributed to the publication through laboratory experiments, data collection and organization, results discussion, manuscript draft writing, manuscript editing and revision (in total 50/100 %).
4. **Kovrlija, I**., Pańczyszyn E., Demir, O., Laizane, M., Corazzari, M., Locs, J., Loca, D. Doxorubicin-loaded octacalcium phosphate particles as controlled release drug delivery systems: physico-chemical characterization, in vitro drug release and evaluation of cell death pathway, *International Journal of Pharmaceutics*, 653, 2024, 123932. doi: 10.1016/j.ijpharm.2024.123932 (Scopus, Open Access, IF 5.3, Q1, CiteScore 10.7).
    - Kovrlija, I. contributed to the publication through writing the original draft, reviewing and editing, conceptualization, visualization, formal analysis, and investigation (in total 75/100 %).
5. Bordbar Khiabani, A., **Kovrlija, I**., Locs, J., Loca, D., Gasik, M. Octacalcium Phosphate-Laden Hydrogels on 3D-Printed Titanium Biomaterials Improve Corrosion Resistance in Simulated Biological Media, *International Journal of Molecular Sciences*, 2023, 24, 13135. doi: 10.3390/ijms241713135 (Scopus, Open Access, IF 4.9, Q1, CiteScore 8.1).
    - Kovrlija I. contributed to the publication throughg writing – the original draft preparation, visualization, formal analysis, and investigation (in total 50/100 %).

The results of the Thesis were presented at nine scientific conferences.

1. **Kovrlija I**., Nascimben M., Bordbar-Khiabani A., Menshikh K., Gasik M., Combes C., Rimondini L., Locs J., Loca D. Tailoring the production technology and utilization of octacalcium phosphate for precise patient-centred applications in musculoskeletal field. *12th World Biomaterials Congress*, 26.-31. May 2024, Daegu, South Korea; (I.K. poster presentation).
2. **Kovrlija, I**., Demir, O., Laizane, M., Locs, J., Loca, D. Novel drug delivery vehicle: doxorubicin-loaded octacalcium phosphate. *33rd Annual Conference of the European Society of Biomaterials*, 04–08 September 2023, Davos, Switzerland. (I. K. – poster presentation).
3. **Kovrlija, I**., Menshikh, K., Demir, O., Locs, J., Loca, D., Octacalcium phosphate: journey of creating a unique drug delivery vehicle. *The XVIIIth Conference of the European Ceramic Society*, 02–06 July 2023, Lyon, France. (I. K. —student speech contest).
4. **Kovrlija, I**., Menshikh, K., Marsan, O., Rey, C., Combes, C., Locs, J., Loca, D. Scale-Up of Octacalcium Phosphate via Hydrolysis Route: Effect on Physico-Chemical Characteristics and In-Vitro Cytocompatibility with Bone Marrow-Derived Mesenchymal Stem Cells. *Tissue Engineering and Regenerative Medicine International Society European Chapter Meeting*, 28–31 March 2023, Manchester, UK. (I. K. – oral presentation).
5. **Kovrlija, I**., Menshikh, K., Marsan, O., Rey, C., Combes, C., Locs, J., Loca, D. Phase transformation from α-tricalcium phosphate to octacalcium phosphate via hydrolysis route. *Scandinavian Society for Biomaterials 16th annual meeting*, 21–14 March 2023, Roros, Norway. (I. K. – poster presentation).
6. **Kovrlija, I.,** Barbut, C., Locs, J., Loca, D. Incorporation and effect of lidocaine hydrochloride on octacalcium phosphate. *32nd Annual Conference of the European Society of Biomaterials*, 04–08 September 2022, Bordeaux, France. (I. K. – poster presentation).
7. **Kovrlija, I**., Locs, J., Loca, D. Unravelling the Behaviour of Octacalcium Phosphate in Various Model Solutions. *Scandinavian Society for Biomaterials 15th annual meeting*, 13–15 June 2022, Jurmala, Latvia. (I. K. – poster presentation).
8. **Kovrlija, I.,** Barbut, C., Locs, J., Loca, D. Effects of the synthesis conditions on the hydrolysis of α-tricalcium phosphate to octacalcium phosphate. *31st Annual Conference of the European Society for Biomaterials*, 2021 (online). (I. K. – poster presentation).
9. **Kovrlija, I**., Locs, J., Loca, D. Octacalcium phosphate: a contemporary drug delivery system for local biologically active substances – a review. *Scandinavian Society for Biomaterials 14th Annual Meeting*, 2021 (online). (I. K. – poster presentation).

The results of the PhD Thesis were presented at other scientific events.

1. Locs, J., **Kovrlija, I**., Choudhary, R., Loca, D. Roadmap from upscaling and rapid synthesis towards first-ever consolidation of OCP. *33rd Conference and annual meeting of the International Society for Ceramics in Medicine*, 17–20 October 2023, Solothurn, Switzerland. (J.L. invited talk).
2. Bordbar Khiabani, A., **Kovrlija, I.,** Locs, J., Loca, D., Gasik, M. Octacalcium Phosphate Embedded Hydrogels on 3D Printed Titanium Improve the Corrosion Performance in Simulated Biological Media. *31st Annual Meeting of European*

Orthopaedic Research Society, 27–29 September 2023, Porto, Portugal. (A. B. K. – oral presentation).

3. Loca, D., **Kovrlija, I.,** Pylostomou, A., Locs, J. Can Octacalcium Phosphate Be Used as a Doxorubicin Delivery Platform? *Tissue Engineering and Regenerative Medicine International Society – Americas Chapter Annual Meeting*, 11–14 April 2023, Boston, USA. (D. L. – poster presentation).
4. Menshikh, K., **Kovrlija, I.,** Miola, M., Cochis, A., Rimondini, L. Synthetic pre-vascularized porous scaffold as an engineered environment for the in vitro osteosarcoma model. *Tissue Engineering and Regenerative Medicine International Society European Chapter Meeting*, 28 June – 1 July 2022, Krakow, Poland. (K. M. – poster presentation).
5. Menshikh, K., **Kovrlija, I**., Miola, M., Cochis, A., Rimondini, L. Freeze-dried Composition of Alginate and Bioglass as an Engineered Environment for the Osteosarcoma Model. *Scandinavian Society for Biomaterials 15th annual meeting*, 13–15 June 2022, Jurmala, Latvia. (K. M. – poster presentation).
6. **Kovrlija, I**., Locs, J., Loca, D. Octacalcium phosphate: synthesis, characterization and functionalization. *4th Premurosa Summer School*, 15–19 May 2024, Riga, Latvia. (I. K. – oral presentation).
7. **Kovrlija, I**., Locs, J., Loca, D. Unravelling the Behaviour of Octacalcium Phosphate in Various Model Solutions. *3rd Premurosa Summer School*, 20–24 June 2023, Belgrade, Serbia. (I. K. – poster presentation).
8. **Kovrlija, I.,** Locs, J., Loca, D. Smart personalized degradable biomaterials for bone tissue regeneration. *2nd Premurosa Summer School*, 19–24 October 2022, Porto, Portugal. (I. K. – oral presentation).
9. **Kovrlija, I**., Loca, D. Octacalcium phosphates: promising instruments for local drug delivery in bone regeneration. Baltic Biomaterials Centre of Excellence Summer School on "Scientific writing", 23–27 November 2020, online. (I. K. – oral presentation).

Other scientific publications published during the development of the Thesis.

1. **Kovrlija I**., K. Menshikh, H. Abreu, A. Cochis, L. Rimondini, O. Marsan, C. Rey, C. Combes, J. Locs, D. Loca, Challenging Applicability of ISO 10993-5 for Calcium Phosphate Biomaterials Evaluation: Towards More Accurate In Vitro Cytotoxicity Assessment, *Biomaterials Advances*, 160, 213866, 2024. doi: 10.1016/j.bioadv.2024.213866 (Scopus, Open Access).
2. Aunina, K., Ramata-Stunda, A., **Kovrlija, I**., Tracuma, E., Merijs-Meri, R., Nikolajeva, V., Loca, D. Exploring the Interplay of Antimicrobial Properties and Cellular Response in Physically Crosslinked Hyaluronic Acid/ε-Polylysine Hydrogels, *Polymers*, 15(8): 1915, 2023. doi:10.3390/polym15081915 (Scopus, Open Access).
3. Mosina, M., **Kovrlija, I**., Stipniece, L., Locs, J. Gallium containing calcium phosphates: Potential antibacterial agents or fictitious truth, *Acta Biomaterialia*, 150, 48–57, 2022. doi: 10.1016/j.actbio.2022.07.063 (Scopus, Open Access).
4. **Kovrlija, I**., Locs, J., Loca, D. Incorporation of Barium Ions into Biomaterials: Dangerous Liaison or Potential Revolution? *Materials*, 14(19), 2021, p. 5772. doi: 10.3390/ma14195772 (Scopus, Open Access).

MAIN RESULTS OF THE THESIS

Optimization of OCP synthesis methodology

Despite the fact that the potential of OCP to stimulate bone regeneration is reported to be higher than that of HAp [3,42,43], a moderately narrow window of opportunity to obtain it and the complexity of synthesis hinders the scientific community, as well as industry, from proactive involvement [23,32]. Both key routes to obtain OCP have their advantages and disadvantages, and the main pros and cons are highlighted in Table 1.

Table 1

Advantages and Disadvantages of Precipitation and Hydrolysis Routes for OCP Synthesis [31, 44-47].

Precipitation		**Hydrolysis**	
Pros	**Cons**	**Pros**	**Cons**
Faster reaction	Minimum two precursors	Only one precursor	Slower reaction
Higher yields	Dose rate regulation	No dose rate	Yield is limited to the initial precursor amount
/	Higher temperatures (60 °C–80 °C)	Lower temperatures (25 °C–60 °C)	/
/	Washing of the precipitate needed	No washing step	/
/	pH regulation always needed	pH regulation could be avoided	/

Hydrolysis of low-temperature α-TCP to OCP

After considering the pros and cons of the synthesis pathways, the hydrolysis route aligned more with the proposed objectives of the PhD Thesis. According to the literature, both DCPD and α-TCP have been used as precursors in hydrolysis. However, DCPD has higher solubility than α-TCP, it can be more easily affected by carbon dioxide from the atmosphere, and in lower temperatures (< 30 °C), it takes months to transform to OCP [21]. Thus, α-TCP has been chosen as the sole precursor in OCP synthesis.

Traditionally, the synthesis of α-TCP involves heating the materials that contain calcium and phosphate, such as β-TCP, to temperatures of 1300 °C or higher for an extended duration (~ 2–3 h). This conventionally synthesized α-TCP manifests as a coarse powder necessitating subsequent milling, which yields particles with a wide size distribution and generates an

amorphous phase [44]. To avoid it and to use a more energy-efficient way, low-temperature α-TCP (LT-α-TCP) was made from ACP with high SSA (> 70 m^2/g) (precipitation from diammonium phosphate solution and calcium nitrate tetrahydrate solution) that was heat treated at 650 °C (Fig. 2) [44].

The following OCP synthesis was performed in the acidic media (0.0016 M orthophosphoric acid (H_3PO_4) from the aforementioned LT-α-TCP, with unremitting stirring, at room temperature (22 °C) [45]. The samples were dried at 37 °C (overnight), and, to evaluate whether the obtained OCP was pure, the products were subjected to multiple analysis techniques (see Fig. 2).

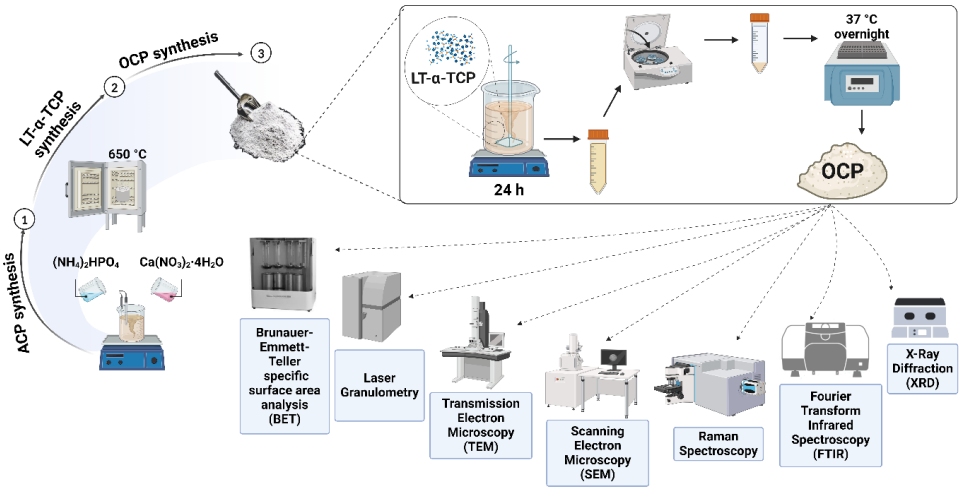

Fig. 2. General scheme of OCP synthesis methodology and overview of the used characterization methods in determining the OCP phase.

The as-synthesized sample (marked with OCP1) has been analyzed with a set of preselected characterization methods able to deliver the data on different levels. Phase compositions were studied with the X-ray diffraction technique (XRD, PANalytical Aeris diffractometer, The Netherlands), and the crystalline phase identification was done by using the PDF-2 database from the International Centre for Diffraction Data (ICDD). To get the information on the phases at the molecular level, Fourier transform infrared spectroscopy (FTIR, Nicolet iS 50, Thermo Scientific, USA) and Raman spectroscopy (LabRAM HR 800 microscope, Horiba Jobin Yvon, Japan) have been used as the chosen techniques. The morphology of the powders was characterized with scanning electron microscopy (SEM, Tescan Mira\LMU, Tescan, Czech Republic) and transmission electron microscopy (TEM, Tecnai F20, FEI). Particle size distribution was determined using laser granulometry (Malvern Mastersizer 3000), whereas specific surface area was measured using Brunnauer–Emmet–Teller method (BET, QUADRASORB SI and Quadra Win).

The XRD pattern of OCP is very specific. The characteristic low angle (100) maxima at 4.72 2θ degrees and a peak doublet at 9.44 (200) 2θ degrees and 9.77 (010) 2θ degrees (Fig 3 A), were shown in the obtained OCP1 [46]. Even though these markings make OCP easy to

recognize among other CaPs, the region of 25–35 2θ degrees is known to overlap with the XRD maxima of HAp (Fig. 3 A), due to the close relationship of OCP and HAp structures [46–48]. However, the lack of HAp maxima at 10.8 2θ degrees is one indicator of no or minimal HAp presence. Another important part to observe is the aforementioned doublet at 9.4 and 9.7 2θ degrees because the most intense OCP peak (4.7) is superimposed to the X-ray diffusion background, hence not easily accessible and affected by the plate-like morphology that causes preferential orientations. The influence of the background can later interfere with Rietveld's calculations used to determine the quantity of the specific phase.

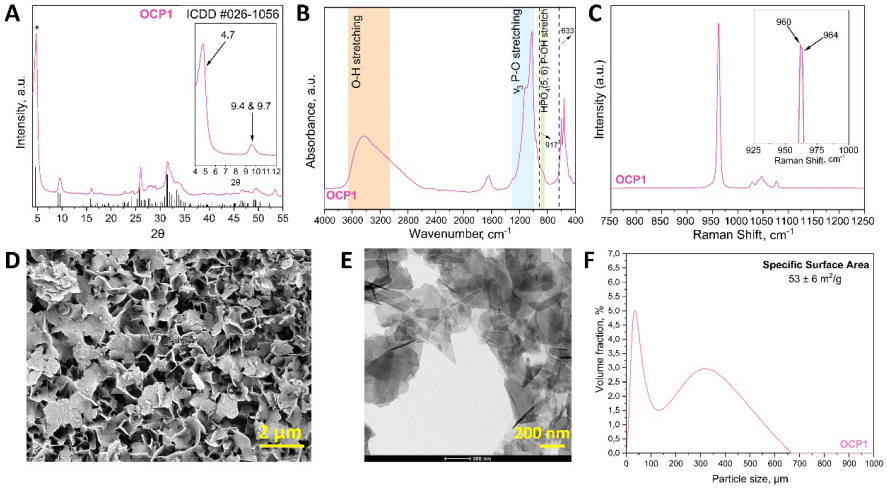

Fig. 3. A set of analyses confirming the obtained OCP purity: A – XRD diffractogram; B – FTIR spectra; C – Raman spectra; D – SEM micrograph; E – TEM micrograph; F – Particle size distribution and SSA (* – the XRD peak at 4.7 2θ degrees).

Another distinctive feature of OCP's unit cell is two HPO_4^{2-} crystallographic sites, labeled $HPO_4(5)$ and $HPO_4(6)$; their P–(OH) stretch and OH in-plane bend cannot be distinguished via the XRD method. The $HPO_4(5)$ group is situated in the hydrated layer, and the $HPO_4(6)$ group is located at the junction of the apatite and hydrated layers; however, they are different ($HPO_4(6)$ has a shorter and stronger intermolecular hydrogen bond than that of $HPO_4(5)$) [49]. HPO_4 groups are not found in HAp, and their presence can further discriminate between these two phases. Therefore, FTIR and Raman spectroscopy were used to examine the samples' molecular structure and help to confirm the purity of the OCP phase (Fig. 3 B and C) [49]. Specific OCP absorbance bands that differentiate it from other CaPs were highlighted in OCP1 spectra – HPO_4^{2-} bending and O–H stretching modes (Fig. 3 B, orange and green shading). The most significant HPO_4 absorbance bands assigned to OCP are: 1295 cm^{-1} (OH in-plane deformation mode) and 917 cm^{-1} (P(6)–(OH) stretch of a strongly hydrogen-bonded HPO_4^{2-} ion), also the v3 stretching mode of PO_4^{3-} and HPO_4^{2-}, at 1077 cm^{-1}, 1093 cm^{-1}, and 1121 cm^{-1}. The absence of a detectible 3572 cm^{-1} OH^- band for HAp is one of the pointers of a pure OCP formation (or at least with a negligible HAp presence, shown in [45]). OH^- absorbance band at 633 cm^{-1}, usually assigned to the OH^- libration movement in HAp, was found as a shoulder in

OCP (627 cm^{-1}); however, according to Fowler et al. [49], it also represents a libration movement of the $H_2O(4)$ water molecule of OCP. In Raman spectra, the most intense bands are located between 900–1000 cm^{-1}, corresponding to the ν_3 triple-degenerate asymmetric P–O stretching mode and partly to the ν_1 symmetric P–O stretching vibration. A specific band for OCP is located at 958 cm^{-1} (Fig. 3 C, most intense peak) [49]. However, the large mass may also be associated with the convolution of several crystalline phases composed of the main band at 960 cm^{-1} and the shoulder at 964 cm^{-1}, associated with ν_1 PO_4 of OCP, and it could indicate a low crystallized OCP phase.

OCP crystals exhibit plate-like morphology, and the sizes of the crystals depend on the synthesis route. The formation of the particular OCP crystals is thought to be connected to the Hartman–Perdok theory of periodic bond chains, which says that a constant path of strong bonds within the crystal structure has a portion of the lattice that is cut by a certain face (hkl) [47]. For OCP, the plates grow in the [001] direction, with the largest face (100), and these interconnections lead to the formation of spherical aggregates that resemble sand roses. SEM analysis (Fig. 3 D) showed the surface morphology of OCP1, which resembled small, loosely aggregated plate-like particles (2–5 μm in size, thickness in nm range), interconnected in a rose shape. Small plate-like crystals of different sizes were seen when the OCP's inner structure was analyzed with TEM (Fig. 3 E) (50–300 nm approximately). It was also noticed that crystals were overlapping and entwining, which led them to form agglomerates of different sizes that were seen in SEM. BET measurements showed that OCP1 had a large SSA of 53 ± 6 m^2/g. The high value of SSA may suggest higher physicochemical and biological reactivity of the material, which could have a very strong effect on the cells. The evolution of the particle size distribution (a bimodal curve, Fig. 3 F) showed that the smallest primary particle size was in the array of 5–25 μm, totaling in ~ 5 % volume. The occurrence of the secondary distribution in the range of 150–500 μm indicated that the particles were unevenly agglomerated.

The first objective of the research was successfully achieved, and it demonstrated the feasibility of obtaining pure OCP powder from LT-α-TCP. However, the yield of the product was ~ 100 mg per batch, which was not sufficient for potential application and subsequent *in vitro/in vivo* studies. Consequently, an endeavor to augment the product's yield was initiated.

OCP synthesis scale-up, phase formation kinetics and *in silico* model of the synthesis progression from LT-α-TCP to OCP

After obtaining pure OCP from LT-α-TCP (at room temperature in 24 h, OCP1), the next step was to optimize the settings and try to achieve a higher product yield. The synthesis methodology of LT-α-TCP hydrolysis was scaled up a hundredfold (100 mg → 1g → 10 g). During the process of scale-up optimization, two additional aspects were followed – phase formation kinetics from LT-α-TCP to OCP and the development of an *in silico* model for tracking the stage of the OCP synthesis.

OCP synthesis scale-up

The acquired data have shown that with a constant liquid-to-solid ratio of the precursors, the time of the OCP synthesis has increased with the amount of the initial LT-α-TCP used. In the tenfold scale-up, the OCP phase was achieved after 72 h (OCP2, 1 g), and in the hundredfold scale-up, OCP was obtained after 180 h (OCP3, 10 g).

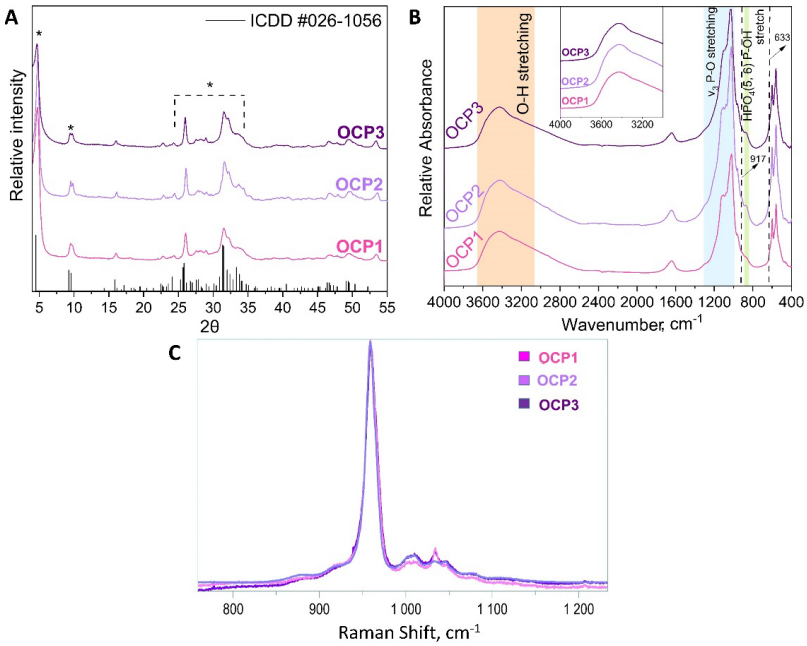

Fig. 4. Final OCP phases obtained in three levels of scale-up. A –XRD pattern; * marks the main maxima mentioned in the text, and the reference simulated pattern (ICDD entry #026-1056) corresponds to the main maxima of the OCP triclinic phase; B – FTIR spectra; C – Raman spectra.

Characteristic XRD peaks of OCP have been detected – 4.7 degrees and a doublet at 9.4 and 9.7 2θ degrees (Fig. 4 A) [23,50]. Same as in the original synthesis level (OCP1, 100 mg), the pattern in the region of 25–35 2θ degrees was not very well resolved [20]. FTIR ν_3P–O stretching mode at 1300–1000 cm^{-1}, for the OCP2 and OCP3 (Fig. 4 B), clearly showed the

strongest lines expected for the OCP phase, and in Raman, the ν_1P–O stretching mode was accentuated (Fig. 4 C). The assignment of the most specific bands of OCP was discussed in the previous section. To observe the possible variances of composition within a single sample, micro and macro spots in Raman were recorded and discussed within the manuscript [45]. The obtained results suggested that the formation and/or dissolution of the phases were closely linked to the size of the starting powder's grains (or aggregates).

According to the laser granulometry, both OCP2 and OCP3 had similar particle sizes as OCP1, whereas their specific surface area was slightly higher than that of OCP1, 66 ± 5 m^2/g and 63 ± 8 m^2/g, respectively.

OCP phase formation kinetics

A detailed progression of the OCP phase formation has been followed during the synthesis of OCP3 (10 g) as a function of time. The total duration of the synthesis was 180 h, and the pH was monitored throughout the entire time. Throughout the synthesis monitoring, the focus was placed on important XRD maxima of all present phases and the variations in the reaction media pH. XRD patterns were used to visualize the gradual evolution of the crystalline phase from LT-α-TCP, as an initial phase, towards the combination of LT-α-TCP, DCPD, and OCP, and ending with the pure OCP phase (Fig. 5) [51,52]. The characteristic maxima that were highlighted are maxima at 4.7, 9.4 and 9.7 2θ degrees (belonging to OCP triclinic structure), 11.7, 20.9 and 29.2 2θ degrees (belonging to DCPD monoclinic structure) and 12.1, 22.1 and 22.9 2θ degrees (belonging to α-TCP monoclinic structure).

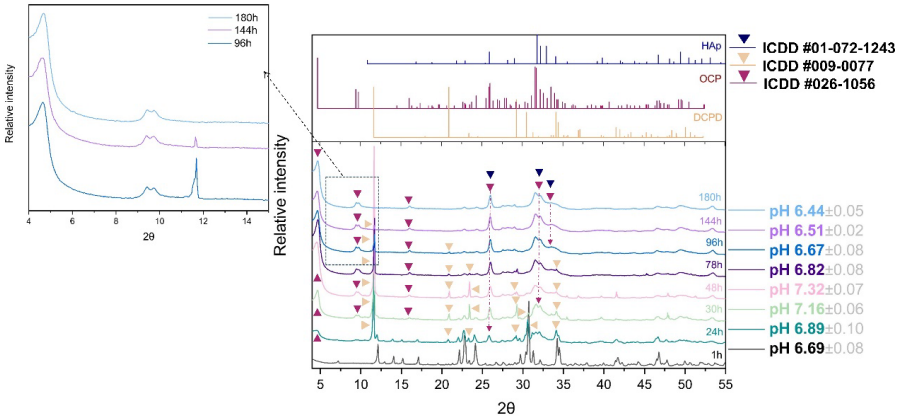

Fig. 5. Synthesis of OCP3: XRD patterns showing the transition from LT-α-TCP, via DCPD to OCP phase, supplemented by the change in pH. The reference simulated patterns (ICDDs) correspond to the main maxima of the HAp, OCP, and DCPD [45].

The variations in the pH helped to discern the underlying chemical background (through chemical equations) of the phase changes, as the release of ions (e.g. OH^-, H^+) directly influences the solution pH. The general chemical equation displaying the hydrolysis of LT-α-TCP to OCP is the following: $3Ca_3(PO_4)_2 + 7H_2O \rightarrow Ca_8(HPO_4)_2(PO_4)_4 \cdot 5H_2O + Ca(OH)_2$. However, this equation implies an increase in the solution pH, which is connected to the direct uptake of PO_4^{3-} into the OCP phase and an equivalent release of soluble calcium hydroxide

($Ca(OH)_2$). As it was seen by the XRD patterns, DCPD was formed as an intermediary phase during the hydrolysis, which was not shown in this equation, hence the general chemical reaction is inadequate. With the observed changes in the pH (Fig. 5) and with the indispensable help of Professor Christian Rey from the University of Toulouse, the progression from LT-α-TCP to OCP was broken down into several distinct steps, as outlined below.

1. Dissolution step.

Before the addition of LT-α-TCP, the orthophosphoric acid solution pH was 2.80 ± 0.15, and once the precursor was added, the solution pH rapidly increased and stabilized at 6.69 ± 0.08 after 1 h. This initial event aligned with the fast dissolution of LT-α-TCP and could be represented by the equation $Ca_3(PO_4)_2 + 3H_2O \rightarrow 3Ca^{2+} + H_2PO_4^- + HPO_4^{2-} + 3OH^-$ (which corresponds to the 6.69 pH). Moreover, it ensures a release of OH^-, which sets the reaction medium at an almost neutral pH related to the buffering zone of orthophosphate anions. A distinct change in the phases was evident when the progression was observed via SEM. The presence of LT-α-TCP, presented with thin thread-like crystals, was seen; however, due to the ongoing dissolution process, small needle- or plate-like crystals started to appear within the LT-α-TCP agglomerates (Fig. 6, 1 h).

2. Precipitation step.

Given the solubility characteristics of LT-α-TCP and the initial acidic dissolution that shifted the solution pH towards an alkaline environment, the resulting solution is supersaturated regarding OCP, DCPD, and even HAp. Nevertheless, HAp had a smaller incline to form than the other two phases due to their better ability to nucleate and grow (higher crystallization rates) [53,54].

3. Growth step of DCPD and OCP phases.

Due to the preferential crystal growth rate of DCPD, LT-α-TCP to DCPD conversion was faster than that of LT-α-TCP to OCP. The following equation can be used as a representation of the process: $Ca_3(PO_4)_2 + 3H_2O \rightarrow 3Ca^{2+} + H_2PO_4^- + HPO_4^{2-} + 3OH^-$, raising the pH up to 7.32 ± 0.07 (Fig. 5). XRD patterns follow the chemical equation, and at the highest pH value (48 h, OCP3 synthesis), the (020) maximum, 11.7 2θ degrees, intensifies markedly compared to any other diffraction peak, pointing at the presence of DCPD (Fig. 5). Hydrolysis, as a continuous process, resulted in a mixture of OCP and DCPD in the system. With making a parallel to SEM findings, it could be corroborated that at 24 h, 30 h, and 48 h time points, when the amount of DCPD increased, a gradual change from thread-like particles to larger and thicker plate-like particles was observed (Fig. 6, 24 h, 30 h, 48 h). Larger and considerably more massive plates were ascribed to DCPD (Fig. 6, 30 h, yellow arrow) and smaller, thinner plate-like crystals to OCP (Fig. 6, 30 h, yellow circle). However, this is difficult to differentiate due to the high morphological similarity of the two phases.

4. DCPD to OCP conversion step.

By complete dissolution of LT-α-TCP, DCPD became the most soluble phase of the system and the precursor for the transformation into OCP, showed in the final equation:

$8\ CaHPO_4 \cdot 2H_2O \rightarrow Ca_8(PO_4)_4(HPO_4)2 \cdot 5H_2O + 2H_3PO_4 + 11H_2O.$

This reaction leads to the release of protons into the solution, which, together with the buffering properties of the present phosphate medium, results in the final pH of 6.44 ± 0.05. At the end

of the synthesis, OCP's plate-like morphology, with noticed fragmentation of the larger particles and the presence of the spherical aggregates could be detected (Fig. 6, 180 h).

By using the Rietveld refinement and SEM [52], the progression of the OCP and intermediary phase formation has also been quantified and, together with their morphology, displayed in Fig. 6. The phases evolved with time from 100 % of LT-α-TCP (in the first hour) to ~ 37 % of DCPD and ~ 63 % of OCP (at 27 h) and ended with ~ 100 % of OCP.

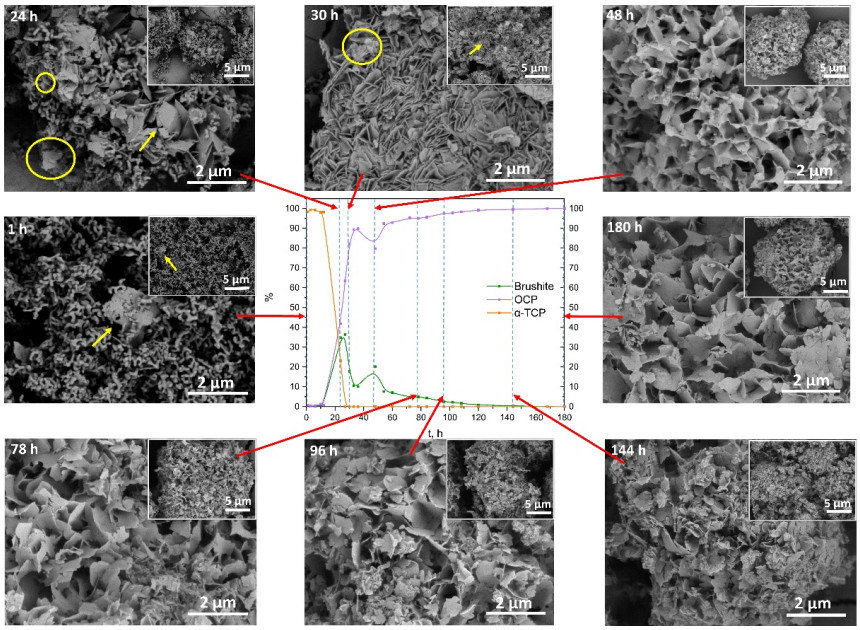

Fig. 6. SEM micrographs of OCP formation (scale bar 5 µm and 2 µm) connected (red arrow) to the according point (dashed line) in the phase content diagram constructed on the XRD quantitative data. The yellow arrow directs to potential DCPD particles, while the yellow circle marks the potential OCP plates [45].

To check if the scaled-up technology affects the cytocompatibility of OCP, the intermediate products and final products of the OCP3 synthesis were subjected to direct contact with human bone mesenchymal stem cells (hBMSC) and the results were compared with OCP1 and OCP2 (Fig. 7 A). The 'Control' represented cells cultivated on polystyrene without CaP powder samples. The results yielded > 80 % of cell metabolic activity. This also indicated that if the technology were upgraded even more in the future, the trace amounts of transient phases and the final phase would be safe for the cells of the bone microenvironment. Visual analysis coupled with immunofluorescent staining, intended to show the cell morphology, indicated a possible CaP particle internalization within the cells when hBMSCs were subjected to direct contact with the powders (Fig. 7 B).

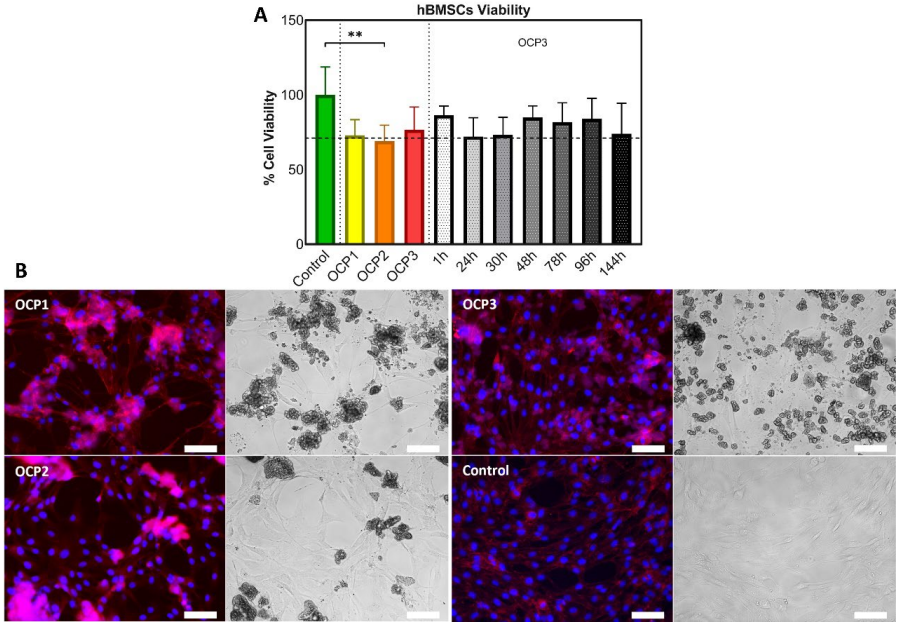

Fig. 7. A – *In vitro* cell viability of OCP1, OCP2, OCP3 and intermediary phases during OCP3 synthesis. Based on one-way ANOVA with Tukey's correction, significant differences between groups of samples were indicated with asterisks (** for $p \leq 0.01$). B – hBMSCs morphology on the third day of cultivation in direct contact with final OCP samples (OCP1, OCP2, OCP3) in the concentration of 0.5 mg/mL. Control represented cells on polystyrene. Immunofluorescent (left columns) and bright-field (right columns) microscopy. Image bar scale: 125 µm.

In silico **modelling of the synthesis progression from LT-α-TCP to OCP**

Conducting comprehensive laboratory experiments is essential for producing and evaluating engineered biomaterials. This includes synthesizing and characterizing their properties and examining the biocompatibility between the surface's physicochemical properties and the adjacent biological microenvironment. However, the chemistry of CaP is exceptionally diverse, allowing for the potential formation of numerous phases depending on specific experimental conditions. Furthermore, the actual experiment conditions may deviate slightly from the intended ones, and this could be attributed to factors such as experimental errors or approximations. To advance towards the new era of artificial intelligence (AI) and to strengthen the collaboration with the University of Eastern Piedmont, together with Dr. M. Nascimben et al. [55] we have developed an automated analysis sequence designed to create a decision support system for monitoring the synthesis progression from LT-α-TCP to OCP.

The goal was to combine the computational protocols capable of determining the synthesis stage (or potential end of it) and the data retrieved from the XRD and FTIR patterns from OCP3 synthesis (10 g yield, 180 h). The analysis sequence contained machine learning (ML)

techniques for feature ranking, spatial filtering, and dimensionality reduction, which were needed in order to tune the automatic recognition of the synthesis stages (Fig. 8).

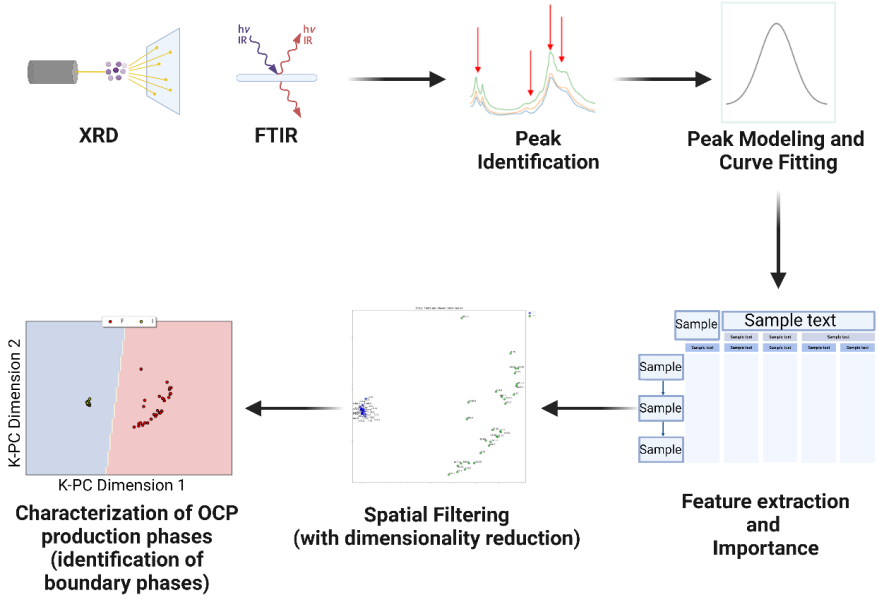

Fig. 8. Schematic process of establishing the machine learning technique for determining the stage of OCP production based on XRD and FTIR spectra [55].

The synthesis progression was monitored with XRD and FTIR (see the previous chapter), and the first two time points (i.e., 1 h and 24 h), as well as the last two time points (144 h and 180 h), were chosen as representative for the initial and final stage of the synthesis, respectively. The analysis pipeline then subjected this data to a preprocessing technique used in ML, called spatial filtering, which enhanced the separation between different classes or patterns from XRD/FTIR. This subset was then employed to recognize OCP production phases.

The combination of expertise in synthesizing and characterizing OCP and a newly developed algorithm capable of identifying at which stage the production of OCP is has brought a promising foundation for a decision support system explicitly tailored for OCP synthesis monitoring. Integration of XRD/FTIR data sets and AI would enable researchers to construct a more robust and informative feature set for training the machine-learning model, which would ultimately lead to a more balanced and accurate model with reduced bias and variance.

Application potential of OCP

As one of the important components of bone tissue inorganic phase, OCP has extensive application possibilities in bone tissue engineering. Its significance stems from the ability to release crucial calcium and phosphate ions in the human body, essential for regulating the new bone deposition. Up until now, OCP has been functionalized as a bone cement [34], a composite scaffold with different polymers (alginate, gelatin, collagen, PEGT, etc.) [35–37], as a coating on titanium or titanium alloy implants [29,38] and as a drug/ion delivery vehicle [23], but clinical applications of the OCP-based biomaterials currently remain at the starting point.

To test the OCP biological potential and to bridge the gap towards clinical application, in the second part of the PhD research, OCP was utilized in the development of two composite biomaterials for the biomedical field. Firstly, OCP was doped with doxorubicin hydrochloride to create an effective drug delivery system for bone cancer treatment. Secondly, OCP was combined with alginate in a composite coating on 3D-printed titanium alloys to test whether it could improve their corrosion resistance.

Octacalcium phosphate and doxorubicin hydrochloride: novel drug delivery system for cancer treatment

Doxorubicin hydrochloride (DOX, doxorubicin), derived from *Streptomyces peucetius var. caesius*, water-soluble and photosensitive, is one of the widely used representatives of anti-cancer drugs [56]. Even though DOX is an effective anti-neoplastic agent it causes multiple systemic toxicities, extending from nausea and hematopoietic suppression to an increased risk of doxorubicin-induced cardiomyopathy [57,58]. Moreover, only a small fraction of any systemically given dose reaches the surgical site. Thus, the use of local anticancer delivery systems could be a solution to achieve high drug levels at the cancer site. Exploring the inherent pathways of programmed cell death (PCD) such as apoptosis, necrosis, or ferroptosis is crucial for tissue engineering (to mimic natural tissue development), drug development (drugs exert their effects by inducing or inhibiting PCD), therapeutic strategies and normal cellular development (eliminating unwanted or damaged cells) [59,60]. Given that the malfunction of intracellular pathways is also a potential trigger for cancer initiation in the human body, comprehending whether PCD is attributed to apoptosis (the death of cells that occurs as a normal and controlled part of development) or ferroptosis (the death of cells that occurs due to genetic changes in iron homeostasis) can contribute to the development of innovative drug delivery systems for future cancer treatments.

Execution of OCP synthesis at room temperature has demonstrated the potential for *in situ* drug loading. The significance lies in the hypothesis that achieving drug loading during the initial stages of OCP formation can result in an exceptionally high drug encapsulation capacity [41]. Given that the stages of LT-α-TCP transformation to OCP involve the release of OH^- and HPO_4^{2-}, they also play a role in the formation of the hydrated layer in the OCP. This, in turn, reinforced the idea that incorporating DOX during the *in situ* OCP synthesis could potentially result in drug loading within the hydrated layer. At the same time, a high specific surface area

of OCP that was achieved and its plate-like particle morphology, potentially make OCP more effective and more favorable in regard to cell responses. Thus, to develop a novel DDS, the emphasis was placed on three steps:

1) **materials' physicochemical property profile** once it was functionalized with DOX in a large concentration range (from 1 wt% to 20 wt% of theoretical LT-α-TCP content);

2) ***in vitro* release kinetics of doxorubicin** during the period of six weeks; and

3) **assessment of the cytocompatibility and the mechanism of PCD**.

A schematic representation of the development of doxorubicin-loaded octacalcium phosphate (DOX-OCP) as a drug delivery system is shown in Fig. 9 [61].

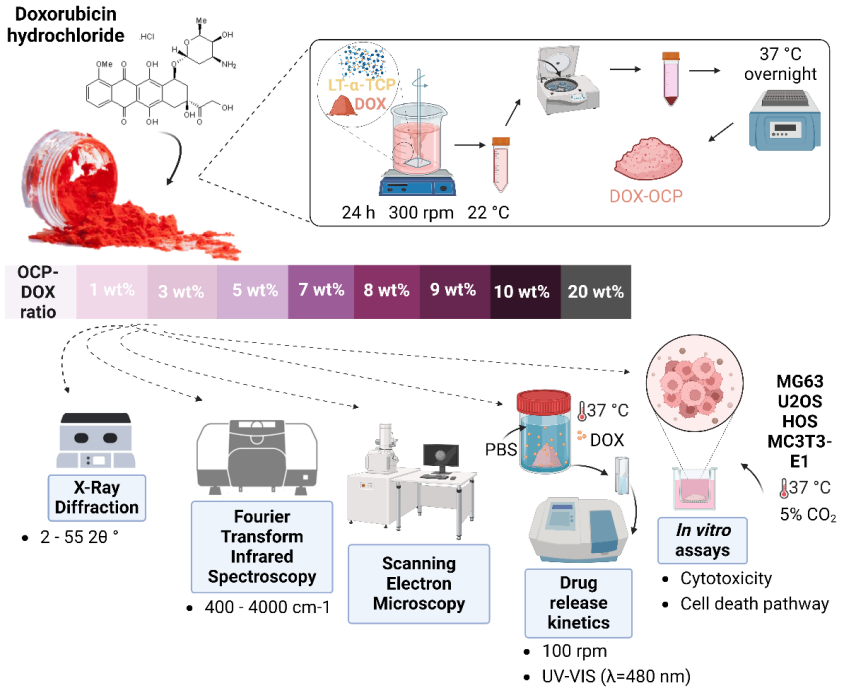

Fig. 9. Schematic representation of the development and characterization approach of doxorubicin-loaded octacalcium phosphate.

To test the maximum amount of DOX incorporation while still preserving the OCP phase 1 wt%, 3 wt%, 5 wt%, 7 wt%, 8 wt%, 9 wt%, 10 wt%, and 20 wt% DOX (of initial LT-α-TCP amount; 1DOX-OCP, 3DOX-OCP, 5DOX-OCP, 7DOX-OCP, 8DOX-OCP, 9DOX-OCP, 10DOX-OCP, 20DOX-CaP) were added to the OCP synthesis medium, and the synthesis lasted for 24 h. By means of XRD analysis, the representative OCP diffraction maxima (low angle (100) maximum, at 2θ = 4.7 degrees and a doublet (200) and (010) at 9.4 degrees and 9.7 degrees) have been detected in the synthesis products where up to 10 wt % of DOX was added (Fig. 10 A and B). If compared with pure OCP, DOX-OCP diffractograms exhibited a slight shift of the maxima 4.7 2θ degrees and 26.1 2θ degrees towards the lower 2θ degrees and a change in intensity. This indicates the lattice expansion in the DOX-OCP system, which

suggests that the drug was incorporated into the crystal structure of OCP. Moreover, the stabilization of the OCP structure depends on the amount of DOX used for the OCP-DOX synthesis. When the quantity of added DOX was above 10 wt%, it hindered the c-axis growth in the OCP structure and destabilized the overall transformation process from LT-α-TCP to OCP. XRD patterns of the tested materials showed that the prominent maxima for LT-α-TCP still persisted at 12.1 and 30.7 2θ degrees, with double maxima at approximately 22.8 and 34 2θ degrees (Fig. 10 A and B) [61]. This means that the drug was being adsorbed onto the LT-α-TCP phase, and the inability of LT-α-TCP to dissolve led to the formation of LT-α-TCP-DOX DDS and not DOX-OCP, which was the set goal.

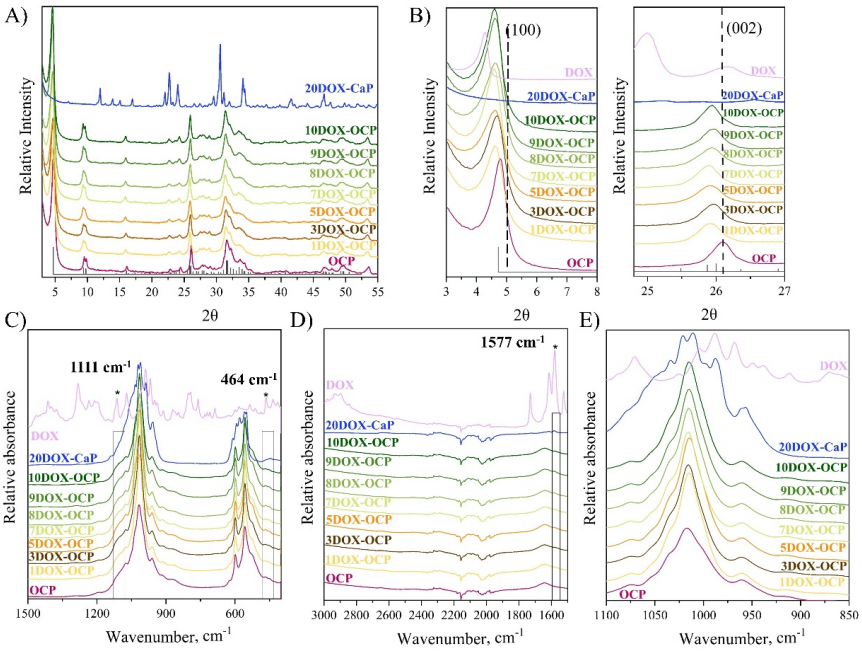

Fig. 10. Physicochemical property profile of DOX-OCP: A – XRD patterns, where ICDD entry #026-1056 corresponds to OCP triclinic phase; B – XRD patterns of OCP and DOX-OCPs. Maxima at 4.7 2θ degrees and 26.1 2θ degrees correspond to (100) and (002) planes, respectively; C, D – FTIR spectra of DOX-OCP. The star and the combining brackets mark the bands that have changed due to DOX incorporation.

Based on FTIR analysis, all of the products (aside 20DOX-CaP) have typical absorbance bands of the OCP phase (Fig. 10 C and D): 1077 cm^{-1}, 1296 cm^{-1}, and 1120 cm^{-1} from the PO_4^{3-} ν_3 stretching mode, and 524, 560, 601, and 627 cm^{-1} from PO_4^{3-} ν_4 domain. Furthermore, P-OH stretching at 917 cm^{-1} and 861 cm^{-1}, associated with the HPO_4^{2-} ion, has been seen. To a certain degree, the influence of strong DOX absorbance bands can also be seen in DOX-OCPs. The increasing intensity of the band in the 1570 cm^{-1} region (Fig. 10 D) signifies an antisymmetric COO^- stretch that could form a strong DOX absorbance band in that position. Moreover, DOX's prominent peak at ~ 1111 cm^{-1} led to a widening of the PO_4^{3-} ν_3 stretching

domain compared to the same region in pure OCP. Consequently, a slight shoulder band can be discerned in the FT-IR spectra of DOX-OCP systems (Fig. 10 C). Bands at 1193 cm^{-1}, associated with HPO_4(5), showed reduced intensity with the increase in DOX content in DOX-OCP systems, suggesting the beginning of OCP hydrolysis to CDHAp.

After the loading of DOX, OCP's plate-like particles appeared to be more overlapping and entwining with the increase of DOX amount in the samples, consequently directing them to form agglomerates in the size of 1–20 μm (Fig. 11 A–G). As it was found previously both in XRD and FTIR data analysis, the highest wt% of the theoretically applied amount of DOX (20 wt%) led to the inhibition of the OCP phase and preservation of elongated grain-like particles typical for α-TCP (Fig. 11 H) [61].

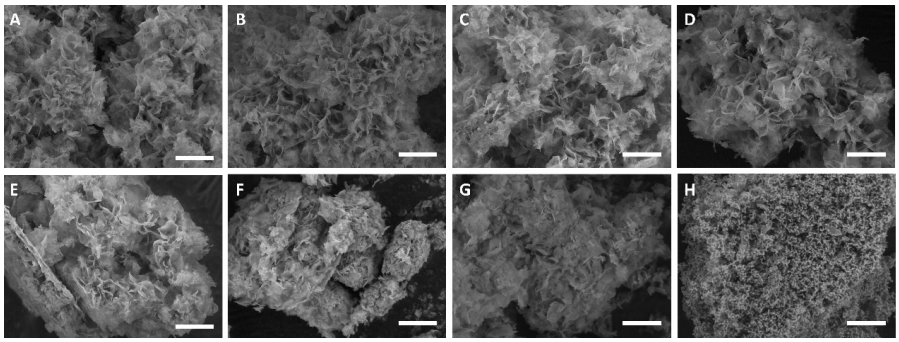

Fig. 11. SEM micrographs of DOX-OCP (1–10 wt%) and DOX-CaP (20 wt%): a – 1 wt%, b – 3 wt%, c – 5 wt%, d – 7 wt%, e – 8 wt%, f – 9 wt%, g – 10 wt%, and h – 20 wt%; scale bar is 5 μm.

For the theoretical DOX loading content of 1 wt%, 5 wt%, and 10 wt% (content), the amount of incorporated DOX was 0.093 ± 0.01 wt% with the loading efficiency of 9.6 ± 1.9 %, 1.54 ± 0.1 wt% with the loading efficiency of 20.85 ± 1.29 % and 2.02 ± 0.06 wt% with the loading efficiency of 21.8 ± 0.73 %, respectively (Fig. 12 A). Nonetheless, when 20 wt% of DOX was used in the OCP synthesis, which did not result in the OCP phase formation, the highest DOX incorporation of 2.66 ± 0.24 wt% was observed. However, the loading efficiency was relatively low – 15.99 ± 1.36 %. This simultaneous action of drug adsorption on the surface may have hindered the formation of OCP while exhibiting a higher detected drug content [61].

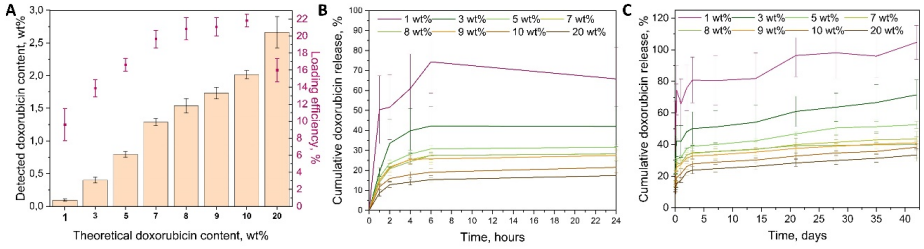

Fig. 12. A – Total DOX content and DOX loading efficiency in DOX loaded samples; B – DOX initial burst release in the first 24 h (%); and C – total DOX release during six weeks (%).

When analyzing DOX release from the developed DOX-OCP delivery systems, it was observed that within the first 24 hours, an early burst release of DOX occurred, ranging from approximately 17 % to 75 % (Fig. 12 B) from the total amount of DOX in the DDS. Subsequently, a sustained and consistent release was monitored for up to six weeks (Fig. 12 C). The initial burst release of doxorubicin molecules from the surface of OCP may be attributed to the physical adsorption of the drug, driven by electrostatic forces or hydrogen bonding. This occurs between the positively charged DOX molecules and the negatively charged OCP. In contrast, the continued release of DOX thereafter may be elucidated by a robust chemical interaction (Ca–O), which hinders the drug's escape from the DOX-OCP drug delivery system [61]. Furthermore, it was found that the cumulative release percentage plateau was inversely proportional to the theoretical doxorubicin content. For instance, in the case of 5DOX-OCP, 23.6 ± 1.6 % (28.00 ± 3.68 μg) was released after two hours, 38.9 ± 1.3 % (46.3 ± 4.2 μg) after 72 hours, and 52.5 ± 2.3 % (62.3 ± 5.8 μg) after 42 days. Meanwhile, the 10DOX-OCP reached 15.9 ± 1.3 % after two hours, 27.7 ± 1.7 % after 72 hours, and 38.3 ± 2.0 % after 42 days. It was observed that the lower the amount of incorporated doxorubicin, the higher the drug release rate. This observation may be attributed to the phase transformation of OCP to calcium-deficient hydroxyapatite [62,63], while lower drug amounts may lead to a faster transformation, consequently resulting in a quicker release. It was also determined that for all DOX-OCPs, the active substance was released gradually from the DDS, and the release profile followed the Freundlich isotherm [63].

***In vitro* assays**

The influence of DOX on MG63 (cancer cells) and MC3T3-E1 (normal cells) cells was studied to compare the cell response to the DOX-OCP drug delivery system. The inclusion of both cell lines allows for a comprehensive analysis of the system's effectiveness in bone cancer treatment and post-tumor excision treatments, offering insights into its potential to reduce metastases. The impact of DOX release on MG63 and MC3T3-E1 cell viability was assessed by exposing cells to OCP and DOX-OCPs (Fig. 13 A). Obtained results revealed that the culture medium treated with 1DOX-OCP, 5DOX-OCP, and 10DOX-OCP suppressed MG63 cells over the course of 7 days (54.1 %, 12.4 %, and 5.7 % of cell viability, respectively). On the other hand, between day 3 and day 7 of MC3T3-E1 cell cultivation, pure OCP, 1DOX-OCP, and

5DOX-OCP demonstrated a stimulatory effect, leading to an increase in cell viability (from 58.5 % to 93.4 % for 1DOX-OCP and from 36.9 % to 67.4 % for 5DOX-OCP). The increase in viability could be due to the cell's slow adjustment to stress caused by the changes or due to the presence of elevated Ca^{2+} ion concentration in the cell medium released from OCP that activated the extracellular calcium-sensing receptors and enhanced the proliferation of the cells [64,65]. The inhibitory effect of 10DOX-OCP on cell viability was notably greater than that of 5DOX-OCP and 1DOX-OCP, providing further evidence of its pronounced inhibitory effect on MG63 cells (Fig. 13 A).

As the preliminary viability tests showed that the DOX-OCP system is lethal to MG63 cells in all concentrations, the lowest incorporated DOX was chosen for further analysis. To assess PCD in osteosarcoma cells (OS), more variety in used cell lines was needed as OS have high genetic heterogeneity. Due to them having different phenotypes, they can express different differentiation capacities and tumour formation capacities and as a result, they can have diverse responses to certain treatments. Hence, 1DOX-OCP was retested with U2OS, MG63, and HOS cell lines. All of the three chosen cell lines are human cell lines commonly used in research; however, they have genetic and phenotype differences, which are preferred for pre-clinical assessments. Similar to the previous cytocompatibility assessments, the outcomes showed a noteworthy reduction in the viability of all examined osteosarcoma cells when exposed to 1DOX-OCP (MG63 – 0.32 ± 0.2 %, HOS – 0.17 ± 0.02 %, and U2OS – 0.25 ± 0.02 % of cell viability) (Fig. 13 B). The variances in cell viability between 1DOX-OCP and DOX may stem from the immediate accessibility of the drug at its final concentration in the positive control group (DOX), whereas doxorubicin from 1 wt % of DOX-OCP was released gradually over time, aligning with the findings of the *in vitro* drug release study (Fig. 12 B and C). To see whether the sensitivity of OS cells will increase towards the ferroptosis, DOX-OCP was combined with the ferroptosis inhibitor Ferrostatin-1 (Fer-1) [66]. The results showed no significant difference (Fig. 13 C) in OS cell survival in the presence of 1DOX-OCP+Fer-1 compared to 1DOX-OCP alone (Fig. 13 C). This pointed out that ferroptosis is not involved in DOX-OCP-induced cell death in OS cells. As ferroptosis was excluded, the next step was to check apoptosis by testing the levels of cleaved poly (ADP-ribose) polymerase (PARP) [67,68], considered as a guarantee of apoptosis by western blotting analysis. Results showed increased expression of cleaved PARP in HOS and MG-63 cells exposed to 1DOX-OCP, confirming the induction of apoptotic cell death (Fig. 13 D) [61]. The *in vitro* assays were done in collaboration with Dr. E. Panczyszyn from the University of Eastern Piedmont in Italy and with Dr. O. Demir from the Riga Technical University.

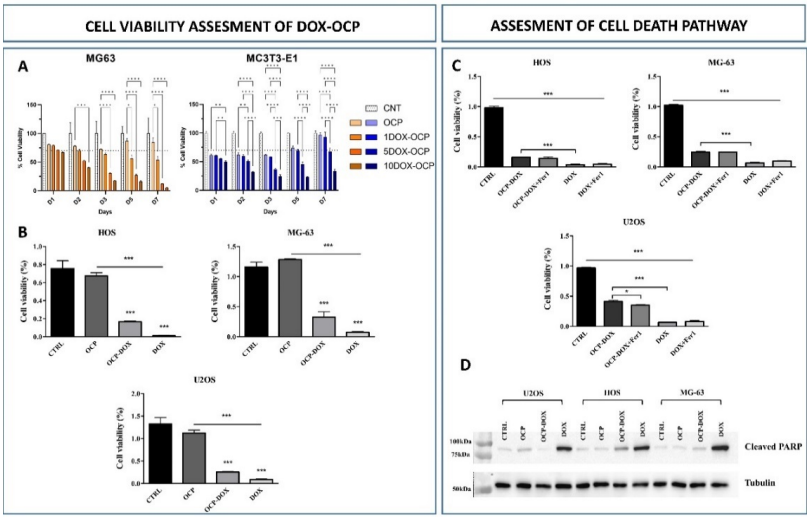

Fig. 13. Cell viability studies of DOX-OCP. A – Cell viability assay of MG63 cells and MC3T3-E1 cells with OCP, 1DOX-OCP, 5DOX-OCP, and 10DOX-OCP; B – Sensitivity of OS cells to 1DOX-OCP, OCP, and DOX; C – cell viability of U2OS, HOS, and MG63 cells in combination with 10 μM of Fer1 (1DOX-OCP+Fer-1, DOX+Fer-1); D – Protein levels of cleaved PARP. Histograms represent mean ± s.d.; $n = 3$; statistically significant differences: * for $p < 0.05$, ** for $p < 0.005$, *** for $p < 0.001$, **** for $p < 0.0001$.

OCP-embedded hydrogel coatings as metallic implant anticorrosion enhancers

Titanium alloys (Ti) are extensively utilized as biomaterials for fabricating dental and orthopedic implants, primarily owing to their exceptional mechanical characteristics and favorable biocompatibility. These alloys exhibit reasonable corrosion resistance under typical physiological conditions (pH ≈ 7), as their surfaces are naturally enveloped with dense protective oxide layers. Nevertheless, in inflammatory conditions that lower the environment pH, interactions with reactive oxygen species, lactic acid, hydroperoxyl radicals, and hypochlorous acid (released by leukocytes into the extracellular environment) affect the corrosion resistance of Ti surfaces. An effective strategy for improving corrosion resistance is surface modification of Ti by hydrogel coatings. To test whether the OCP particles improve the Ti protection even further, a collaboration was formed with Aalto University. Together with Dr. A. Bordbar-Khiabani et al. [38], sodium alginate (Alg) and OCP powder were combined in a composite coating and tested for their electrochemical behavior on Ti alloys. A schematic representation of the experimental setup is shown in Fig. 14.

In brief, aqueous Alg solution (3 wt %) and OCP were combined into a composite having a 70 : 30 wt% inorganic : organic phase ratio (later referred to as Alg/OCP) and further used to cover the surface of 3D-printed titanium substrates. Titanium alloy discs (d = 10 mm) – Ti Gr2 and Ti Gr23 alloy were covered with approximately 10 mg of the coatings (Alg and Alg/OCP) and compared with respect to their performance against corrosion. To test the effects of the

inflammatory conditions, three simulation media with pH 7.4 ± 0.1 (normal – N), pH 5.2 ± 0.1 (inflammatory – I) and pH 3.0 ± 0.2 (severe inflammatory – SI) were made, and immersion tests were performed at 37 ± 0.5 °C in slightly anaerobic conditions.

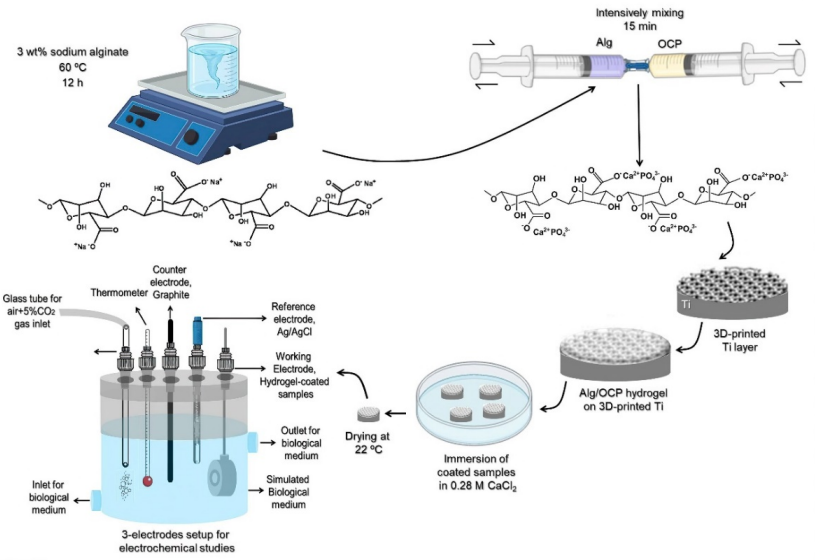

Fig. 14. Schematic representation of the experimental set-up for obtaining and electrochemical characterization of 3D printed Ti alloys with Alg/OCP coating [38].

Physicochemical properties of the coatings were characterized prior to (marked as Alg/OCP) and after one hour-long immersions in the respective media – marked as Alg/OCP N, I, SI (Fig. 15). Characteristic XRD diffraction maxima of OCP were observed, and an amorphous broad halo that was seen in the XRD pattern was specific to sodium-alginate biopolymer (Fig. 15 A). FTIR showed the vibrations of HPO_4^{2-} at 917 cm^{-1}, 875 cm^{-1}, 1007 cm^{-1}, and 1295 cm^{-1} that belong to OCP and a broad band centered at approximately 3500 cm^{-1}, which corresponds to the stretching vibrations of the hydroxyl groups (Fig. 15 B).

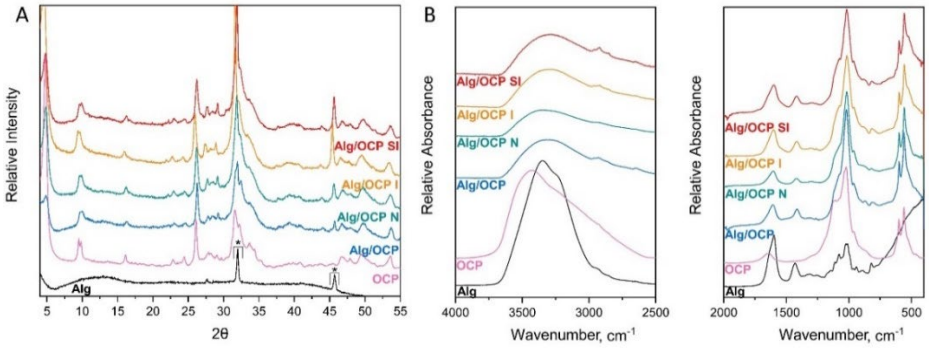

Fig. 15. Physico-chemical characterization of Alg/OCP coating prior to and after the immersion in the respective media (normal – N, inflammatory – I, and severely inflammatory – SI). A – XRD patterns, B – FTIR spectra in different wavenumber regions [38].

Electrochemical impedance spectroscopy (EIS) is usually used to characterize the electrochemical processes, such as the evaluation of the performance of protective coatings on metals against corrosion. The Nyquist plot was used as a frequency response plot and the Bode modulus was used to represent the gain and phase of a system as a function of frequency. The obtained results of EIS and the constant phase element (CPE) [69] (measurement of coating's capacity shown via CPE_{dl} (interface between a substrate and a solution) and Rct (resistance to charge transfer)) were presented and explained in detail within the A. Bordbar-Khiabani et al. study [38].

Shortly, the Nyquist plots for both inflammatory and severely inflammatory conditions illustrated a declining pattern in the capacitive loop diameters, which indicated a reduction in the corrosion resistance [69,70] and the Bode amplitude plot, shown in the low-frequency range of the impedance modulus, also corroborated this trend [38]. The Rct values of samples with Alg/OCP coatings were notably greater (23.09 ± 0.10 k$\Omega \cdot cm^2$ and 25.12 ± 0.39 k$\Omega \cdot cm^2$ for TiGr2 and TiGr23, respectively) than those of the bare 3D-printed Ti samples (17.63 ± 0.33 k$\Omega \cdot cm^2$ and 20.66 ± 0.73 k$\Omega \cdot cm^2$ for TiGr2 and TiGr23, respectively). This suggests that the Alg/OCP coating effectively forms a robust barrier, impeding the penetration of corrosive ions into the substrate. Additionally, the presence of OCP further enhanced the resistance (Rc) of Alg hydrogel (e.g., 12.33 ± 0.83 k$\Omega \cdot cm^2$ Alg and 18.84 ± 0.75 k$\Omega \cdot cm^2$ Alg/OCP for TiGr2), suggesting that OCP particles may fortify the crosslinking degree of the Alg hydrogel coating and enhance the bonding force at the interface between the coating and the substrate in normal conditions. This led to an increase in the coating's density. Consequently, the Alg/OCP-coated samples exhibited higher Rc values than those coated with pure Alg. The reduction in Rc values observed in coated samples under inflammatory and severe inflammatory conditions (e.g., I: 7.15 ± 0.91 k$\Omega \cdot cm^2$ Alg/OCP and SI: 3.01 ± 0.53 k$\Omega \cdot cm^2$ Alg/OCP for TiGr2) can be attributed to the hydrogels becoming less stable due to their dissolution by hydrochloric acid and hydrogen peroxide [38,69].

CONCLUSIONS

1. Tenfold and hundredfold scale-up of the hydrolysis (from LT-α-TCP) yielded the final 1 g and 10 g of pure OCP; however, the increase of the synthesis yield required the extension of the synthesis duration from 72 h (1 g) to 180 h (10 g).

2. LT-α-TCP transformation into the OCP phase transpired through brushite as an intermediary phase.

3. During the synthesis of the DOX-OCP drug delivery system, the addition of > 10 wt% of doxorubicin (from the initial LT-α-TCP amount) inhibits OCP phase formation.

4. DOX-OCP alters the proliferation profile of MG63 and MC3T3 cells, which is influenced by both DOX concentrations in the cell medium and the contact time of DOX-OCP/cell environment.

5. Apoptosis was the primary pathway of programmed cell death induced in osteosarcoma cells by the DOX-OCP drug delivery system.

6. OCP particles in the alginate hydrogel matrix increased the electrical charge transfer resistance at the Ti substrate and alginate/OCP coating interface.

REFERENCES

[1] S. Liu, B. Wang, S. Fan, Y. Wang, Y. Zhan, D. Ye, Global burden of musculoskeletal disorders and attributable factors in 204 countries and territories : a secondary analysis of the Global Burden of Disease 2019 study, BMJ Open. 12 (2022). https://doi.org/10.1136/bmjopen-2022-062183.

[2] B.E. Wilson, S. Jacob, M.L. Yap, J. Ferlay, F. Bray, M.B. Barton, Estimates of global chemotherapy demands and corresponding physician workforce requirements for 2018 and 2040: a population-based study, Lancet Oncol. 20 (2019) 769–780. https://doi.org/10.1016/S1470-2045(19)30163-9.

[3] T. Albrektsson, C. Johansson, Osteoinduction, osteoconduction and osseointegration, Eur Spine J. 10 (2001) 96–101.

[4] C. Rey, C. Combes, C. Drouet, M.J. Glimcher, Bone mineral: Update on chemical composition and structure, Osteoporos. Int. 20 (2009) 1013–1021. https://doi.org/10.1007/s00198-009-0860-y.

[5] H. Yuan, H. Fernandes, P. Habibovic, J. De Boer, A.M.C. Barradas, A. De Ruiter, W.R. Walsh, C.A. Van Blitterswijk, J.D. De Bruijn, Osteoinductive ceramics as a synthetic alternative to autologous bone grafting, Proc. Natl. Acad. Sci. U. S. A. 107 (2010) 13614–13619. https://doi.org/10.1073/pnas.1003600107.

[6] T. Ariizumi, H. Kawashima, H. Hatano, T. Yamagishi, N. Oike, Osteoinduction and Osteoconduction with Porous Beta-Tricalcium Phosphate Implanted after Fibular Resection in Humans, J. Biomater. Nanobiotechnol. 10 (2019) 159–173. https://doi.org/10.4236/jbnb.2019.103009.

[7] R.Z. LeGeros, Properties of osteoconductive biomaterials: Calcium phosphates, Clin. Orthop. Relat. Res. (2002) 81–98. https://doi.org/10.1097/00003086-200202000-00009.

[8] W. Habraken, P. Habibovic, M. Epple, M. Bohner, Calcium phosphates in biomedical applications: Materials for the future?, Mater. Today. 19 (2016) 69–87. https://doi.org/10.1016/j.mattod.2015.10.008.

[9] S. V Dorozhkin, M. Epple, Biological and Medical Significance of Calcium Phosphates, Angew. Chem. Int. Ed. 41 (2002) 3130–3146.

[10] T. Wach, M. Kozakiewicz, Fast-Versus Slow-Resorbable Calcium Phosphate Bone Substitute Materials — Texture Analysis after 12 Months of Observation, Materials (Basel). 13 (2020) 3854.

[11] T.J. Brunner, R.N. Grass, M. Bohner, W.J. Stark, Effect of particle size, crystal phase and crystallinity on the reactivity of tricalcium phosphate cements for bone reconstruction, J. Mater. Chem. 17 (2007) 4072–4078. https://doi.org/10.1039/b707171j.

[12] Uskokovic Vuk, T.A. Desai, Phase composition control of calcium phosphate nanoparticles for tunable drug delivery kinetics and treatment of osteomyelitis. I. Preparation and drug release, J. Biomed. Mater. Res. - Part A. 101 A (2013) 1416–1426. https://doi.org/10.1002/jbm.a.34426.

[13] G. Daculsi, R.Z. LeGeros, E. Nery, K. Lynch, B. Kerebel, Transformation of biphasic calcium phosphate ceramics in vivo : Ultrastructural and physicochemical characterization, J. Biomed. Mater. Res. 23 (1989) 883–894.

[14] M.S. Johnsson, G.H. Nancollas, The Role of Brushite and Octacalcium Phosphate in Apatite Formation, Crit. Rev. Oral Biol. Med. 3 (1992) 61–82. https://doi.org/10.1177/10454411920030010601.

[15] J. Vecstaudza, M. Gasik, J. Locs, Amorphous calcium phosphate materials: Formation, structure and thermal behaviour, J. Eur. Ceram. Soc. 39 (2019) 1642–1649. https://doi.org/10.1016/j.jeurceramsoc.2018.11.003.

[16] M. Mosina, J. Locs, Synthesis of amorphous calcium phosphate: A review, Key Eng. Mater. 850 KEM (2020) 199–206. https://doi.org/10.4028/www.scientific.net/KEM.850.199.

[17] N. Temizel, G. Girisken, A.C. Tas, Accelerated transformation of brushite to octacalcium phosphate in new biomineralization media between 36.5 °c and 80 °c, Mater. Sci. Eng. C. 31 (2011) 1136–1143. https://doi.org/10.1016/j.msec.2011.04.009.

[18] A. Dosen, R.F. Giese, Thermal decomposition of brushite, CaHPO4 ·2H2O to monetite CaHPO4 and the formation of an amorphous phase, Am. Mineral. 96 (2011) 368–373. https://doi.org/10.2138/am.2011.3544.

[19] L.C.Chow, E.D. Eanes, Octacalcium phosphate, 2001. https://doi.org/10.1007/springerreference_39293.

[20] C.C. Rey, C. Combes, C. Drouet, Synthesis and physical chemical characterizations of octacalcium phosphate-based biomaterials for hard-tissue regeneration, 2019. https://doi.org/10.1016/B978-0-08-102511-6.00008-X.

[21] O. Suzuki, G. Insley, Octacalcium Phosphate Biomaterials, Woodhead Publishing Series in Biomaterials, 2020.

[22] S. Ban, J. Hasegawa, T. Jinde, Phase Transformation of Octacalcium Phosphate in vivo and in vitro, Dent. Mater. J. 11 (1992) 130–140217. https://doi.org/10.4012/dmj.11.130.

[23] I. Kovrlija, J. Locs, D. Loca, Octacalcium phosphate: Innovative vehicle for the local biologically active substance delivery in bone regeneration, Acta Biomater. 135 (2021) 27–47. https://doi.org/10.1016/j.actbio.2021.08.021.

[24] T. Anada, A. Araseki, S. Matsukawa, T. Yamasaki, S. Kamakura, O. Suzuki, Effect of octacalcium phosphate ionic dissolution products on osteoblastic cell differentiation, Key Eng. Mater. 361-363 I (2008) 31–34. https://doi.org/10.4028/www.scientific.net/kem.361-363.31.

[25] Y. Sai, Y. Shiwaku, T. Anada, K. Tsuchiya, T. Takahashi, O. Suzuki, Capacity of octacalcium phosphate to promote osteoblastic differentiation toward osteocytes in vitro, Acta Biomater. 69 (2018) 362–371. https://doi.org/10.1016/j.actbio.2018.01.026.

[26] Y. Shiwaku, K. Tsuchiya, L. Xiao, O. Suzuki, Effect of calcium phosphate phases affecting the crosstalk between osteoblasts and osteoclasts in vitro, J. Biomed. Mater. Res. - Part A. 107 (2019) 1001–1013. https://doi.org/10.1002/jbm.a.36626.

[27] N. Miyatake, K.N. Kishimoto, T. Anada, H. Imaizumi, E. Itoi, O. Suzuki, Effect of partial hydrolysis of octacalcium phosphate on its osteoconductive characteristics, Biomaterials. 30 (2009) 1005–1014. https://doi.org/10.1016/j.biomaterials.2008.10.058.

[28] F. Barrère, C.M. Van Der Valk, R.A.J. Dalmeijer, G. Meijer, C.A. Van Blitterswijk, K. De Groot, P. Layrolle, Osteogenecity of octacalcium phosphate coatings applied on

porous metal implants, J. Biomed. Mater. Res. - Part A. 66 (2003) 779–788. https://doi.org/10.1002/jbm.a.10454.

[29] P. Habibovic, C.M. Van Der Valk, C.A. Van Blitterswijk, K. De Groot, G. Meijer, Influence of octacalcium phosphate coating on osteoinductive properties of biomaterials, J. Mater. Sci. Mater. Med. 15 (2004) 373–380. https://doi.org/10.1023/B:JMSM.0000021104.42685.9f.

[30] R.Z. LeGeros, Preparation of Octacalcium Phosphate (OCP): A Direct Fast Method, Calcif. Tissue Int. (1985) 194–197.

[31] S. Graham, P.W. Brown, The low temperature formation of octacalcium phosphate, J. Cryst. Growth. 132 (1993) 215–225. https://doi.org/10.1016/0022-0248(93)90265-X.

[32] Christophe Drouet, Apatite formation: why it may not work as planned, and how to conclusively identify apatite compounds., Biomed Res. Int. 2013 (2013) Article ID 490946. http://dx.doi.org/10.1155/2013/490946.

[33] O. Suzuki, Octacalcium phosphate (OCP)-based bone substitute materials, Jpn. Dent. Sci. Rev. 49 (2013) 58–71. https://doi.org/10.1016/j.jdsr.2013.01.001.

[34] O. Demir, A. Pylostomou, D. Loca, Octacalcium phosphate phase forming cements as an injectable bone substitute materials : Preparation and in vitro structural study, Biomater. Adv. J. 157 (2024). https://doi.org/10.1016/j.bioadv.2023.213731.

[35] Y. Tanuma, T. Anada, Y. Honda, T. Kawai, S. Kamakura, S. Echigo, O. Suzuki, Granule size-dependent bone regenerative capacity of octacalcium phosphate in collagen matrix, Tissue Eng. - Part A. 18 (2012) 546–557. https://doi.org/10.1089/ten.tea.2011.0349.

[36] T. Fuji, T. Anada, Y. Honda, Y. Shiwaku, H. Koike, S. Kamakura, K. Sasaki, O. Suzuki, Octacalcium phosphate-precipitated alginate scaffold for bone regeneration, Tissue Eng. - Part A. 15 (2009) 3525–3535. https://doi.org/10.1089/ten.tea.2009.0048.

[37] O. Suzuki, Y. Shiwaku, R. Hamai, Octacalcium phosphate bone substitute materials: Comparison between properties of biomaterials and other calcium phosphate materials, Dent. Mater. J. 39 (2020) 187–199. https://doi.org/10.4012/dmj.2020-001.

[38] A. Bordbar-Khiabani, I. Kovrlija, J. Locs, D. Loca, M. Gasik, Octacalcium Phosphate-Laden Hydrogels on 3D-Printed Titanium Biomaterials Improve Corrosion Resistance in Simulated Biological Media, Int. J. Mol. Sci. 24 (2023). https://doi.org/10.3390/ijms241713135.

[39] M.R. Newman, D.S.W. Benoit, Local and targeted drug delivery for bone regeneration, Curr. Opin. Biotechnol. 40 (2016) 125–132. https://doi.org/10.1016/j.copbio.2016.02.029.

[40] A. Lebugle, A. Rodrigues, P. Bonnevialle, J.J. Voigt, P. Canal, F. Rodriguez, Study of implantable calcium phosphate systems for the slow release of methotrexate, Biomaterials. 23 (2002) 3517–3522.

[41] Q.L. Tang, Y.J. Zhu, J. Wu, F. Chen, S.W. Cao, Calcium phosphate drug nanocarriers with ultrahigh and adjustable drug-loading capacity: One-step synthesis, in situ drug loading and prolonged drug release, Nanomedicine Nanotechnology, Biol. Med. 7 (2011) 428–434. https://doi.org/10.1016/j.nano.2010.12.005.

[42] O. Suzuki, S. Kamakura, T. Katagiri, M. Nakamura, B. Zhao, Y. Honda, R. Kamijo,

Bone formation enhanced by implanted octacalcium phosphate involving conversion into Ca-deficient hydroxyapatite, Biomaterials. 27 (2006) 2671–2681. https://doi.org/10.1016/j.biomaterials.2005.12.004.

[43] Y. Murakami, Y. Honda, T. Anada, H. Shimauchi, O. Suzuki, Comparative study on bone regeneration by synthetic octacalcium phosphate with various granule sizes, Acta Biomater. 6 (2010) 1542–1548. https://doi.org/10.1016/j.actbio.2009.10.023.

[44] Z. Irbe, D. Loca, A. Pura, L. Berzina-Cimdina, Synthesis and properties of α-tricalcium phosphate from amorphous calcium phosphate as component for bone cements, Key Eng. Mater. 721 KEM (2017) 182–186. https://doi.org/10.4028/www.scientific.net/KEM.721.182.

[45] I. Kovrlija, K. Menshikh, O. Marsan, C. Rey, C. Combes, J. Locs, D. Loca, Exploring the Formation Kinetics of Octacalcium Phosphate from Alpha-Tricalcium Phosphate : Synthesis Scale-Up , Determination of Transient Phases , Their Morphology and Biocompatibility, Biomolecules. 13 (2023).

[46] W.E. Brown, M. Mathew, M.S. Tung, Crystal chemistry of octacalcium phosphate, Prog. Cryst. Growth Charact. 4 (1981) 59–87. https://doi.org/10.1016/0146-3535(81)90048-4.

[47] R.A. Terpstra, P. Bennema, Crystal morphology of octacalcium phosphate: Theory and observation, J. Cryst. Growth. 82 (1987) 416–426. https://doi.org/10.1016/0022-0248(87)90333-2.

[48] W.E. Brown, J.R. Lehr, J.P. Smith, A. William Frazier, Crystallography of octacalcium phosphate [5], J. Am. Chem. Soc. 79 (1957) 5318–5319. https://doi.org/10.1021/ja01576a068.

[49] B.O. Fowler, M. Marković, W.E. Brown, Octacalcium Phosphate. 3. Infrared and Raman Vibrational Spectra, Chem. Mater. 5 (1993) 1417–1423. https://doi.org/10.1021/cm00034a009.

[50] M. Robin, S. Von Euw, G. Renaudin, S. Gomes, J.M. Krafft, N. Nassif, T. Azaïs, G. Costentin, Insights into OCP identification and quantification in the context of apatite biomineralization, CrystEngComm. 22 (2020) 2728–2742. https://doi.org/10.1039/c9ce01972c.

[51] N. Döbelin, Validation of XRD phase quantification using semi-synthetic data, Powder Diffr. 35 (2020) 262–275. https://doi.org/10.1017/S0885715620000573.

[52] N. Döbelin, Interlaboratory study on the quantification of calcium phosphate phases by Rietveld refinement, Powder Diffr. 30 (2015) 231–241. https://doi.org/10.1017/S088571561500038X.

[53] J.C. Heughebaert, G.H. Nancollas, Kinetics of crystallization of octacalcium phosphate, J. Phys. Chem. 88 (1984) 2478–2481. https://doi.org/10.1021/j150656a012.

[54] J.P. Barone, G.H. Nancollas, The Seeded Growth of Calcium Phosphates. The Kinetics of Growth of Dicalcium Phosphate Dihydrate on Enamel, Dentin, and Calculus, J. Dent. Res. 57 (1978) 153–161. https://doi.org/10.1177/00220345780570010901.

[55] M. Nascimben, I. Kovrlija, J. Locs, D. Loca, L. Rimondini, Fusion and classification algorithm of octacalcium phosphate production based on XRD and FTIR data, Sci. Rep. (2024) 1–11. https://doi.org/10.1038/s41598-024-51795-0.

[56] S. Sritharan, N. Sivalingam, A comprehensive review on time-tested anticancer drug doxorubicin, Life Sci. 278 (2021) 119527. https://doi.org/10.1016/j.lfs.2021.119527.

[57] S.Y. van der Zanden, X. Qiao, J. Neefjes, New insights into the activities and toxicities of the old anticancer drug doxorubicin, FEBS J. 288 (2021) 6095–6111. https://doi.org/10.1111/febs.15583.

[58] R.D. Olson, P.S. Mushlin, Doxorubicin cardiotoxicity: analysis of prevailing hypotheses, FASEB J. 4 (1990).

[59] X. Liu, S. Du, S. Wang, K. Ye, Ferroptosis in osteosarcoma: A promising future, Front. Oncol. 12 (2022) 1–9. https://doi.org/10.3389/fonc.2022.1031779.

[60] C.M. Pfeffer, A.T.K. Singh, Apoptosis: A target for anticancer therapy, Int. J. Mol. Sci. 19 (2018). https://doi.org/10.3390/ijms19020448.

[61] I. Kovrlija, E. Pańczyszyn, O. Demir, M. Laizane, M. Corazzari, J. Locs, D. Loca, Doxorubicin loaded octacalcium phosphate particles as controlled release drug delivery systems: Physico-chemical characterization, in vitro drug release and evaluation of cell death pathway, Int. J. Pharm. 653 (2024) 1–14. https://doi.org/10.1016/j.ijpharm.2024.123932.

[62] N. Ito, M. Kamitakahara, K. Ioku, Preparation and evaluation of spherical porous granules of octacalcium phosphate/hydroxyapatite as drug carriers in bone cancer treatment, Mater. Lett. 120 (2014) 94–96. https://doi.org/10.1016/j.matlet.2014.01.040.

[63] M. Parent, H. Baradari, E. Champion, C. Damia, M. Viana-trecant, Design of calcium phosphate ceramics for drug delivery applications in bone diseases : A review of the parameters affecting the loading and release of the therapeutic substance, J. Control. Release. 252 (2017) 1–17. https://doi.org/10.1016/j.jconrel.2017.02.012.

[64] M. Akutsu, Y. Kano, S. Tsunoda, K. Suzuki, Y. Yazawa, Y. Miura, Schedule-dependent interaction between paclitaxel and doxorubicin in human cancer cell lines in vitro, Eur. J. Cancer. 31 (1995) 2341–2346. https://doi.org/10.1016/0959-8049(95)00448-3.

[65] J. Wang, J. de Boer, K. de Groot, Proliferation and differentiation of osteoblast-like MC3T3-E1 cells on biomimetically and electrolytically deposited calcium phosphate coatings., J. Biomed. Mater. Res. A. 90 (2009) 664–670. https://doi.org/10.1002/jbm.a.32128.

[66] G. Miotto, M. Rossetto, M.L. Di Paolo, L. Orian, R. Venerando, A. Roveri, A.M. Vučković, V. Bosello Travain, M. Zaccarin, L. Zennaro, M. Maiorino, S. Toppo, F. Ursini, G. Cozza, Insight into the mechanism of ferroptosis inhibition by ferrostatin-1, Redox Biol. 28 (2020) 101328. https://doi.org/10.1016/j.redox.2019.101328.

[67] S. Wang, E.A. Konorev, S. Kotamraju, J. Joseph, S. Kalivendi, B. Kalyanaraman, Doxorubicin induces apoptosis in normal and tumor cells via distinctly different mechanisms: Intermediacy of H2O2- and p53-dependent pathways, J. Biol. Chem. 279 (2004) 25535–25543. https://doi.org/10.1074/jbc.M400944200.

[68] G.V. Chaitanya, J.S. Alexander, P.P. Babu, PARP-1 cleavage fragments: Signatures of cell-death proteases in neurodegeneration, Cell Commun. Signal. 8 (2010) 1–11. https://doi.org/10.1186/1478-811X-8-31.

[69] N. Yoshimoto, I. Wahyudhin, A. Yabuki, Colloids and Surfaces A : Physicochemical and Engineering Aspects Self-healing polymer coating with efficient delivery for

alginates and calcium nitrite to provide corrosion protection for carbon steel, Colloids Surfaces A Physicochem. Eng. Asp. 662 (2023) 130970. https://doi.org/10.1016/j.colsurfa.2023.130970.

[70] A. Bordbar-khiabani, M. Gasik, Electrochemical behavior of additively manufactured patterned titanium alloys under simulated normal , inflammatory , and severe inflammatory conditions, J. Mater. Res. Technol. 26 (2023) 356–370. https://doi.org/10.1016/j.jmrt.2023.07.113.

PROMOCIJAS DARBS IZVIRZĪTS ZINĀTNES DOKTORA GRĀDA IEGŪŠANAI RĪGAS TEHNISKAJĀ UNIVERSITĀTĒ

Promocijas darbs zinātnes doktora (*Ph. D.*) grāda iegūšanai tiek publiski aizstāvēts 2024. gada 6. septembrī plkst. 14 Rīgas Tehniskās universitātes Dabaszinātņu un tehnoloģiju fakultātē, Paula Valdena ielā 3, 272. auditorijā.

OFICIĀLIE RECENZENTI

Docente *Dr. sc. ing.* Agnese Brangule,
Rīgas Stradiņa universitāte, Latvija

Profesors *Dr. chem*. Māris Turks,
Rīgas Tehniskā universitāte

Asociētā profesore *Dr.* Sabine van Rijt,
Institute for Technology-Inspired Regenerative Medicine (*MERLN*), Nīderlande

APSTIPRINĀJUMS

Apstiprinu, ka esmu izstrādājusi šo promocijas darbu, kas iesniegts izskatīšanai Rīgas Tehniskajā universitātē zinātnes doktora (*Ph. D.*) grāda iegūšanai. Promocijas darbs zinātniskā grāda iegūšanai nav iesniegts nevienā citā universitātē.

Ilijana Kovrlija ……. (paraksts)
Datums: 06.09.2024

Promocijas darbs sagatavots kā tematiski vienota zinātnisko publikāciju kopa. Tajā ir kopsavilkums latviešu un angļu valodā un piecas *SCI* publikācijas. Publikācijas uzrakstītas angļu valodā, to kopējais apjoms ir 84 lpp.

ANOTĀCIJA

Promocijas darba izstrādes gaitā optimizēta oktakalcija fosfāta (OCP) sintēzes metodoloģija un mērogošana, kā izejvielu izmantojot zemtemperatūras α-trikalcija fosfātu (α-TCP), kā arī izveidots visaptverošs iegūtā OCP analīzes profils. Izmantojot fizikāli ķīmiskās analīzes datus, tika izveidots *in silico* modelis, kas spēj identificēt OCP iegūšanas stadijas un starpproduktus. Iegūtais OCP tika izmantots divos veidos – kā doksorubicīna hidrohlorīda (DOX) zāļu piegādes sistēma un kā aizsargpārklājums pret koroziju titāna implantiem. Doksorubicīna-oktakalcija fosfāta (DOX-OCP) zāļu piegādes sistēmas ietekme uz MG63 (vēža šūnām) un MC3T3-E1 (preosteoblastu šūnām) novērtēta *in vitro* pētījumos, kā arī pētīta aktīvās vielas izdalīšanās kinētika. Izveidotajiem nātrija alginmāta/oktakalcija fosfāta (Alg/OCP) kompozītpārklājumiem novērtēta to elektroķīmiskā uzvedība titāna sakausējumos iekaisuma apstākļos.

Promocijas darbs uzrakstīts kā vienota zinātnisko publikāciju kopa ar kopsavilkumu latviešu un angļu valodā, kurā secīgi apkopoti dati par piecām *SCI* publikācijām. Kopsavilkums ietver 15 attēlus un vienu tabulu, tam seko pieci pielikumi, kopumā veidojot 173 lappuses, ieskaitot elektroniski pieejamo papildu informāciju.

SATURS

PATEICĪBA

Pirmkārt, vēlos pateikties par iespēju piedalīties *PREMUROSA*, *BBCE* un *RISEus2* projektos, kas finansēja manu promocijas darbu un ļāva apmeklēt visus lieliskos institūtus, zinātniskās konferences un tīklošanās pasākumus.

Ir daudz detaļu un pieredzes, kas man bija svarīgas pēdējo četru gadu laikā, šeit minēšu tikai dažas no vissvarīgākajām.

Vispirms – paldies profesoriem Dagnijai un Jānim Ločiem, kuri bija man līdzās ne tikai kā darba vadītāji, bet arī kā draugi un atbalsts, kad vien tas bija nepieciešams! Vēlos pateikties par miljoniem "ātro jautājumu", par daudzajiem apgūtajiem zinātniskajiem faktiem, par iespēju parādīt, ko es varu sasniegt, par uzticēšanos man, par daudzajām tikšanās reizēm un, pats galvenais, par to, ka parādījāt man, kas ir īsts mentors.

Vēlos pateikties savai ģimenei – mammai, tētim, Dankai, Savai, Danai un Vasilije – par jūsu beznosacījumu atbalstu, lai iestātos doktorantūrā, un par visu pirms studijām un studiju laikā, bez kura nekas no paveiktā nebūtu iespējams. Paldies manām labākajām draudzenēm Majai, Isidorai, Majai un Dakai, kuras vienmēr bija blakus ar savu atbalstu un sapratni! Milicai – par garajām sarunu stundām par visām jaunajām lietām, kultūrām un darba izaicinājumiem! Unai un Kićai – par vislabāko un vissvarīgāko kompāniju, ko es tik ļoti novērtēju. Aertam – par atbalstu, mīlestību un smiekliem, kas visu padarīja vieglāku. Un, visbeidzot, vēlos pateikties visiem "maniem cilvēkiem", kurus satiku šī ceļojuma laikā, kuri man iemācīja daudzas lietas un kurus tagad varu saukt par saviem draugiem (jūs atpazīsiet sevi).

Īpašs paldies Līgai un Janai, bez kuru nesavtīgās palīdzības nebūtu iespējama promocijas darba latviešu valodas kopsavilkuma tapšana zinātnes nozarei atbilstošā terminoloģijā!

SAĪSINĀJUMI

ACP	amorfs kalcija fosfāts
Alg	nātrija alginmāts
Alg/OCP	alginmāts/oktakalcija fosfāts
BET	*Brunauer–Emmett–Teller* metode
CaP(s)	kalcija fosfāts(-i)
CDHAp	hidroksilapatīts ar kalcija deficītu
CPE	konstantās fāzes elements
CPE_{dl}	robežvirsma starp substrātu un šķīdumu
DCPD/Brushite	dikalcija fosfāta dihidrāts
DDS(s)	zāļu piegādes sistēma(-as)
DLC	zāļu (aktīvās vielas) saturs
DOX	doksorubicīna hidrohlorīds
DOX-OCP	doksorubicīnu saturošs oktakalcija fosfāts
nDOX-OCP	n masas% aktīvās vielas (no sākotnējā zemtemperatūras α-trikalcija fosfāta)
EIS	elektroķīmiskā impedances spektroskopija
Fer-1	ferostatīns-1
FTIR	Furjē transformācijas infrasarkanā spektroskopija
HAp	hidroksilapatīts
hBMSC	cilvēka kaulu mezenhimālās cilmes šūnas
I	iekaisuma vide
ICDD	Starptautiskais difrakcijas datu centrs
LT-α-TCP	zemtemperatūras α-trikalcija fosfāta
ML	mašīnmācīšanās
N	normāla ķermeņa vide
NMR	kodolmagnētiskā rezonanse
OCP	oktakalcija fosfāts
OS	osteosarkomas šūnas
PARP	poli (ADP-ribozes) polimerāze
PBS	fosfātu fizioloģiskais buferšķīdums
PBT	polibutilēna tereftalāts
PCD	programmēta šūnu nāve
PEGT	polietilēna glikotereftalāts
Rc	pretestība
Rct	pretestība lādiņa pārnesei
SEM	skenējošā elektronu mikroskopija
SI	smaga iekaisuma vide
SSA	īpatnējais/specifiskais virsmas laukums
TCP (α, β)	trikalcija fosfāts (α, β)
TEM	transmisijas elektronu mikroskopija

TGA	termogravimetriskā analīze
Ti Gr2	99.3 masas% no sākotnējā titāna
Ti Gr23	Al 5,4 masas%, V 3,8 masas%, Fe 0,2 masas%, C 0,009 masas% no sākotnējā titāna
XRD	rentgenstaru difraktometrija

PROMOCIJAS DARBA VISPĀRĒJS RAKSTUROJUMS

Ievads un literatūras apskats

Arvien pieaugošais cilvēku skaits, kas sirgst ar muskuloskeletālās sistēmas slimībām (2019. gadā reģistrēti 322,75 miljoni muskuloskeletālās sistēmas saslimšanas gadījumu) [1], tostarp ar kaulu vēzi (prognozēts, ka līdz 2040. gadam kaulu vēža gadījumu skaits pasaulē sasniegs 26 miljonus [2]) un nepilnīgu kaulu reģenerāciju, rada nepieciešamību meklēt efektīvus risinājumus kaulu defektu ārstēšanai un kaulaudu reģenerācijai. Reģeneratīvās medicīnas galvenais mērķis ir pēc iespējas precīzāk atdarināt dabiskā kaula īpašības, lai reģenerācijas process pacientiem būtu ātrāks un vieglāks. Ņemot vērā to, ka cīņā ar slimībām nereti ir nepieciešama dažādu medikamentu lietošana, papildu mērķis ir mazināt aktīvo vielu sistēmiskas lietošanas sekas, kas var būt pat letālas. Turklāt – neatkarīgi no plānotā pielietojuma – materiālam ir precīzi jāatbilst "zelta standartam", proti, tam jābūt biosaderīgam, biorezorbējošam un osteoinduktīvam, t. i., jāstimulē šūnu diferenciācija par preosteoblastiem [3].

Pateicoties biosaderībai, osteokonduktivitātei un spējai struktūrā iekļaut dažādus medikamentus/jonus, kalcija fosfāti (CaP), kas sastopami arī cilvēka organismā kā kaulu un zobu neorganiskā komponente, ir perspektīvi biomateriāli izmantošanai kaulaudu reģenerācijā [4–8]. CaP var klasificēt pēc tādām fizikāli ķīmiskajām īpašībām kā Ca/P molārā attiecība, šķīdība, kristāliskums, daļiņu lielums, morfoloģija un īpatnējais virsmas laukums (*SSA*), kā arī pēc to pielietojuma veida (nanodaļiņas, pamatnes, pārklājumi utt.). Hidroksilapatīts (HAp, $Ca_{10}(PO_4)_6(OH)_2$), visbiežāk izmantotā CaP fāze, atrodams cietajos audos nestehiometriskā formā. Fizioloģiskos apstākļos HAp ir visstabilākā fāze, un tā galvenais trūkums ir lēna biorezorbcija [9, 10]. Otrs visbiežāk izmantotais CaP ir trikalcija fosfāts (TCP, $Ca_3(PO_4)_2$). Kaulaudu reģenerācijai galvenokārt izmanto α- un β-TCP polimorfās modifikācijas [11]. α-TCP plaši izmanto kaulu cementos un citos kaulu implantmateriālos, jo tam piemīt lieliska biosaderība, un tas uzrāda pozitīvus rezultātus *in vivo* [1]. Tomēr α-TCP raksturīga strauja biorezorbcija organismā, kas nesakrīt ar kaulaudu veidošanās ātrumu [12, 13]. Trīs CaP fāzes, t. i., amorfais kalcija fosfāts (ACP, $Ca_3(PO_4)_2 \cdot nH_2O$), dikalcija fosfāta dihidrāts (brušīts jeb DCPD, $CaHPO_4 \cdot 2H_2O$) un oktakalcija fosfāts (OCP, $Ca_8(HPO_4)_2(PO_4)_4 \cdot 5H_2O$), tiek uzskatītas par kaulu minerālās komponentes jeb bioloģiskā apatīta prekursoriem [8, 14]. Pateicoties amorfai struktūrai, kā arī hidratētā slāņa un struktūras defektu klātbūtnei, ACP ir raksturīga augsta šķīdība un biorezorbcijas ātrums, kā arī augsta bioaktivitāte [15, 16]. DCPD raksturīga slāņveida struktūra, ko veido CO un PO_4^{3-} slāņi, kas izkārtoti paralēli *c* asij un savstarpēji saistīti ar ūdeņraža saitēm no struktūras ūdens molekulām [17, 18]. DCPD veidojas skābos ūdens šķīdumos pie pH 2–6, un viena no galvenajām DCPD priekšrocībām ir tā tieksme pārveidoties par OCP vai hidroksilapatītu ar kalcija deficītu (CDHAp), tāpēc to bieži izmanto pašcietējošu CaP kaulu cementu izstrādē.

Trešais prekursors, t. i., OCP, ir vislīdzīgākais HAp. Galvenokārt līdzība ir strukturāla, proti, apatīta slāņu izkārtojums paralēli (100) plaknei un hidratēto slāņu izkārtojums starp apatīta slāņiem [19, 20]. Šis specifiskais apatīta kristalogrāfisko plakņu (biezums ~ 1,1 nm)

izkārtojums un relatīvi tukšais hidratētais slānis (biezums ~ 0,8 nm) [21] nosaka OCP tieksmi gan *in vitro*, gan *in vivo* pārveidoties par termodinamiski stabilāku CDHAp fāzi [2, 3]. OCP un HAp struktūras līdzības pakāpi ietekmē ūdens molekulu klātbūtne hidratētajā slānī. Analoga OCP pārvēršanās par apatītu notiek kaulu veidošanās procesā [8]. Turklāt hidratētā slāņa klātbūtne ievērojami atvieglo dažādu jonu un molekulu iekļaušanu OCP struktūrā [23]. No bioloģiskā viedokļa HPO_4^{2-} jonu izdalīšanās no OCP [24] stimulē kaulu šūnas (piemēram, osteoblastus, osteocītus, osteoklastus [25]) un veicina makrofāgu migrāciju uz implantācijas vietu [21]. Vairāki pētījumi liecina, ka OCP var samazināt tādu proiekaisuma citokīnu kā nekrozes faktora alfa un interleikīna-1 sekrēciju, tādējādi uzrādot pretiekaisuma īpašības [26, 27]. Turklāt vairākas zinātniskās grupas, piemēram, pētījumos par OCP pārklājumiem uz titāna [28] un polietilēna gliko-tereftalāta/polibutilēna tereftalāta (PEGT/PBT) [29] implantmateriāliem, ir pierādījušas OCP osteoinduktivitāti.

Pastāv divi galvenie OCP sintēzes ceļi – nogulsnēšana [20, 30] un hidrolīze [17, 31]. OCP sintēzē izmantotās kalcija (Ca^{2+}) un fosfāta (PO_4^{3-}) jonus saturošās izejvielas var būt dažādas. Nogulsnēšanas metodēs parasti tiek izmantotas kalcija acetāta, kalcija karbonāta, nātrija dihidrogēnortofosfāta un fosforskābes kombinācijas, savukārt hidrolīzē visbiežāk izmantotie prekursori ir DCPD vai α-TCP. Abi procesi ir sarežģīti un atkarīgi no pH, temperatūras, maisīšanas ātruma, jonu stipruma u. c. savstarpēji saistītiem tehnoloģiskajiem parametriem [23, 32]. Augstāka sintēzes temperatūra saīsina OCP iegūšanas laiku, jo pastāv kinētiski labvēlīgāki apstākļi šīs fāzes veidošanai. Savukārt paaugstināts pH var izraisīt citu fāžu (piemēram, CDHAp) nogulsnēšanos. Iepriekšminētie faktori var ietekmēt arī OCP kristālu izmēru un morfoloģiju, kā arī to bioloģisko iedarbību [20, 33]. Nogulsnēšanās rezultātā var veidoties plānas, iegarenas un šķiedrveida daļiņas, savukārt hidrolīzes rezultātā vienlaikus var veidoties gan plānas plākšņveida daļiņas, gan sīkākas spirālveida daļiņas. Līdz ar to ir svarīgi izvēlēties piemērotus sintēzes apstākļus, kas ļautu ne vien iegūt tīras fāzes OCP, bet arī kontrolēt daļiņu morfoloģiju specifiskiem pielietojumiem.

Lai identificētu iegūto CaP fāžu raksturīgās iezīmes un morfoloģiju, ir nepieciešams izmantot vairāku metožu pieeju. Lai apstiprinātu konkrētas fāzes klātbūtni, tiek izmantota rentgenstaru difraktometrija (*XRD*), Furjē transformācijas infrasarkano spektroskopija (*FTIR*), Ramana spektroskopija, skenējošā elektronu mikroskopija (SEM), kodolmagnētiskā rezonanse (*NMR*), termogravimetriskā analīze (TGA), transmisijas elektronu mikroskopija (TEM), *Brunauer-Emmett-Teller* metode (BET), lāzera granulometrija u. c. Tomēr OCP lielā līdzība ar CDHAp [23] apgrūtina kvantitatīvu fāžu analīzi, jo OCP un CDHAp raksturīgo *XRD* maksimumu pārklāšanās var traucēt Rītvelda analīzei. Citi šķēršļi, kas tika konstatēti, analizējot literatūru, ietver salīdzinoši nelielu tīras OCP fāzes iznākumu (~ 100 mg – 2 g), šauru OCP sintēzes pH diapazonu (pH no 5 līdz 7), piemērotu OCP sintēzes temperatūru, kā arī ierobežotās OCP apstrādes iespējas augstās temperatūrās (> 80 ºC) [23].

Ņemot vērā OCP potenciālu, aizvien tiek meklēti inovatīvi veidi, kā šo CaP fāzi izmantot reģeneratīvajā medicīnā. Līdz šim OCP ir izmantots kaulu cementos [34], kompozītmateriālos ar polimēriem (alginātu, želatīnu, kolagēnu, PEGT u. c.) pamatņu izstrādei kaulu defektu rekonstrukcijai [35–37], kā arī pārklājumos uz titāna sakausējumu implantiem, lai uzlabotu metāla virsmu bioloģiskās īpašības [29, 38]. Ņemot vērā to, ka reģeneratīvās medicīnas mērķi

ietver arī tādu sistēmisku slimību kā osteoporoze novēršanu un zāļu lietošanas biežuma un toksicitātes samazināšanu vēža slimniekiem, bioaktīvo jonu un zāļu kombinēšana ar kalcija fosfātiem ir guvusi ievērojamu popularitāti. Piemēram, lai uzlabotu OCP bioaktivitāti, tas ticis modificēts ar tādiem bioaktīviem joniem kā karbonāts (CO_3^{2-}), magnijs (Mg^{2+}), cinks (Zn^{2+}) un stroncijs (Sr^{2+}) [23]. OCP izmantots arī zāļu piegādes sistēmu (*DDS*) izveidē, lai uzlabotu terapeitisko līdzekļu (bisfosfonātu, ibuprofēna, metotreksāta) biopieejamību, izmantojot lokālu aktīvo vielu piegādi [23]. Tradicionālās (sistēmiskās) zāļu piegādes metodes darbojas caur asinsrites sistēmu, kas var izraisīt dažādas blakusparādības, ieskaitot sistēmisku toksicitāti un suboptimālu piegādi mērķa vietā [39]. Lai novērstu šos trūkumus, lokālas aktīvo vielu piegādes mērķis ir samazināt sākotnējo straujo zāļu izdalīšanos un pielāgot aktīvo vielu izdalīšanās profilu defekta vietai un konkrētajai slimībai. Ņemot vērā to, ka ļaundabīgie kaulu audzēji (visbiežāk osteosarkoma (OS)) veido aptuveni 40 % no visiem kaulu audzējiem [2], daži no centieniem izmantot OCP kā aktīvo vielu nesēju vērsti uz metotreksātu saturoša OCP un OS šūnu līniju mijiedarbības novērtēšanu [40]. Pētījumi, kas saistīti ar OCP modificēšanu ar zālēm, galvenokārt vērsti uz bisfosfonātu pievienošanu OCP, tādēļ ir ļoti svarīgi izstrādāt jaunas *DDS*, kas spētu efektīvi kontrolēt pretvēža zāļu lokālu ievadīšanu un īstermiņa/ilgtermiņa iedarbību. Šādas *DDS* spētu mazināt ķīmijterapijas rezistenci un no devas atkarīgās toksicitātes attīstību. Ir izvirzīta hipotēze, ka, ja zāļu pievienošana tiek veikta *in situ* OCP sintēzes sākumposmā, rezultātā var iegūt OCP *DDS* ar īpaši augstu zāļu jeb aktīvās vielas saturu (*DLC*) [41]. Lai gan OCP ir uzrādījis augstu potenciālu kā bioloģiski aktīvu jonu/molekulu piegādes sistēma, ir maz datu par aktīvo vielu izdalīšanās mehānismiem no OCP, kā arī par zāļu/jonu pievienošanas ietekmi uz OCP fāzes veidošanos.

Pētījuma pamatojums

Veicot rūpīgu literatūras analīzi un paturot prātā pierādīto OCP nozīmīgumu, šajā promocijas darbā galvenā uzmanība tika vērsta uz zinātniskajā literatūrā iztrūkstošu sistemātisku pētījumu veikšanu par OCP iegūšanu un izmantošanu, tādējādi zināmā mērā aizpildot konstatēto zināšanu trūkumu. Promocijas darba izstrādes gaitā optimizēta OCP sintēzes metode un veikta sintēzes mērogošana, izstrādātas un raksturotas pretvēža *DDS* uz OCP bāzes, kā arī pārbaudīta OCP pielietojamība kompozītmateriālu pārklājumu izveidē. Promocijas darba shēma redzama 1. attēlā.

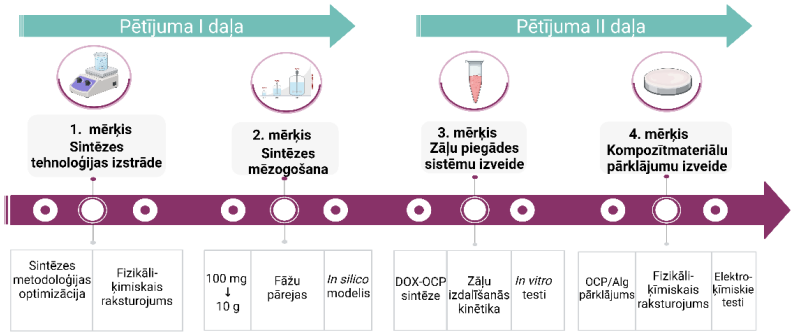

1. att. Promocijas darba shēma (OCP – oktakalcija fosfāts; Alg – alginmāts; DOX – doksorubicīns; DOX-OCP – doksorubicīnu saturošs oktakalcija fosfāts).

Mērķis un uzdevumi

Promocijas darba mērķis bija optimizēt OCP sintēzes metodi, lai iegūtu stabilu OCP ar augstu fāžu tīrību, pētīt iegūtā OCP pielietojamību zāļu piegādes sistēmu izveidē, kā arī izveidot OCP saturošu kompozītpārklājumu. Lai sasniegtu mērķi, definēti vairāki uzdevumi.

1. Optimizēt OCP sintēzes metodi, izmantojot zemtemperatūras α-trikalcija fosfāta (LT-α-TCP) hidrolīzi, un raksturot iegūtā OCP fizikāli ķīmiskās īpašības.
2. Optimizēt sintēzes metodes mērogošanu, noteikt OCP veidošanās starpproduktus un izstrādāt *in silico* modeli OCP sintēzes beigu punkta noteikšanai, pamatojoties uz *XRD* un *FTIR* rezultātiem.
3. Izveidot zāļu piegādes sistēmu vēža ārstēšanai, kombinējot OCP ar antineoplastisku aktīvo vielu – doksorubicīna hidrohlorīdu (DOX-OCP).
4. Izveidot OCP saturošus hidrogēla pārklājumus metāla implantiem, kas spēj uzlabot metāla implantu noturību pret koroziju.

Aizstāvēšanai izvirzītās tēzes

1. Simtkārtēja OCP sintēzes mērogošana izmantojot LT-α-TCP hidrolīzi istabas temperatūrā neietekmē gala produkta fizikāli ķīmiskās īpašības (fāžu sastāvu, molekulāro struktūru un morfoloģiju).
2. Doksorubicīnu OCP daļiņās var iekļaut līdz 10 masas% no sākotnējā OCP prekursora daudzuma. Lielāka doksorubicīna satura izmantošana novērš OCP fāzes veidošanos. Sintezētais produkts var tikt izmantots kā palēninātas izdalīšanās pretvēža zāļu piegādes sistēma.
3. OCP izmantošana pārklājumos uz 3D drukātiem Ti bāzes metāliskiem implantiem ietekmē elektrisko lādiņu pārneses pretestību uz substrāta un pārklājuma robežvirsmas.

Zinātniskā novitāte

1. Nosakot fāžu pārvērtības reakcijas laikā no LT-α-TCP uz OCP, ar ķīmisko vienādojumu palīdzību aprakstīta pakāpeniska pāreja no LT-α-TCP fāzes uz OCP fāzi caur DCPD kā starpproduktu.
2. Doksorubicīna hidrohlorīda saturam DOX-OCP sistēmā pārsniedzot 10 masas% (no sākotnējā LT-α-TCP daudzuma), tiek kavēta OCP fāzes veidošanās. Pierādīts, ka DOX-OCP daļiņas izraisa osteosarkomas šūnu nāvi apoptozes ceļā.

Praktiskā nozīme

Promocijas darba gaitā optimizēta OCP iegūšanas metodika, izvēloties LT-α-TCP kā vienīgo izejmateriālu, kura ražošanai nepieciešams mazāks enerģijas patēriņš, kas atbilst Eiropas Zaļā kursa izvirzītajiem mērķiem. OCP sintēzes metodes mērogošanas rezultātā iegūti ievērojami

OCP fāzes apjomi, kas padara šo procesu potenciāli pievilcīgu ražošanai. Iegūto OCP var tālāk izmantot kā izejmateriālu:

1) inovatīvu zāļu piegādes sistēmu izveidei lokālai osteosarkomas ārstēšanai;
2) OCP saturošu pārklājumu izveidei, kas uzlabotu 3D drukātu titāna sakausējumu izturību pret koroziju.

Publikācijas un promocijas darba aprobācija

SCI zinātniskās publikācijās

1. **Kovrlija I**., Locs, J., Loca D. Octacalcium phosphate: Innovative vehicle for the local biologically active substance delivery in bone regeneration, *Acta Biomaterialia*, 135, 2021, pp. 27–47. doi: 10.1016/j.actbio.2021.08.021 (Scopus, Open Access, IF 9,4, Q1, CiteScore 16,8).
    - Kovrlijas I. ieguldījums publikācijā: rakstīšana – melnraksta rakstīšana, pārskatīšana un rediģēšana, vizualizāciju veidošana (kopā 85/100 %).
2. **Kovrlija I**., Menshikh K., Marsan O, Rey C., Combes C., Locs, J., Loca D. Exploring the Formation Kinetics of Octacalcium Phosphate from Alpha-Tricalcium Phosphate: Synthesis Scale-Up, Determination of Transient Phases, Their Morphology and Biocompatibility, *Biomolecules*, 13, 2023, 462. doi:10.3390/biom13030462 (Scopus, Open Access, IF 4,8, Q1, CiteScore 9,4).
    - Kovrlijas I. ieguldījums publikācijā: rakstīšana – melnraksta rakstīšana, pārskatīšana un rediģēšana, konceptualizācija, vizualizāciju veidošana, formālā analīze, izpēte (kopā 80/100 %).
3. Nascimben M., **Kovrlija I**., Locs, J., Loca D., L. Rimondini. Fusion and classification algorithm of octacalcium phosphate production based on XRD and FTIR data, *Scientific Reports*, 14:1489, 2024, 1–11. doi: 10.1038/s41598-024-51795-0 (Scopus, Open Access, IF 3,8, Q1, CiteScore 6,9).
    - Kovrlijas I. ieguldījums publikācijā: laboratorijas eksperimenti, datu ievākšana un organizēšana, rezultātu apspriešana, melnraksta rakstīšana un rediģēšana (kopā 50/100 %).
4. **Kovrlija I**., Pańczyszyn E., Demir O., Laizane M., Corazzari M., Locs J., Loca D. Doxorubicin-loaded octacalcium phosphate particles as controlled release drug delivery systems: physico-chemical characterization, in vitro drug release and evaluation of cell death pathway, *International Journal of Pharmaceutics*, 653, 2024, 123932. doi: 10.1016/j.ijpharm.2024.123932 (Scopus, Open Access, IF 5,3, Q1, CiteScore 10,7).
    - Kovrlijas I. ieguldījums publikācijā: rakstīšana – melnraksta rakstīšana, pārskatīšana un rediģēšana, konceptualizācija, vizualizāciju veidošana, formālā analīze, izpēte (kopā 75/100 %).
5. Bordbar Khiabani A., **Kovrlija I**., Locs J., Loca D., Gasik, M. Octacalcium Phosphate-Laden Hydrogels on 3D-Printed Titanium Biomaterials Improve Corrosion Resistance in Simulated Biological Media, *International Journal of Molecular Sciences*, 2023, 24, 13135. doi: 10.3390/ijms241713135 (Scopus, Open Access, IF 4,9, Q1, CiteScore 8,1).
    - Kovrlijas I. ieguldījums publikācijā: rakstīšana – melnraksta rakstīšana, vizualizāciju veidošana, formālā analīze un izpēte (kopā 50/100 %).

Zinātniskās konferences, kurās prezentēti promocijas darba rezultāti

1. **Kovrlija I.,** Nascimben M., Bordbar-Khiabani A., Menshikh K., Gasik M., Combes C., Rimondini L., Locs J., Loca D. Tailoring the production technology and utilization of octacalcium phosphate for precise patient-centred applications in musculoskeletal field. *12th World Biomaterials Congress*, 2024. gada 26.–31. maijs 2024, Degu, Dienvidkoreja; (I. K. stenda referāts).
2. **Kovrlija I.**, Demir O., Laizane M., Locs J., Loca D. Novel drug delivery vehicle: doxorubicin-loaded octacalcium phosphate. *33rd Annual Conference of the European Society of Biomaterials*, 2023. gada 4.–8. septembris, Davosa, Šveice. (I. K. stenda referāts).
3. **Kovrlija I.**, Menshikh. K., Demir O., Locs J., Loca D., Octacalcium phosphate: journey of creating a unique drug delivery vehicle. *The XVIIIth Conference of the European Ceramic Society*, 2023. gada 2.–6. jūlijs, Liona, Francija. (I. K. mutiskais referāts, studentu runas konkurss).
4. **Kovrlija I.**, Menshikh K., Marsan O., Rey C., Combes C., Locs J., Loca D. Scale-Up of Octacalcium Phosphate via Hydrolysis Route: Effect on Physico-Chemical Characteristics and In-Vitro Cytocompatibility with Bone Marrow-Derived Mesenchymal Stem Cells. *Tissue Engineering and Regenerative Medicine International Society European Chapter Meeting*, 2023. gada 28.–31. marts, Mančestera, Lielbritānija. (I. K. mutiskais referāts).
5. **Kovrlija I.,** Menshikh K., Marsan O., Rey C., Combes C., Locs J., Loca D. Phase transformation from α-tricalcium phosphate to octacalcium phosphate via hydrolysis route. *Scandinavian Society for Biomaterials 16th annual meeting*, 2023. gada 12.–14. marts, Roros, Norvēģija. (I. K. stenda referāts).
6. **Kovrlija I.**, Barbut C., Locs J., Loca D. Incorporation and effect of lidocaine hydrochloride on octacalcium phosphate. *32nd Annual Conference of the European Society of Biomaterials*, 2022. gada 4.–8. septembris, Bordo, Francija. (I. K. stenda referāts).
7. **Kovrlija I.**, Locs J., Loca D. Unravelling the Behaviour of Octacalcium Phosphate in Various Model Solutions. *Scandinavian Society for Biomaterials 15th annual meeting*, 2022. gada 13.–15. jūnijs, Jūrmala, Latvija. (I. K. stenda refrāts).
8. **Kovrlija I.,** Barbut C., Locs J., Loca D. Effects of the synthesis conditions on the hydrolysis of α-tricalcium phosphate to octacalcium phosphate. *31st Annual Conference of the European Society for Biomaterials*, 2021 (tiešsaistē). (I. K. stenda referāts).
9. **Kovrlija I.**, Locs J., Loca D. Octacalcium phosphate: a contemporary drug delivery system for local biologically active substances – a review. *Scandinavian Society for Biomaterials 14th Annual Meeting*, 2021 (tiešsaistē). (I. K. stenda referāts).

Citi zinātniskie pasākumi, kuros prezentēti promocijas darba rezultāti

1. Locs J., **Kovrlija I**., Choudhary R., Loca D. Roadmap from upscaling and rapid synthesis towards first-ever consolidation of OCP. *33rd Conference and annual meeting of the International Society for Ceramics in Medicine*, 2023. gada 17.–20. oktobris, Solotuma, Šveice. (J. L. uzaicināta runa).
2. Bordbar Khiabani A., **Kovrlija I**., Locs J., Loca D., Gasik M. Octacalcium Phosphate Embedded Hydrogels on 3D Printed Titanium Improve the Corrosion Performance in

Simulated Biological Media. *31st Annual Meeting of European Orthopaedic research Society*, 2023. gada 27.–29. septembris, Porto, Portugāle. (A. B. K. mutiskais referāts).

3. Loca D., **Kovrlija I.**, Pylostomou A., Locs J., Can Octacalcium Phosphate Be Used As a Doxorubicin Delivery Platform? *Tissue Engineering and Regenerative Medicine International Society – Americas Chapter Annual Meeting*, 2023. gada 11.–14. aprīlis, Bostona, ASV. (D. L. stenda referāts).
4. Menshikh K., **Kovrlija I.**, Miola M., Cochis A., Rimondini L.Synthetic pre-vascularized porous scaffold as an engineered environment for the in vitro osteosarcoma model. *Tissue Engineering and Regenerative Medicine International Society European Chapter Meeting*, 2022. gada 28. jūnijs–1. jūlijs, Krakova, Polija. (K. M. stenda referāts).
5. Menshikh K., **Kovrlija I.**, Miola M., Cochis A., Rimondini L. Freeze-dried Composition of Alginate and Bioglass as an Engineered Environment for the Osteosarcoma Model. *Scandinavian Society for Biomaterials 15th annual meeting*, 2022. gada 13.–15. jūnijs, Jūrmala, Latvija. (K. M. stenda referāts).
6. **Kovrlija I.**, Locs J., Loca D. Octacalcium phosphate: synthesis, characterization and functionalization. *4th Premurosa Summer School*, 2023. gada 15.–19. maijs, Rīga, Latvija. (I. K. mutiskais referāts).
7. **Kovrlija I.**, Locs J., Loca D. Unravelling the Behaviour of Octacalcium Phosphate in Various Model Solutions. *3rd Premurosa Summer School*, 2022. gada 20.–24. jūnijs, Belgrada, Serbija. (I. K. stenda referāts).
8. **Kovrlija I**., Locs J., Loca D. Smart personalized degradable biomaterials for bone tissue regeneration. *2nd Premurosa Summer School*, 2021. gada 19.–24. oktobris, Porto, Portugāle. (I. K. mutiskais referāts).
9. **Kovrlija I**., Loca D. Octacalcium phosphates: promising instruments for local drug delivery in bone regeneration. *Baltic Biomaterials Centre of Excellence Summer School on "Scientific writing",* 2020. gada 23.–27. novembris, tiešsaistē. (I. K. mutiskais referāts).

Citas zinātniskās publikācijas, kas publicētas promocijas darba izstrādes laikā

1. **Kovrlija I**., K. Menshikh, H. Abreu, A. Cochis, L. Rimondini, O. Marsan, C. Rey, C. Combes, J. Locs, D. Loca, Challenging Applicability of ISO 10993-5 for Calcium Phosphate Biomaterials Evaluation: Towards More Accurate In Vitro Cytotoxicity Assessment, *Biomaterials Advances*, 160, 213866, 2024. doi: 10.1016/j.bioadv.2024.213866 (Scopus, Open Access).
2. Aunina K., Ramata-Stunda A., **Kovrlija I**., Tracuma E., Merijs-Meri R., Nikolajeva V., Loca D., Exploring the Interplay of Antimicrobial Properties and Cellular Response in Physically Crosslinked Hyaluronic Acid/ε-Polylysine Hydrogels. *Polymers*, 15 (8): 1915, 2023. doi: 10.3390/polym15081915 (Scopus, Open Access).
3. Mosina M., **Kovrlija I**., Stipniece L., Locs J. Gallium containing calcium phosphates: Potential antibacterial agents or fictitious truth. *Acta Biomaterialia*, 150, 48–57, 2022. doi: 10.1016/j.actbio.2022.07.063 (Scopus, Open Access).
4. **Kovrlija I.**, Locs, J., Loca D. Incorporation of Barium Ions into Biomaterials: Dangerous Liaison or Potential Revolution? *Materials*, 14 (19), 2021, pp. 5772. doi: 10.3390/ma14195772 (Scopus, Open Access).

PROMOCIJAS DARBA GALVENIE REZULTĀTI

OCP sintēzes metodoloģijas optimizācija

Neraugoties uz to, ka OCP piemīt augstāks potenciāls stimulēt kaulaudu reģenerāciju, salīdzinot ar HAp [21,42,43], samērā ierobežotās iegūšanas iespējas un sarežģītais sintēzes process kavē tā attīstību gan zinātniskā, gan rūpnieciskā līmenī [23, 32]. Abām galvenajām OCP sintēzes metodēm ir priekšrocības un trūkumi, kas apkopoti 1. tabulā.

1. tabula

OCP nogulsnēšanas un hidrolīzes sintēžu metožu priekšrocības un trūkumi [31, 44–47]

Nogulsnēšana		**Hidrolīze**	
Priekšrocības	**Trūkumi**	**Priekšrocības**	**Trūkumi**
Ātrāka reakcija	Vismaz divi prekursori	Tikai viens prekursors	Lēnāka reakcija
Augstāka ražība	Dozēšanas ātruma regulēšana	Nav dozēšanas ātruma ierobežojumu	Ražība ierobežota līdz sākotnējam prekursora daudzumam
/	Augstākas temperatūras (60–80 °C)	Zemākas temperatūras (25–60 °C)	/
/	Nepieciešama nogulšņu attīrīšana	Nav attīrīšanas posma	/
/	Vienmēr nepieciešama pH regulēšana	Iespējams izvairīties no pH regulēšanas	/

Zemtemperatūras α-TCP hidrolīze līdz OCP

Apsverot sintēzes ceļu priekšrocības un trūkumus, tika secināts, ka hidrolīzes metode precīzāk atbilst promocijas darba mērķiem. Saskaņā ar literatūras datiem kā prekursors hidrolīzē tiek izmantots gan DCPD, gan α-TCP, tomēr DCPD ir augstāka šķīdība nekā α-TCP, to vieglāk ietekmē atmosfēras CO_2, kā arī zemākās temperatūrās (< 30 °C) tā pārveidošanai par OCP ir nepieciešami vairāki mēneši [21]. Tādējādi par prekursoru OCP sintēzē tika izvēlēts α-TCP.

Parasti α-TCP sintēze ietver ilgstošu (~ 2–3 h) kalciju un fosfātu saturošu materiālu, piemēram, β-TCP, karsēšanu 1300 °C vai augstākā temperatūrā. Šādā veidā sintezēts α-TCP parasti ir rupjgraudains pulveris, kam nepieciešama turpmāka malšana, kuras rezultātā rodas daļiņas ar plašu izmēru sadalījumu un veidojas amorfa fāze [48]. Lai no tā izvairītos un lai samazinātu enerģijas patēriņu, zemtemperatūras α-TCP (LT-α-TCP) tika iegūts, karsējot ACP ar augstu īpatnējās virsmas laukumu (*SSA* > 70 m^2/g; izgulsnēts no diamonija fosfāta un kalcija nitrāta tetrahidrāta šķīdumiem) 650 °C (2. att.) [48].

OCP tika sintezēts no LT-α-TCP skābā vidē (0,0016 M ortofosforskābē (H_3PO_4)) istabas temperatūrā (22 °C), uzturot konstantus maisīšanas apstākļus [46]. Pēc sintēzes paraugi tika žāvēti 37 °C (uz nakti), un, lai novērtētu iegūtā OCP tīrību, iegūtie produkti tika analizēti, izmantojot vairākas metodes (2. att.).

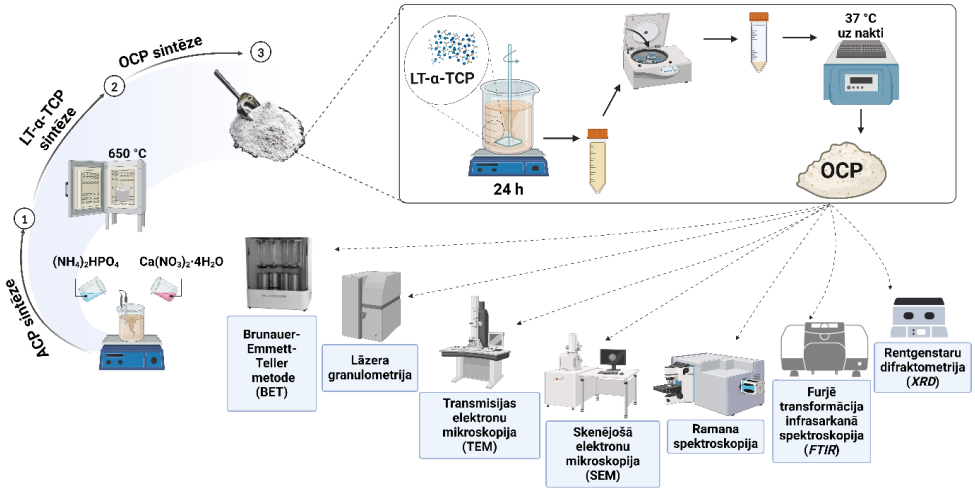

2. att. OCP sintēzes metodoloģijas vispārējā shēma un OCP fāzes noteikšanā izmantotās analīzes metodes.

OCP paraugi (apzīmēti ar OCP1) pēc sintēzes tika analizēti, izmantojot iepriekš izvēlētu metožu kopumu, kas ļauj raksturot OCP dažādos līmeņos. Fāžu sastāva analīzei izmantota rentgenstaru difraktometrija (*XRD*, *PANalytical Aeris*, Nīderlande), kristālisko fāžu identifikācija veikta, izmantojot Starptautiskā difrakcijas datu centra (*ICDD*) PDF-2 datubāzi. Lai iegūtu informāciju par mijiedarbībām molekulārā līmenī, izmantota Furjē transformācijas infrasarkanā spektroskopija (*FTIR*, *Nicolet iS 50, Thermo Scientific*, ASV) un Ramana spektroskopija (*LabRAM HR 800*, *Horiba Jobin Yvon*, Japāna). Pulverveida materiālu morfoloģijas raksturošanai izmantota skenējošā elektronu mikroskopija (SEM, *Tescan Mira/LMU*, *Tescan*, Čehija) un transmisijas elektronu mikroskopija (TEM, *Tecnai F20*, *FEI*), daļiņu izmēra sadalījums noteikts ar lāzera granulometriju (*Malvern Mastersizer 3000*), īpatnējais virsmas laukums mērīts ar *Brunnauer-Emmet-Teller* metodi (BET, *QUADRASORB SI* un *Quadra Win*).

OCP rentgendifrakcijas aina ir ļoti specifiska, kas ļauj OCP atšķirt no citām CaP fāzēm. OCP1 rentgendifrakcijas ainā novērojams raksturīgais zema leņķa maksimums (100) pie 2θ=4,72° un difrakcijas maksimumu dublets – maksimums (200) pie 2θ = 9,44° un maksimums (010) pie 2θ = 9,77° (3. A att.) [49]. Lai gan šie OCP raksturīgie *XRD* maksimumi atšķir to no citām CaP fāzēm, tomēr apgabalā 2θ = 25–35° OCP *XRD* maksimumi pārklājas ar HAp fāzes *XRD* maksimumiem abu fāžu struktūrālās līdzības dēļ (3. A att.) [49–51]. Tomēr HAp raksturīgā maksimuma pie 2θ = 10,8° trūkums liecina par HAp fāzes neesamību vai tās minimālu klātbūtni pētāmajā paraugā. Otrs svarīgs rādītājs, kas jānovēro, ir iepriekšminētais maksimumu dublets pie 2θ = 9,4° un 2θ = 9,7°, jo intensīvākais OCP maksimums, kas atrodas

zemo leņķu reģionā (pie 2θ = 4,7°), ir grūti pieejams un pārklājas ar fona troksni, kas var traucēt kvantitatīvai fāžu sastāva noteikšanai, izmantojot Rītvelda metodi, kā arī to ietekmē OCP plākšņveida morfoloģija.

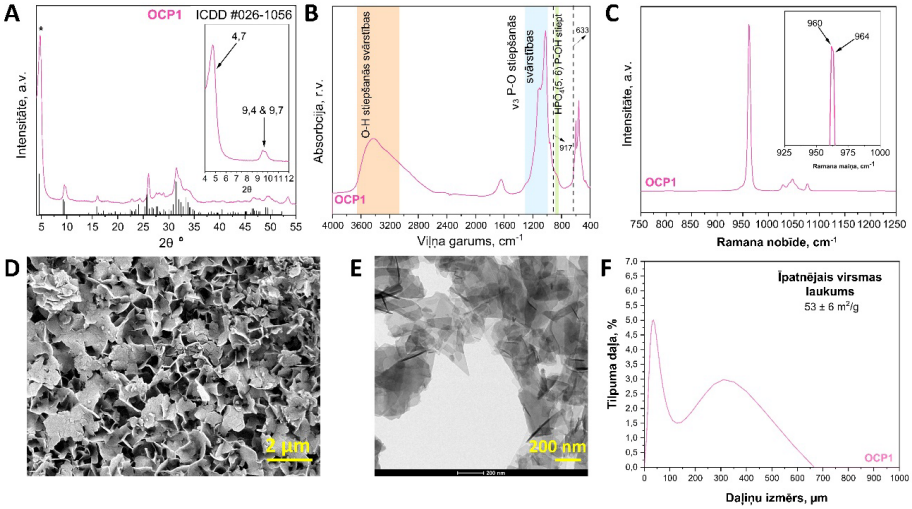

3. att. Analīžu kopums, kas apstiprina iegūtā OCP tīrību: A – *XRD* difraktogramma (* – *XRD* maksimums pie 2θ = 4,7°); B – *FTIR* spektri; C – Ramana spektri; D – SEM mikrofotogrāfija; E – TEM mikrofotogrāfija; F – daļiņu izmēru sadalījums un *SSA*.

OCP elementāršūnas īpatnība ir divas HPO_4^{2-} kristalogrāfiskās vietas, kas apzīmētas ar HPO4(5) un HPO4(6), kuru P-(OH) stiepšanos un OH liekšanos plaknē nav iespējams detektēt, izmantojot *XRD* metodi. HPO4(5) grupa atrodas hidratētajā slānī, HPO4(6) grupa atrodas uz apatīta un hidratētā slāņa robežvirsmas, turklāt abas grupas atšķiras, proti, HPO4(6) grupai ir īsāka un stiprāka starpmolekulārā ūdeņraža saite nekā HPO4(5) grupai [52]. HPO4 grupas nav sastopamas HAp, un to klātbūtne ir vēl viena iezīme, kas atšķir šīs divas fāzes. Tādēļ, lai noteiktu paraugu molekulāro struktūru un apstiprinātu OCP fāzes tīrību, tika izmantota *FTIR* un Ramana spektroskopija (3. B, C att.) [52]. OCP1 spektros atzīmētas OCP raksturīgākās absorbcijas joslas, kas to atšķir no citām CaP fāzēm, t. i., HPO_4^{2-} liekšanās un O-H saišu stiepšanās vibrācijas (3. B att., oranžais un zaļais tonējums). Nozīmīgākās OCP raksturīgās HPO4 grupu joslas detektētas pie 1295 cm^{-1} (OH deformācija plaknē) un pie 917 cm^{-1} (P(6)-(OH) saišu stiepšanās vibrācijas HPO_4^{2-} jonos, kas saistīti ar stiprām ūdeņraža saitēm), kā arī PO_4^{3-} v_3 un HPO_4^{2-} vibrācijas pie 1077 cm^{-1}, 1093 cm^{-1} un 1121 cm^{-1}. HAp raksturīgās OH^- absorbcijas joslas pie 3572 cm^{-1} trūkums spektros ir viens no tīras fāzes OCP veidošanās rādītājiem (vai liecina par nenozīmīgu HAp daudzumu [46]). OH^- absorbcijas josla pie 633 cm^{-1}, ko parasti attiecina uz HAp OH^- vibrācijām, tika detektēta kā plecs (627 cm^{-1}), tomēr saskaņā ar *Fowler et al.* [52] to var attiecināt arī uz H2O(4) svārstībām OCP ūdens molekulās. Ramana spektros visintensīvākās joslas atrodas starp 900–1000 cm^{-1}, kas atbilst trīskārtēji deģenerētām P-O v_3 asimetriskām stiepšanās vibrācijām un daļēji P-O v_1 simetriskām stiepšanās vibrācijām. OCP raksturīgā Ramana josla atrodas pie 958 cm^{-1} (3. C att., visintensīvākais maksimums) [52]. Tomēr tās augstā intensitāte var būt saistīta arī ar vairāku kristālisko fāžu

konvolūciju, ko veido galvenā josla pie 960 cm^{-1} un plecs pie 964 cm^{-1}, kas attiecināms uz PO_4 v_1 vibrācijām, un tas varētu liecināt par zema kristāliskuma OCP fāzes veidošanos.

OCP kristāliem raksturīga plākšņveida morfoloģija, un kristālu izmēri ir atkarīgi no sintēzes metodes. Tiek uzskatīts, ka specifisko OCP kristālu veidošanās ir saistīta ar Hartmana-Perdoka teoriju par periodiskām saišu ķēdēm, kas nosaka, ka kristāliskajā struktūrā pastāvīgs stipro saišu ceļš ir tāda režģa daļa, kuru sadala noteikta (hkl) plakne [50]. OCP plāksnītes aug [001] virzienā, veidojoties lielākajai virsmai (100), un tās, savstarpēji saistoties, veido sfēriskus agregātus, kas atgādina smilšu rozes. SEM mikrofotogrāfijā (3. D att.) redzama OCP1 virsmas morfoloģija – mazas, brīvi agregētas plākšņveida daļiņas (platums 2–5 μm, biezums nanometru diapazonā), kas savstarpēji savienotas rozes formā. Analizējot OCP iekšējo struktūru ar TEM (3. E att.), tika novēroti dažāda lieluma (aptuveni 50–300 nm) plākšņveida kristāli. Kā arī tika novērots, ka kristāli pārklājas un ir savstarpēji savijušies, kā rezultātā tie veido dažāda lieluma aglomerātus, kas tika novēroti arī SEM. BET mērījumi parādīja, ka OCP1 ir liels *SSA* – 53 ± 6 m^2/g. Lielais *SSA* savukārt var liecināt par augstāku materiāla fizikāli ķīmisko un bioloģisko reaktivitāti, kas var būtiski ietekmēt materiāla mijiedarbību ar šūnām. Bimodāls daļiņu izmēru sadalījums (3. F att.) liecina, ka vismazākais primāro daļiņu izmērs 5–25 μm robežās veido ~ 5 % kopējā tilpuma. Sekundārais sadalījums 150–500 μm diapazonā liecina, ka daļiņas ir nevienmērīgi aglomerētas.

Iegūtie rezultāti uzskatāmi parāda, ka no LT-α-TCP ir iespējams iegūt tīru OCP fāzi, tādējādi veiksmīgi sasniedzot pirmo pētījuma mērķi. Taču, ņemot vērā to, ka produkta iznākums bija tikai ~100 mg, kas nav pietiekams daudzums OCP potenciālās izmantošanas pētījumiem un tiem sekojošajiem *in vitro/in vivo* pētījumiem, tika sākta OCP sintēzes mērogošana, lai palielinātu produkta iznākumu.

OCP sintēzes mērogošana, fāzes veidošanās kinētikas pētījumi un sintēzes attīstības gaitas (LT-α-TCP => OCP) *in silico* modeļa izveide

Pēc tīras fāzes OCP iegūšanas no LT-α-TCP (OCP1, istabas temperatūrā, 24 h laikā) nākamais solis bija optimizēt sintēzes parametrus un iegūt lielāku produkta iznākumu. LT-α-TCP hidrolīzes sintēzes metode tika palielināta simtkārtēji (100 mg → 1g → 10 g). Sintēzes tehnoloģijas mērogošanas optimizācijas procesā tika sekots līdzi diviem papildu aspektiem – fāzes veidošanās kinētikai no LT-α-TCP līdz OCP un *in silico* modeļa izstrādei OCP sintēzes posmu raksturošanai.

OCP sintēzes mērogošana

Iegūtie rezultāti parādīja, ka pie nemainīgas prekursoru šķidrās/cietās fāzes attiecības OCP sintēzes laiks palielinās līdz ar izejas LT-α-TCP daudzumu. Desmitkārtējā palielinājumā OCP fāze tika iegūta pēc 72 h (OCP2, 1 g), savukārt simtkārtējā palielinājumā – pēc 180 h (OCP3, 10 g). *XRD* difrakcijas ainās detektēti raksturīgie OCP triklīnās struktūras maksimumi: zema leņķa maksimums (100) pie 2θ = 4,7° un maksimumu ((200) un (010)) dublets pie 2θ = 9,4° un 2θ = 9,7° (4. A att.) [23, 53]. Tāpat kā sākotnējā (OCP1, 100 mg) sintēzes līmenī, *XRD* maksimumi apgabalā no 2θ = 25 līdz 2θ = 35° nav labi izšķirami [20]. OCP2 un OCP3 *FTIR* spektros (4. B att.) P-O ν_3 stiepšanās vibrācijām, kas liecina par OCP fāzi, atbilst visintensīvākās absorbcijas joslas pie 1300–1000 cm^{-1}.

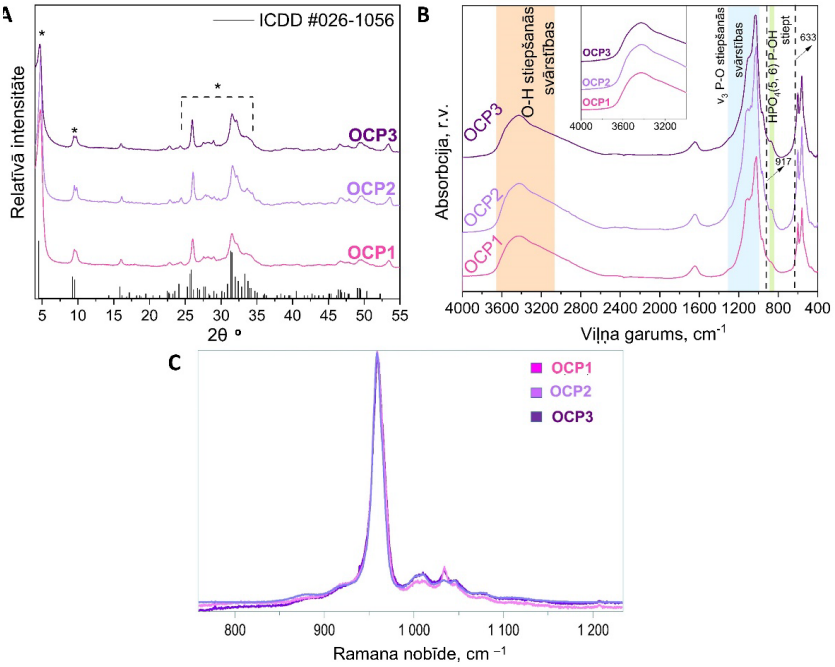

4. att. OCP fāžu, kas iegūtas trīs mērogošanas līmeņos: A – *XRD* ainas (* apzīmē galvenos maksimumus, kas minēti tekstā; references aina (*ICDD* ieraksts Nr. 026-1056) atbilst OCP triklīnās fāzes galvenajiem maksimumiem); B – *FTIR* spektri; C – Ramana spektri.

Ramana spektrā izceltas P-O ν_1 stiepšanās vibrācijas (4. C att.). Specifiskākās OCP spektru joslas tika apspriestas iepriekšējā nodaļā. Lai novērtētu iespējamo sastāva neviendabīgumu viena parauga ietvaros, tika veikti Ramana mikro- un makromērījumi [46]. Iegūtie rezultāti liecina, ka fāžu veidošanās un/vai šķīšana ir cieši saistīta ar izejas pulvera graudu (vai agregātu) izmēru. Saskaņā ar lāzergranulometrijas mērījumu rezultātiem gan OCP2, gan OCP3 ir ar līdzīgu daļiņu izmēru kā OCP1, tomēr OCP2 un OCP3 *SSA* (attiecīgi 66 ± 5 m^2/g un 63 ± 8 m^2/g) ir nedaudz lielāks par OCP1 *SSA*.

OCP fāzes veidošanās kinētika

OCP3 (10 g) sintēzē tika novērota detalizēta OCP fāzes veidošanās gaita atkarībā no laika. Kopējais sintēzes laiks bija 180 h, un visu sintēzes laiku tika kontrolēts pH. Sintēzes monitoringa laikā uzmanība tika pievērsta visu klātesošo fāžu *XRD* maksimumiem un reakcijas vides pH svārstībām. Lai vizualizētu pakāpenisku kristālisko fāžu pāreju no LT-α-TCP kā sākotnējās fāzes uz LT-α-TCP, DCPD un OCP maisījumu un visbeidzot – tīru OCP fāzi, tika izmantotas *XRD* ainas (5. att.) [54, 55]. *XRD* ainās atzīmēti maksimumi pie 2θ = 4,7°, 2θ = 9,4° un 2θ = 9,7° 2θ, kas atbilst OCP triklīnai struktūrai, 2θ = 11,7°, 2θ = 20,9° un 2θ = 29,2°, kas atbilst DCPD monoklīnai struktūrai, un 2θ = 12,1°, 2θ = 22,1° un 2θ = 22,9°, kas atbilst LT-α-TCP monoklīnai struktūrai.

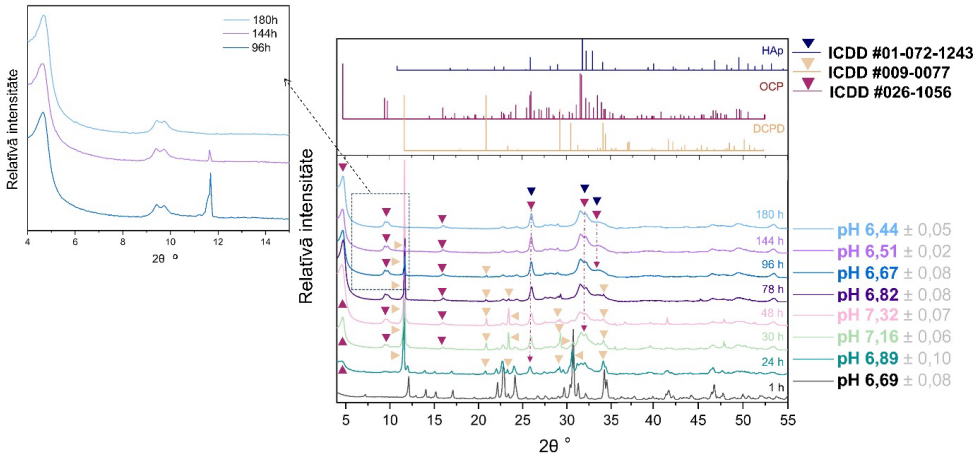

5. att. OCP3 sintēze: *XRD* ainas, kas parāda pāreju no LT-α-TCP caur DCPD uz OCP fāzi, ko papildina pH izmaiņas. References ainas (*ICDD*) atbilst HAp, OCP un DCPD galvenajiem maksimumiem [46].

Reakcijas vides pH izmaiņas palīdz noteikt fāžu pārejas pamatā esošo ķīmisko fonu (izmantojot ķīmiskos vienādojumus), jo jonu (piemēram, OH^-, H^+) izdalīšanās tieši ietekmē šķīduma pH. Vispārējais ķīmiskais vienādojums, kas attēlo LT-α-TCP hidrolīzi par OCP, ir šāds:

$$3Ca_3(PO_4)_2 + 7H_2O \rightarrow Ca_8(HPO_4)_2(PO_4)_4 \cdot 5H_2O + Ca(OH)_2.$$

Šis vienādojums liecina par šķīduma pH palielināšanos, kas ir saistīta ar tiešu PO_4^{3-} iekļaušanos OCP fāzē un līdzvērtīgu šķīstošā kalcija hidroksīda ($Ca(OH)_2$) izdalīšanos. Kā redzams no *XRD* ainām, hidrolīzes laikā kā starpfāze veidojās DCPD, kas šajā vienādojumā nav parādīts, tāpēc vispārējā ķīmiskā reakcija nav atbilstoša. Ņemot vērā novērotās pH izmaiņas (5. att.), sadarbībā ar Tulūzas Universitātes profesoru Kristianu Reju (*Christian Rey*) pāreja no LT-α-TCP uz OCP tika sadalīta vairākos atsevišķos posmos, kā izklāstīts turpmāk.

1. Šķīšanas posms

   Pirms LT-α-TCP pievienošanas ortofosforskābes šķīduma pH bija 2,80 ± 0,15, bet pēc prekursora pievienošanas šķīduma pH strauji pieauga un stundas laikā nostabilizējās pie pH 6,69 ± 0,08. Šis sākotnējais etaps atbilst LT-α-TCP straujai šķīšanai, un to var attēlot ar vienādojumu: $Ca_3(PO_4)_2 + 3H_2O \rightarrow 3Ca^{2+} + H_2PO_4^- + HPO_4^{2-} + 3OH^-$. Turklāt šķīšanas laikā notiek OH^- izdalīšanās, kā rezultātā reakcijas vides pH tuvojas neitrālam pH, kas saistīts ar ortofosfāta anjonu buferēšanas diapazonu. Izmantojot SEM, novērotas izteiktas fāžu izmaiņas. Redzami plāni pavedienveida LT-α-TCP kristāli, un šķīšanas rezultātā LT-α-TCP aglomerātos veidojas nelieli adatveida vai plākšņveida kristāli (6. att., 1 h).

2. Nogulsnēšanās posms

   Ņemot vērā LT-α-TCP šķīdību un tā sākotnējo šķīšanu skābē, kas tuvina šķīduma pH bāziskam, iegūtais šķīdums ir pārsātināts attiecībā pret OCP, DCPD un pat HAp. Tomēr HAp veidošanās ir maz iespējama, salīdzinot ar abām pārējām fāzēm, to labākas nukleācijas un augšanas spējas (straujākas kristalizācijas) dēļ [56, 57].

3. DCPD un OCP fāžu veidošanās posms

   Pateicoties piemērotākam DCPD kristālu augšanas ātrumam, LT-α-TCP pārvēršanās par DCPD notiek ātrāk nekā LT-α-TCP pārvēršanās par OCP. Procesu, kā rezultātā pH pieaug līdz 7,32 ± 0,07 (5. att.), var aprakstīt, izmantojot šādu vienādojumu:

   $$Ca_3(PO_4)_2 + 3H_2O \rightarrow 3Ca^{2+} + H_2PO_4^- + HPO_4^{2-} + 3OH^-.$$

   XRD ainas atbilst ķīmiskajam vienādojumam, un pie augstākās pH vērtības (48 h, OCP3 sintēze) maksimuma (020) pie $2\theta = 11{,}7°$, intensitāte ievērojami pieaug, salīdzinot ar jebkuru citu difrakcijas maksimumu, liecinot par DCPD klātbūtni (5. att.). Nepārtrauktā hidrolīzes procesā sistēmā veidojās OCP un DCPD maisījums. SEM rezultāti apstiprina, ka, palielinoties DCPD daudzumam, notiek pakāpeniska pāreja no pavedienveidīgām daļiņām uz lielākām un biezākām plākšņveida daļiņām (6. att., 24 h, 30 h, 48 h). Lielāki un ievērojami masīvāki plākšņveida kristāli attiecināmi uz DCPD (6. att., 30 h, dzeltenā bultiņa), savukārt mazāki un plānāki plākšņveida kristāli – uz OCP (6. att., 30 h, dzeltenais aplis). Tomēr abu fāžu augstās morfoloģiskās līdzības dēļ tās ir grūti atšķirt.

4. Fāžu pārejas posms no DCPD uz OCP

   Pēc LT-α-TCP pilnīgas izšķīšanas DCPD kļūst par sistēmas vislabāk šķīstošo fāzi un OCP prekursoru, kā parādīts vienādojumā

   $$8\ CaHPO_4 \cdot 2H_2O \rightarrow Ca_8(PO_4)_4(HPO_4)2 \cdot 5H_2O + 2H_3PO_4 + 11H_2O.$$

Šī reakcija izraisa protonu izdalīšanos šķīdumā, kas kopā ar fosfātu vides buferējošajām īpašībām pazemina pH līdz 6,44 ± 0,05. Sintēzes beigās tika konstatēta OCP raksturīgā plākšņveida morfoloģija, lielāko daļiņu fragmentācija un sfērisku agregātu klātbūtne (6. att., 180 h).

OCP un starpfāžu veidošanās tika mērīta kvantitatīvi, izmantojot Rītvelda metodi, un rezultāti kopā ar morfoloģijas izmaiņām atspoguļoti 6. attēlā [55]. Fāžu pāreja sākas no 100 % LT-α-TCP (1 h) līdz ~ 37 % DCPD/~ 63 % OCP (27 h) un beidzas ar ~ 100 % OCP.

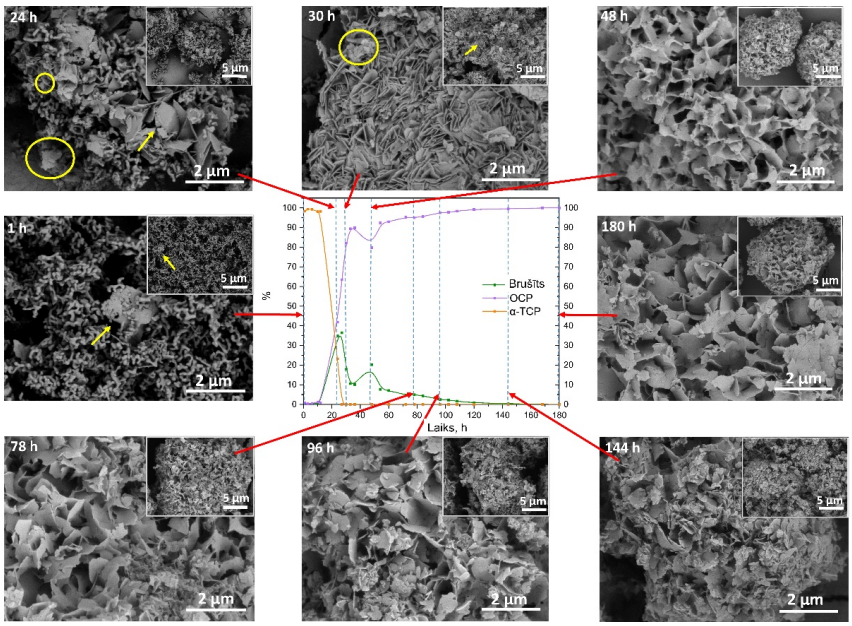

6. att. OCP sintēzes procesā iegūto produktu SEM mikrofotogrāfijas (mērogs ir 5 µm un 2 µm), kas savienotas (sarkanā bultiņa) ar attiecīgo laika punktu (pārtrauktā līnija) fāžu satura diagrammā, kas konstruēta pēc *XRD* kvantitatīvajiem datiem. Dzeltenā bultiņa norāda uz potenciālajām DCPD daļiņām, dzeltenais aplis marķē potenciālās OCP plāksnītes [46].

Lai pārbaudītu, vai mērogotā tehnoloģija ietekmē OCP citosaderību, OCP3 sintēzes starpprodukti un galaprodukti tika pakļauti tiešam kontaktam ar cilvēka kaulu mezenhimālajām cilmes šūnām (hBMSC), un rezultāti tika salīdzināti ar OCP1 un OCP2 (7. A att.). Kontrolei tika izmantotas šūnas, kas kultivētas uz polistirola šūnu kultivēšanas plates bez CaP pulvera paraugiem. Rezultāti liecina, ka šūnu metaboliskā aktivitāte ir > 80 %. Tas apliecina, ka gadījumā, ja tehnoloģija tiktu mērogota uz vēl lielākiem apjomiem, nelieli starpproduktu piemaisījumi, kā arī galaprodukti būtu droši kaulaudu šūnām. Vizuālā analīze, izmantojot imūnfluorescences krāsošanu, kuras mērķis ir parādīt šūnu morfoloģiju, liecina par iespējamu CaP daļiņu internalizāciju hBMSC šūnās, kas pakļautas tiešam kontaktam ar pulveriem (7. B att.).

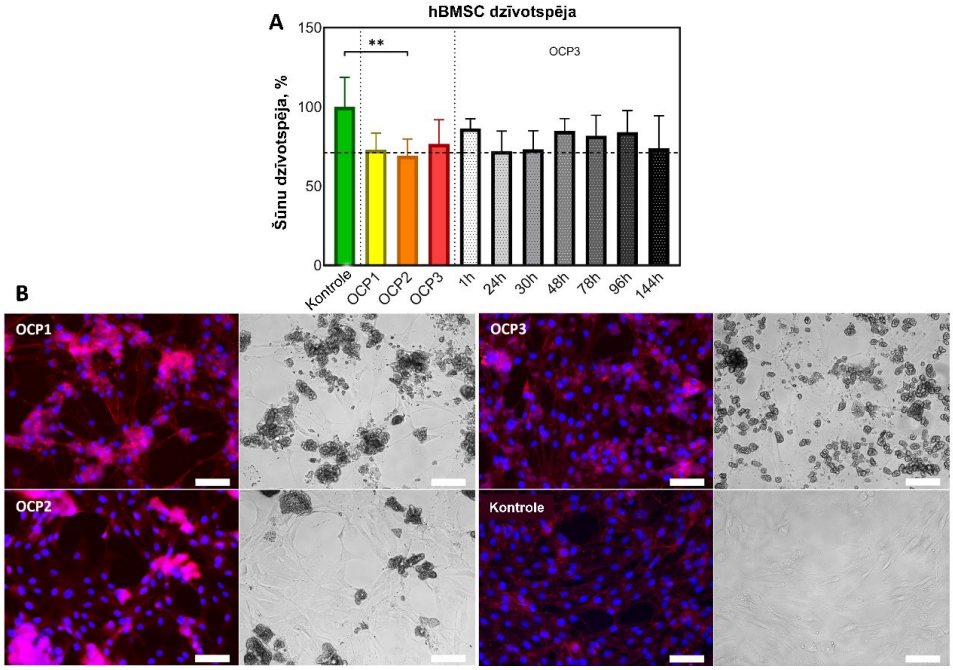

7. att. A – *In vitro* šūnu dzīvotspēja tiešā kontaktā ar OCP1, OCP2, OCP3 un OCP3 sintēzes starpfāzēm (pamatojoties uz vienfaktora dispersiju analīzi ANOVA Tukeja (*Tukey*) korekciju, būtiskas atšķirības starp paraugu grupām tika atzīmētas ** $p \leq 0{,}01$); B – hBMSCs morfoloģija trešajā kultivēšanas dienā tiešā kontaktā ar OCP paraugiem (OCP1, OCP2, OCP3 pulveru koncentrācija 0,5 mg/mL). Kontrolei tika izmantotas šūnas, kas kultivētas uz polistirola šūnu kultivēšanas plates. Imunofluorescences (kreisās puses kolonnas) un gaišā lauka (labās puses kolonnas) mikroskopija. Mērogs – 125 μm.

Sintēzes attīstības gaitas (LT-α-TCP => OCP) *in silico* modeļa izveide

Visaptverošu laboratorijas eksperimentu veikšana ir būtiska biomateriālu ražošanā un novērtēšanā. Šādi eksperimenti ietver sintēzi un raksturošanu, kā arī virsmas fizikāli ķīmisko īpašību un bioloģiskās mikrovides biosaderības izpēti. Tomēr CaP ķīmiskais sastāvs ir ārkārtīgi daudzveidīgs, un atkarībā no konkrētiem eksperimenta apstākļiem var veidoties daudzas fāzes. Turklāt faktiskie eksperimenta apstākļi var nedaudz atšķirties no plānotajiem, un to var izskaidrot ar tādiem faktoriem kā eksperimentālās kļūdas un tuvinājumi. Lai virzītos uz jauno mākslīgā intelekta (*AI*) laikmetu un stiprinātu sadarbību ar Austrumu Pjemontas Universitāti, kopā ar *M. Nascimben et al.* [58] promocijas darba gaitā izstrādāta automatizēta analīzes secība, kas paredzēta, lai izveidotu lēmumu atbalsta sistēmu sintēzes progresa uzraudzībai no LT-α-TCP uz OCP.

Mērķis bija apvienot skaitļošanas protokolus, kas ļauj noteikt sintēzes stadiju (vai tās iespējamās beigas), un datus, kas iegūti no OCP3 sintēzes (10 g iznākums, 180 h) *XRD* ainām un *FTIR* spektriem. Analīzes secība ietvēra mašīnmācīšanās (*ML*) paņēmienus funkciju ranžēšanai, telpiskajai filtrēšanai un dimensionalitātes samazināšanai, kas nepieciešams, lai precizētu sintēzes posmu automātisko atpazīšanu (8. att.).

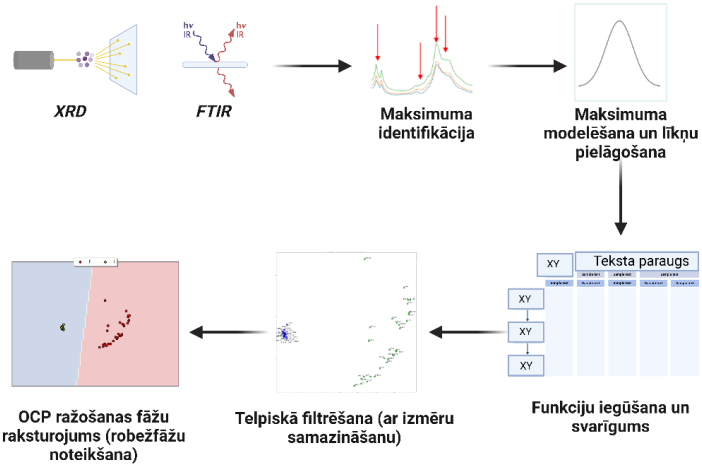

8. att. Mašīnmācīšanās metodes izveides procesa shēma, lai noteiktu OCP veidošanās posmus, pamatojoties uz iegūtajām *XRD* ainām un *FTIR* spektriem [58].

Sintēzes norise tika raksturota, izmantojot *XRD* un *FTIR* datus (sk. iepriekšējo nodaļu). Pirmie divi sintēzes laika punkti (t. i., 1 h un 24 h) tika izvēlēti kā sintēzes sākumposma, pēdējie divi laika punkti (144 h un 180 h) – kā sintēzes beigu posma raksturotāji. Pēc tam šie dati tika pakļauti priekšapstrādei, ko izmanto *ML* (saukta par telpisko filtrēšanu), kas uzlabo dažādu *XRD/FTIR* grupu atdalīšanu. Iegūtā datu apakškopa tika izmantota, lai atpazītu OCP veidošanās posmus.

OCP sintēzes un raksturošanas pieredzes apvienojums ar izstrādātu algoritmu, kas spēj noteikt, kādā stadijā ir OCP veidošanās, ir devis daudzsološu pamatu lēmumu atbalsta sistēmai, kas īpaši pielāgota OCP sintēzes uzraudzībai. *XRD/FTIR* datu kopu un mākslīgā intelekta integrācija ļautu pētniekiem izveidot stabilāku un informatīvāku pazīmju kopu *ML* modeļa apgūšanai, kas ļautu izveidot līdzsvarotāku un precīzāku modeli ar samazinātu novirzi un dispersiju.

OCP pielietojuma potenciāls

OCP kā vienai no svarīgākajām kaulaudu neorganiskās fāzes sastāvdaļām ir plašas pielietošanas iespējas kaulaudu inženierijā. Tā nozīme ir saistīta ar spēju izdalīt cilvēka organismam svarīgos kalcija un fosfāta jonus, kas ir būtiski, lai regulētu jaunu kaulu veidošanos. Līdz šim OCP ir izmantots kā kaulu cements [34], kompozītmateriāla pamatne ar dažādiem polimēriem (alginmāts, želatīns, kolagēns, PEGT u. c.) [35–37], kā pārklājums uz titāna vai titāna sakausējuma implantiem [29, 38] un kā zāļu/jonu piegādes sistēma [23], taču biomateriālu uz OCP bāzes klīniskais pielietojums patlaban ir tikai sākuma stadijā.

Lai pārliecinātos par OCP bioloģisko potenciālu un tuvinātu to klīniskam pielietojumam, promocijas darba otrajā daļā OCP tika izmantots divu kompozītbiomateriālu izstrādē biomedicīnas jomai. Pirmkārt, OCP tika modificēts ar doksorubicīna hidrohlorīdu, lai izveidotu efektīvu zāļu piegādes sistēmu kaulu vēža ārstēšanai. Otrkārt, OCP tika sajaukts ar alginātu, lai iegūtu kompozītmateriāla pārklājumu uz 3D drukātiem titāna sakausējumiem un pārbaudītu, vai tas var uzlabot to izturību pret koroziju.

Oktakalcija fosfāts un doksorubicīna hidrohlorīds. Jauna zāļu piegādes sistēma vēža ārstēšanai

Doksorubicīna hidrohlorīds (DOX, doksorubicīns), kas tiek iegūts no *Streptomyces peucetius var. caesius*, kas šķīst ūdenī un ir gaismjutīgs, ir viens no plašāk izmantotajiem pretvēža zāļu pārstāvjiem [59]. Neskatoties uz to, ka DOX ir efektīvs antineoplastisks līdzeklis, tas var izraisīt sistēmisku toksicitāti, sākot ar sliktu dūšu un beidzot ar palielinātu doksorubicīna izraisītas kardiomiopātijas risku [60, 61]. Turklāt tikai neliela daļa no jebkuras sistēmiski ievadītas devas sasniedz ķirurģiskās operācijas vietu, tāpēc lokālu pretvēža piegādes sistēmu izmantošana varētu būt risinājums, lai sasniegtu augstas aktīvo vielu koncentrācijas vēža skartajā vietā. Programmētas šūnu nāves (*PCD*) raksturīgo ceļu, piemēram, apoptozes, nekrozes vai feroptozes, izpēte ir ļoti svarīga audu inženierijā (lai imitētu dabisko audu attīstību), zāļu izstrādē (zāles iedarbojas, inducējot vai inhibējot *PCD*), terapeitiskajās stratēģijās un normālā šūnu attīstībā (nevēlamo vai bojāto šūnu likvidēšanā) [62, 63]. Ņemot vērā, ka iekššūnu ceļu darbības traucējumi ir arī potenciāls vēža ierosinātājs cilvēka organismā, izpratne par to, vai *PCD* ir saistīta ar apoptozi (šūnu bojāeja, kas notiek kā normāla un kontrolēta šūnu attīstības daļa) vai feroptozi (šūnu bojāeja, ko izraisa ģenētiskas izmaiņas dzelzs homeostāzē), var palīdzēt izstrādāt inovatīvas zāļu piegādes sistēmas vēža ārstēšanai nākotnē.

OCP sintēze tiek veikta istabas temperatūrā, savukārt vairākums zāļu ir jutīgas pret paaugstinātām temperatūrām, tāpēc OCP modificēšana ar aktīvajām vielām *in situ* OCP sintēzes laikā varētu būt potenciāla metode doksorubicīnu saturoša oktakalcija fosfāta (OCP-DOX) iegūšanai. Turklāt, izvēloties šādu stratēģiju, varētu panākt, ka aktīvā viela OCP struktūrā tiek iekļauta jau no paša OCP sintēzes sākuma, tādējādi nodrošinot augstu aktīvās vielas saturu OCP daļiņās [41]. Ņemot vērā to, ka α-TCP pārveidošanās gaitā par OCP notiek OH^- un HPO_4^{2-} izdalīšanās un šiem izdalītajiem joniem ir nozīme OCP hidratētā slāņa

veidošanās procesā, iespējams, ka, pievienojot DOX jau OCP sintēzes sākuma posmā, tiktu panākta aktīvās vielas iekļaušanās OCP hidratētajā slānī. Papildus minētajam, OCP lielais īpatnējais virsmas laukums un tā plākšņveida daļiņu morfoloģija potenciāli padara OCP efektīvāku un labvēlīgāku šūnu atbildes reakcijās. Tādējādi, promocijas darbā izstrādājot inovatīvas *DDS*, uzsvars tika likts uz trīs galvenajiem iegūtā DOX-OCP īpašību raksturošanas posmiem.

1. **Iegūtā DOX-OCP fizikāli ķīmiso īpašību novērtējums** pēc tam, kad tas tika funkcionalizēts ar DOX plašā koncentrāciju diapazonā (no 1 masas% līdz 20 masas% no LT-α-TCP satura).
2. ***In vitro* doksorubicīna izdalīšanās kinētikas novērtējums** sešu nedēļu periodā.
3. **DOX-OCP *in vitro* biosaderības un *PCD* mehānisma novērtējums**.

Shematisks attēlojums DOX-OCP kā zāļu piegādes sistēmas izstrādei redzams 9. attēlā [64].

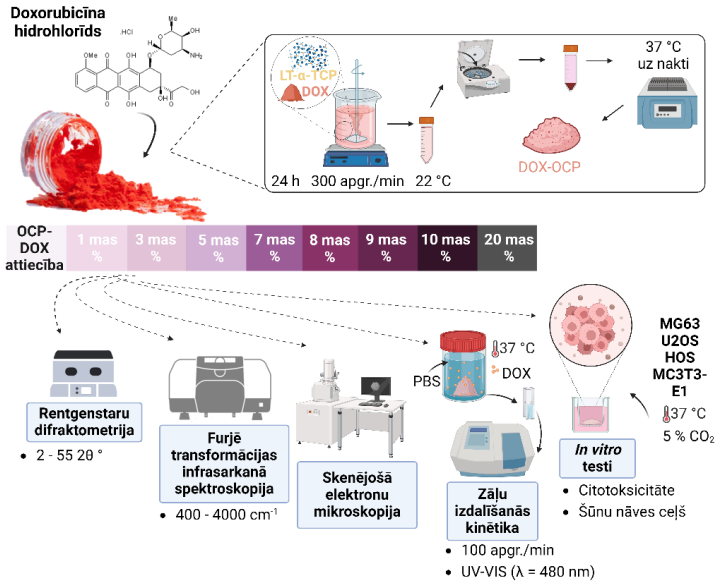

9. att. Doksorubicīnu saturoša oktakalcija fosfāta izstrādes un raksturošanas pieejas shematisks attēlojums.

Lai pārbaudītu kā DOX saturs ietekmē OCP fāzes veidošanos, OCP sintēzes vidē tika pievienoti 1 masas%, 3 masas%, 5 masas%, 7 masas%, 8 masas%, 9 masas%, 10 masas% un 20 masas% aktīvās vielas (no sākotnējā LT-α-TCP daudzuma, 1DOX-OCP, 3DOX-OCP, 5DOX-OCP, 7DOX-OCP, 8DOX-OCP, 9DOX-OCP, 10DOX-OCP, 20DOX-CaP), un sintēze ilga 24 stundas. Izmantojot *XRD* analīzi, detektēti raksturīgie OCP difrakcijas maksimumi (zema leņķa (100) maksimums pie 2θ = 4,7° un dublets (200) un (010) pie 2θ = 9,4° un 2θ = 9,7°) sintēžu produktos, kam tika pievienots līdz 10 masas% DOX (10. A, B att.). Salīdzinot ar tīru OCP, DOX-OCP difraktogrammās bija vērojama neliela maksimumu, pie 2θ = 4,7° un 2θ=26,1°, nobīde uz zemākiem 2θ grādiem un difrakcijas maksimumu intensitātes izmaiņas, liecinot par kristāliskā režģa izplešanos DOX-OCP sistēmā, kas savukārt liecina par aktīvās

vielas iekļaušanos OCP kristāliskajā struktūrā. Turklāt tika novērots, ka OCP struktūras stabilizācija ir atkarīga no DOX daudzuma, kas izmantots OCP-DOX sintēzē. Iegūtie rezultāti parādīja, ka, ja pievienotā DOX daudzums pārsniedz 10 masas% (no sākotnējā LT-α-TCP daudzuma), tas kavē c ass augšanu OCP struktūrā un destabilizē kopējo transformācijas procesu no LT-α-TCP uz OCP. Pēc rūpīgas *XRD* ainu analīzes secināts, ka, DOX daudzumam pārsniedzot 10 masas% (no sākotnējā LT-α-TCP daudzuma), saglabājas LT-α-TCP raksturīgie maksimumi pie 12,1 un 30,7 2θ grādiem ar dubultiem maksimumiem pie aptuveni 2θ = 22,8° un 2θ = 34° (10. A, B att.) [64]. Šie rezultāti liecina, ka DOX tika adsorbēts uz LT-α-TCP daļiņu virsmas jau OCP sintēzes sākumā, kavējot LT-α-TCP šķīšanas procesu, tādējādi sintēzes gaitā veidojot LT-α-TCP-DOX DDS, nevis DOX-OCP, kas bija definētais mērķis.

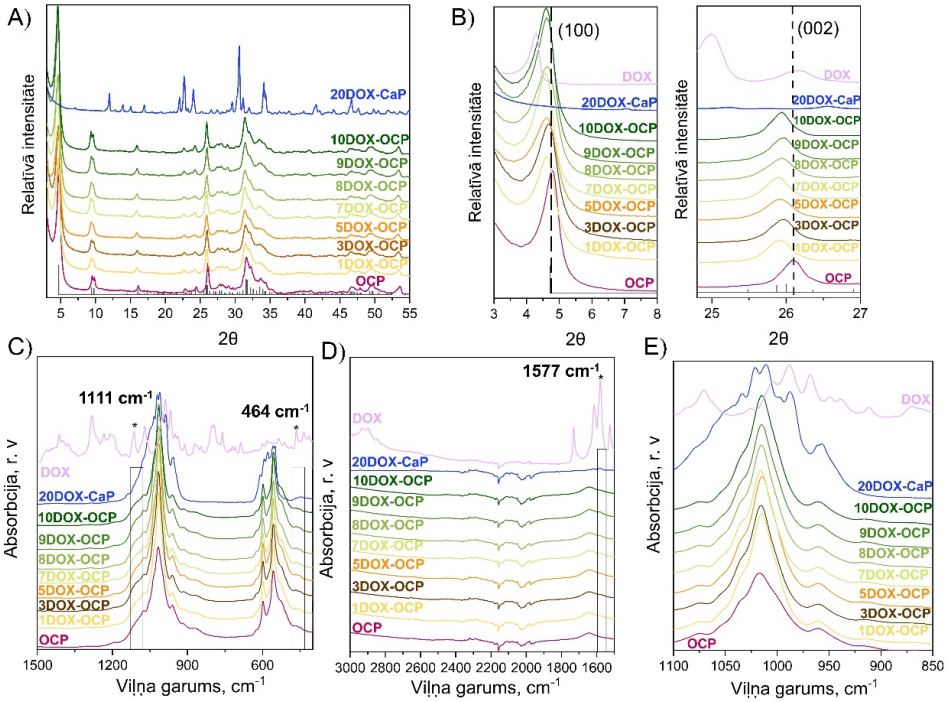

10. att. DOX-OCP fizikāli-ķīmisko īpašību profils: A – *XRD* ainas, kur *ICDD* ieraksts Nr. 026-1056 atbilst OCP triklīnajai fāzei; B – OCP un DOX-OCP *XRD* ainas. Maksimumi pie 2θ = 4,7° un 2θ = 26,1° atbilst attiecīgi (100) un (002) plaknēm; C, D – DOX-OCP *FTIR* spektri. Zvaigznīte un apvienojošās iekavas (C un D attēlos) apzīmē joslas, kas ir izmainījušās DOX iekļaušanas dēļ.

FTIR rezultātu analīze parādīja, ka visiem iegūtajiem DOX saturošajiem produktiem (izņemot 20DOX-CaP) ir novērojamas tipiskas OCP fāzei raksturīgas absorbcijas joslas (10. C, D att.): PO_4^{3-} ν_3 svārstības pie 1077 cm^{-1}, 1296 cm^{-1} un 1120 cm^{-1}, PO_4^{3-} ν_4 svārstības pie 524 cm^{-1}, 560 cm^{-1}, 601 cm^{-1} un 627 cm^{-1}, kā arī P-OH svārstības pie 917 cm^{-1} un 861 cm^{-1}. Papildus DOX-OCP *FTIR* spektros tika novērotas salīdzinoši nelielas absorbcijas joslu izmaiņas, kas saistītas ar DOX klātbūtni izveidotajās zāļu piegādes sistēmās. Šīs izmaiņas redzamas kā pieaugošā absorbcijas joslas intensitāte 1570 cm^{-1} apgabalā, kas liecina par

antisimetriskām COO^- saišu svārstībām. Turklāt konstatēts, ka DOX izteiktais maksimums pie ~ 1111 cm^{-1} palielina PO_4^{3-} ν_3 absorbcijas joslas platumu, līdz ar to DOX-OCP *FTIR* spektros, palielinoties DOX saturam OCP, var novērot aizvien izteiktāku pleca joslu (10. C att.). Analizējot ar HPO_4(5) saistītās svārstības pie 1193 cm^{-1}, secināts, ka, palielinoties DOX saturam OCP, to intensitāte samazinās, kas liecina par būtisku HPO_4(5) grupu samazināšanos, liecinot par OCP hidrolīzes sākumu par CDHAp.

Analizējot skenējošās elektronu mikroskopijas datus, secināts, ka, palielinoties DOX daudzumam paraugos, OCP plākšņveida daļiņām ir tendence vairāk pārklāties citai ar citu, veidojot aglomerātus izmēru 1–20 μm diapozonā (11. A–G att.). Arī SEM mikrofotogrāfijas apstiprināja *XRD* un *FTIR* datu analīzē konstatēto, ka paraugos, kas sintezēti, izmantojot 20 masas% DOX (no sākotnējā LT-α-TCP daudzuma), novērojama OCP fāzes inhibīcija, par ko liecina LT-α-TCP raksturīgo iegareno graudaino daļiņu saglabāšanās gala produktā (11. H att.) [64].

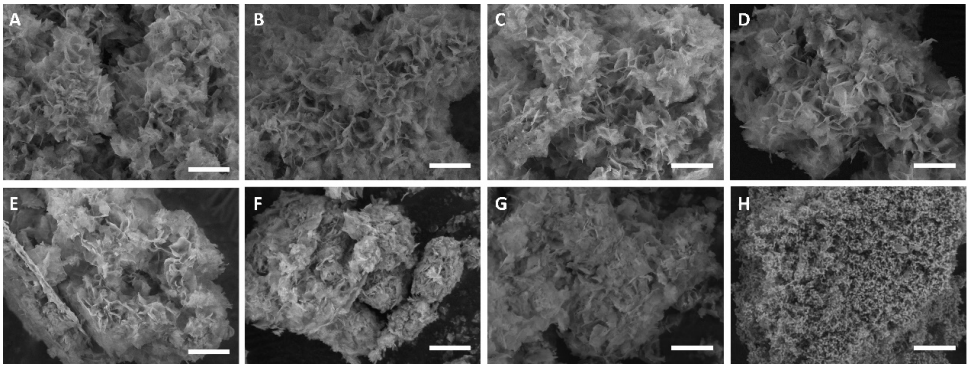

11. att. DOX-OCP (1-10 masas%) un DOX-CaP (20 masas%) SEM mikrofotogrāfijas: A – 1 masas%; B – 3 masas%; C – 5 masas%; D – 7 masas%; E – 8 masas%; F – 9 masas%; G – 10 masas% un H – 20 masas%; mērogs – 5 μm.

Analizējot DOX saturu DOX-OCP *DDS*, secināts, ka, ja teorētiskais sintēzē izmantotais DOX daudzums (no sākotnējā LT-α-TCP daudzuma) bija 1, 5 un 10 masas%, tad attiecīgi DOX saturs DOX-OCP DDS sasniedza 0,093 ± 0,01 masas% ar iekļaušanas efektivitāti 9,6 ± 1,9 %, 1,54 ± 0,1 masas% ar iekļaušanas efektivitāti 20,85 ± 1,29 % un 2,02 ± 0,06 masas% ar iekļaušanas efektivitāti 21,8 ± 0,73 % (12. A att.). Ja OCP sintēzē tika izmantoti 20 masas% DOX, kas inhibēja OCP fāzes veidošanos, izveidotajā DOX-CaP sistēmā tika konstatēts vislielākais DOX saturs – 2,66 ± 0,24 masas%. Tai pat laikā DOX iekļaušanas efektivitāte bija salīdzinoši zema – 15,99 ± 1,36 %. Iespējams, uz LT-α-TCP virsmas adsorbētais DOX kavē OCP veidošanos, vienlaikus uzrādot lielāku detektēto zāļu saturu [64].

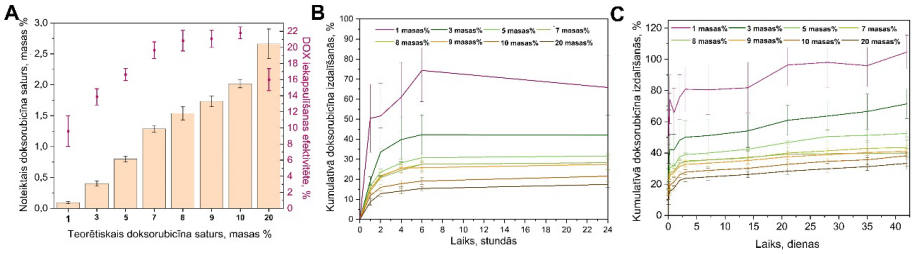

12. att. A – kopējais DOX saturs un DOX iekļaušanas efektivitāte DOX saturošos CaP paraugos; B – DOX sākotnējā straujā izdalīšanās pirmajās 24 stundās (%) un C – kopējais izdalītais DOX daudzums sešu nedēļu periodā (%).

Analizējot DOX izdalīšanos no pagatavotajām DOX-OCP piegādes sistēmām, tika novērots, ka pirmajās 24 stundās notiek strauja DOX izdalīšanās (~ 17–75 % no kopējā DOX daudzuma *DDS*; 12. B att.), kam seko ilgstoša un vinmērīga aktīvās vielas izdalīšanās (12. C att.). Doksorubicīna molekulu sākotnējo straujo izdalīšanos no OCP virsmas var saistīt ar aktīvās vielas fizikālo adsorbciju, ko izraisa elektrostatiskie spēki vai ūdeņraža saites. Tas notiek starp pozitīvi lādētām DOX molekulām un negatīvi lādēto OCP. Turpretī DOX turpmāku izdalīšanos var izskaidrot ar spēcīgu ķīmisko mijiedarbību (Ca-O), kas kavē zāļu izdalīšanos no DOX-OCP zāļu piegādes sistēmas [64]. Turklāt pētījumā tika konstatēts, ka kumulatīvās izdalīšanās procentuālais plato ir apgriezti proporcionāls teorētiskajam doksorubicīna saturam. Piemēram, 5DOX-OCP gadījumā 23,6 ± 1,6 % (28,00 ± 3,68 μg) DOX izdalījās pēc divām stundām, 38,9 ± 1,3 % (46,3 ± 4,2 μg) DOX pēc 72 stundām un 52,5 ± 2,3 % (62,3 ± 5,8 μg) DOX pēc 42 dienām. Savukārt 10DOX-OCP gadījumā pēc divām stundām izdalījās 15,9 ± 1,3 % DOX, pēc 72 stundām – 27,7 ± 1,7 % DOX un pēc 42 dienām – 38,3 ± 2,0 % DOX.

Papildus tika novērots – jo mazāks ir doksorubicīna saturs DOX-OCP, jo ātrāk aktīvā viela izdalās. Šo novērojumu var izskaidrot ar OCP fāzes pārveidošanos par kalcija deficīta hidroksilapatītu [64, 65], kas novērots 1DOX-OCP zāļu piegādes sistēmām. Tika arī noteikts, ka visu DOX-OCP gadījumā aktīvā viela no DDS izdalās pakāpeniski un izdalīšanās profils atbilst Froindliha izotermai [65].

***In vitro* testi**

Lai salīdzinātu šūnu atbildes reakciju uz izveidotajām DOX-OCP zāļu piegādes sistēmām, tika pētīta to ietekme uz MG63 (vēža šūnas) un MC3T3-E1 (preosteoblastiskas šūnas) šūnām. Abu šūnu līniju izmantošana pētījumā ļauj visaptveroši analizēt sistēmas efektivitāti kaulu vēža ārstēšanā, sniedzot ieskatu par tās potenciālu metastāžu samazināšanā, kā arī ļauj spriest par DOX-OCP ietekmi uz veselajām kaula šūnām.

DOX ietekme uz MG63 un MC3T3-E1 šūnu dzīvotspēju novērtēta, analizējot OCP un DOX-OCP pulverus netiešā kontaktā ar abām šūnu līnijām (13. A att.). Iegūtie rezultāti parādīja, ka šūnu vide, kas apstrādāta ar 1DOX-OCP, 5DOX-OCP un 10DOX-OCP, septiņu dienu laikā nomāca MG63 šūnu dzīvotspēju (attiecīgi samazinot to līdz 54,1 %, 12,4 % un 5,7 %). Tai pat laikā, analizējot paraugu ietekmi uz MC3T3-E1 šūnu līniju, secināts, ka starp trešo un septīto MC3T3-E1 šūnu kultivēšanas dienu tīrs OCP, 1DOX-OCP un 5DOX-OCP uzrādīja šūnu

stimulējošu iedarbību (šūnu dzīvotspēja pieauga no 58,5 % līdz 93,4 % 1DOX-OCP un no 36,9 % līdz 67,4 % 5DOX-OCP gadījumā). Dzīvotspējas pieaugums varētu būt saistīts ar šūnu lēno pielāgošanos pārmaiņu izraisītajam stresam vai ar paaugstinātu Ca^{2+} jonu koncentrāciju šūnu vidē, kas izdalās no OCP, aktivizējot ārpusšūnu kalcija jutīgos receptorus un pastiprinot šūnu vairošanos [64, 66, 67]. 10DOX-OCP inhibējošā ietekme uz šūnu dzīvotspēju bija ievērojami lielāka nekā 5DOX-OCP un 1DOX-OCP, kas ir papildu pierādījums tā izteiktajai inhibējošajai ietekmei uz MG63 šūnām (13. A att.).

Sākotnējie dzīvotspējas testi parādīja, ka DOX-OCP sistēma ir letāla MG63 šūnām visās koncentrācijās, tāpēc tālākai analīzei tika izvēlēta DOX-OCP kompozīcija ar zemāko DOX saturu. Lai mērķtiecīgi novērtētu PCD osteosarkomas šūnās (OS), bija nepieciešama lielāka izmantoto šūnu līniju daudzveidība, jo OS raksturīga augsta ģenētiskā heterogenitāte. Dažādām osteosarkomas šūnu līnijām ir atšķirīgi fenotipi, tāpēc tās var būt ar atšķirīgām diferenciācijas un audzēju veidošanas spējām, līdz ar to ar atšķirīgu reakciju uz noteiktu ārstēšanas veidu. Tāpēc 1DOX-OCP tika atkārtoti testēts, izmantojot U2OS, MG63 un HOS cilvēka vēža šūnu līnijas. Visas trīs izvēlētās šūnu līnijas bieži izmanto zinātniskajos pētījumos, tomēr tām ir ģenētiskas un fenotipiskas atšķirības, kas ir vēlamas daudzpusīgam pirmsklīniskam biomateriāla novērtējumam. Līdzīgi kā iepriekš, iegūtie rezultāti liecināja par ievērojamu visu pētīto osteosarkomas šūnu dzīvotspējas samazināšanos 1DOX-OCP iedarbības rezultātā (MG63 – 0,32 ± 0,2 %, HOS – 0,17 ± 0,02 % un U2OS – 0,25 ± 0,02 % no šūnu dzīvotspējas) (13. B att.). Šūnu dzīvotspējas atšķirības starp 1DOX-OCP un DOX var būt saistītas ar tūlītēju zāļu pieejamību to galīgajā koncentrācijā pozitīvās kontroles grupā (DOX), savukārt doksorubicīns no 1DOX-OCP laika gaitā izdalījās pakāpeniski, kas atbilst *in vitro* zāļu izdalīšanās pētījuma rezultātiem (12. B, C att.). Lai noskaidrotu, vai OS šūnu jutība pret feroptozi palielināsies, DOX-OCP tika pievienots feroptozes inhibitors Ferrostatīns-1 (Fer-1) [68]. Iegūtie rezultāti neuzrādīja būtiskas OS šūnu dzīvotspējas izmaiņas (13. C att.) 1DOX-OCP+Fer-1 klātbūtnē, salīdzinot ar 1DOX-OCP (13. C att.), tāpēc secināts, ka feroptoze nav saistīta ar DOX-OCP izraisīto šūnu nāvi. Ņemot vērā to, ka feroptoze tika izslēgta, nākamais solis bija apoptozes pārbaude, pārbaudot šķeltās poli (ADP-ribozes) polimerāzes (PARP) līmeni [69, 70], ko uzskata par apoptozes pierādījumu, izmantojot Vesternblota metodi. Rezultāti uzrādīja palielinātu šķeltās PARP ekspresiju HOS un MG-63 šūnās, kas tika pakļautas 1DOX-OCP iedarbībai, apstiprinot apoptotiskās šūnu nāves indukciju (13. D att.) [64]. *In vitro* testi tika veikti sadarbībā ar Dr. E. Panczišinu (E. Panczyszyn) no Austrumu Pjemontas universitātes Itālijā (University of Eastern Piedmont) un *Dr.* O. Demiru no Rīgas Tehniskās universitātes.

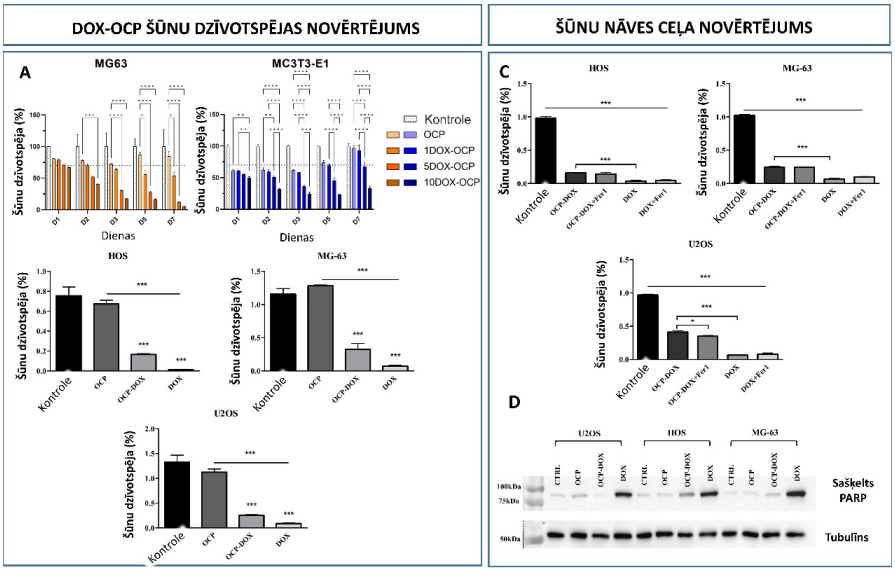

13. att. Šūnu dzīvotspējas pētījumi DOX-OCP klātbūtnē: A – MG63 šūnu un MC3T3-E1 šūnu dzīvotspējas pārbaude OCP, 1DOX-OCP, 5DOX-OCP un 10DOX-OCP pulveru klātbūtnē; B – OS šūnu jutība pret 1 masas% DOX saturošu OCP pulveri, OCP un DOX; C – U2OS, HOS un MG63 šūnu dzīvotspēja kombinācijā ar 10 μM Fer1 (OCP-DOX+Fer-1, DOX+Fer-1); D – sašķeltā PARP proteīnu līmenis. Histogrammās attēlota vidējā vērtība ± standartnovirze; n = 3; statistiski nozīmīgas atšķirības: * pie $p < 0,05$, ** pie $p < 0,005$, *** pie $p < 0,001$, **** pie $p < 0,0001$.

OCP saturoši hidrogēla pārklājumi metāla implantu pretkorozijas noturības uzlabošanai

Titāna sakausējumus (Ti) plaši izmanto kā biomateriālus zobu un ortopēdisko implantu izgatavošanai, galvenokārt to izcilo mehānisko īpašību un biosaderības dēļ. Šiem sakausējumiem fizioloģiskos apstākļos (pH ≈ 7) piemīt mērena izturība pret koroziju, jo to virsmas dabiski pārklāj blīvi aizsargājoši oksīdu slāņi. Tomēr iekaisuma apstākļos, kas pazemina vides pH, mijiedarbības ar reaktīvajām skābekļa formām, pienskābi, hidroperoksilradikāļiem un hipohlorskābi (ko leikocīti izdala ārpussūnu vidē) ietekmē Ti virsmu izturību pret koroziju. Kā vienu no stratēģijām, lai efektīvi uzlabotu metāla implantu izturību pret koroziju, var izmantot Ti virsmas modificēšanu ar hidrogēla pārklājumiem. Lai pārbaudītu, vai OCP daļiņas spēj vēl vairāk uzlabo Ti virsmu pretkorozijas īpašības, tika izveidota sadarbība ar Alto Universitāti. Kopā ar *A. Bordbar-Khiabani et al.* [38] nātrija algināts (Alg) un OCP tika apvienoti kompozītpārklājumā, pārbaudot to elektroķīmiskos raksturlielumus attiecībā uz Ti sakausējumiem.

Eksperimentālās gaitas shematisks attēlojums redzams 14. attēlā. Proti, izmantojot Alg šķīdumu ūdenī (3 masas%) un OCP, tika izveidoti kompozītmateriāli ar neorganiskās/organiskās fāzes attiecību 70 : 30 masas% (turpmāk apzīmēts kā Alg/OCP) un

izmantoti, lai pārklātu 3D drukātu titāna substrātu virsmu. Titāna sakausējuma diski (d = 10 mm) – Ti Gr2 un Ti Gr23 sakausējums – tika pārklāti ar aptuveni 10 mg pārklājuma (Alg un Alg/OCP) un salīdzināta to pretkorozijas noturība 37 ± 0,5 °C temperatūrā viegli anaerobos apstākļos trīs simulācijas vidēs ar dažādiem pH: pH 7,4 ± 0,1 (normāla ķermeņa vide – N), pH 5,2 ± 0,1 (iekaisuma vide – I) un pH 3,0 ± 0,2 (smaga iekaisuma vide – SI).

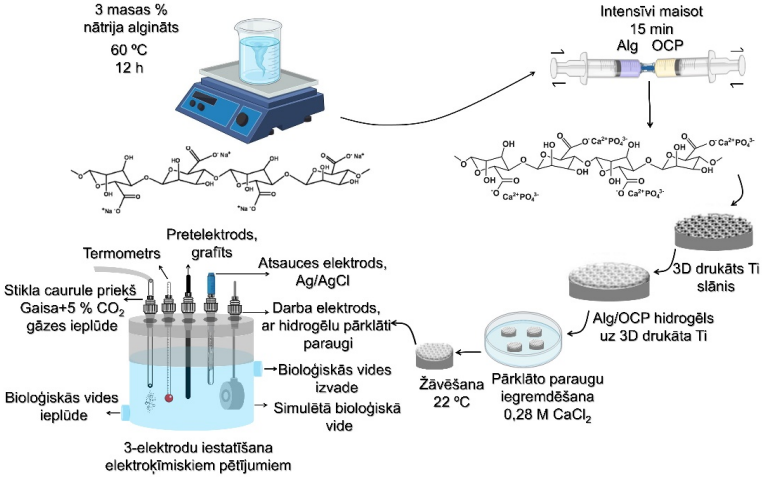

14. att. Ar Alg/OCP pārklātu 3D drukātu Ti sakausējumu iegūšana un elektroķīmiskā raksturošana [38].

Pārklājumu fizikāli ķīmiskās īpašības tika raksturotas pirms (apzīmēti kā Alg/OCP) un pēc vienas stundas ilgas iegremdēšanas attiecīgajā vidē – apzīmēti kā Alg/OCP N, I, SI (15. att.). Tika novēroti OCP raksturīgie *XRD* difrakcijas maksimumi, un amorfais platais difrakcijas maksimums, kas bija redzams *XRD* ainā, atbilda nātrija algināta biopolimēram (15. A att.). *FTIR* uzrādīja HPO_4^{2-} svārstības pie 917 cm^{-1}, 875 cm^{-1}, 1007 cm^{-1} un 1295 cm^{-1}, kā arī plašu joslu, kas iecentrēta pie aptuveni 3500 cm^{-1} un kas atbilst hidroksilgrupu svārstībām (15. B att.).

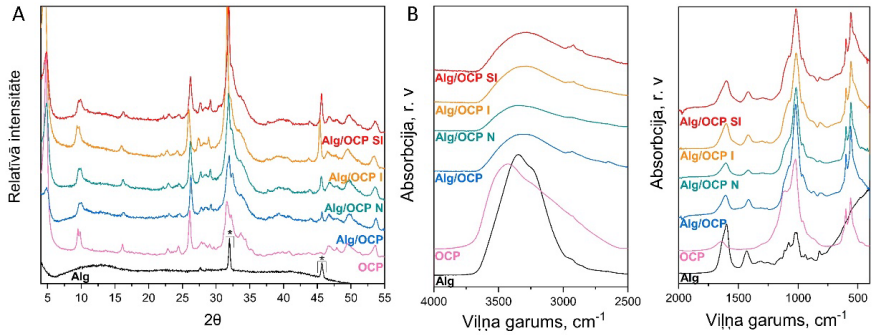

15. att. Alg/OCP pārklājuma fizikāli ķīmiskais raksturojums pirms un pēc iegremdēšanas attiecīgajā vidē (normāla ķermeņa vide – N, iekaisuma vide – I un smaga iekaisuma vide – SI). A – *XRD* ainas; B – *FTIR* spektri dažādos viļņa skaitļa reģionos [38].

Elektroķīmisko impedances spektroskopiju (EIS) parasti izmanto elektroķīmisko procesu raksturošanai, piemēram, metālu aizsargpārklājumu veiktspējas novērtēšanai. Nikvista grafiks tika izmantots kā frekvences raksturlīkne, un Bodes modulis tika izmantots, lai reprezentētu sistēmas pieaugumu un fāzi kā frekvences funkciju. Iegūtie EIS dati un konstantās fāzes elementa (*CPE*) [71] (pārklājuma kapacitātes mērījums, kas parādīts, izmantojot CPE_{dl} (robežvirsma starp substrātu un šķīdumu) un Rct (pretestība lādiņa pārnesei)) rezultāti ir parādīti un detalizēti izskaidroti *A. Bordbar-Khiabani et al.* zinātniskajā publikācijā [38].

Nikvista grafikos gan iekaisuma, gan smaga iekaisuma apstākļos novērojama kapacitatīvo cilpu diametru samazināšanās, kas liecina par korozijas pretestības samazināšanos [71, 72]. Šo tendenci apstiprina arī Bodes amplitūdas grafiks, kas parādīts impedances moduļa zemo frekvenču diapazonā [38]. Rct vērtības paraugiem ar Alg/OCP pārklājumiem bija ievērojami lielākas (23,09 ± 0,10 kΩ · cm^2 un 25,12 ± 0,39 kΩ · cm^2, kas attiecas uz TiGr2 un TiGr23) nekā 3D drukāta Ti paraugiem bez pārklājumiem (17,63 ± 0,33 kΩ · cm^2 un 20,66 ± 0,73 kΩ · cm^2, kas attiecas uz TiGr2 un TiGr23). Tas liecina, ka Alg/OCP pārklājums efektīvi veido izturīgu barjeru, kavējot korozīvo jonu iekļūšanu substrātā. Turklāt OCP klātbūtne vēl vairāk palielina Alg hidrogēla pretestību (Rc) (piemēram, 12,33 ± 0,83 kΩ · cm^2 Alg un 18,84 ± 0,75 kΩ · cm^2 Alg/OCP pārklājumam uz TiGr2), kas liecina, ka normālos apstākļos OCP daļiņas var pastiprināt Alg hidrogēla pārklājuma šķērssaistīšanās pakāpi, palielinot pārklājuma blīvumu un sasaistīšanās spēku robežvirsmā starp pārklājumu un substrātu. Tas arīdzan izskaidro lielākas Rc vērtības paraugiem, kas bija pārklāti ar Alg/OCP, salīdzinot ar paraugiem, kas pārklāti ar tīru Alg. Savukārt Rc vērtību samazināšanos, kas novērota pārklātajos paraugos iekaisuma un spēcīga iekaisuma apstākļos (piemēram, I: 7,15 ± 0,91 kΩ·cm^2 Alg/OCP un SI: 3,01 ± 0,53 kΩ·cm^2 Alg/OCP TiGr2 gadījumā), var skaidrot ar hidrogēlu šķīšanu sālsskābē un ūdeņraža peroksīdā [38, 71].

SECINĀJUMI

1. Desmitkārtējas un simtkārtējas LT-α-TCP hidrolīzes mērogošanas rezultātā var iegūt 1 g un 10 g tīra OCP, tomēr sintēzes iznākuma palielināšanai nepieciešams ilgāks sintēzes laiks – 72 h (1 g OCP) un 180 h (10 g OCP).

2. LT-α-TCP pārveidošanās par OCP notiek caur brušītu kā starpprodukta fāzi.

3. DOX-OCP zāļu piegādes sistēmas sintēzes laikā pievienojot vairāk nekā 10 masas% doksorubicīna no sākotnējā LT-α-TCP daudzuma, tiek kavēta OCP fāzes veidošanās.

4. DOX-OCP ietekmē mainās MG63 un MC3T3 šūnu vairošanās profils, ko ietekmē gan DOX koncentrācijas šūnu vidē, gan DOX-OCP/šūnu vides kontakta laiks.

5. DOX-OCP daļiņas izraisa osteosarkomas šūnu nāvi apoptozes ceļā.

6. OCP daļiņas alginmāta hidrogēla matricā palielina elektriskā lādiņa pārneses pretestību pie Ti substrāta un alginmāta/OCP pārklājuma robežvirsmas.

ATSAUCES

[1] W. Habraken, P. Habibovic, M. Epple, M. Bohner, Calcium phosphates in biomedical applications: Materials for the future?, Mater. Today. 19 (2016) 69–87. https://doi.org/10.1016/j.mattod.2015.10.008.

[2] S. Ban, J. Hasegawa, T. Jinde, Phase Transformation of Octacalcium Phosphate in vivo and in vitro, Dent. Mater. J. 11 (1992) 130–140217. https://doi.org/10.4012/dmj.11.130.

[3] O. Suzuki, G. Insley, Octacalcium Phosphate Biomaterials, Woodhead Publishing Series in Biomaterials, 2020.

[4] S. Liu, B. Wang, S. Fan, Y. Wang, Y. Zhan, D. Ye, Global burden of musculoskeletal disorders and attributable factors in 204 countries and territories : a secondary analysis of the Global Burden of Disease 2019 study, BMJ Open. 12 (2022). https://doi.org/10.1136/bmjopen-2022-062183.

[5] B. E. Wilson, S. Jacob, M. L. Yap, J. Ferlay, F. Bray, M. B. Barton, Estimates of global chemotherapy demands and corresponding physician workforce requirements for 2018 and 2040: a population-based study, Lancet Oncol. 20 (2019) 769–780. https://doi.org/10.1016/S1470-2045(19)30163-9.

[6] T. Albrektsson, C. Johansson, Osteoinduction, osteoconduction and osseointegration, Eur Spine J. 10 (2001) 96–101.

[7] C. Rey, C. Combes, C. Drouet, M. J. Glimcher, Bone mineral: Update on chemical composition and structure, Osteoporos. Int. 20 (2009) 1013–1021. https://doi.org/10.1007/s00198-009-0860-y.

[8] H. Yuan, H. Fernandes, P. Habibovic, J. De Boer, A. M. C. Barradas, A. De Ruiter, W. R. Walsh, C. A. Van Blitterswijk, J. D. De Bruijn, Osteoinductive ceramics as a synthetic alternative to autologous bone grafting, Proc. Natl. Acad. Sci. U. S. A. 107 (2010) 13614–13619. https://doi.org/10.1073/pnas.1003600107.

[9] T. Ariizumi, H. Kawashima, H. Hatano, T. Yamagishi, N. Oike, Osteoinduction and Osteoconduction with Porous Beta-Tricalcium Phosphate Implanted after Fibular Resection in Humans, J. Biomater. Nanobiotechnol. 10 (2019) 159–173. https://doi.org/10.4236/jbnb.2019.103009.

[10] R. Z. LeGeros, Properties of osteoconductive biomaterials: Calcium phosphates, Clin. Orthop. Relat. Res. (2002) 81–98. https://doi.org/10.1097/00003086-200202000-00009.

[11] S. V Dorozhkin, M. Epple, Biological and Medical Significance of Calcium Phosphates, Angew. Chem. Int. Ed. 41 (2002) 3130–3146.

[12] T. Wach, M. Kozakiewicz, Fast-Versus Slow-Resorbable Calcium Phosphate Bone Substitute Materials — Texture Analysis after 12 Months of Observation, Materials (Basel). 13 (2020) 3854.

[13] T. J. Brunner, R. N. Grass, M. Bohner, W. J. Stark, Effect of particle size, crystal phase and crystallinity on the reactivity of tricalcium phosphate cements for bone reconstruction, J. Mater. Chem. 17 (2007) 4072–4078. https://doi.org/10.1039/b707171j.

[14] V.Uskokovic, T. A. Desai, Phase composition control of calcium phosphate nanoparticles for tunable drug delivery kinetics and treatment of osteomyelitis. I.

Preparation and drug release, J. Biomed. Mater. Res. – Part A. 101 A (2013) 1416–1426. https://doi.org/10.1002/jbm.a.34426.

[15] G. Daculsi, R. Z. LeGeros, E. Nery, K. Lynch, B. Kerebel, Transformation of biphasic calcium phosphate ceramics in vivo: Ultrastructural and physicochemical characterization, J. Biomed. Mater. Res. 23 (1989) 883–894.

[16] M. S. Johnsson, G. H. Nancollas, The Role of Brushite and Octacalcium Phosphate in Apatite Formation, Crit. Rev. Oral Biol. Med. 3 (1992) 61–82. https://doi.org/10.1177/10454411920030010601.

[17] J. Vecstaudza, M. Gasik, J. Locs, Amorphous calcium phosphate materials: Formation, structure and thermal behaviour, J. Eur. Ceram. Soc. 39 (2019) 1642–1649. https://doi.org/10.1016/j.jeurceramsoc.2018.11.003.

[18] M. Mosina, J. Locs, Synthesis of amorphous calcium phosphate: A review, Key Eng. Mater. 850 KEM (2020) 199–206. https://doi.org/10.4028/www.scientific.net/KEM.850.199.

[19] N. Temizel, G. Girisken, A. C. Tas, Accelerated transformation of brushite to octacalcium phosphate in new biomineralization media between 36.5 °C and 80 °C, Mater. Sci. Eng. C. 31 (2011) 1136–1143. https://doi.org/10.1016/j.msec.2011.04.009.

[20] A. Dosen, R. F. Giese, Thermal decomposition of brushite, $CaHPO_4 \cdot 2H_2O$ to monetite CaHPO4 and the formation of an amorphous phase, Am. Mineral. 96 (2011) 368–373. https://doi.org/10.2138/am.2011.3544.

[21] L. C. Chow, E. D. Eanes, Octacalcium phosphate, 2001. https://doi.org/10.1007/springerreference_39293.

[22] C. C. Rey, C. Combes, C. Drouet, Synthesis and physical chemical characterizations of octacalcium phosphate-based biomaterials for hard-tissue regeneration, 2019. https://doi.org/10.1016/B978-0-08-102511-6.00008-X.

[23] I. Kovrlija, J. Locs, D. Loca, Octacalcium phosphate: Innovative vehicle for the local biologically active substance delivery in bone regeneration, Acta Biomater. 135 (2021) 27–47. https://doi.org/10.1016/j.actbio.2021.08.021.

[24] T. Anada, A. Araseki, S. Matsukawa, T. Yamasaki, S. Kamakura, O. Suzuki, Effect of octacalcium phosphate ionic dissolution products on osteoblastic cell differentiation, Key Eng. Mater. 361-363 I (2008) 31–34. https://doi.org/10.4028/www.scientific.net/kem.361-363.31.

[25] Y. Sai, Y. Shiwaku, T. Anada, K. Tsuchiya, T. Takahashi, O. Suzuki, Capacity of octacalcium phosphate to promote osteoblastic differentiation toward osteocytes in vitro, Acta Biomater. 69 (2018) 362–371. https://doi.org/10.1016/j.actbio.2018.01.026.

[26] Y. Shiwaku, K. Tsuchiya, L. Xiao, O. Suzuki, Effect of calcium phosphate phases affecting the crosstalk between osteoblasts and osteoclasts in vitro, J. Biomed. Mater. Res. - Part A. 107 (2019) 1001–1013. https://doi.org/10.1002/jbm.a.36626.

[27] N. Miyatake, K. N. Kishimoto, T. Anada, H. Imaizumi, E. Itoi, O. Suzuki, Effect of partial hydrolysis of octacalcium phosphate on its osteoconductive characteristics, Biomaterials. 30 (2009) 1005–1014. https://doi.org/10.1016/j.biomaterials.2008.10.058.

[28] F. Barrère, C. M. Van Der Valk, R. A. J. Dalmeijer, G. Meijer, C. A. Van Blitterswijk,

K. De Groot, P. Layrolle, Osteogenecity of octacalcium phosphate coatings applied on porous metal implants, J. Biomed. Mater. Res. – Part A. 66 (2003) 779–788. https://doi.org/10.1002/jbm.a.10454.

[29] P. Habibovic, C. M. Van Der Valk, C. A. Van Blitterswijk, K. De Groot, G. Meijer, Influence of octacalcium phosphate coating on osteoinductive properties of biomaterials, J. Mater. Sci. Mater. Med. 15 (2004) 373–380. https://doi.org/10.1023/B:JMSM.0000021104.42685.9f.

[30] R.Z. LeGeros, Preparation of Octacalcium Phosphate (OCP): A Direct Fast Method, Calcif. Tissue Int. (1985) 194–197.

[31] S. Graham, P. W. Brown, The low temperature formation of octacalcium phosphate, J. Cryst. Growth. 132 (1993) 215–225. https://doi.org/10.1016/0022-0248(93)90265-X.

[32] C. Drouet, Apatite formation: why it may not work as planned, and how to conclusively identify apatite compounds, Biomed Res. Int. 2013 (2013) Article ID 490946. http://dx.doi.org/10.1155/2013/490946.

[33] O. Suzuki, Octacalcium phosphate (OCP)-based bone substitute materials, Jpn. Dent. Sci. Rev. 49 (2013) 58–71. https://doi.org/10.1016/j.jdsr.2013.01.001.

[34] O. Demir, A. Pylostomou, D. Loca, Octacalcium phosphate phase forming cements as an injectable bone substitute materials: Preparation and in vitro structural study, Biomater. Adv. J. 157 (2024). https://doi.org/10.1016/j.bioadv.2023.213731.

[35] Y. Tanuma, T. Anada, Y. Honda, T. Kawai, S. Kamakura, S. Echigo, O. Suzuki, Granule size-dependent bone regenerative capacity of octacalcium phosphate in collagen matrix, Tissue Eng. – Part A. 18 (2012) 546–557. https://doi.org/10.1089/ten.tea.2011.0349.

[36] T. Fuji, T. Anada, Y. Honda, Y. Shiwaku, H. Koike, S. Kamakura, K. Sasaki, O. Suzuki, Octacalcium phosphate-precipitated alginate scaffold for bone regeneration, Tissue Eng. - Part A. 15 (2009) 3525–3535. https://doi.org/10.1089/ten.tea.2009.0048.

[37] O. Suzuki, Y. Shiwaku, R. Hamai, Octacalcium phosphate bone substitute materials: Comparison between properties of biomaterials and other calcium phosphate materials, Dent. Mater. J. 39 (2020) 187–199. https://doi.org/10.4012/dmj.2020-001.

[38] A. Bordbar-Khiabani, I. Kovrlija, J. Locs, D. Loca, M. Gasik, Octacalcium Phosphate-Laden Hydrogels on 3D-Printed Titanium Biomaterials Improve Corrosion Resistance in Simulated Biological Media, Int. J. Mol. Sci. 24 (2023). https://doi.org/10.3390/ijms241713135.

[39] M. R. Newman, D. S. W. Benoit, Local and targeted drug delivery for bone regeneration, Curr. Opin. Biotechnol. 40 (2016) 125–132. https://doi.org/10.1016/j.copbio.2016.02.029.

[40] A. Lebugle, A. Rodrigues, P. Bonnevialle, J. J. Voigt, P. Canal, F. Rodriguez, Study of implantable calcium phosphate systems for the slow release of methotrexate, Biomaterials. 23 (2002) 3517–3522.

[41] Q. L. Tang, Y. J. Zhu, J. Wu, F. Chen, S. W. Cao, Calcium phosphate drug nanocarriers with ultrahigh and adjustable drug-loading capacity: One-step synthesis, in situ drug loading and prolonged drug release, Nanomedicine Nanotechnology, Biol. Med. 7 (2011) 428–434. https://doi.org/10.1016/j.nano.2010.12.005.

[42] O. Suzuki, S. Kamakura, T. Katagiri, M. Nakamura, B. Zhao, Y. Honda, R. Kamijo, Bone formation enhanced by implanted octacalcium phosphate involving conversion into Ca-deficient hydroxyapatite, Biomaterials. 27 (2006) 2671–2681. https://doi.org/10.1016/j.biomaterials.2005.12.004.

[43] Y. Murakami, Y. Honda, T. Anada, H. Shimauchi, O. Suzuki, Comparative study on bone regeneration by synthetic octacalcium phosphate with various granule sizes, Acta Biomater. 6 (2010) 1542–1548. https://doi.org/10.1016/j.actbio.2009.10.023.

[44] X. Yang, X. Gao, Y. Gan, C. Gao, X. Zhang, K. Ting, B. M. Wu, Z. Gou, Facile synthesis of octacalcium phosphate nanobelts: Growth mechanism and surface adsorption properties, J. Phys. Chem. C. 114 (2010) 6265–6271. https://doi.org/10.1021/jp911576f.

[45] E. Boanini, M. Gazzano, K. Rubini, A. Bigi, Collapsed Octacalcium Phosphate Stabilized by Ionic Substitutions, Cryst. Growth Des. (2010). https://doi.org/10.1021/cg100494f.

[46] I. Kovrlija, K. Menshikh, O. Marsan, C. Rey, C. Combes, J. Locs, D. Loca, Exploring the Formation Kinetics of Octacalcium Phosphate from Alpha-Tricalcium Phosphate: Synthesis Scale-Up, Determination of Transient Phases, Their Morphology and Biocompatibility, Biomolecules. 13 (2023).

[47] A. Ressler, I. Ivanišević, A. Žužić, N. Somers, The ionic substituted octacalcium phosphate for biomedical applications: A new pathway to follow ?, Ceram. Int. (2021). https://doi.org/10.1016/j.ceramint.2021.12.126.

[48] Z. Irbe, D. Loca, A. Pura, L. Berzina-Cimdina, Synthesis and properties of α-tricalcium phosphate from amorphous calcium phosphate as component for bone cements, Key Eng. Mater. 721 KEM (2017) 182–186. https://doi.org/10.4028/www.scientific.net/KEM.721.182.

[49] W. E. Brown, M. Mathew, M. S. Tung, Crystal chemistry of octacalcium phosphate, Prog. Cryst. Growth Charact. 4 (1981) 59–87. https://doi.org/10.1016/0146-3535(81)90048-4.

[50] R. A. Terpstra, P. Bennema, Crystal morphology of octacalcium phosphate: Theory and observation, J. Cryst. Growth. 82 (1987) 416–426. https://doi.org/10.1016/0022-0248(87)90333-2.

[51] W. E. Brown, J. R. Lehr, J. P. Smith, A. William Frazier, Crystallography of octacalcium phosphate [5], J. Am. Chem. Soc. 79 (1957) 5318–5319. https://doi.org/10.1021/ja01576a068.

[52] B. O. Fowler, M. Marković, W. E. Brown, Octacalcium Phosphate. 3. Infrared and Raman Vibrational Spectra, Chem. Mater. 5 (1993) 1417–1423. https://doi.org/10.1021/cm00034a009.

[53] M. Robin, S. Von Euw, G. Renaudin, S. Gomes, J. M. Krafft, N. Nassif, T. Azaïs, G. Costentin, Insights into OCP identification and quantification in the context of apatite biomineralization, CrystEngComm. 22 (2020) 2728–2742. https://doi.org/10.1039/c9ce01972c.

[54] N. Döbelin, Validation of XRD phase quantification using semi-synthetic data, Powder Diffr. 35 (2020) 262–275. https://doi.org/10.1017/S0885715620000573.

[55] N. Döbelin, Interlaboratory study on the quantification of calcium phosphate phases by

Rietveld refinement, Powder Diffr. 30 (2015) 231–241. https://doi.org/10.1017/S088571561500038X.

[56] J. C. Heughebaert, G. H. Nancollas, Kinetics of crystallization of octacalcium phosphate, J. Phys. Chem. 88 (1984) 2478–2481. https://doi.org/10.1021/j150656a012.

[57] J. P. Barone, G. H. Nancollas, The Seeded Growth of Calcium Phosphates. The Kinetics of Growth of Dicalcium Phosphate Dihydrate on Enamel, Dentin, and Calculus, J. Dent. Res. 57 (1978) 153–161. https://doi.org/10.1177/00220345780570010901.

[58] M. Nascimben, I. Kovrlija, J. Locs, D. Loca, L. Rimondini, Fusion and classification algorithm of octacalcium phosphate production based on XRD and FTIR data, Sci. Rep. (2024) 1–11. https://doi.org/10.1038/s41598-024-51795-0.

[59] S. Sritharan, N. Sivalingam, A comprehensive review on time-tested anticancer drug doxorubicin, Life Sci. 278 (2021) 119527. https://doi.org/10.1016/j.lfs.2021.119527.

[60] S. Y. van der Zanden, X. Qiao, J. Neefjes, New insights into the activities and toxicities of the old anticancer drug doxorubicin, FEBS J. 288 (2021) 6095–6111. https://doi.org/10.1111/febs.15583.

[61] R. D. Olson, P. S. Mushlin, Doxorubicin cardiotoxicity: analysis of prevailing hypotheses, FASEB J. 4 (1990).

[62] X. Liu, S. Du, S. Wang, K. Ye, Ferroptosis in osteosarcoma: A promising future, Front. Oncol. 12 (2022) 1–9. https://doi.org/10.3389/fonc.2022.1031779.

[63] C. M. Pfeffer, A. T. K. Singh, Apoptosis: A target for anticancer therapy, Int. J. Mol. Sci. 19 (2018). https://doi.org/10.3390/ijms19020448.

[64] I. Kovrlija, E. Pańczyszyn, O. Demir, M. Laizane, M. Corazzari, J. Locs, D. Loca, Doxorubicin loaded octacalcium phosphate particles as controlled release drug delivery systems: Physico-chemical characterization, in vitro drug release and evaluation of cell death pathway, Int. J. Pharm. 653 (2024) 1–14. https://doi.org/10.1016/j.ijpharm.2024.123932.

[65] N. Ito, M. Kamitakahara, K. Ioku, Preparation and evaluation of spherical porous granules of octacalcium phosphate/hydroxyapatite as drug carriers in bone cancer treatment, Mater. Lett. 120 (2014) 94–96. https://doi.org/10.1016/j.matlet.2014.01.040.

[66] M. Parent, H. Baradari, E. Champion, C. Damia, M. Viana-Trecant, Design of calcium phosphate ceramics for drug delivery applications in bone diseases: A review of the parameters affecting the loading and release of the therapeutic substance, J. Control. Release. 252 (2017) 1–17. https://doi.org/10.1016/j.jconrel.2017.02.012.

[67] M. Akutsu, Y. Kano, S. Tsunoda, K. Suzuki, Y. Yazawa, Y. Miura, Schedule-dependent interaction between paclitaxel and doxorubicin in human cancer cell lines in vitro, Eur. J. Cancer. 31 (1995) 2341–2346. https://doi.org/10.1016/0959-8049(95)00448-3.

[68] J. Wang, J. de Boer, K. de Groot, Proliferation and differentiation of osteoblast-like MC3T3-E1 cells on biomimetically and electrolytically deposited calcium phosphate coatings, J. Biomed. Mater. Res. A. 90 (2009) 664–670. https://doi.org/10.1002/jbm.a.32128.

[69] G. Miotto, M. Rossetto, M. L. Di Paolo, L. Orian, R. Venerando, A. Roveri, A. M. Vučković, V. Bosello Travain, M. Zaccarin, L. Zennaro, M. Maiorino, S. Toppo,

F. Ursini, G. Cozza, Insight into the mechanism of ferroptosis inhibition by ferrostatin-1, Redox Biol. 28 (2020) 101328. https://doi.org/10.1016/j.redox.2019.101328.

[70] S. Wang, E. A. Konorev, S. Kotamraju, J. Joseph, S. Kalivendi, B. Kalyanaraman, Doxorubicin induces apoptosis in normal and tumor cells via distinctly different mechanisms: Intermediacy of H2O2- and p53-dependent pathways, J. Biol. Chem. 279 (2004) 25535–25543. https://doi.org/10.1074/jbc.M400944200.

[71] G. V. Chaitanya, J. S. Alexander, P. P. Babu, PARP-1 cleavage fragments: Signatures of cell-death proteases in neurodegeneration, Cell Commun. Signal. 8 (2010) 1–11. https://doi.org/10.1186/1478-811X-8-31.

[72] N. Yoshimoto, I. Wahyudhin, A. Yabuki, Colloids and Surfaces A: Physicochemical and Engineering Aspects Self-healing polymer coating with efficient delivery for alginates and calcium nitrite to provide corrosion protection for carbon steel, Colloids Surfaces A Physicochem. Eng. Asp. 662 (2023) 130970. https://doi.org/10.1016/j.colsurfa.2023.130970.

[73] A. Bordbar-Khiabani, M. Gasik, Electrochemical behavior of additively manufactured patterned titanium alloys under simulated normal, inflammatory, and severe inflammatory conditions, J. Mater. Res. Technol. 26 (2023) 356–370. https://doi.org/10.1016/j.jmrt.2023.07.113.

APPENDICES/PIELIKUMI

Appendix 1
1. pielikums

Octacalcium phosphate: Innovative vehicle for the local biologically active substance delivery in bone regeneration

Ilijana Kovrlija, Janis Locs, Dagnija Loca

Acta Biomaterialia, 135 (2021), 27–47, DOI: 10.1016/j.actbio.2021.08.021

I.K. input: **w**riting – original draft and review & editing, conceptualization, visualization, formal analysis, investigation.

Acta Biomaterialia 135 (2021) 27–47

Contents lists available at ScienceDirect

Acta Biomaterialia

journal homepage: www.elsevier.com/locate/actbio

Review article

Octacalcium phosphate: Innovative vehicle for the local biologically active substance delivery in bone regeneration

Ilijana Kovrlija[a], Janis Locs[a,b], Dagnija Loca[a,b,*]

[a] Rudolfs Cimdins Riga Biomaterials Innovation and Development Centre, Institute of General Chemical Engineering, Faculty of Materials Science and Applied Chemistry, Riga Technical University, Pulka 3, Riga, LV-1007, Latvia
[b] Baltic Biomaterials Centre of Excellence, Headquarters at Riga Technical University, Riga, Latvia

ARTICLE INFO

Article history:
Received 23 April 2021
Revised 9 August 2021
Accepted 14 August 2021
Available online 25 August 2021

Keywords:
Biomaterials
Octacalcium phosphate
Drug delivery
Bone tissue regeneration
Calcium phosphate

ABSTRACT

Disadvantages of conventional drug delivery systems (DDS), such as systemic circulation, interaction with physiochemical factors, reduced bioavailability, and insufficient drug concentration at bone defect site, have underlined the importance of developing efficacious local drug delivery systems. Octacalcium phosphate (OCP) is presumed to be the precursor of biologically formed apatite, owing to its similarity to hydroxyapatite (HAp) and readiness to convert to it. Specific crystal structure of OCP is constructed of compiled apatite layers and water layers, which make possible the incorporation of various ions in its structure, making it feasible to alter the overall effect OCP has in the system. Next to that intrinsic property, characteristics as high solubility, biodegradability and osteoconductivity have made it indispensable to tailor OCP as a carrier material. In this review, we present the main characteristics and progress done on utilizing OCP as an innovative vehicle and provide suggestions for possible research pathways and advantages for local drug delivery in bone tissue engineering.

Statement of significance

Octacalcium phosphate (OCP), being a precursor to biologically formed apatite, has many assets when compared to other calcium phosphates. Owing to its highly pertinent structure, it is being used as a vehicle for biologically active substances or ions for bone regeneration. However, orchestrating drug delivery systems with OCP, in order to achieve the best possible outcome, is still a pioneering concept, and the all-encompassing data is still scarce. Although several articles have been published on this matter, to this date there is no systematic overview pointing out the benefits that OCP can bring in the field of drug delivery. Here we offer a comprehensive overview, starting from the OCP synthesis to its structure, morphology, and the biological significance OCP has.

1. Introduction

The surge of market demand for regenerative therapies and replacement models in bone tissue engineering has been constant in the past few decades. This trend has led the focus of several research areas to an abundance of material variations, which are able to mimic properties of the native bone as close as possible [1]. Regenerative approach's main endeavor is osteogenesis, which is the process of bone formation and development. Osteogenesis is promoted by osteoinduction that encompasses the recruitment and stimulation of cells to further advance into preosteoblasts. On the other hand, osteoconduction is the capacity of bone-forming cells to progress across a matrix surface, and moderately replace it with the new bone over a certain time period [2]. As the gold standard is to have a material that exhibits osteoinductive properties (e.g. hydroxyapatite and tricalcium phosphate [3,4]), it is detrimental to guide the research in the direction of finding the possible nominees.

As highly effective and reliable materials, calcium phosphates (CaPs) have been heavily utilized and investigated in the rapidly growing field of local drug delivery. This is mainly due to their abundant presence in the human bone, as well as desirable in-

* Corresponding author at: Rudolfs Cimdins Biomaterials Innovations and Development Centre of Riga Technical University, Pulka Street 3, LV-1007, Riga, Latvia.
E-mail address: dagnija.loca@rtu.lv (D. Loca).

https://doi.org/10.1016/j.actbio.2021.08.021

trinsic properties, when it comes to osteoconductivity and osteoinductivity, bioactivity and biodegradability. For these purposes, CaP biomaterials used for the drug delivery, in general, are classified in four groups: calcium phosphate nanoparticles (CPNPs); calcium phosphate coatings; calcium phosphate scaffolds and calcium phosphate cements (CPCs). In literature, it can be found that nanoparticles comprised from HAp, dicalcium phosphate dihydrate (DCPD), α-tricalcium phosphate (α-TCP), β-tricalcium phosphate (β-TCP) and amorphous calcium phosphate (ACP) were successfully functionalized with active substances such as doxorubicin [5], triethylene glycol dimethacrylate [6], RALA delivery peptide [7], ibuprofen [8] and alendronate [9]. The combination of HAp and β-TCP with active substances (tetracycline hydrochloride [10], slimvastine [11], gentamicin sulphate [12], isoniazid and rifampicin [13] and antifungal agents [14]) is also used in form of coatings, scaffolds and cements, whereas ACP is used in coatings and scaffolds with addition of tobramycin [15] and various other therapeutic agents [16]. DCPD and α-TCP have been implemented also within scaffolds and cements [17,18], and their combined effect with vascular endothelial growth factor and copper ions [19], gentamicin [20], sodium fusidate [21] and bovine serum albumin [22] has been examined. Additionally, highly positive effects of bioactive CaPs on bone regeneration have been recorded throughout various studies, where the most often used ions are magnesium (Mg^{2+}), strontium (Sr^{2+}), zinc (Zn^{2+}), fluoride(F^-) and others [23–25].

Apart from the aforementioned classification, calcium phosphates can also differ in Ca/P molar ratio, particle size, morphology, specific surface area (SSA), solubility and crystallinity. Therefore, the overall CaPs ability to be combined with the different drugs can vary. Up to this point, CaPs have been tailored to load different sets of antibiotics, anti-inflammatory drugs, growth factors, bisphosphonates (as drugs for the prevention of the loss of bone density), cytokines (in the interest of osteogenesis enhancement), and they have also been used as gene delivery vectors for both DNA and RNA loads [26,27].

Despite their advantages, the application of CaPs in DDS field comes with several challenges to overcome. One of them arises when obtaining the CaP nanoparticles, where avoiding the particulate particle size range (>200 nm) is important as it can lead to manifestation of toxicity *in vivo*. Usually it transpires through excess delivery of calcium ions (Ca^{2+}) into the cells [26,28,29]. Likewise, for example, coatings can display weak stability and adhesion with the implant surface. Involvement of the high temperature in-processing or post-processing can further influence the mechanical properties and cohesion of the coating [28,30,31]. This is the reason why most of the drugs in CaP coatings are introduced via adsorption, and burst release of poorly attached drugs is an impending possibility [28]. A similar disadvantage can be observed in CaP scaffolds. In order to avoid that, it is essential to choose an appropriate size (>100 nm), chemical structure and adequate synthesis method of selected calcium phosphate DDS [32]. Contemporary studies have tried to address the challenges in incorporating biologically active substances, by applying different loading methods [33–39]. Some of the newly used approaches are flame spray pyrolysis (FSP) – for engineering inorganic drug delivery nanocarriers [38], a two-stage cold isostatic pressing and gelling approach – for fabrication of strontium and vancomycin-doped calcium polyphosphate beads [33], electrochemical deposition – for strontium loading, on octacalcium phosphate (OCP) coatings [34] etc. As far as the fabrication of CaP scaffolds extends, another difficulty is to control the pore size and distribution, as well as their interconnectivity and percentage of porosity. An appropriate density and mechanical strength is ensured by sintering at high temperatures. The limitations of CPCs are connected to their final properties, which result from the drug incorporation and changes in the drug activity and its bioavailability.

Being a member of calcium orthophosphates, OCP has been hypothesized as a precursor of biological apatite crystals due to its structure (apatite structure characteristic layers being parallel to the (100) plane with hydrated layers in between) [40] and capacity for converting itself to the thermodynamically more stable phase, hydroxyapatite, both *in vitro* and *in vivo* [41]. OCP is typically synthesized through the precipitation of aqueous solutions containing Ca^{2+} and phosphate ions (PO_4^{3-}) [42–45] or via hydrolysis of α-TCP [46–48] or DCPD [49,50]. OCP is considered to have a higher affinity towards organic molecules than other calcium phosphates [51]. This is due to the specific arrangement of the structure, crystallographic planes and a relatively empty hydrated layer, where incorporation of distinct ions and molecules is much more feasible [52,53]. Moreover, it has been postulated that, if the drug loading is performed *in situ* during the first stages of OCP synthesis, it can lead to ultrahigh drug loading capacity (DLC). This is due to the many binding sites, which are derived from CaP clusters with an ultrahigh specific surface area where the drug molecules are adsorbed on the surface. These DDSs are also able to ensure prolonged drug release [54]. Tang et al. [54] managed to achieve the ultrahigh DLC of 1.96 g ibuprofen/g carrier for one of the drug delivery systems, with a specific surface area of 98.03 $m^2\ g^{-1}$.

One of the advantages of OCP is that it has higher solubility than the stoichiometric hydroxyapatite, thus directly affecting the drug release kinetics and the overall release profile. Comparison of properties of OCP and other biologically relevant calcium phosphates is summarized in Table 1. Also, OCP's unique structure makes realizable the incorporation of ions within it [55], and that opens a set of pathways to biological functionalization and drug delivery. However, upon thorough literature review, we found that OCP has not been widely employed as a drug delivery system in comparison to HAp and other CaPs, and the research done is still scarce.

2. Octacalcium phosphate structure

Octacalcium phosphate, $Ca_8(HPO_4)_2(PO_4)_4x5H_2O$, with Ca/P molar ratio of 1.33 exhibits a triclinic crystal structure with lattice parameters a = 19.692 Å, b = 9.523 Å, c = 6.835 Å, α = 90.15°, β = 92.54°, γ = 108.65° [55]. The OCP structure has been portrayed parallel to the (100) plane, which is extended along the c-axis and bordered by the (010), (001), and (011) planes (Fig. 1). The faces of OCP (100) are more hydrated, which affects the ability of Ca^{2+} and PO_4^{3-} ions to attach themselves, and subsequently causes the crystals to grow slower along the plate shaped (100) axis with the lowest interfacial energy. This is thought to be the main reason why the smaller plate –like crystals are the most dominant ones in OCP crystal morphology [59]. The alternately packed structure is made of an apatite layer and a water layer, comprised of ten water molecules (H_2O) in the unit cell, which resemble a channel going along the c-axis [52]. This is one of the main attributes that makes OCP somewhat comparable to HAp. The bonds made through the two hydrogen phosphate (HPO_4^{2-}) groups in the hydrated layer are the ones keeping the entire edifice together [60]. One HPO_4^{2-} group is connected with the apatitic layer and the other one is between the two apatitic layers, portraying itself as Ca-HPO_4Ca bound together with interlinking H_2O molecule [60]. The overall structural correlation has to be observed from the water molecules side as well, more precisely from the O5 and O4 molecule [52]. The O5 water molecule can be found around the center of the hydrated part of the OCP lattice. It is not connected to any Ca^{2+} ion, and since it is lightly bound, it can leave the area. O4 molecule position and the level of substitution with hydroxyl ion (OH^-) is important for observing the similarity of OCP struc-

Table 1
Summary of the main properties of biologically relevant CaPs [56–58].

Compound	Formula	Ca/P molar ratio	Solubility at 25 °C, -log(Ksp)	Solubility at 37 °C, -log(Ksp)	pH stability at 25 °C	Density, g/cm^3
Monocalcium phosphate monohydrate (MCPM)	$Ca(H_2PO_4)_2 \times H_2O$	0.5	1.14	No data	0.0 – 2.0	2.23
Monocalcium phosphate anhydrate (MCPA)	$Ca(H_2PO_4)_2$	0.5	1.14	No data	Stable >100 ℃	2.58
Dicalcium phosphate dihydrate (DCPD, brushite)	$CaHPO_4 \times 2H_2O$	1.0	6.59	6.63	2.0 – 6.0	2.32
Dicalcium phosphate anhydrate (DCPA, monetite)	$CaHPO_4$	1.0	6.90	7.02	Stable >100 ℃	2.89
Octacalcium phosphate (OCP)	$Ca_8(HPO_4)_2(PO_4)_4 \times 5H_2O$	1.33	96.6	95.9	5.5 – 7.0	2.61
α-tricalcium phosphate (α-TCP)	α-$Ca_3(PO_4)_2$	1.5	25.5	25.5	Cannot precipitate in aq solutions	2.86
β-tricalcium phosphate (β-TCP)	β-$Ca_3(PO_4)_2$	1.5	28.9	29.5	Cannot precipitate in aq solutions	3.07
Amorphous calcium phosphate (ACP)	$Ca_x(PO_4)_y \times nH_2O$	1.2 – 2.2	Not precisely measured	Not precisely measured	Always metastable	2.52
Calcium-deficient hydroxyapatite (CDHAp)	$Ca_{10-x}(HPO_4)_x(PO_4)_{6-x}(OH)_{2-x}$ $(0<x<1)$	1.5 – 1.67	≈85.1	≈85.1	6.5 – 9.5	No data
Hydroxyapatite (HAp)	$Ca_{10}(PO_4)_6(OH)_2$	1.67	116.8	117.2	9.5 – 12	3.16
Tetracalcium phosphate (TTCP)	$Ca_4(PO_4)_2O$	2.0	38 – 44	37 – 42	Cannot precipitate in aq solutions	3.05

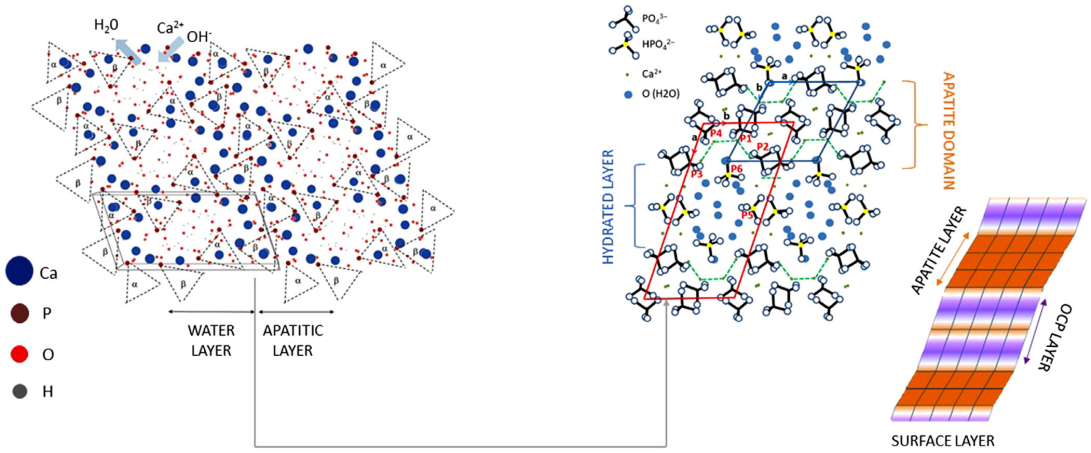

Fig. 1. Structure of six OCP unit cells from the view on the (001) plane followed by a close up of a single OCP unit cell, displaying the arrangement of PO_4^{3-} and HPO_4^{2-} groups with the corresponding water molecules. Possible interlayering of OCP and HAp, within the same crystal, representing their arrangements is shown on the right side. (Source: Reprinted from reference [75] with permission from Elsevier and from reference [76], with permission from the Royal Society of Chemistry.)

ture to the one of HAp and for existence of OCP polymorphs. Due to the potential differences in hydrogen-bond positioning of the four HPO_4^{2-} groups and water molecules in the water layer of the OCP unit cell, appearance of polymorphs can be observed [52,61]. Two of Ca^{2+} ions and one PO_4^{3-} are found within the water layer, with an approximate width of around 0.8 nm. On the other hand, the apatitic layer contains six more Ca^{2+} ions and one more PO_4^{3-} than the water layer, with estimated thickness of 1.1 nm [62]. Even so, the positions of Ca^{2+} and PO_4^{3-} that determine the thickness of the layers, are also the ones that set the coupling of their specific conjunctions with additional bonding interactions. This enables the possibility of ions or drugs to be incorporated among them [62]. The interactions of OCP with different groups such as carboxylic acids, biological molecules or ion substitutes are shown to be advantageous in better functionalization of OCP, but all of them affect the structure to a certain degree. Ameliorating effect, with regard to the structure, was most prominently displayed while using cetyltrimethylammonium bromide (CTAB) (yielding in satisfying OCP phase purity and a high degree of crystallinity [51]) and succinate ions (they restricted the motion of water molecules incrementing the stability of OCP [62]). This is highly beneficial for repairing bone defects, but during the synthesis, preparation set-

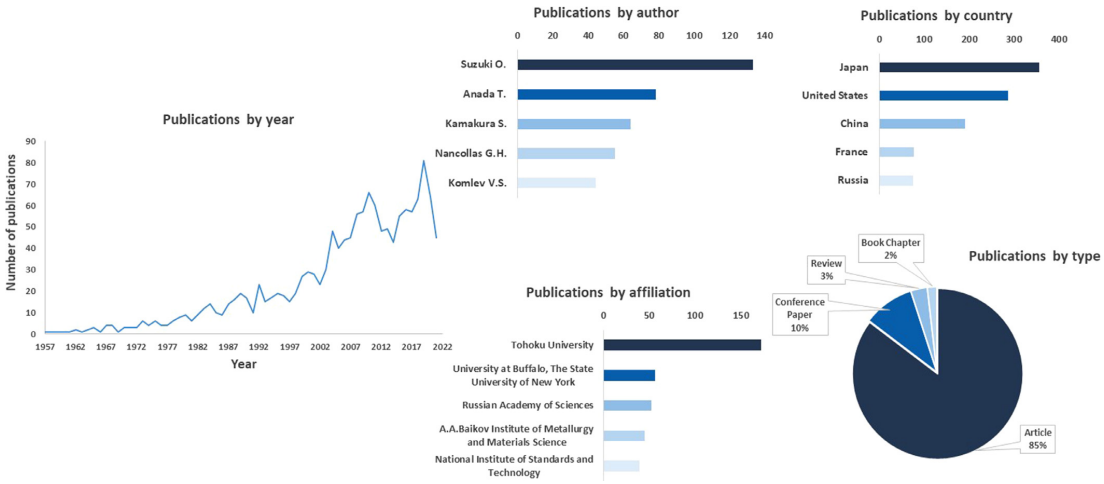

Fig. 2. Number of published scientific papers with the keyword "octacalcium phosphate" for the period of 1957-2021. Additional analyzed data, that has been presented, encompasses five authors with corresponding number of papers, based on the matching keyword from Scopus database. Five high-ranking countries and affiliations, as well as the type of publications found on Scopus, have been portrayed based on the keyword "octacalcium phosphate".

tings have to be considered. The preparation conditions are indispensable for producing an array of chemical and physical properties of OCP. These characteristics are pivotal as they affect OCP crystal morphologies, which in return induce deviations in their osteoconductivity [40]. The indicated mitigates the cells to exhibit a better attachment profile and differentiation on a surface with better accessibility and more binding sites. Combined effect leads to an ameliorated effect on bone formation. However, the implications of the ion effect on the overall OCP structure are manifold. A destabilizing effect can be seen with the incorporation of Mg^{2+} ions [63–67] and also with Sr^{2+} ions, where the extent of destabilization is dependent on the concentration of Sr^{2+} [68–71]. The concentration subordination was also noticed with F^{-} ions which resulted in the decreased amount of OCP (if the F^{-} concentration was increased), whereas the amount of apatite intensified [72]. The inhibitory effect of Zn^{2+} ions [65,73], alongside with Mg^{2+}, was also displayed through the hydrolysis of OCP to HAp phase where the DCPD phase was favored [74], while Zn^{2+} ions additionally endorsed the formation of amorphous phase. Further explanation of the effects can be found in the subsections of 7.1. in the article.

3. Formation of octacalcium phosphate

The description of OCP crystallography was first mentioned in 1957 by Brown et al. [77]. During the next decades, the interest in OCP synthesis has increased. A search for "octacalcium phosphate" in the Scopus database on 01.07.2021. resulted in 1452 scientific papers, with roughly 9% (133 papers) of them being published by O.Suzuki (Fig. 2). In addition to the statistical summary of the number of publications and respective authors, the overview of the top five mentioned affiliations and countries has been presented (Fig. 2). Summarizing the percentage of publications by type, the need for a review article on OCP as DDS becomes clear.

Active research on the majority of CaPs started in the middle of 20th century. However, every year there are around 2500 papers published on hydroxyapatite, whereas only about 50 on OCP. One question arises: why? Even though the bone regeneration potential for OCP is reported to be higher when compared to HAp, the complexity in synthesis and the control of product phase purity and a relatively narrow window of opportunity to obtain it (see in following sections), holds back the scientific community from an active engagement. Furthermore, additional hindrance can be the characterisation of the obtained phase in the final product, due to the high similarity of structure with HAp [78].

To this date several options for synthesizing OCP exist, but the two key pathways - precipitation and hydrolysis are the most commonly used ones.

3.1. Synthesis of octacalcium phosphate through precipitation route

If precipitation reaction has been employed, it is possible to differentiate among the precipitation medium and the use of aqueous [42,43,51,79–81] or water-ethanol medium [82]. Starting sources of Ca^{2+} and PO_4^{3-} ions are usually combinations of calcium acetate ($Ca(C_2H_3O_2)_2$) [44,51,67,83–85], sodium acid phosphate [42,46], calcium carbonate ($CaCO_3$) [49,86,87] and phosphoric acid (H_3PO_4). In most cases, reactant solutions/suspensions are mixed under constant stirring, while the pH and temperature are kept within the appropriate window. The collected precipitates are washed, dried, and characterised in order to evaluate the composition of obtained OCP. Several parameters (Fig. 3) are of significant importance for the purity and morphology of the obtained OCP crystals - rate of starting solution addition, molarity, stirring rate, pH, temperature etc.

The rate of addition of one solution into another can affect Ca/P molar ratio, OCP phase content, purity and crystallinity. Suzuki's team [62] has compared the flow rate of starting suspensions. Too low of a flow rate (1.3 mL/min) resulted in an unknown phase of CaP, while the flow rate of 4.1 mL/min was followed with a uniform OCP phase. When they examined the influence on a large-scale synthesis of 100 L, the too high dose rate (116 mL/min) produced a product with 44.8% of OCP and 55.2% of HAp, whereas a flow of 30 mL/min ended in a mix of 77.59% of OCP and 22.41% HAp. The next factor that needs to be monitored is the molarity of starting suspensions. Initially, the reactants need to be water soluble and as pure as possible in order to lead to the appropriate final product. The Ca/P molar ratio of OCP is 1.33, albeit in the literature it fluctuates from nonstoichiometric Ca-deficient form, with the Ca/P molar ratio of 1.28 [88–91] to the form with excess of calcium, up to the Ca/P molar ratio of 1.48 [92–94]. Obtaining higher

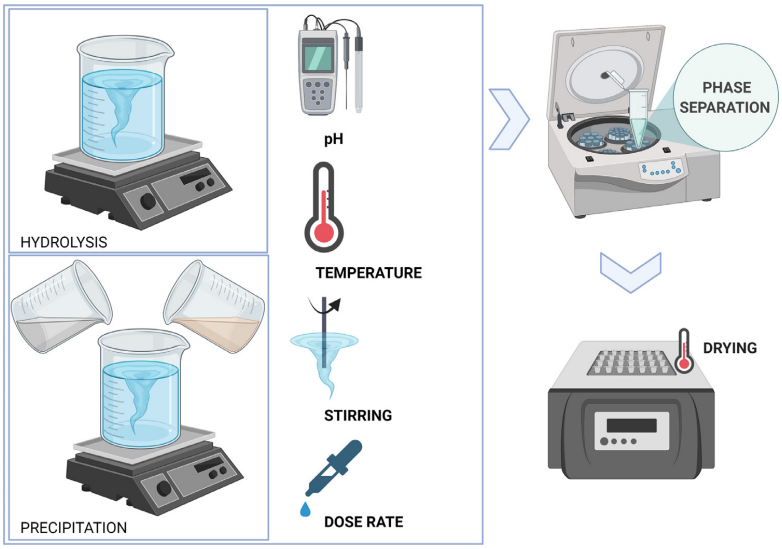

Fig. 3. Schematic presentation of the several main parameters for the synthesis of OCP. Figure created in BioRender.com.

Ca/P molar ratio requires the adjustment of parameters i.e. temperature and stirring. Both need to be increased in order to get a homogenous slurry, and if the Ca/P molar ratio is <1, the purity of obtained OCP is potentially compromised [62]. Stirring rate is of greater importance in larger volumes of synthesis. However, in smaller batches, if the mixing is not supplemented it can lead to inhomogeneity, both in terms of chemical composition and in temperature. This response is mostly due to the interference of the nucleation process by the turbulent flow [62]. As it was shown in the study by Sugiura et al. [95] the CaP phases and morphological changes differed in regard to the stirring. In a non-stirring system after 40 min ACP spherical particles transformed into a mixture of CaP single crystals (fiber aggregates) and OCP polycrystals (irregular form). However, under stirring, in the same time range, next to the CaP crystals that formed aggregates, DCPD single crystals (plates) were observed. In experiments performed by An et al. [96], it was observed that with an increase of mixing speed the formation of DCPD was slower, whereas in conditions of perfusion, the formation was completely inhibited. Moreover, in a separate research it was shown that with an increase of stirring, from 200 to 400 rpm, the content of DCPD was decreased from 39.6 to 20.1% [97]. The stability of the entire structure of OCP depends on pH and temperature of the reaction, while at the same time it can influence the size and morphology of the crystals (Fig. 4) and also possible conversion to a different CaP phase [46,98]. Approximate range of pH for OCP phase formation and stabilization is preferably between 5.0 and 7.0 [62,90,98–100]. The samples from Yokoi and the ones in Barinov's review, which were synthesized by the precipitation method, showed more of a thin elongated shape and lamellar crystals made of wafers. The shape can be greatly influenced by pH [55,101]. Higher values of pH and temperature decrease the stability of OCP, owing to the fact that the supersaturation with respect to OCP (which leads to the precipitation), is lower at lower conditions. This results in slower precipitation and growth of OCP crystals [78,98,102]. If the pH rises, it should be followed with lowering the temperature of the reaction. This potential surge leads to the precipitation of HAp due to the elevated presence of OH^- ions, which favor HAp instead of OCP. Finally,

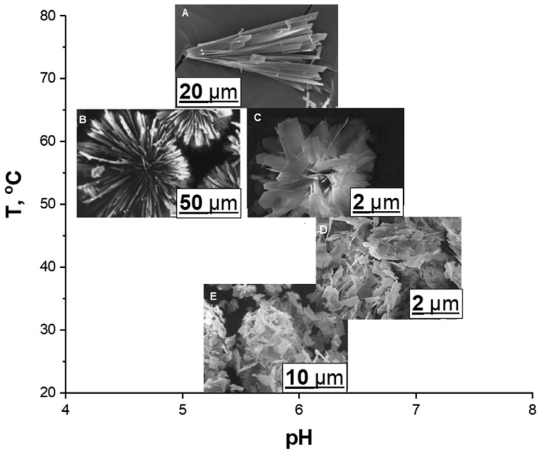

Fig. 4. Narrow region of pH and temperatures favorable for the synthesis of OCP through precipitation (picture A and B) and hydrolysis route (picture C-E). As it can be seen from the reference scanning electron microscopy (SEM) images, the change in these physical conditions has a substantial impact on the morphology of obtained OCP products.
(Source: Reproduced from reference [67,47,106,110], with permission from Elsevier, American Chemical Society and Pleiades Publishing.)

temperatures higher than 80 ℃ (100-130 ℃ [67,103]) start to break down the water layer within the structure and cause it to collapse, forming HAp [62]. Due to the different starting sources of Ca^{2+} and PO_4^{3-}, and the effect that pH has on phosphoric acid, several reaction schemes associated with this synthesis pathway have been illustrated below [104].

$$8Ca^2 + 6PO_4^{3-} + 2H^+ + 5H_2O \rightarrow 2[OCP] \quad (1)$$

$$8Ca^{2+} + 6HPO_4^{2-} + 5H_2O \rightarrow 2[OCP] + 4H^+ \quad (2)$$

$$H_2PO_4^- + (OH)^- \rightarrow PO_4^{3-} + H_2O \quad (3)$$

$$2H_2PO_4^- + 2e^- \rightarrow 2HPO_4^{2-} + H_2 \quad (4)$$

$$H_2PO_4^- + 2e^- \rightarrow PO_4^{3-} + H_2 \quad (5)$$

3.2. Synthesis of octacalcium phosphate through hydrolysis route

The most common precursors for synthesis of OCP via hydrolysis are DCPD or α-TCP. The reactions are elucidated in the scheme 6 for DCPD and in the scheme 7 for α-TCP [75]. While the process itself is greatly dependent on the entwined effect of the temperature and pH, other factors, i.e. stir rate and ionic strength are important, but not so crucial [47,105,106], as it was shown that pure OCP phase can be obtained in conditions without stirring [105]. If the temperature of the system is increased, the time of conversion of either of the two aforementioned precursors is greatly shortened due to the more kinetically conducive conditions which favor the formation of the OCP phase [46,105]. All of the parameters have to be considered in order to not get the mixture of the precursor and OCP and to avoid the subsequent hydrolysis of OCP into HAp. If pH is lower than 4.5, the main phase that can be observed in the final product is DCPD and, if it is higher than 6.5, formation of the HAp transpires [62]. In separate experiments done by teams of Tripathi and Nakahira, pure OCP was obtained by hydrolysis, and the morphology they observed were thin plate-like particles mixed with finer whisker-like particles [60,48]. However, the morphology can vary in regard to the aforementioned conditions (Fig. 4). The effect of the particle morphology of OCP was further examined [107–109] and it has been recounted that it influenced the attachment, spreading, and growth of the cells. Rat periosteal cells and bone marrow stromal cells were able to attach, spread and proliferate on long-plate like crystal structures of OCP, but when the crystals were acicular and had spherical shape, aforesaid behavior was not registered [107,108].

$$8CaHPO_4 \times 2H_2O \rightarrow Ca_8(HPO_4)_2(PO_4)_4 \times 5H_2O + 2H_3PO_4 + 11H_2O \quad (6)$$

$$3Ca_3(PO_4)_2 + 7H_2O \rightarrow Ca_8(HPO_4)_2(PO_4)_4 \times 5H_2O + Ca(OH)_2 \quad (7)$$

4. Characterisation of the octacalcium phosphate

Once the most effective pathway and the optimum conditions for obtaining the OCP phase are established, characterisation of the product is of paramount importance. Identification of the present phase and distinguishing the co-existence of other calcium phosphate phases is necessary, in order to claim the purity of OCP. Due to the high resemblance of OCP apatite layer to the structure of HAp, the discrimination between OCP and HAp has proven to be, in all respects, challenging. Enclosed in the literature, several techniques have been employed for the characterisation purposes. The main are: X-Ray diffraction (XRD), Fourier Transformation Infrared Spectroscopy (FT-IR), Nuclear Magnetic Resonance (NMR) and Raman Spectroscopy. However, it should be noted that a multi-technique approach is the only way to attain the most reliable results.

4.1. X-ray diffraction

Crystal structure of calcium phosphates can be differentiated by assessing the similarity between the angles of diffraction peaks and reference positions, recorded in a database [111]. Each calcium phosphate has a specific reflection (or a plethora of them) that could help separate it from the others alike. XRD pattern of OCP (Fig. 5.) has a unique low angle (100) maxima, at 2θ 4.72 degrees and a doublet (200) and (010) at 2θ 9.44 degrees and 9.77 degrees, respectively. These are referred to as common identifiers [75,112,113]. Additional present maxima of OCP are approximately in positions 2θ 26.5, 28.7, 32.6, and 33.6 degrees, ascribed to the diffraction of (002, 260 and 700) plane [88,92,99,114].

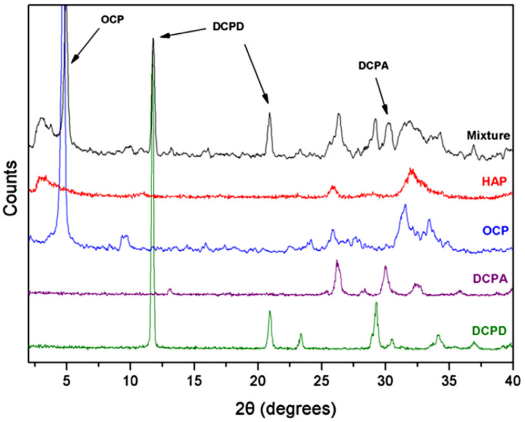

Fig. 5. XRD pattern of octacalcium phosphate with characteristic patterns of HAp, DCPD, DCPA and their mixture for easy comparison.
(Source: Reprinted from reference [115], with permission from Elsevier)

4.2. Fourier transformation infrared spectroscopy

Based on the study by Fowler et al. [61], detailed description of the main positions of OCP characteristic bands, is comprised in the Table 2.

The symmetric v_3 stretching mode (of PO_4) with characteristic bands at 1077 cm^{-1}, 1295 cm^{-1} and 1193 cm^{-1}, as well as O_3PO-H stretching at 917 cm^{-1} and 861 cm^{-1}, assigned to the HPO_4^{2-} ion, are most commonly used to differentiate OCP from HAp and other mixtures (Fig. 6).

Table 2
FT-IR vibrations for OCP (w, weak; m, medium; s, strong; sh, shoulder).

Molecular ions	Assignment	OCP band
HPO_4^{2-}	O_3PO-H stretching	2440 w 6
	P-O stretching (υ_3 PO_4)	1295 w 6
		1193 w 5
		1137 sh
		1121 s 6
		1103 s 5
		1000 sh
	O_3PO-H stretching	917 w 6
		861 w 5
	Bending (ν_4 PO_4)	524 w
PO_4^{3-}	P-O stretching (υ_3 PO_4)	1055 s
		1037 s
		1023 s
	P-O stretching (ν_1 PO_4)	962 w
	Bending (ν_4 PO_4)	601 m
	Bending (ν_2 PO_4)	560 m
		466 w
PO_4^{3-}, HPO_4^{2-}	P-O stretching (υ_3 PO_4)	1077 s
	P-O bending (ν_4 PO_4)	575 sh
H_2O	Stretching	3600
		3525
	Bending	1642
	Libration	627 sh

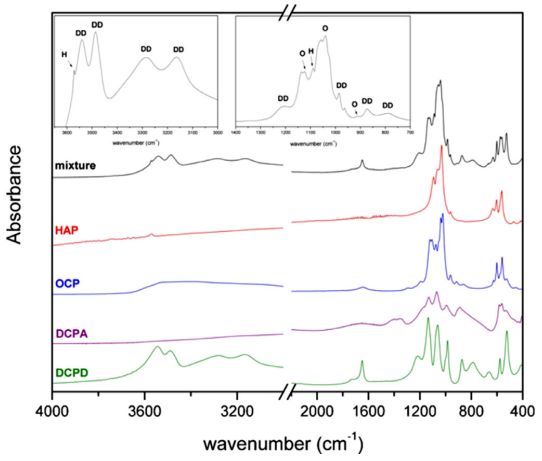

Fig. 6. FT-IR spectra of OCP with characteristic patterns of HAp, DCPD, and DCPA for easy comparison. The abbreviations DD, O and H refer to DCPD, OCP and HAp, respectively.
(Source: Reprinted from reference [115], with permission from Elsevier)

4.3. Nuclear magnetic resonance

As of recently, evidence of OCP presence is being obtained by nuclear magnetic resonance, in particular, ^{31}P NMR [116–123]. Due to the six non-equivalent phosphorous sites (PO_4^{3-} (P1 to P4) and HPO_4^{2-} (P5, P6)), ^{31}P NMR made considerable contribution in characterising the hydrogen environments of OCP[116]. From the chemical formula of OCP, it was assumed that ^{31}P signals of the PO_4^{3-} and HPO_4^{2-} groups should possess an intensity ratio of 1:0.5, but throughout the literature, the intensity ratio was found to be 1:0.92. The quantification of OCP to the fraction of 10 wt% is easily accomplished with ^{31}P solid state NMR [124]. Notable OCP peaks are at 3.7 ppm (P1), 3.3 ppm (P2/P4), 2.0 ppm (P3), and -0.2 ppm (P5, P6) (Fig. 7)[117]. In a study by Laurencin et al., ^{43}Ca NMR has also been used for OCP identification. Sixteen sets of data, complementary to eight duplicates stemming from OCP, with values Ca 1, 2 – -12.6 ppm, Ca 3, 4 – 7.8 ppm, Ca 5,6 – - 7.8 ppm, Ca 7, 8 – -11 ppm, Ca 9,10 – 3.8 ppm, Ca 11, 12 – 27.7 ppm, Ca 13, 14 – 8.2 ppm and Ca 15, 16 – -18.2 ppm were described [125]. Moreover, NMR has been beneficial in analysis of OCP incorporation processes for various carboxylic rich molecules [117,126].

4.4. Raman spectroscopy

Another analytical technique, used mostly to have a more desirable results when discriminating OCP from HAp, is Raman spectroscopy (Fig. 8). The assignments of multiple OCP bands depend on excitation power of the used laser [61]. The typical Raman spectra of OCP exhibits v_1 PO_4 double band at 955 and 964 cm^{-1}, v_1 HPO_4 band at 1008, 995 and 977 cm^{-1}, v_1 HPO_4 P-OH stretching modes at 924, 935, 945 cm^{-1} and v_2 HPO_4 band at 407 cm^{-1} [61,124,127–129]. Robin et al. [124] have used the characteristic shoulder of OCP at 964 cm^{-1} to evaluate the presence of OCP with $\geq$ 70 wt% content. Furthermore, a slight shift of the maxima of the v_1 PO_4 band (955 and 964 cm^{-1} for OCP and 958 cm^{-1} for HAp) and presence of 407 and 1008 cm^{-1} bands were used to investigate the overlapping with HAp and to record the minimum presence of OCP in the sample mixture (first detection point at 10% OCP, 90% HAp). Detailed record of OCP bands in correlation with different laser excitements has been provided by Fowler et al. [61].

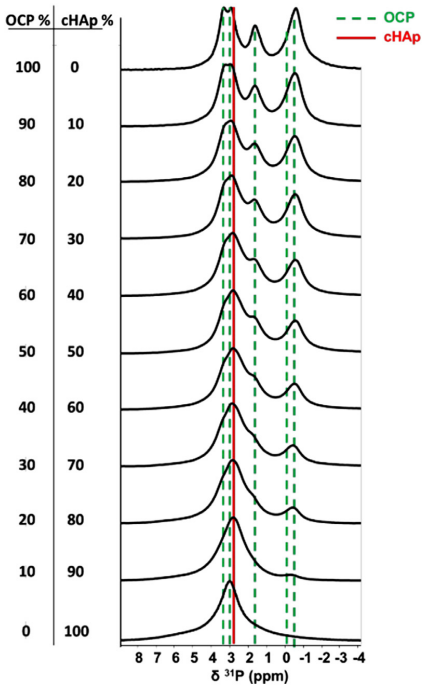

Fig. 7. ^{31}P single pulse MAS spectra of OCP and CDHAp, depicting characteristic shifting of the peaks.
(Source: Reprinted from reference [124], with permission from Royal Society of Chemistry)

Having all the aforementioned information about OCP, and possibility of having a mixture of certain phases, discerning the specific patterns is extremely difficult. The main reason being, the fact that phase patterns may overlap substantially, especially between OCP and HAp [130]. Even though this is seen as a benefit from the biomineralization context, in characterisation it is a considerable obstacle. For morphology assessment, most commonly used methods are SEM and transmission electron microscopy (TEM). To acquire further discrepancy and to quantify OCP phase purity, Rietveld refinement coupled with XRD [124,130], deconvolution methods of the spectra and X-ray photoelectron spectroscopy (XPS) [131,132], are starting to gain the interest of the scientific community. Furthermore, Shurtakova et al. [112] presented one more way of possible future analysis of OCP and its identification in biomineralization process: analysis by pulsed electron paramagnetic resonance (EPR).

5. Hydrolysis of octacalcium phosphate to hydroxyapatite

As we have previously mentioned, OCP is presumed to be the precursor of biologically formed apatite [40,133,134]. Although it is known that OCP is a metastable phase [52], and it converts to a thermodynamically more stable phase, HAp [134], the mechanism that transpires during this conversion is still not completely clear. It is hypothesized that hydrolysis of OCP occurs through dissolution-reprecipitation, in conjunction with ion diffusion-crystallization in the water layer of OCP. Depending on the calcium availability and the release of phosphate ions, reaction scheme (8) of the hydrolysis to HAp has been postulated [89,135]. Additionally, the hydrated layer is presumed to be the location where the protons and HPO_4^{2-} diffuse. The change in this posi-

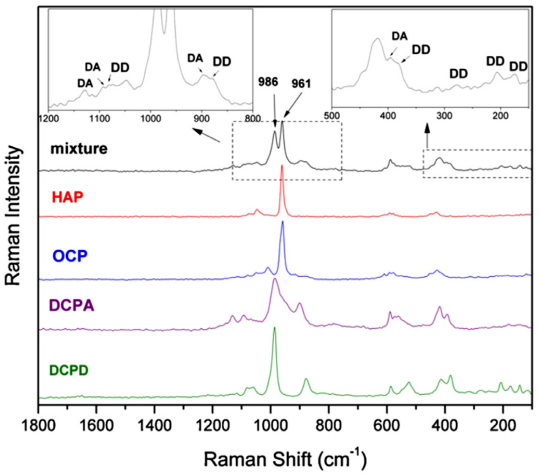

Fig. 8. Raman spectra of OCP with characteristic patterns of HAp, DCPD, and DCPA for easy comparison. The abbreviations DD and DA refer to DCPD and DCPA, respectively.
(Source: Reprinted from reference [115] with permission from Elsevier)

tion, makes the crystal structure to reconstruct and crystallize into HAp [136].

$$\frac{10}{8}Ca_8H_2(PO_4)_6 \times 5H_2O \rightarrow Ca_{10}(PO_4)_6(OH)_2 + \frac{3}{2}H_3PO_4 + \frac{17}{4}H_2OCa_8H_2(PO_4)_6 \times 5H_2O + 2Ca^{2+} \rightarrow Ca_{10}(PO_4)_6(OH)_2 + 4H^+ + 3H_2O \quad (8)$$

Mineralization studies have suggested that the entire process starts with the formation of ACP nanometer-sized clusters – usually referred as Posner's CaP clusters ($Ca_9(PO_4)_6$) [137–139]. Unremitting calcium uptake, ACP converts into OCP and eventually into apatite, which is why both contain similar complexes within their structural unit [140]. Based on the extensive study, conducted by Habraken et al. [140], once the ribbons, with Ca/P molar ratio 1, were formed, a composition of $[Ca_6(HPO_4)_4(PO_4)_2]^{2-}$ was found, corresponding to the formula of Ca deficient OCP. From this point, the present phase transformed into the composition of OCP ($Ca_8(HPO_4)_2(PO_4)_4$) with elongated plates and Ca/P molar ratio of 1.33. The aggregation process continued, involving the hydrogen bonding and continued binding of calcium ions, followed by the loss of structural water layer, which lead to a further cross-linking of the complexes, and densification of the structure. Elimination of HPO_4^{2-} from the water layer, has shown to be the necessary step for the phase transformation, moreover, it has been postulated to be also the rate-determining step of the conversion [87]. Yokoi et al. [87] hypothesized that the water layer functions as a diffusion pathway for HPO_4^{2-} and its thickness is possibly one of the key factors in the transformation of OCP to HAp (more information within the section 7.1.5.). During the conversion OCP crystals absorb calcium ions and release hydrogen phosphate ions (through their deprotonation via hydrolysis [118]), which makes the process progress spontaneously, irreversibly, and topotaxially, without alteration of original crystal morphology [141]. Hydrolysis of OCP was examined in *in vitro* [87,99,118,142,143] and *in vivo* conditions [144,145]. Tseng et al. [118] studied transformation mechanism at the molecular level, and they confirmed that after 4h, first traces of HAp appear, while at 12h, structural transition is completed. No changes were visible after 96h. Similar results were provided by Arellano-Jiménez et al. [99], where they followed the transition in water media with a starting pH of 7.2 for 30 min, 1, 6 and 12h. After 1h, a mixture between OCP and HAp was present, but at 12h pattern was assigned to HAp. Suzuki et al. [90] compared hydrolysis of OCP in different pH solutions, and when the solution was at pH 11 it postponed the rate of transition, in comparison to the pH 7.4. Furthermore, different physiological media have been analyzed, in respect to the conversion of OCP into HAp [89,103,146–148]. When tested in deionized water [147], upon 6 h the product consisted of both OCP and CDHAp, whereas after 48 h OCP phase disappeared completely, signaling that the hydrolysis is over. Moreover, it was noted that after the conversion specific surface area increased from 16 to 45 m^2/g. Identic samples were tested in *in vivo* conditions and in culture media (10% FBS containing α-minimal essential medium (α-MEM)). In the culture medium after 21 days OCP converted to CDHAp, however, a portion of OCP still remained. After 21 days in rat calvarial defect, implanted OCP seemed to advance more slowly, but with the same tendency [147]. OCP, with SSA 10.6 m^2g^{-1}, was studied in simulated body fluid (SBF), on 36.5°C, and the pH 7.25 [149]. Hydrolysis of OCP to HAp transpired to a small extent during 28 days in SBF. Structural changes were not detected by XRD, albeit the morphology of the OCP recorded on SEM and transmission electron microscope (TEM) had some changes. Before immersing in SBF, crystals had sharp edges and a flat plane, while after 14 days, many flake-like round precipitates were observed. The results of this study were, to some extent, confirmed by Kobayashi et al. [141], stating that the conversion undergoes not only dissolution-reprecipitation process, but also a hydrolytic process within the OCP structure. XRD and FT-IR displayed minuscule changes in OCP characteristic pattern, confirming that the hydrolysis of OCP into HAp progressed slowly. Petrakova et al. [148], examined conversion of OCP granules (500–1000 μm) in supersaturated calcification solution (SCS), Dulbecco's phosphate-buffered saline (DPBS), normal saline (NS) and Dulbecco's modified Eagle's medium (DMEM). pH of all solutions was around 7. In SCS, both OCP hydrolysis and precipitation of the amorphous phase, transpired, while in DPBS needle-like crystals stayed the same. The reason is probably due to the calcium ions not being released, while phosphate ions exhibited a constant release. New OCP-like phase formed in DMEM, which indicated the incorporation of organic molecule, thus substantially reducing the hydrolysis of OCP. Being that DMEM is a cell growth media, the results of osteosarcoma cell cultivation on OCP displayed that pre-treatment augmented the cytocompatibility of the granules. According to the authors, OCP dissolved in the solution of NS [148]. Considering that the aforementioned conversion kinetic experiments were studied at different conditions (media, pH, temperature, etc.), they cannot be quantitatively compared. However, we have made the efforts to graphically display two representative cases of the OCP – CDHAp transition, in time, implemented at 37 °C (Fig. 9).

In addition, the effect of the temperature on the hydrolysis of OCP was investigated [43]. Isothermal calorimetry at 25, 38 and 60°C, displayed that conversion of OCP to HAp materialized faster at higher temperatures (Fig. 10). At 60°C, after 4 h, HAp maxima started to appear. After 11 h, further transformation of OCP to HAp continued and by 19 h, the hydrolysis was completed.

6. Biological significance of octacalcium phosphate

CaP are continuously used for inducement of bone formation, but being one of the key elements of bone is not enough to ensure the successfulness of the process of regeneration itself. The main reason is that the bone is additionally populated with cells, macromolecules, and blood vessels [59]. With that being noted,for OCP to have the potential to promote bone regeneration, properties as achieving osteoconductivity through osteoblast differentiation

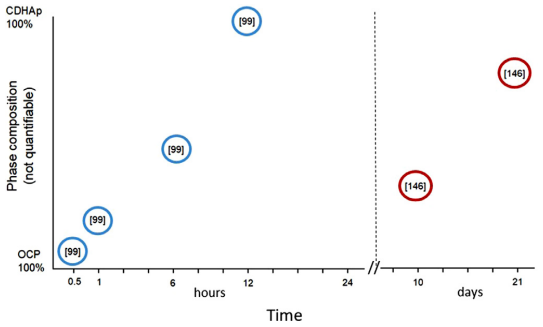

Fig. 9. Schematic presentation of the OCP/CDHAp transformation kinetics. Blue circles were used to present the *in vitro* progress in physiological pH conditions, while the red circles displayed the *in vivo* conditions.

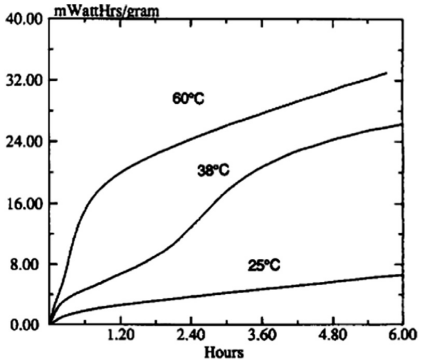

Fig. 10. Calorimetric curves displaying the rate of the heat evolution during the OCP/CDHAp conversion.
(Source: Reprinted from reference [43], with permission from Elsevier)

and osteoclast formation and biodegradability have to be met [62]. Convergence of OCP to apatitic crystals suggests that biodegradation could be instigated via cell-mediated osteoclast resorption rather than a simple dissolution process [142]. As it was already mentioned, OCP has the tendency to convert to the thermodynamically stable HAp. This change has been hypothesized to be an important factor when it comes to regulating osteoblast differentiation and osteoclast formation. The stromal cell line ST2 cells [150–153], derived from mouse bone marrow stromal cells and primary calvarial osteoblastic cells were used to examine the proliferation and osteoblastic differentiation influenced by OCP [62,109,136,154].

Saito et al. [155], examined the effect of OCP implantation on the cellular activity of osteocytes, embedded in newly formed bone in critical-sized rat calvarial defects. OCP was in the form of granules, with specific surface areas of roughly 20 – 40 m^2/g and a plate-like morphology. Eight weeks upon implantation new bone formation was noticed (3.1 ± 1.0 mm^2 ± SD). PDPN-positive cells, DMP1, and SOST/sclerostin, which serve as the expression of osteocyte markers, were also observed. Osteocytes, fibroblasts and multinucleated osteoclast-like cells were detected on the surface of the OCP crystals. The effect of OCP on angiogenesis was tested with implanting octacalcium phosphate/gelatin composite (OCP/Gel) in rat calvaria critical-sized defect, for 2 and 4 weeks [156]. Composites, with highly porous structure and pore size of 100–500 µm (displayed in microfocus X-ray computed tomography system (micro-CT) images), showed thick blood vessel-like structures connecting from the median superior sagittal sinus. The formation of blood vessels suggests neovascularization. Volume of newly formed vessels was around 2.5 mm^3, and their number roughly 80 [/], after 2 weeks, and 60, after 4 weeks. When it came to bone formation, OCP/Gel had substantially higher formation of the new bone, in comparison to only gelatin. Volume of the newly formed bone was 55 [mm^3] and regenerated bone mass was also around 55 [%] [156].

Another composite, OCP and hyaluronic acid (HA), in the form of granules (300 – 500 µm diameter) was prepared and implanted in the subperiosteal region of mouse calvaria, for 3 and 6 weeks [157]. The formation of cells through tartrate-resistant acid phosphatase (TRAP-positive) osteoclast-like cells from RAW246 cells with RANKL, was visible, which can serve as a sign that the biodegradability was ameliorated with addition of HA. Molecular weights of HA, 90 × 10^4 (HA 90) and 600 × 10^4 (HA 600), exhibited enhancement of osteoconductivity at post-implantation, especially during the early stage of bone formation (after 3 weeks). However, their effect differed. HA 90 was resorbed and the process of new bone formation started around OCP, whereas HA 600 stayed moderately unresorbed [157]. OCP was deployed also in the form of coatings, on a magnesium alloy and pure titanium discs [158,159]. HAp deposited on the Mg alloy had a 20% lower corrosion rate than OCP, while both suppressed corrosion and foreign-body reaction in *in vivo*. Furthermore, titanium discs, with homogenous deposit of plate like OCP, were used subsequently for the drug loading.

Another factor that has an influence on the biological response of OCP is its stoichiometry [88]. The results of the study verified that the partially hydrolyzed OCP (OCPphl, Ca/P molar ratio 1.37) had the best results when it came to enhancement of bone formation. Findings were compared to the Ca-deficient OCP, with Ca/P molar ratio of 1.28 (CaDOCP), and to the OCP hydrolyzate (OCPhl) obtained via hydrolysis of OCP, with the molar ratio of 1.48 [88]. The pore sizes of OCPphl, CaDOCP and OCPhl granules were 0.277, 0.393 and 0.278 mm, respectively, while the porosity was at 87.6, 87.2 and 90.2%. The rate of bone formation for OCPphl was constant, but OCPhl increased its rate with the implantation duration (highest on day 56). For CaDOCP bone formation was observed on day 14 and it gradually improved up to the day 56. Biodegradability of OCPphl was similar to OCPhl. Secretion of inflammatory cytokines, IL-1β and TNF-α, has been reduced significantly more with OCPphl than with CaDOCP in days 7, 14 and 28. Furthermore, alkaline phosphatase (ALP) and osteoblast differentiation markers (osteocalcin, Col1a1 and osteopontin) supported the capability of bone formation on OCPphl as shown by histomorphometric tests [88].

In addition to the extensive research presented on the benefits of OCP, in respect to its osteoconductivity, two different studies aimed at determining does OCP show evidence of osteoinductivity [160,161]. In the first case OCP-coated porous structure on a titanium alloy (Ti6Al4V), with a rough surface, due to the sharp vertical crystals, was implanted in the condyle and bone was detected in the center of the implant [160]. In the experiment conducted by Habibovic et al., OCP was deposited on Ti6Al4V, HAp, biphasic calcium phosphate ceramics (BCP) and on polyethylene glyco terephthalate/polybutylene terephthalate (PEGT±PBT) copolymer. The coated materials were implanted in the muscle fascia. The presence of OCP coating increased the osteoinductive potential of all biomaterials by inducing ectopic bone formation [161].

6.1. Biological activity of octacalcium phosphate in comparison to other biologically relevant calcium phosphates

The differentiation and OCP potential for the bone regeneration, with rapid substitution to bone, was analyzed with different CaPs. Among all the CaPs, OCP presented the highest capacity

to increase ALP activity [62]. As it was presumed, the implanted OCP enhanced bone formation more than HAp [147]. In a different study, the tissue response and osteoconductivity of OCP block and sintered HAp block, were compared [162]. OCP block demonstrated approximately 30% replacement with newly formed bone, 4 weeks after implantation, whereas sintered HAp block had no replacement with bone, in the same time frame [162]. Moreover, both blocks had a gap between them and the defect site, when implanted, and no fibrous tissue penetration was observed in the case of the OCP block. This has indicated that the OCP had higher osteoconductivity than HAp [162]. Same research group went a step further, and compared the effect of OCP foam scaffold and the OCP compact [163]. OCP foam generated materialization of the mature bone, along with blood vessels, as early as two weeks post implantation, with the amount only increasing at four weeks post implantation. In contrast, the results inside the OCP compact were negligible [163]. The diametral tensile strength (DTS) of the OCP block was 1.0 ± 0.2 MPa, while the one of the OCP foam was 0.15 ± 0.04 MPa. Microporosity of OCP block was 69.0 ± 1.6%, and porosity of OCP foam was 69.4% ± 0.04%.

Osteoblastic differentiation of ST-2 cells was measured by ALP enzymatic activity and it was demonstrated that the activity increased with the increasing amounts of OCP coating [109], whereas for HAp, the ALP activity was constant regardless of the amount of HAp used. ALP staining, which hydrolyzes pyrophosphate and provides inorganic phosphate to augment mineralization [164], was more intense with OCP than with HAp. Moreover, the expression of osteogenic markers, including osterix (Osx) and collagen type I (Col-1), was also enhanced for OCP [136]. When implanted in rabbit bone marrow and compared with β-TCP [88], OCP had approximately same results for bone formation as β-TCP, but with OCP it increased gradually until day 56. Moreover, osteocalcin staining was more concentrated on OCP than on β-TCP, while enhancement of osteopontin adsorption was only noted for OCP and not for β-TCP. Kobayashi et al. [141] compared the osteoconductivity of OCP and ACP. Eight weeks after the implantation in the calvarium of twelve-week-old male Wistar rats, ACP showed 16.9 ± 2.9% percentage of new bone in the defect (n-Bone%) and OCP 38.2 ± 4.3%.

It is presumed that the solubility of CaP ceramics can have an effect on osteoclast resorption activity, with CaPs of higher solubility having a better after-effect [165]. More on OCP solubility, under different conditions, can be found in the work done by Tung et al. [166]. This has been corroborated by comparing β-TCP's, HAp's and OCP's resorbability and enhancement of bone formation [167]. Particle size for OCP and HAp was between 300 and 500 µm and for β-TCP between 250 and 500 µm. The percentage of remaining implants in the defect (r-Imp%) for OCP, β-TCP, and HAp was 6.58 ± 1.46, 23.4 ± 6.82, and 39.0 ± 6.86, respectively. The n-Bone% within the OCP, β-TCP, and HAp groups was 63.3 ± 7.52, 42.8 ± 13.6, and 24.2 ± 7.82, respectively. These results indicated that OCP is the most resorbable one, and it enhanced bone formation in the periosteum of the calvarium more than the other CaPs. Taking into account the histological observation, it was concluded that the OCP is resorbed faster in the connective tissue than in the bone tissue, as it was found only in the newly formed bone [167]. Comparison of OCP and HAp bone regeneration capabilities can be seen in the Fig. 11.

Shiwaku et al. [168] examined the crosstalk between osteoblasts and osteoclasts when OCP was implanted. They reported that, large tartrate-resistant acid phosphatase (TRAP)- positive cells, used for demonstrating multinucleated osteoclasts, were observed more regularly in the cultures with OCP or β-TCP disks compared to HAp disks. The OCP's ability to promote formation of osteoclasts was similar to the β-TCP, which induced the activation of EphrinB2 (EfnB2) ligands on osteoclasts [168]. However, OCP and HAp/OCP mixtures promoted complement component 3a (C3a) expression, that is exuded by osteoclasts to enhance osteoblast differentiation. This showed how the effect of different CaPs can result in a dissimilar regulatory mechanism for bone regeneration [168]. When compared to the other highly effective CaP, results showed that the percentages of remaining implants of OCP coupled with recombinant human bone morphogenetic protein-2 (rhBMP-2) were considerably lower than that of HAp and β-TCP. At the same time the percentages of newly formed bone of OCP/BMP were radically higher than that of HAp and β-TCP [169,170]. Comparison of OCP and β-TCP bone regeneration capabilities can be seen in the Fig. 12.

Additionally, OCP was combined with ACP, in ratios 75:25, 50:50 and 25:75, and implanted in critical sized rat calvarial defect [141]. Results from the radiographic examination (8 weeks postimplantation) displayed that the radiopacity of the 25:75 mixture was significantly higher than that of the other combinations, or OCP and ACP implants individually (63.2 ± 11.8%). The implantations were also assessed regarding the bone formation, and newly formed bone was observed around the implanted mixture. This approach gives an insight of potential functionalization of OCP with biological molecules that can further help with the bone regeneration process due to the combined ameliorating effect they have exhibited [133,171].

All these studies confirm the significant role that OCP plays in the process of bone formation. Biodegradability and osteoconductivity, shown through resorption by osteoclasts with following formation of new bone tissue, have made it clear that OCP should be in the forefront of research, regarding bone regeneration.

7. Octacalcium phosphate as a drug delivery system

Bone regeneration is a complicated physiological scheme of systematic series of mechanisms that are performed in order to produce restoration of bone form and function. CaP biomaterials are in the forefront of bone tissue engineering, due to the possibility to elicit a controlled reaction around the defect site and to ultimately be replaced by newly formed tissue [172,173]. As the current research continues to evolve, innovative therapies are being used as a supplement to traditional methods for enhancement and acceleration of the overall regeneration process. Furthermore, they aim to tackle systemic conditions, such as osteoporosis [172]. Administration of biologically active substances is one strategy, and it is implemented through a systemic or local drug delivery pathway. In order to augment biodistribution of drugs, local drug delivery is proving to be essential [174–177]. Traditional systemic drug delivery route occurs through the circulatory system, which could lead to an outcome of numerous side effects, organ complications, systemic toxicity and under par deliverance to the targeted defect [174]. To eschew these disadvantages, local agent delivery tends to minimize burst release and establish the desired release profile, unique to the defect site. In order to develop a new DDS, various factors need to be considered. Selection of a suitable drug, materials used for a successful matrix, drug release mechanism and kinetics need to interoperate to accomplish a delivery profile that would yield a drug dispension over a long period of time, in a controlled manner [178,179]. If such a construct is produced, it will ensure improved patient compliance, reduced frequency of drug intake, accumulation and toxicity, as well as a controlled system in terms of diffusion and dissolution [178]. The drug-loading efficiency and release kinetic of CaPs, make them the prospective candidate for delivering therapeutic agents in bone regeneration [180].

Operationalization of OCP for drug delivery purposes is still a pioneering concept and a lot more *in vitro* and *in vivo* investigations are required. However, due to its beneficial effects on the bone formation, OCP has been used for incorporation of ions, bisphosphonates and several other molecules summarized in Table 3.

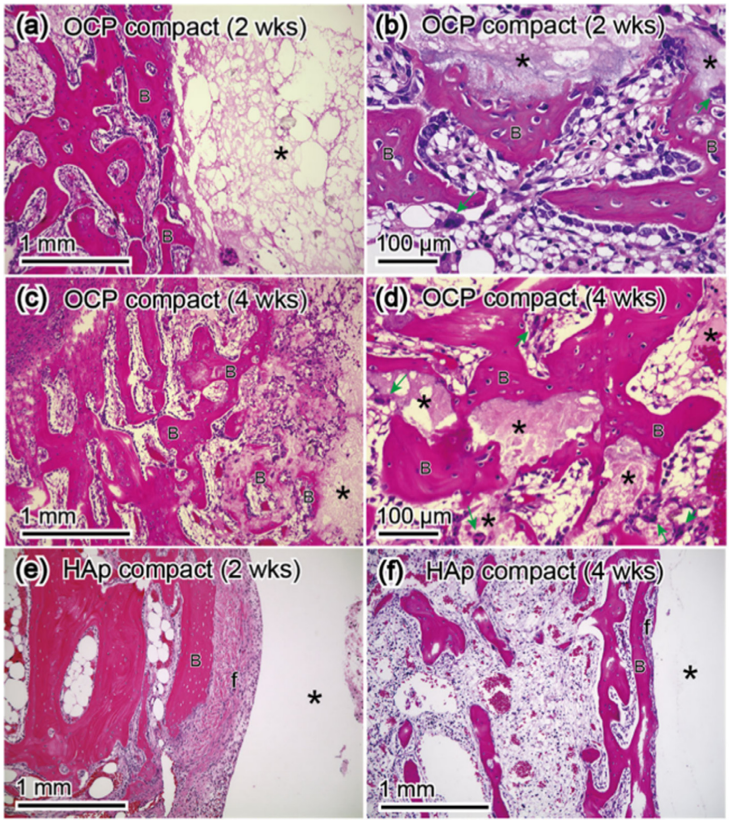

Fig. 11. Comparison of histological images of OCP and HAp, 2 weeks and 4 weeks after implantation. Legend: B indicates bone, * points to implanted materials, f refers to fibrous tissue, and green arrows indicate multinucleated giant cells.
(Source: Reprinted from reference [162], with permission from Springer Science)

Table 3
Current, biologically active, ion/molecule delivery systems based on OCP.

Active substance	Exhibited effect	Source
Carbonate ions (CO_3^{2-})	Enhance osteoblast proliferation with minor changes in morphology; increased Ca/P molar ratio	[182–185]
The pyromellitic acid	Imparts fluorescent properties to OCP	[186]
Magnesium ions (Mg^{2+})	Enhance collagen type I production and increases cell proliferation	[63–66]
Strontium ions (Sr^{2+})	Improve the viability, proliferation and osteogenic differentiation of bone mesenchymal stem cells (mBMSC)	[68–70,187]
Iron ions (Fe^{3+})	Greater surface roughness is noticed; promote proliferation, spreading, adhesion and osteogenic differentiation of mBMSC	[70,187]
Fluoride ions (F^-)	Stimulate the primary attachment and proliferation of cells	[72,188]
Zoledronate (ZOL)	Inhibits osteoclast activity and promotes osteoblast growth and differentiation and displays anti-angiogenetic properties	[84]
Alendronate (AL)	Inhibits osteoclast activity and promotes osteoblast growth and differentiation	[83,189]
Methotrexate	Suppresses human osteosarcoma cell proliferation	[190]
Ascorbic acid phosphate (AscP)	Slow-release profile; promotes differentiation of the osteoblast-like cells	[191]
Silver nanoparticles (AgNPs)	Support osteoblast viability and differentiation, as well as inhibition of the growth of pertinent bacteria	[192]

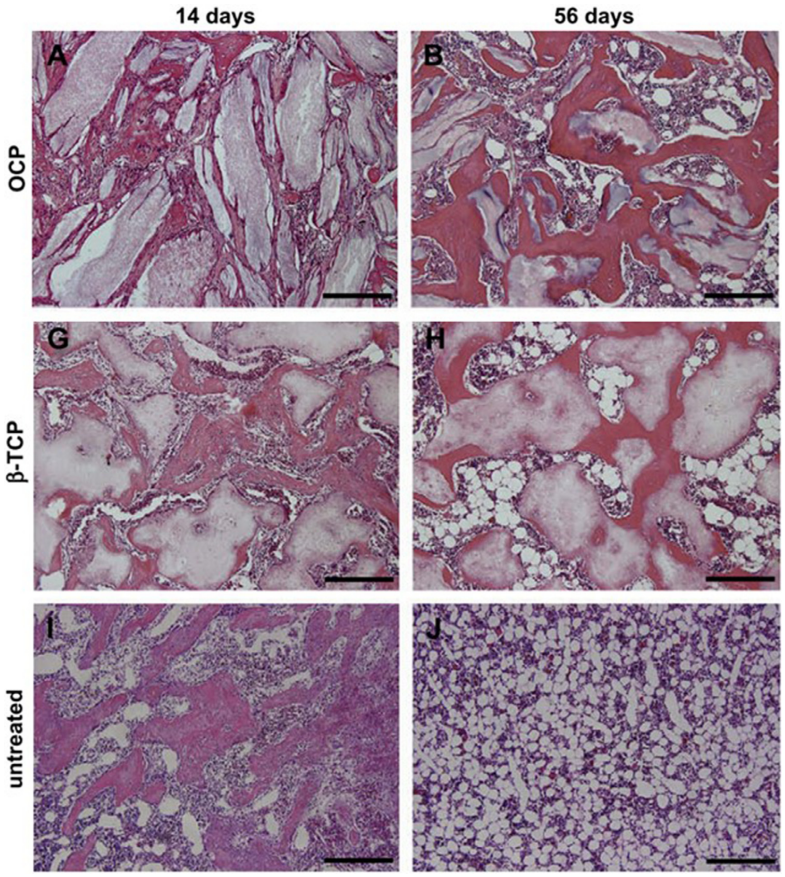

Fig. 12. Comparison of histological images of OCP, β-TCP and untreated area, 2 weeks and 8 weeks after implantation. Bars = 200 μm. (Source: Reprinted from reference [88], with permission from Elsevier)

A plethora of studies, on incorporation of different therapeutic agents in OCP, had an end goal of achieving high values of drug-loading capacity. This has been done through approaches such as hydrothermal method (262.9 mg/g of adsorbed ibuprofen) [181], *in situ* dropwise precipitation (5.2 wt% of alendronate and 3.5 wt% of zoledronate) [84], Matrix Assisted Pulsed Laser Evaporation (MAPLE) (5.5 of magnesium and 0.6 at.% of strontium)[66], electrochemical deposition (5–20% Sr^{2+} substituted coatings) [34] and others.

7.1. Functionalization of octacalcium phosphate with bioactive ions

Incorporation of bioactive ions into the structure of CaPs is one of the essential and heavily utilized methods to regulate crystallinity, stability, structure and biocompatibility for the further applications in bone tissue engineering [193]. Moreover, these bioactive ions embedded in the structure of CaP are vital for the biomineralization and various biological responses [68]. OCP has been enhanced by carbonate (CO_3^{2-}), magnesium (Mg^{2+}), zinc (Zn^{2+}), strontium (Sr^{2+}), iron (Fe^{3+}) and fluoride (F^-) ions.

7.1.1. Carbonate ions

Carbonate ions are present in bone mineral and in enamel [194,195] and the functionalization of various CaPs with them has been extensively investigated, especially with HAp [196,197]. CO_3^{2-} incorporation into OCP is done through the substitution of phosphate ions which are smaller and planar [182]. The disproportion in size leads to the formation of type B carbonate apatite, leading to the decrease of crystalline lattice in a-axis and increase in c-axis [182–184]. Shen et al. examined the overall influence of carbonate ions on physicochemical properties, structure and cellular proliferation and differentiation on substituted OCP [184]. They observed minor changes in crystal morphology and lattice constant. Carbonated OCP, due to the incorporation of the ions, exhibited increased Ca/P molar ratio, which is also hypothesized to be the reason of the ameliorated effect of OCP on the regulation of osteoblast activity and bone formation [184,185].

7.1.2. Magnesium and zinc ions

Magnesium is one of the most crucial elements that are accumulated in hard tissues, comprising 0.44 [w/w]% of enamel, 1.24 [w/w]% of dentine and 0.72 [w/w]% of bone [25]. As a divalent cation, Mg^{2+} competes for growth sites on the crystal surface, with already embedded Ca^{2+} within the OCP structure. This is the main reason why it has an inhibitory effect on the longitudinal growth of OCP crystals [63,64]. When substituted, the surrounding oxygen atoms undergo internal relaxation, due to the fact that the ionic size of Mg^{2+} is smaller than the one of Ca^{2+}, however the unit

cell dimensions and shape remain relatively constant [65]. Incorporation of Mg^{2+} up to the concentration of 15 atom % yields the pure OCP phase, but if the concentrations are higher (20-50 atom %), the obtained product is DCPD [67]. Moreover, magnesium hinders the hydrolysis of OCP to HAp [74]. Regarding the role it has in bone formation, Mg^{2+} has exhibited a positive influence on collagen type I production and it enhanced osteoblast-like MG63 cells proliferation [66]. Another metal from this group that was incorporated within OCP is Zn^{2+}. Similar to Mg^{2+}, Zn^{2+} is also essential for the bone tissue and with other CaPs it exhibited higher proliferation, osteogenic differentiation [25] and antibacterial properties [198,199]. Incorporation of Zn^{2+} is more favorable substitute of the Ca^{2+} ion within the OCP, as compared to Mg^{2+}, which is due to the decreased coordination numbers (for Zn^{2+} in OCP they are 4 or 5, depending on the atomic sites, whereas for Mg^{2+} it is the fivefold or sixfold coordination). Supplemental reason is formation of more covalent bonds between Zn^{2+} and the surrounding oxygen ions in the crystal lattice [65]. The presence of zinc also inhibited the hydrolysis of OCP into apatite and it endorsed the formation of amorphous-like apatitic phase of OCP [73]. When the ion loading of Mg^{2+} and Zn^{2+} on OCP is compared with the loading on HAp, it can be seen that the incorporation in HAp is not energetically favorable, while the substitution in OCP is more suitable [65].

7.1.3. Strontium and ferric ions

Strontium substitution in OCP structure has been researched due to the high potential it has for advance of bioactivity and osteogenesis in bone repair. In the study done by Matsunaga et al. [69], Sr^{2+} with the concentration of 10^{-4} mol/L was satisfactorily incorporated instead of Ca^{2+} in OCP structure by the exchange of ions. It stabilized the metastable OCP crystals to prevent apatite resorption, as well as promoted apatite nucleation during bone remodeling, but the crystal lattice became enlarged in the a- and c-axis [68]. Stabilization of the OCP structure is dependent on the concentration of Sr^{2+}. If the concentration is too high (>10 mM) it can lead to a significant decrease of Ca/P molar ratio and subsequently, with an even further increase of the ion concentration, the growth of the c-axis is inhibited. At the same time the a,b-axis are promoted, leading to the destabilization of the overall composition [68]. Moreover, the newly substituted OCP crystals exhibited good abilities in boosting viability, proliferation and osteogenic differentiation of bone mesenchymal stem cells [68]. Strontium-substituted OCP coatings synthesized by electrochemical deposition demonstrated that with the ratio of Sr/(Sr + Ca) between 5–20% of Sr^{2+} in coatings, pronounced enhancement of MC3T3-E1 cell proliferation was observed. However, 1% Sr^{2+}-substituted coating displayed a superior osteoinductive activity over the other samples. This was probably due to the fact that smaller concentrations do not significantly alter coating microstructure and composition, resulting in favorable osteogenesis [34]. When Sr^{2+} was incorporated in HAp, it displayed substitution of roughly 25 mol %, whereas OCP can incorporate more Sr^{2+} by Ca^{2+} ion exchange process (from 25-33 mol %) [69]. Nonetheless, the highest substitution of HAp with Sr^{2+} that was recorded in the literature (100% SrHAp [200]), was not yet achieved with OCP.

In a different paper, Shi et al. compared the effect of divalent (Sr^{2+}) and trivalent cations (Fe^{3+}) on the OCP crystal in regard to the structure, formation and morphology [70]. Sr^{2+} is more similar to Ca^{2+} when it comes to the ionic radii, and consequently the crystal morphology was not significantly altered. Crystals remained plate-like with lamellar structures, but a slight surface roughness was observed due to the uncompleted incorporation of the ions, whereas the rest of the undoped Sr^{2+} was washed out. If [Sr^{2+}] in the hydrated layer is more than 10^{-4}M, the measured interplanar distance of 0.335 nm indicates the expansion which transpired most likely at the energetically favorable sites, Ca-3 and Ca-8, while the Ca-4 site was partially replaced [70]. Fe-OCP, exhibited a higher transition of phosphate groups in comparison with Sr-OCP, and Ca^{2+} was replaced in one part with Fe^{3+}, but also with Fe hydroxyl ions ($Fe(OH)_2^{+}$ or $Fe(OH)^{2+}$). The placement of Fe^{3+}, according to Raman spectroscopy, can initiate different coordination environments of orthophosphate groups, whereas Sr^{2+} mainly influences the water layer. Crystal morphology of Fe-OCP displayed greater surface roughness as the Fe^{3+} ions were not only incorporated within the structure itself, but the paucity of them were also adsorbed on the crystal surface [70]. Follow up studies were done by the same team and they additionally focused on protein affinity, ion release and cytological responses of the ion-doped OCP treated under hot air at different temperatures (110–200°C) [187]. Sr-OCP's surface potential did not change to a great extent, while Fe-OCP had a superior solubility and after the treatment it released a higher-dose of Ca^{2+}, producing a gradual decrease of surface electronegativity. Furthermore, the concentrations of released Fe^{3+} and Sr^{2+} from the samples were considerably higher than that of the controls during immersion process. The mBMSC demonstrated good spreading morphology with Fe-OCP and Sr-OCP samples, as well as a satisfactory cellular affinity. Moreover, both of the OCP samples with incorporated ions displayed initial release controlled cytological responses, mainly promoting the proliferation, spreading, adhesion and osteogenic differentiation of mBMSC [170]. Fe^{3+} ions, with porous OCP/poly(lactic-co-glycolic acid) (PLGA) scaffolds, were additionally used to test the release influence on angiogenesis in *in vivo*. The main research goal was to see is it possible for the construct to repair cancerous bone defects and deliver a prospective revascularization strategy [201]. Scaffolds (FeOCP/PLGA, 50 – 150 μm pore size) and a control sample of OCP (con-OCP/PLGA), were implanted subcutaneously into the back of rats. Blood vessels densities of OCP/PLGA, 4 weeks after surgery were 99.8 ± 9.8 per mm^2 of the section area, while con-OCP/PLGA exhibited 48.6 ± 6.3 per mm^2. The diameter of capillary vessels in con-OCP/PLGA had an average of 7.8 μm, whereas FeOCP/PLGA increased to 15.1 μm in average. The larger new blood vessel amount, the greater blood vessel diameter, and the higher expression of specific markers (hypoxia-inducible factors-1α (HIF-1 α) could be seen after 4 and 12 weeks. Additionally, vascular endothelial cell specific marker (CD31) and vascular endothelial growth factor (VEGF-A)), were observed 4 and 12 weeks after surgery [201]. They demonstrated exceptionally accelerated angiogenesis from FeOCP/PLGA. Nevertheless, the results showed positive angiogenic ability of implantation, for both Fe^{3+} laden scaffold and OCP itself.

7.1.4. Fluoride ions

Alongside the effect different cations have on OCP, one of the anions - F^{-}, has been incorporated within the structure of the OCP and the influence on morphological and structural changes [72,188], as well as the proliferation of osteoblastic cells and adsorption of bovine serum albumin (BSA) has been described [188]. The size of the OCP crystals was susceptible to the F^{-} concentration and it caused the reduction of the thickness of OCP lamella when the concentration of the ion increased from 0.1 to 1 ppm [72]. Iijima's team showed that fluoride triggered the apatite-OCP intergrowth and the decrease of the OCP stability, while the thin plate-like morphology remained. A similar observation of the enhancement of the apatitic products was done by Shiwaku's team and once more OCP displayed irregular platy morphology of the crystals that were approximately 5 μm in length [188]. The sample with 3.2 wt% of F^{-} stimulated the primary attachment and proliferation of mouse bone marrow stromal ST-2 cells by 1.5 times more than for pure OCP. Furthermore, the amount of the adsorbed BSA onto hydrolyzed apatitic crystals per unit surface area was somewhat higher than with the undoped OCP [188]. Even though

BSA is perceived to be a strong inhibitor of the crystal growth of calcium phosphates *in vitro*, the BSA adsorption on OCP was only described by a Langmuirian model, without an additional clarification of structural interactions [62]. Another benefit of incorporation of fluoride ions is that they promote the hydrolysis of OCP to HAp, at low concentrations (0.01M), and at the same time enhance the crystallinity of apatite [74]. However, precipitation of OCP is favorable at F^- concentrations between 0.3 and 0.4 mg/L, while in Tris – HCl buffer solution, the limit is between 2 and 5 mg/L. [202,203]. Because of this potential conversion, fluoride can also be used to modify the morphology of OCP crystals. Low-dose of fluoride (0.05 – 1 mg/L) on OCP crystal formation showed plate-like crystal formation in solutions with and without F^- up to 0.3 mg/L. Nevertheless, at concentrations of 0.4 mg/L, they were replaced by the rod-like apatite crystals [204].

7.1.5. Carboxylic and dicarboxylic ions

Additional ions have been mentioned as well. For example, the influence of the carboxylic-rich macromolecules (e.g. sodium poly(aspartic acid), sodium polyacrylate) caused the decrease of crystal growth by reducing the length of the blades which compose the spherule morphology. However, if the concentration of carboxylic macromolecules is even more increased, it can lead to the formation of hollow microspheres [47,110,205]. Marković et al. intercalated OCP with dicarboxylic ions i.e., succinate, adipate, suberate, sebacate, fumarate, and citrate ions [206,207]. They observed that carboxylates with an odd number of carbon atoms (e.g., malonate and azelate), formed different CaPs other than OCP. However, when carboxylates had an even number of carbon atoms, OCP was formed, with slightly larger interplanar spacing of d(100) (1.868 nm). When succinate ions (Suc) in solution are introduced to OCP structure, they replace the HPO_4^{2-} within the water layer and move the basal spacing (d_{100}/Å) from 18.7 to 21.5, resulting in enlargement of interplanar distance [208]. This also alters the movement of water molecules and increases the stability of OCP. The stability is substantially higher with reference to the hydrolysis reaction at high pH, while the delocalization of the HPO_4^{2-} ions within the water layer becomes difficult [117]. Similar OCP carboxylates, like fumarate, malate and adipate ions, when incorporated, displayed an increase in a-axis dimensions determined from the powder X-ray diffraction (XRD) patterns (d_{100} was 2.15 nm, 1.96 nm and 2.37 nm, respectively). This complemented the length of the carbon chain of the incorporated ion [52]. Yokoi et al. [87,209] concluded that reactivity of OCP with incorporated suberate (Sub) ions and succinate incorporated ions is higher than that of pure OCP. They presume the reason is the thickness of the hydrated layer where hydrogen phosphate ions must move in order to transform from OCP to HAp. Increasing the thickness of the hydrated layer increases the diffusion channels and accelerates diffusion of ions such as dicarboxylate ions. Upon the incorporation of both ions at the same time, results showed that if the Suc/(Suc + Sub) molar fractions were higher than 0.45, Suc was favorably incorporated into the OCP structure, but if the values ranged from 0.60–1.0, Sub was preferentially intercalated [210]. Aoki et al. [211] incorporated aspartate within OCP (Asp-OCP, 100 nm size with 42 m^2/g SSA) and tested absorption of formaldehyde. The aldehyde molecules moved into the water layer of OCP and interacted with the carboxylic chain (absorbed amount of aldehyde was 3.1×10^{-3} mol/g, while activated charcoal exhibited 1.6×10^{-3} mol/g). This implies that the substituted OCP has potential in being an absorbent, with size-selective absorption properties that depend on the interlayer distance. Non-incorporation of analyzed carboxylate ions can happen due to the symmetry requirement of the sites inside the OCP structure. It is possible that they do not have a compatible anion charge and geometry for connecting pairs of calcium ions through the water layer of OCP [206]. A follow up study was done to expand the range of the types of carboxylic acids that can be incorporated into OCP. Pyromellitic acid (1,2,4,5-benzenetetracarboxylic acid), which is a type of tetracarboxylic acid, was successfully intercalated into OCP by a wet chemical method [183]. It exhibited impartment of fluorescent properties of OCP which can be beneficial for the development of a theranostic materials [183]. Even with the size restrictions, and a narrow window of opportunity, Yokoi et al. recently managed to incorporate a tetravalent carboxylic acid (pyromellitic acid) into OCP [186]. They also confirmed that combination of pyromellitic acid and OCP produced blue emission under UV light, which could enable the development of a theranostic material used in bone repair and fluorescence diagnosis. Detailed description of the site positions of possible incorporations of carboxylic ions can be found in the study by Marković et al. [207].

Ion substitution was, at this point, the most used approach of functionalization of OCP in order to control its biocompatibility and influence stability. The summary of ions applied, and their respective effective outcome is presented in the Fig. 13.

7.2. Octacalcium phosphate/bisphosphonate drug delivery system

The bisphosphonates (BPs) are highly potent and have a wide array of beneficial effects. The mechanism they inhibit in the mevalonate pathway, which blocks many osteoclast activities, is supposedly the key factor for their direct antitumor effect [84]. In addition, they are employed for the regulation of discrepancy between osteoblast bone formation and disproportionate osteoclast bone resorption, leading to the antiosteoporotic effect [84]. Similar effect of chelation to CaP bioceramics and enhancement of bone regeneration *in vivo*, has been observed with calcium-binding bone morphogenetic protein 2 (BMP-2) [212], and with a synergistic effect of alendronate and BMP-2 [213]. In the work done by Forte and colleagues [84], OCP was functionalized with BPs, more precisely zoledronate (ZOL) and alendronate (AL). After the OCP was synthesized by a precipitation method, ZOL and AL were added separately dropwise over a period of 10 min. The incorporation of the AL did not alter the OCP lattice constants and the XRD patterns were almost consistent with the ones from pure OCP. However, the crystals have exhibited a small reduction in size when it comes to the dimensions. XRD results for ZOL were different and the presence of another phase was shown, corresponding to the calcium zoledronate [84]. With this procedure, they concluded that the OCP was stabilized due to presence of the drugs. When it comes to the effect on the osteoblast viability and differentiation, AL and ZOL enhance the production of the osteocalcin, collagen type I and osteoprotegerin (OPG). Human monocyte (OC) and human umbilical vein endothelial cells' (HUVEC) viability and differentiation was inhibited, indicating that ZOL and AL preserved their antiresorptive and anti-tumor properties within the OCP [84]. The ability of alendronate to interact with the calcium from OCP and a beneficial effect it has on the enhancement of osteoblast differentiation and activity, was further examined by Boanini's team [83,189]. Emphasis was also given to the inhibition of osteoclast proliferation. OCP coating on titanium substrates obtained by matrix assisted pulsed laser evaporation (MAPLE) technique was observed for antiresorptive effect [83]. Characterisation of the OCP coatings revealed the characteristic XRD maxima of OCP at 4.7 degrees 2θ, which indicates the presence of OCP as a single phase. Additionally, 20 mM calcium alendronate monohydrate (cAL20) at 9.1 degrees 2θ was observed, which is characteristic for samples with AL content. Meanwhile, rod-like crystals together with cauliflower-like aggregates were found with scanning electron microscopy (SEM) [83]. Similar observation regarding

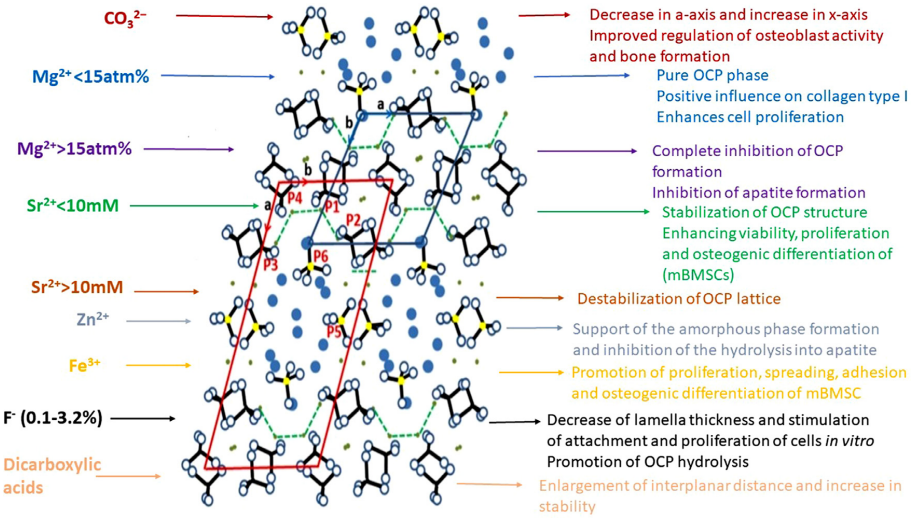

Fig. 13. Effects of the different ions on octacalcium phosphate. OCP structure reprinted from reference [75], with permission from Elsevier.

the beneficial effect on osteoblast differentiation and osteoclast resorption, was made in a different research done by Boanini's group [189]. This being a clear indicator of the synergistic impact OCP-AL demonstrates.

7.3. Alternative functionalization of octacalcium phosphate

7.3.1. Ibuprofen molecules

In the research done by Li et al. [181], OCP and HAp synthesized by a facile hydrothermal method were used as carriers for ibuprofen (IBU) molecules. IBU is considered as a nonsteroidal anti-inflammatory drug with short biological half-life (2 h) and good pharmacological activity. The hydrothermal method in presence of glutamic acid, hydrophobic drug molecules and urea, was used as a way to regulate the crystallization behavior of OCP. Also they increased its reaction yield, which in return provided ample binding sites for adsorption of drug molecules. Significant impact of urea was observed on the crystal formation of OCP, as well as on its conversion to HAp phase. Generation of OH^- ions resulted in accumulated output of HPO_4^{2-} and PO_4^{3-} ions. This enlarged the supersaturation degree of OCP, favoring the fast nucleation rate over the growth rate of crystal [181]. The addition of urea was also beneficial for IBU regarding its solubility and good adsorption rate, due to an extraordinarily high specific surface area which ensured a big number of binding sites for the loading of drug molecules [181]. Higuchi model was used to describe the release kinetics of IBU from the materials that contained more than 25 wt.% of the drug, displaying a sustained release. The maximum amount of released drug in PBS was 262.9 mg/g for OCP and 223.5 mg/g for HAp. Furthermore, the drug release for HAp was much faster. 50% of IBU was released after 30 min, and total release was reached after 24h. OCP, on the other hand, exhibited the release of 10% of adsorbed IBU after 30 min, and the remaining 90 % slowly during 36 h. Obtaining the nanostructured OCP has been proposed as a promising direction in material science [51]. Yang et al. tried to steer and modulate the structure using cetyltrimethylammonium bromide (CTAB), which was used due to its high potential of forming vesicles over the value of critical micelle concentration (CMC) and capacity to transform lamellar structures [51]. CTAB acts as a surfactant and topical antiseptic. CTAB was used on more than one instance to produce nanofibers [214,215], and in the work mentioned, through molecule-assisted wet-chemical method, OCP nanobelts were obtained without impurities. OCP nanobelts displayed a highly favored orientation along the particular (100) direction, which is a sign of anisotropic growth resulting in the good phase purity and a high degree of crystallinity [51]. As opposed to the hydrothermal method of synthesis, CTAB, in combination with wet-chemical process showed that crystal growth of OCP was dependent on concentration of CTAB. It was observed that the increase led to the formation of lamellar micelles structures and preservation of the OCP long nanobelts. Alendronate sodium (AS) was used as an antiresorptive drug molecule within proposed OCP nanobelt system. OCP demonstrated exceptional affinity towards the AS and it displayed a 2-fold and 4-fold increase in AS adsorption, which is higher in comparison to thermolyzed HAp nanobelts [51]. Research done by Yang and his team should be considered as highly valuable since it demonstrated the possibility of attaining pure OCP nanostructures that can be used as a lucrative therapeutic drug carriers.

7.3.2. Methotrexate

Slow release of an antineoplastic agent, methotrexate (MTX), was tested in combination with OCP [216]. Different amounts of MTX (2, 4 and 6%) were incorporated in OCP for testing *in vitro* and *in vivo* pharmacokinetics and biocompatibility of the construct. Hardness (daN) of the implants decreased with increase of their MTX content. The amounts of released drug in *in vitro* conditions, rose to 95.2%, 68.3% and 71.9% for granules containing 2%, 4% or 6% of MTX, respectively. In *in vivo* conditions, 75% of the drug remained after 24h, and 25% after 7 days. After 4 months osteogenesis was observed in fibrous tissue. A mixture of OCP and HAp was investigated by Ito's research group as a new potential drug carrier for targeting bone cancer with MTX [190]. They postulated that OCP releases the drug during the transformation into HAp and, in addition, they synthesized it into a spherical porous granular shape (1000μm). The obtained construct was able to load and retain the drug with the release profile being continuous for at least 48 h. Furthermore, the human osteosarcoma (HOS) cell proliferation was significantly inhibited [190].

7.3.3. Ascorbic acid phosphate

The effect of ascorbic acid phosphate (AscP), an osteogenesis-promoting drug, was also closely investigated on spherical porous granules of OCP and HAp [191]. When the concentration of AscP was less than or equal to 0.1 mM, the formation of the granules was successful. High amount of the loaded AscP (3.1 μmol/g) on the granules showed slow-release profile in pH 7.4 buffer solution with the concentration reaching to 0.019 mM after 7 days. ALP activity was significantly enhanced and the differentiation of the osteoblast-like cells was promoted due to the AscP hydrolysis to ascorbic acid [191].

7.3.4. Silver nanoparticles

Another important issue that needs to be addressed is bacterial infection of orthopedic implants. In another work done by Forte and her colleagues, OCP was functionalized with silver nanoparticles (AgNPs), using polydopamine (PDA), to trigger the deposition of AgNPs to the PDA functionalized OCP [192]. Moreover, they compared OCP and α-TCP, demonstrating benefits that OCP exhibits as a potential DDS. Morphology plays a vital role in the amount of PDA deposited onto a certain CaP [192]. Albeit α-TCP porous particles can load more PDA than OCP flat crystals, in OCP it is spread throughout the entire surface area. PDA in α-TCP, clusters into aggregates, which leads to a greater, more homogeneous distribution of AgNPs in OCP. Compositions exhibited a remarkable antibacterial activity against three Gram positive (*S. aureus, S. epidermidis, E. faecalis*) and three Gram negative (*E. coli, K. pneumoniae and P. aeruginosa*) reference strains, following a 24 h incubation period. OCPdAg5 and αTCPdAg5 (8.2 and 4.7% content of AgNPs, respectively) were selected as they have proven themselves as the most efficient against bacterial growth without cytotoxicity on osteoblasts and without interference with osteoblast proliferation and activity [192]. In the study done by Sugiura et al. [217], approximately 10 mmol/L of Ag^{+} was incorporated in OCP. It demonstrated antibacterial activity towards *S. aureus, Escherichia coli, and Streptococcus mutans*, slight change in color, and low cytotoxicity toward undifferentiated MC3T3-E1 cells and differentiated MC3T3-E1 osteoblastic cell line.

7.3.5. Amino acids

In a recent study performed by Josipovic et al. [218], the influence of different amino acids (L-lysine, Lys; L-aspartic acid, Asp; L-serine, Ser; L-tyrosine,Tyr; L-asparagine, Asn; and L-phenylalanine, Phe) on the formation of OCP seed crystals in metastable solution at pH 7.4 was examined. The overall influence on the structure of OCP varied from inhibition to promotion.Phe indicated the greatest promotion effect of calcium-deficient apatite, which was credited to the establishment of its aggregates in a solution and Ser was shown to be the most efficient inhibitor of precipitation of a crystalline phase.

8. Future directions and conclusions

Being one of the main components of the bone tissue, CaPs have been deployed in a great number of applications throughout the field of bone tissue engineering. Their importance lies in the possibility to provide calcium and phosphate ions, which are essential for the regulation of bone deposition and bone resorption [26]. Calcium and phosphate homeostasis depends on a complex, closely regulated system that involves various ions (Ca, P, Mg), hormones (calciotropic hormones, parathyroid hormone etc.), vitamin D, growth factors and other compounds. The regulation is maintained by the entwined actions in the intestine, kidneys and bone [219,220]. In addition to the biocompatibility and biodegradability they offer, CaPs are used for drug delivery purposes affecting the reducibility of dosage and frequency of administration. This in returnauses fewer side effects [59]. They are relatively easy to prepare and they have satisfying storage capacities. When compared to other drug delivery constructs, CaPs are more stable than liposomes and they exhibit less toxicity than silica and carbon nanotubes [59]. All these intrinsic properties work together to ensure a more controlled and reliable drug delivery. Nevertheless, achieving a satisfying loading capacity and a more tunable drug-release profile remains a significant challenge.

Among different orthophosphates, OCP has been securing the position of the most promising one for bone tissue regeneration. As OCP is thought to be the precursor phase for apatite formation, it has been used in a different set of studies. Additional benefit OCP elucidates is the rapid conversion to the apatite form, upon implantation. The end goals were to achieve maximum refinement of the OCP structure itself and to examine the effect it has on the surrounding environment. The possibility to obtain OCP at room temperature through different routes like hydrolysis or precipitation opened the feasibility to influence drug loading and drug release patterns. At the same time a high specific surface area and different set of morphologies of OCP crystals was provided, making them more effective and more favorable in regard to cell responses. Layered OCP structure composed of apatitic layers and hydrated layers, makes the ion and drug incorporation within the structure feasible. The hydrolysis of OCP transpires through a myriad of ion adsorption and exchange processes, which have been assumed to have an effect on the biological outcome, both *in vivo* and *in vitro* settings. Exchange of the HPO_4^{2-} ions is a prime example of the series of actions that determine the conversion of OCP to calcium deficient hydroxyapatite (CDHAp), and in the same time, it affects the biological response of OCP. Nonetheless, however beneficial, the unique structure OCP has, sets forth the challenge in differentiation and establishment of the pure phase. Due to that fact, even if genesis of pure OCP is successful, further complications arise, as OCP is virtually indiscernible from CDHAp. Techniques enclosed in the literature, such as X-Ray diffraction (XRD), Fourier Transformation Infrared Spectroscopy (FT-IR), Nuclear Magnetic Resonance (NMR) and Raman Spectroscopy, do a stellar job of confirming the presence of OCP, but they lack the quantification potential. Utilization of any one of these techniques will show OCP characteristics, attributed only to it, but multi-technique approach is needed to unambiguously claim the phase purity of the obtained product.

The biological influence OCP has in bone regeneration has been first noted more than half a century ago. Since then many studies have tried to pinpoint the exact reason why OCP has an upper hand in comparison to the other CaPs. Existence of a hydrated layer, presence of HPO_4^{2-} ions, simple conversion to HAp or all of the above, have generated the osteoconductive and, in certain cases, osteoinductive response of OCP in *in vivo* settings. When compared to other biologically relevant CaPs (e.g., HAp and β-TCP), OCP has shown to be the most resorbable one, thus enhancing bone formation substantially more (63.3 ± 7.52 OCP, 42.8 ± 13.6 β-TCP, and 24.2 ± 7.82 HAp). Additional asset that has been recorded is the pronounced effect OCP mixtures had, in comparison to the individual implants (e.g., 8 weeks postimplantation radiopacity of 25OCP/75ACP mixture was 63.2 ± 11.8%). With every new research being published, OCP has been continuously proving itself highly valuable in bone formation, while at the same time it has been supporting the migration and proliferation of cells and it facilitated angiogenesis. The indicated precedents are paving the way for future investigations in these directions.

Furthermore, incorporation of molecules in the hydrated layer can ensure a slow-release profile, whilst opening a variety of possibilities for OCP as a vehicle in different drug delivery approaches. Special attention should be given to the possibility of utilizing OCP as a local drug delivery instrument. Up until now, the research

done on this subject was mostly in relation to diverse ion influence and the effect of bisphosphonates (BPs). Bone regeneration has been further promoted with the use of carbonate ions, divalent and trivalent cations i.e., Mg^{2+}, Sr^{2+} and Fe^{3+}, while from the halogens, fluoride has been utilized to achieve the ameliorating effect. A positive influence on enhanced cell proliferation (osteoblast-like MG63 cells, MC3T3-E1 cells and mBMSC) and accelerated angiogenesis (FeOCP/PLGA scaffold) was noticed with Mg^{2+}, Sr^{2+} and Fe^{3+} loaded OCP. Even more, when ion substituted OCP was compared with pure OCP, increased proliferation of mouse bone marrow stromal ST-2 cells and the amount of the adsorbed BSA was higher than with the undoped OCP. In addition to the biological response wanted from the intercalation, the incorporation of active substances can maneuver the crystal structure of OCP. Mg^{2+} ions have demonstrated the ability of modulating the growth of OCP crystals, while Sr^{2+} ions and succinate ions have been proven to stabilize the OCP structure. On the other hand the incorporation of Mg^{2+}, inhibits the conversion of OCP to HAp, while F^{-} stimulates it, yielding more crystalline products.

Drug loading on OCP, in a great extent, has been focused on the effect alendronate and zolendronate exhibit, as they have antiresorptive and anti-tumor properties. Both bisphosphonates enhanced the production of the osteocalcin, collagen type I and osteoprotegerin (OPG), as well as improved osteoblast differentiation and osteoclast resorption. Another postulate of the local drug delivery has been observed with OCP, which is prolonged drug release. Ibuprofen molecules and methotrexate have exhibited slow release over a certain time period, while methotrexate loaded OCP, in *in vivo* conditions, manifested osteogenesis in fibrous tissue. Having all the information summarized within the manuscript, a synergistic approach of different set of drugs and OCP will be worth investigating in future studies. The main objective should be understanding the background of the seamlessly running cascade of actions leading to the bone regeneration.

Even though functionalized OCP crystals demonstrated high potential and are thought to be the future of personalized drug delivery systems, the paucity of information on the complete release profile *in vitro*, the aftermath of the behavior in *in vivo* settings and their correlations and ramifications is evident. One reason for this could be the difficulty of obtaining pure OCP phase, while at the same time maintaining the successful biologically active ion/molecule delivery system. To our knowledge, no research team has been able to provide the quantifiable data regarding the aforementioned issue. Additionally, in the interest of clarifying the mechanisms behind the OCP enhancement of osteoblast differentiation and cell conversion to osteocytes, broader experiments need to be conducted. These studies should encompass the entire progress, starting from the synthesis method and its outcome regarding the size, roughness and particle morphology, different ways of drug loading and induced changes in the structure. Followed by potential applicability as a unique carrier for delivery or diagnostic monitoring purposes. Bearing in mind the demonstrated significance of OCP over other biologically relevant CaP, the above-mentioned difficulties should not hinder the future progress and development of this outstanding drug delivery system. Moreover, the authors believe that attributes like existence of the water layer, presence of HPO_4^{2-} ions, fast conversion to CDHAp and the response it elicits from the cells, outweigh the challenges OCP can cause in the entire process.

Funding

This work was supported by the European Union's Horizon 2020 research and innovation programme under the Marie Skłodowska-Curie grant agreement [No 860462 (PREMUROSA)] and European Union's Horizon 2020 research and innovation programme [under the grant agreement No 857287 (BBCE)].

Declaration of Competing Interest

Authors do not have any conflicts of interest to declare.

Acknowledgment

Authors would like to thank Clara Barbut for her help in the creative process of making the graphical visualization.

References

[1] W. Habraken, P. Habibovic, M. Epple, M. Bohner, Calcium phosphates in biomedical applications: materials for the future? Mater. Today 19 (2016) 69–87, doi:10.1016/j.mattod.2015.10.008.
[2] T. Albrektsson, C. Johansson, Osteoinduction, osteoconduction and osseointegration, Eur. Spine J. 10 (2001) 96–101.
[3] T. Ariizumi, H. Kawashima, H. Hatano, T. Yamagishi, N. Oike, Osteoinduction and osteoconduction with porous beta-tricalcium phosphate implanted after fibular resection in humans, J. Biomater. Nanobiotechnol. 10 (2019) 159–173, doi:10.4236/jbnb.2019.103009.
[4] L. Lin, K.L. Chow, Y. Leng, Study of hydroxyapatite osteoinductivity with an osteogenic differentiation of mesenchymal stem cells, J. Biomed. Mater. Res. Part A (2008), doi:10.1002/jbm.a.31994.
[5] H. Kim, S. Mondal, S. Bharathiraja, P. Manivasagan, M.S. Moorthy, J. Oh, Optimized Zn-doped hydroxyapatite/doxorubicin bioceramics system for efficient drug delivery and tissue engineering application, Ceram. Int. 44 (2018) 6062–6071, doi:10.1016/j.ceramint.2017.12.235.
[6] M.C. Rodrigues, T.L.R. Hewer, G.E. De Souza Brito, V.E. Arana-Chavez, R.R. Braga, Calcium phosphate nanoparticles functionalized with a dimethacrylate monomer, Mater. Sci. Eng. C 45 (2014) 122–126, doi:10.1016/j.msec.2014.08.066.
[7] B.N. Sathy, D. Olvera, T. Gonzalez-Fernandez, G.M. Cunniffe, S. Pentlavalli, P. Chambers, O. Jeon, E. Alsberg, H.O. McCarthy, N. Dunne, T.L. Haut Donahue, D.J. Kelly, RALA complexed α-TCP nanoparticle delivery to mesenchymal stem cells induces bone formation in tissue engineered constructs in vitro and in vivo, J. Mater. Chem. B 5 (2017) 1753–1764, doi:10.1039/c6tb02881k.
[8] K. Madhumathi, T.S. Sampath Kumar, Effect of structure and composition on ibuprofen drug delivery by calcium phosphate nanocarriers, Key Eng. Mater. 529–530 (2013) 495–500, doi:10.4028/www.scientific.net/KEM.529-530.495.
[9] R. Sun, M. Åhlén, C.W. Tai, É.G. Bajnóczi, F. de Kleijne, N. Ferraz, I. Persson, M. Strømme, O. Cheung, Highly porous amorphous calcium phosphate for drug delivery and bio-medical applications, Nanomaterials 10 (2020) 1–18, doi:10.3390/nano10010020.
[10] H.W. Kim, J.C. Knowles, H.E. Kim, Hydroxyapatite/poly(ε-caprolactone) composite coatings on hydroxyapatite porous bone scaffold for drug delivery, Biomaterials 25 (2004) 1279–1287, doi:10.1016/j.biomaterials.2003.07.003.
[11] J. Chou, T. Ito, D. Bishop, M. Otsuka, B. Ben-Nissan, B. Milthorpe, Controlled release of simvastatin from biomimetic β-TCP drug delivery system, PLoS One 8 (2013) 2–7, doi:10.1371/journal.pone.0054676.
[12] D. Loca, J. Locs, K. Salma, J. Gulbis, I. Salma, L. Berzina-Cimdina, Porous hydroxyapatite bioceramic scaffolds for drug delivery and bone regeneration, IOP Conf. Ser. Mater. Sci. Eng. 18 (2011), doi:10.1088/1757-899X/18/19/192019.
[13] M. Zhu, H. Wang, J. Liu, H. He, X. Hua, Q. He, L. Zhang, X. Ye, J. Shi, A mesoporous silica nanoparticulate/β-TCP/BG composite drug delivery system for osteoarticular tuberculosis therapy, Biomaterials 32 (2011) 1986–1995, doi:10.1016/j.biomaterials.2010.11.025.
[14] P.I. Sealy, C. Nguyen, M. Tucci, H. Benghuzzi, J.D. Cleary, Delivery of antifungal agents using bioactive and nonbioactive bone cements, Ann. Pharmacother. 43 (2009) 1606–1615, doi:10.1345/aph.1M143.
[15] M. Stigter, K. De Groot, P. Layrolle, Incorporation of tobramycin into biomimetic hydroxyapatite coating on titanium, Biomaterials 23 (2002) 4143–4153, doi:10.1016/S0142-9612(02)00157-6.
[16] D.R. Bienek, D. Skrtic, Utility of amorphous calcium phosphate-based scaffolds in dental/biomedical applications, Biointerface Res. Appl. Chem. 7 (2017) 1989–1994.
[17] T.J. Brunner, R.N. Grass, M. Bohner, W.J. Stark, Effect of particle size, crystal phase and crystallinity on the reactivity of tricalcium phosphate cements for bone reconstruction, J. Mater. Chem. 17 (2007) 4072–4078, doi:10.1039/b707171j.
[18] M. Bohner, Reactivity of calcium phosphate cements, J. Mater. Chem. 17 (2007) 3980–3986, doi:10.1039/b706411j.
[19] J. Barralet, U. Gbureck, P. Habibovic, E. Vorndran, C. Gerard, C.J. Doillon, Angiogenesis in calcium phosphate scaffolds by inorganic copper ion release, Tissue Eng. - Part A 15 (2009) 1601–1609, doi:10.1089/ten.tea.2007.0370.
[20] R. Meißner, L. Bertol, M.A.U. Rehman, L.A.L. dos Santos, A.R. Boccaccini, Bioprinted 3D calcium phosphate scaffolds with gentamicin releasing capability, Ceram. Int. 45 (2019) 7090–7094, doi:10.1016/j.ceramint.2018.12.212.
[21] H. Noukrati, S. Cazalbou, I. Demnati, C. Rey, A. Barroug, C. Combes, Injectability, microstructure and release properties of sodium fusidate-loaded apatitic

cement as a local drug-delivery system, Mater. Sci. Eng. C 59 (2016) 177–184, doi:10.1016/j.msec.2015.09.070.
[22] G.S. Lee, J.H. Park, U.S. Shin, H.W. Kim, Direct deposited porous scaffolds of calcium phosphate cement with alginate for drug delivery and bone tissue engineering, Acta Biomater. 7 (2011) 3178–3186, doi:10.1016/j.actbio.2011.04.008.
[23] E. O'Neill, G. Awale, L. Daneshmandi, O. Umerah, K.W.H. Lo, The roles of ions on bone regeneration, Drug Discov. Today 23 (2018) 879–890, doi:10.1016/j.drudis.2018.01.049.
[24] A. Laskus, J. Kolmas, Ionic substitutions in non-apatitic calcium phosphates, Int. J. Mol. Sci. 18 (2017) 1–22, doi:10.3390/ijms18122542.
[25] S.H. Lin, W.J. Zhang, X.Q. Jiang, Applications of bioactive ions in bone regeneration, Chin. J. Dent. Res. 22 (2019) 93–104, doi:10.3290/j.cjdr.a42513.
[26] T.J. Levingstone, S. Herbaj, N.J. Dunne, Calcium phosphate nanoparticles for therapeutic applications in bone regeneration, Nanomaterials 9 (2019) 1–22, doi:10.3390/nano9111570.
[27] M. Parent, H. Baradari, E. Champion, C. Damia, M. Viana-Trecant, Design of calcium phosphate ceramics for drug delivery applications in bone diseases: a review of the parameters affecting the loading and release of the therapeutic substance, J. Control. Release 252 (2017) 1–17, doi:10.1016/j.jconrel.2017.02.012.
[28] S. Bose, S. Tarafder, Calcium phosphate ceramic systems in growth factor and drug delivery for bone tissue engineering: a review, Acta Biomater. 8 (2012) 1401–1421, doi:10.1016/j.actbio.2011.11.017.
[29] I. Roy, S. Mitra, A. Maitra, S. Mozumdar, Calcium phosphate nanoparticles as novel non-viral vectors for targeted gene delivery, Int. J. Pharm. 250 (2003) 25–33, doi:10.1016/S0378-5173(02)00452-0.
[30] B. Peter, D.P. Pioletti, S. Laïb, B. Bujoli, P. Pilet, P. Janvier, J. Guicheux, P.Y. Zambelli, J.M. Bouler, O. Gauthier, Calcium phosphate drug delivery system: influence of local zoledronate release on bone implant osteointegration, Bone 36 (2005) 52–60, doi:10.1016/j.bone.2004.10.004.
[31] S. Radin, J.T. Campbell, P. Ducheyne, J.M. Cuckler, Calcium phosphate ceramic coatings as carriers of vancomycin, Biomaterials 18 (1997) 777–782, doi:10.1016/S0142-9612(96)00190-1.
[32] B. Kundu, C. Soundrapandian, S.K. Nandi, P. Mukherjee, N. Dandapat, S. Roy, B.K. Datta, T.K. Mandal, D. Basu, R.N. Bhattacharya, Development of new localized drug delivery system based on ceftriaxone-sulbactam composite drug impregnated porous hydroxyapatite: a systematic approach for in vitro and in vivo animal trial, Pharm. Res. 27 (2010) 1659–1676, doi:10.1007/s11095-010-0166-y.
[33] P. Comeau, M. Filiaggi, A two-stage cold isostatic pressing and gelling approach for fabricating a therapeutically loaded amorphous calcium polyphosphate local delivery system, J. Biomater. Appl. 32 (2017) 126–136, doi:10.1177/0885328217708639.
[34] L. Fan, Y. Zhang, R. Hu, C. Lin, W. Shi, Z. Tian, Strontium substituted octacalcium phosphate coatings by electrochemical deposition and their dose-dependent bioactivities, Mater. Lett. 272 (2020) 127844, doi:10.1016/j.matlet.2020.127844.
[35] A. Szewczyk, A. Skwira, M. Ginter, D. Tajer, M. Prokopowicz, Microwave-assisted fabrication of mesoporous silica-calcium phosphate composites for dental application, Polymers (Basel) 13 (2021) 1–17, doi:10.3390/polym13010053.
[36] G. Goldschmidt, M. Krok-borkowicz, R. Zybała, R. Telle, G. Conrads, K. Schickle, Biomimetic in situ precipitation of calcium phosphate containing silver nanoparticles on zirconia ceramic materials for surface functionalization in terms of antimicrobial and osteoconductive properties, Dent. Mater. 37 (2020) 10–18, doi:10.1016/j.dental.2020.09.018.
[37] T. Tagami, E. Kuwata, N. Sakai, T. Ozeki, Drug incorporation into polymer filament using simple soaking method for tablet preparation using fused deposition modeling, Biol. Pharm. Bull. 42 (2019) 1753–1760.
[38] V. Tsikourkitoudi, J. Karlsson, P. Merkl, E. Loh, B. Henriques-normark, G.A. Sotiriou, Flame-made calcium phosphate nanoparticles with high drug loading for delivery of biologics, Molecules 25 (2020) 1747–1764.
[39] C.S. Id, N. Heriberto, A. Camargo, E. Gemelli, Crystallization of carboplatin-loaded onto microporous calcium phosphate using high- vacuum method : characterization and release study, PLoS One 15 (2020) 1–23, doi:10.1371/journal.pone.0242565.
[40] O. Suzuki, Octacalcium phosphate (OCP)-based bone substitute materials, Jpn. Dent. Sci. Rev. 49 (2013) 58–71, doi:10.1016/j.jdsr.2013.01.001.
[41] Y. Honda, T. Anada, S. Kamakura, S. Morimoto, T. Kuriyagawa, O. Suzuki, The effect of microstructure of octacalcium phosphate on the bone regenerative property, Tissue Eng. - Part A 15 (2009) 1965–1973, doi:10.1089/ten.tea.2008.0300.
[42] R.Z. LeGeros, Rapid communication preparation of octacalcium phosphate (OCP): a direct fast method, Calcif. Tissue Int. (1985) 194–197.
[43] S. Graham, P.W. Brown, Reactions of octacalcium phosphate to form hydroxyapatite, J. Cryst. Growth 165 (1996) 106–115, doi:10.1016/0022-0248(95)00994-9.
[44] X. Yang, L. Zhang, X. Chen, G. Yang, L. Zhang, C. Gao, H. Yang, Z. Gou, Trace element-incorporating octacalcium phosphate porous beads via polypeptide-assisted nanocrystal self-assembly for potential applications in osteogenesis, Acta Biomater. 8 (2012) 1586–1596, doi:10.1016/j.actbio.2011.12.012.
[45] T. Yu, S. Zeng, X. Liu, H. Shi, J. Ye, C. Zhou, Application of Sr-doped octacalcium phosphate as a novel Sr carrier in the α-tricalcium phosphate bone cement, Ceram. Int. 43 (2017) 12579–12587, doi:10.1016/j.ceramint.2017.06.135.
[46] S. Graham, P.W. Brown, The low temperature formation of octacalcium phosphate, J. Cryst. Growth 132 (1993) 215–225, doi:10.1016/0022-0248(93)90265-X.
[47] A. Bigi, E. Boanini, R. Botter, S. Panzavolta, K. Rubini, α-Tricalcium phosphate hydrolysis to octacalcium phosphate: effect of sodium polyacrylate, Biomaterials 23 (2002) 1849–1854, doi:10.1016/S0142-9612(01)00311-8.
[48] G. Tripathi, T. Miyazaki, Synthesis and in vitro biodegradation of pure octacalcium phosphate spheres, Int. J. Appl. Ceram. Technol. 17 (2020) 372–379, doi:10.1111/ijac.13371.
[49] A.Y. Fedotov, V.S. Komlev, A.Y. Teterina, V.P. Sirotinkin, V.F. Shamrai, I.V. Fadeeva, S.M. Barinov, Preparation of octacalcium phosphate from calcium carbonate powder, Inorg. Mater. 49 (2013) 1148–1151, doi:10.1134/S0020168513110058.
[50] V.F. Shamrai, A.E. Karpikhin, A.Y. Fedotov, V.P. Sirotinkin, S.M. Barinov, V.S. Komlev, Structural changes during the hydrolysis of dicalcium phosphate dihydrate to octacalcium phosphate and hydroxyapatite, Inorg. Mater. 51 (2015) 355–361, doi:10.1134/S0020168515040147.
[51] X. Yang, X. Gao, Y. Gan, C. Gao, X. Zhang, K. Ting, B.M. Wu, Z. Gou, Facile synthesis of octacalcium phosphate nanobelts: growth mechanism and surface adsorption properties, J. Phys. Chem. C 114 (2010) 6265–6271, doi:10.1021/jp911576f.
[52] L.C.Chow, E.D. Eanes, Octacalcium phosphate, 2001. https://doi.org/10.1007/springerreference_39293.
[53] K. Wang, Y. Leng, X. Lu, F. Ren, X. Ge, Study of protein adsorption on octacalcium phosphate surfaces by molecular dynamics simulations, J. Mater. Sci. Mater. Med. 23 (2012) 1045–1053, doi:10.1007/s10856-012-4570-1.
[54] Q.L. Tang, Y.J. Zhu, J. Wu, F. Chen, S.W. Cao, Calcium phosphate drug nanocarriers with ultrahigh and adjustable drug-loading capacity: one-step synthesis, in situ drug loading and prolonged drug release, Nanomed. Nanotechnol., Biol. Med. 7 (2011) 428–434, doi:10.1016/j.nano.2010.12.005.
[55] S.M. Barinov, V.S. Komlev, Osteoinductive ceramic materials for bone tissue restoration : octacalcium phosphate (review), 1 (2010) 175–181. https://doi.org/10.1134/S2075113310030019.
[56] S.V. Dorozhkin, A review on the dissolution models of calcium apatites, Prog. Cryst. Growth Charact. Mater. 44 (2002) 45–61, doi:10.1016/S0960-8974(02)00004-9.
[57] S. V. Dorozhkin, Calcium orthophosphates (CaPO4): occurrence and properties, 2016. https://doi.org/10.1007/s40204-015-0045-z.
[58] K. Rubenis, S. Zemjane, J. Vecstaudza, J. Bitenieks, J. Locs, Densification of amorphous calcium phosphate using principles of the cold sintering process, J. Eur. Ceram. Soc. 41 (2021) 912–919, doi:10.1016/j.jeurceramsoc.2020.08.074.
[59] V. Uskoković, D.P. Uskoković, Nanosized hydroxyapatite and other calcium phosphates: chemistry of formation and application as drug and gene delivery agents, J. Biomed. Mater. Res. - Part B Appl. Biomater. 96 B (2011) 152–191, doi:10.1002/jbm.b.31746.
[60] A. Nakahira, S. Aoki, K. Sakamoto, S. Yamaguchi, Synthesis and evaluation of various layered octacalcium phosphates by wet-chemical processing, J. Mater. Sci. Mater. Med. 12 (2001) 793–800, doi:10.1023/A:1017968818168.
[61] B.O. Fowler, M. Marković, W.E. Brown, Octacalcium phosphate. 3. Infrared and Raman vibrational spectra, Chem. Mater. 5 (1993) 1417–1423, doi:10.1021/cm00034a009.
[62] O. Suzuki, G. Insley, Octacalcium phosphate biomaterials, Woodhead Publishing Ser. Biomater. (2020).
[63] A.A. Tsyganova, O.A. Golovanova, Role of Mg2+, Sr2+, and F– ions in octacalcium phosphate crystallization, Inorg. Mater. 53 (2017) 1261–1269, doi:10.1134/S0020168517120184.
[64] F. Barrère, P. Layrolle, C.A. Van Blitterswijk, K. De Groot, Biomimetic calcium phosphate coatings on Ti6Al4V: a crystal growth study of octacalcium phosphate and inhibition by Mg2+ and HCO3-, Bone 25 (1999), doi:10.1016/S8756-3282(99)00145-3.
[65] K. Matsunaga, First-principles study of substitutional magnesium and zinc in hydroxyapatite and octacalcium phosphate, J. Chem. Phys. 128 (2008) 1–11, doi:10.1063/1.2940337.
[66] E. Boanini, P. Torricelli, M. Fini, F. Sima, N. Serban, I.N. Mihailescu, A. Bigi, Magnesium and strontium doped octacalcium phosphate thin films by matrix assisted pulsed laser evaporation, J. Inorg. Biochem. 107 (2012) 65–72, doi:10.1016/j.jinorgbio.2011.11.003.
[67] E. Boanini, M. Gazzano, K. Rubini, A. Bigi, Collapsed octacalcium phosphate stabilized by ionic substitutions, (2010). https://doi.org/10.1021/cg100494f.
[68] H. Shi, X. Ye, T. Wu, J. Zhang, J. Ye, Regulating the physicochemical and biological properties in vitro of octacalcium phosphate by substitution with strontium in a large doping range, Mater. Today Chem. 5 (2017) 81–91, doi:10.1016/j.mtchem.2017.07.003.
[69] K. Matsunaga, H. Murata, Strontium substitution in bioactive calcium phosphates: a first-principles study, J. Phys. Chem. B. 113 (2009) 3584–3589, doi:10.1021/jp808713m.
[70] H. Shi, F. He, J. Ye, Synthesis and structure of iron- and strontium-substituted octacalcium phosphate: effects of ionic charge and radius, J. Mater. Chem. B 4 (2016) 1712–1719, doi:10.1039/c5tb02247a.
[71] H. Shi, X. Ye, J. Zhang, T. Wu, T. Yu, C. Zhou, J. Ye, A thermostability perspective on enhancing physicochemical and cytological characteristics of octacalcium phosphate by doping iron and strontium, Bioact. Mater. 6 (2021) 1267–1282, doi:10.1016/j.bioactmat.2020.10.025.
[72] M. Iijima, D.G.A. Nelson, Y. Pan, A.T. Kreinbrink, M. Adachi, T. Goto, Y. Moriwaki, Fluoride analysis of apatite crystals with a central planar OCP inclu-

sion : concerning the role of F – ions on apatite /OCP / apatite structure formation, Calcif Tissue Int. 4 (1996) 377–384.
[73] Y. Honda, T. Anada, S. Morimoto, Y. Shiwaku, O. Suzuki, Effect of Zn2+ on the physicochemical characteristics of octacalcium phosphate and its hydrolysis into apatitic phases, Cryst. Growth Des. 11 (2011) 1462–1468, doi:10.1021/cg1009835.
[74] A. Bigi, M. Gazzano, A. Ripamonti, N. Roveri, Effect of foreign ions on the conversion of brushite and octacalcium phosphate into hydroxyapatite, J. Inorg. Biochem. 32 (1988) 251–257, doi:10.1016/0162-0134(88)85004-9.
[75] C.C. Rey, C. Combes, C. Drouet, Synthesis and physical chemical characterizations of octacalcium phosphate-based biomaterials for hard-tissue regeneration, 2019. https://doi.org/10.1016/B978-0-08-102511-6.00008-X.
[76] W. Pompe, H. Worch, W.J.E.M. Habraken, P. Simon, R. Kniep, H. Ehrlich, P. Paufler, Octacalcium phosphate - a metastable mineral phase controls the evolution of scaffold forming proteins, J. Mater. Chem. B 3 (2015) 5318–5329, doi:10.1039/c5tb00673b.
[77] W.E. Brown, J.R. Lehr, J.P. Smith, A. William Frazier, Crystallography of octacalcium phosphate [5], J. Am. Chem. Soc 79 (1957) 5318–5319, doi:10.1021/ja01576a068.
[78] Christophe Drouet, Apatite formation: why it may not work as planned, and how to conclusively identify apatite compounds, Biomed Res. Int. 2013 (2013) Article ID 490946, doi:10.1155/2013/490946.
[79] V.S. Komlev, I.V. Fadeeva, A.S. Fomin, L.I. Shvorneva, D. Ferro, S.M. Barinov, Synthesis of octacalcium phosphate by precipitation from solution, Dokl. Chem. 432 (2010) 178–182, doi:10.1134/S0012500810060066.
[80] H. Shi, J. Zhang, X. Ye, T. Wu, T. Yu, J. Ye, Formation and stability of well-crystallized metastable octacalcium phosphate at high temperature by regulating the reaction environment with carbamide, CrystEngComm 21 (2019) 5174–5184, doi:10.1039/c9ce00677j.
[81] B. Mirhadi, B. Mehdikhani, N. Askari, Synthesis of nano-sized β-tricalcium phosphate via wet precipitation, Process. Appl. Ceram. 5 (2011) 193–198, doi:10.2298/pac1104193m.
[82] A. Rodrigues, A. Lebugle, Behavior in wet atmosphere of an amorphous calcium phosphate with an atomic Ca /P Ratio of 1 . 33, 315 (1999) 308–315.
[83] E. Boanini, P. Torricelli, L. Forte, S. Pagani, N. Mihailescu, C. Ristoscu, I.N. Mihailescu, A. Bigi, Antiresorption implant coatings based on calcium alendronate and octacalcium phosphate deposited by matrix assisted pulsed laser evaporation, Colloids Surf. B Biointerfaces 136 (2015) 449–456, doi:10.1016/j.colsurfb.2015.09.044.
[84] L. Forte, P. Torricelli, E. Boanini, M. Gazzano, M. Fini, A. Bigi, Antiresorptive and anti-angiogenetic octacalcium phosphate functionalized with bisphosphonates: an in vitro tri-culture study, Acta Biomater. 54 (2017) 419–428, doi:10.1016/j.actbio.2017.02.040.
[85] Y. Sai, Y. Shiwaku, T. Anada, K. Tsuchiya, T. Takahashi, O. Suzuki, Capacity of octacalcium phosphate to promote osteoblastic differentiation toward osteocytes in vitro, Acta Biomater. 69 (2018) 362–371, doi:10.1016/j.actbio.2018.01.026.
[86] M. Kamitakahara, H. Okamo, M. Tanihara, C. Ohtsuki, Synthesis of octacalcium phosphate intercalated with dicarboxylate ions from calcium carbonate and phosphoric acid, J. Ceram. Soc. Jpn. 116 (2008) 481–485, doi:10.2109/jcersj2.116.481.
[87] T. Yokoi, T. Goto, T. Kato, S. Takahashi, J. Nakamura, T. Sekino, C. Ohtsuki, M. Kawashita, Hydroxyapatite formation from octacalcium phosphate and its related compounds: a discussion of the transformation mechanism, Bull. Chem. Soc. Jpn. 93 (2020) 701–707, doi:10.1246/bcsj.20200031.
[88] N. Miyatake, K.N. Kishimoto, T. Anada, H. Imaizumi, E. Itoi, O. Suzuki, Effect of partial hydrolysis of octacalcium phosphate on its osteoconductive characteristics, Biomaterials 30 (2009) 1005–1014, doi:10.1016/j.biomaterials.2008.10.058.
[89] O. Suzuki, S. Kamakura, T. Katagiri, Surface chemistry and biological responses to synthetic octacalcium phosphate, J. Biomed. Mater. Res. - Part B Appl. Biomater. 77 (2005) 201–212, doi:10.1002/jbm.b.30407.
[90] O. Suzuki, H. Yagishita, T. Amano, T. Aoba, Reversible structural changes of octacalcium phosphate and labile acid phosphate, J. Dent. Res. 74 (1995) 1764–1769, doi:10.1177/00220345950740110801.
[91] Y. Lai, Y. Huang, H. Wang, J. Huang, Z. Chen, C. Lin, Selective formation of ordered arrays of octacalcium phosphate ribbons on TiO2 nanotube surface by template-assisted electrodeposition, Colloids Surf. B Biointerfaces 76 (2010) 117–122, doi:10.1016/j.colsurfb.2009.10.023.
[92] O. Suzuki, Acta biomaterialia octacalcium phosphate : osteoconductivity and crystal chemistry, Acta Biomater. 6 (2010) 3379–3387, doi:10.1016/j.actbio.2010.04.002.
[93] O. Suzuki, H. Yagishita, M. Yamazaki, T. Aoba, Adsorption of bovine serum albumin onto octacalcium phosphate and its hydrolyzates, Cells Mater. 5 (1995) 45–54.
[94] O. Suzuki, Y. Miyasaka, M. Sakurai, M. Nakamura, M. Kagayama, Bone formation on synthetic precursors of hydroxyapatite, Tohoku J. Exp. Med. 164 (1991) 37–50, doi:10.1620/tjem.164.37.
[95] Y. Sugiura, K. Onuma, Y. Kimura, H. Miura, K. Tsukamoto, Morphological evolution of precipitates during transformation of amorphous calcium phosphate into octacalcium phosphate in relation to role of intermediate phase, J. Cryst. Growth 332 (2011) 58–67, doi:10.1016/j.jcrysgro.2011.07.030.
[96] J. An, S.C.G. Leeuwenburgh, J.G.C. Wolke, J.A. Jansen, Effects of stirring and fluid perfusion on the in vitro degradation of calcium phosphate cement/PLGA composites, Tissue Eng. - Part C Methods 21 (2015) 1171–1177, doi:10.1089/ten.tec.2015.0016.
[97] D.P. Minh, N.D. Tran, A. Nzihou, P. Sharrock, D.P. Minh, N.D. Tran, A. Nzihou, P. Sharrock, O. Synthesis, D.P. Minh, N.D. Tran, A. Nzihou, P. Sharrock, One-step synthesis of calcium hydroxyapatite from calcium carbonate and orthophosphoric acid under moderate conditions, Ind. Eng. Chem. Res. Am. Chem. Soc. 52 (4) (2013) 1439–1447.
[98] Y. Liu, R.M. Shelton, J.E. Barralet, Homogeneous octacalcium phosphate precipitation: effect of temperature and pH, Key Eng. Mater. 254–256 (2004) 79–82, doi:10.4028/www.scientific.net/kem.254-256.79.
[99] M.J. Arellano-Jiménez, R. García-García, J. Reyes-Gasga, Synthesis and hydrolysis of octacalcium phosphate and its characterization by electron microscopy and X-ray diffraction, J. Phys. Chem. Solids 70 (2009) 390–395, doi:10.1016/j.jpcs.2008.11.001.
[100] R.M. Shelton, Y. Liu, P.R. Cooper, U. Gbureck, M.J. German, J.E. Barralet, Bone marrow cell gene expression and tissue construct assembly using octacalcium phosphate microscaffolds, Biomaterials 27 (2006) 2874–2881, doi:10.1016/j.biomaterials.2005.12.031.
[101] T. Yokoi, H. Kato, M. Kamitakahara, Formation of octacalcium phosphate with incorporated succinic acid through gel-mediated processing, (2010).
[102] L.C. Chow, Solubility of calcium phosphates, Monogr. Oral Sci. 18 (2001) 94–111, doi:10.1159/000061650.
[103] A. Bigi, A. Ripamonti, G. Cojazzi, M. Gazzano, N. Roveri, Thermal conversion of octacalcium phosphate into hydroxyapatite, J. Inorg. Biochem. 40 (1990) 293–299, doi:10.1016/0162-0134(90)80063-4.
[104] N. Eliaz, N. Metoki, Calcium phosphate bioceramics: a review of their history, structure, properties, coating technologies and biomedical applications, Materials (Basel) (2017) 10, doi:10.3390/ma10040334.
[105] N. Temizel, G. Girisken, A.C. Tas, Accelerated transformation of brushite to octacalcium phosphate in new biomineralization media between 36.5 °c and 80 °c, Mater. Sci. Eng. C 31 (2011) 1136–1143, doi:10.1016/j.msec.2011.04.009.
[106] E.V. Kukueva, V.I. Putlyaev, A.A. Tikhonov, T.V. Safronova, Octacalcium phosphate as a precursor for the fabrication of composite bioceramics, Inorg. Mater. 53 (2017) 212–219, doi:10.1134/S0020168517020066.
[107] C. Danoux, D. Pereira, N. Döbelin, C. Stähli, J. Barralet, C. van Blitterswijk, P. Habibovic, The effects of crystal phase and particle morphology of calcium phosphates on proliferation and differentiation of human mesenchymal stromal cells, Adv. Healthc. Mater. 5 (2016) 1775–1785, doi:10.1002/adhm.201600184.
[108] Y. Liu, R. Shelton, U. Gbureck, J. Barralet, Influence of calcium phosphate crystal morphology on the adhesion, spreading, and growth of bone derived cells, J. Biomed. Mater. Res. - Part A 90 (2009) 972–980, doi:10.1002/jbm.a.32156.
[109] T. Anada, T. Kumagai, Y. Honda, T. Masuda, R. Kamijo, S. Kamakura, N. Yoshihara, T. Kuriyagawa, H. Shimauchi, O. Suzuki, Dose-dependent osteogenic effect of octacalcium phosphate on mouse bone marrow stromal cells, Tissue Eng. - Part A 14 (2008) 965–978, doi:10.1089/ten.tea.2007.0339.
[110] A. Bigi, E. Boanini, M. Borghi, G. Cojazzi, S. Panzavolta, N. Roveri, Synthesis and hydrolysis of octacalcium phosphate: effect of sodium polyacrylate, J. Inorg. Biochem. 75 (1999) 145–151, doi:10.1016/S0162-0134(99)00047-1.
[111] N. Döbelin, Interlaboratory study on the quantification of calcium phosphate phases by Rietveld refinement, Powder Diffr. 30 (2015) 231–241, doi:10.1017/S088571561500038X.
[112] D. Shurtakova, B. Yavkin, M. Gafurov, G. Mamin, S. Orlinskii, L. Kuznetsova, S. Bakhteev, I. Ignatyev, I. Smirnov, A. Fedotov, V. Komlev, Study of radiation-induced stable radicals in synthetic octacalcium phosphate by pulsed EPR, Magn. Reson. Solids 21 (2019), doi:10.26907/mrsej-19105.
[113] X. Ding, A. Li, F. Yang, K. Sun, X. Sun, B-Tricalcium phosphate and octacalcium phosphate composite bioceramic material for bone tissue engineering, J. Biomater. Appl. 34 (2020) 1294–1299, doi:10.1177/0885328220903989.
[114] Y. Shiwaku, Y. Honda, T. Anada, S. Morimoto, T. Masuda, K. Sasaki, O. Suzuki, Analysis of physicochemical properties of octacalcium phosphate prepared by hydrolysis and co-precipitation with fluoride ions, J. Ceram. Soc. Jpn. 118 (2010) 402–405, doi:10.2109/jcersj2.118.402.
[115] I.A. Karampas, C.G. Kontoyannis, Characterization of calcium phosphates mixtures, Vib. Spectrosc. 64 (2013) 126–133, doi:10.1016/j.vibspec.2012.11.003.
[116] Y. Tseng, J. Zhan, K.S.K. Lin, C. Mou, J.C.C. Chan, High resolution 31P NMR study of octacalcium phosphate, Solid State Nucl. Magn. Reson. 26 (2004) 99–104, doi:10.1016/j.ssnmr.2004.06.002.
[117] T.W.T. Tsai, F.C. Chou, Y.H. Tseng, J.C.C. Chan, Solid-state P-31 NMR study of octacalcium phosphate incorporated with succinate, Phys. Chem. Chem. Phys. 12 (2010) 6692–6697, doi:10.1039/b923338e.
[118] Y.H. Tseng, C.Y. Mou, J.C.C. Chan, Solid-state NMR study of the transformation of octacalcium phosphate to hydroxyapatite: a mechanistic model for central dark line formation, J. Am. Chem. Soc. 128 (2006) 6909–6918, doi:10.1021/ja060336u.
[119] S. Von Euw, Y. Wang, G. Laurent, C. Drouet, F. Babonneau, N. Nassif, T. Azaïs, Bone mineral: new insights into its chemical composition, Sci. Rep. 9 (2019) 1–11, doi:10.1038/s41598-019-44620-6.
[120] E. Davies, M.J. Duer, S.E. Ashbrook, J.M. Griffin, Applications of NMR crystallography to problems in biomineralization: refinement of the crystal structure and 31P solid-state NMR spectral assignment of octacalcium phosphate, J. Am. Chem. Soc. 134 (2012) 12508–12515, doi:10.1021/ja3017544.
[121] W.P. Rothwell, J.P. Yesinowskit, High-resolution variable-temperature 31P NMR of solid calcium phosphates, J. Am. Chem. Soc. 102 (1980).
[122] J.P. Yesinowski, H. Eckert, Hydrogen environments in calcium phosphates: H MAS NMR at high spinning speeds? J. Am. Chem. Soc. 109 (1987) 6274–6282.
[123] M. Bak, J.K. Thomsen, H.J. Jakobsen, S.E. Petersen, T.E. Petersen, N.C. Nielsen, Solid-state 13C and 31P NMR analysis of urinary stones, J. Urol. 164 (2000) 856–863.

[124] M. Robin, S. Von Euw, G. Renaudin, S. Gomes, J.M. Krafft, N. Nassif, T. Azaïs, G. Costentin, Insights into OCP identification and quantification in the context of apatite biomineralization, CrystEngComm 22 (2020) 2728–2742, doi:10.1039/c9ce01972c.
[125] D. Laurencin, Y. Li, M.J. Duer, D. Iuga, C. Gervais, C. Bonhomme, A 43Ca nuclear magnetic resonance perspective on octacalcium phosphate and its hybrid derivatives, Magn. Reson. Chem. (2021) 1–14, doi:10.1002/mrc.5149.
[126] Y. Li, D.G. Reid, M.J. Duer, J.C.C. Chan, Solid state NMR—an indispensable tool in organic-inorganic biocomposite characterization; refining the structure of octacalcium phosphate composites with the linear metabolic diacids succinate and adipate, Solid State Nucl. Magn. Reson. 95 (2018) 1–5, doi:10.1016/j.ssnmr.2018.08.004.
[127] P. Hung, Y. Kuo, H. Chen, H.K. Chiang, O.K. Lee, Detection of osteogenic differentiation by differential mineralized matrix production in mesenchymal stromal cells by Raman spectroscopy, PLoS One 8 (2013) 1–7, doi:10.1371/journal.pone.0065438.
[128] S.J. Smith, R. Emery, A. Pitsillides, C.E. Clarkin, S. Mahajan, Detection of early osteogenic commitment in primary cells using Raman spectroscopy †, Analyst 142 (2017) 1962–1973, doi:10.1039/c6an02469f.
[129] N.J. Crane, V. Popescu, M.D. Morris, P. Steenhuis, M.A. Ignelzi, Raman spectroscopic evidence for octacalcium phosphate and other transient mineral species deposited during intramembranous mineralization, Bone 39 (2006) 434–442, doi:10.1016/j.bone.2006.02.059.
[130] N. Döbelin, Validation of XRD phase quantification using semi-synthetic data, Powder Diffr. 35 (2020) 262–275, doi:10.1017/S0885715620000573.
[131] N. Ohtsu, S. Hiromoto, M. Yamane, K. Satoh, M. Tomozawa, Chemical and crystallographic characterizations of hydroxyapatite-and octacalcium phosphate-coatings on magnesium synthesized by chemical solution deposition using XPS and XRD, Surf. Coat. Technol. 218 (2013) 114–118, doi:10.1016/j.surfcoat.2012.12.037.
[132] C.C. Chusuei, Calcium phosphate phase identification using XPS and time-of-flight cluster SIMS, Anal. Chem. 71 (1999) 149–153, doi:10.1021/ac9806963.
[133] Y. Murakami, Y. Honda, T. Anada, H. Shimauchi, O. Suzuki, Comparative study on bone regeneration by synthetic octacalcium phosphate with various granule sizes, Acta Biomater. 6 (2010) 1542–1548, doi:10.1016/j.actbio.2009.10.023.
[134] Y. Honda, S. Kamakura, K. Sasaki, O. Suzuki, Formation of bone-like apatite enhanced by hydrolysis of octacalcium phosphate crystals deposited in collagen matrix, J. Biomed. Mater. Res. - Part B Appl. Biomater. 80 (2007) 281–289, doi:10.1002/jbm.b.30595.
[135] W.E. Brown, M. Mathew, M.S. Tung, Crystal chemistry of octacalcium phosphate, Prog. Cryst. Growth Charact. 4 (1981) 59–87, doi:10.1016/0146-3535(81)90048-4.
[136] O. Suzuki, Y. Shiwaku, R. Hamai, Octacalcium phosphate bone substitute materials: comparison between properties of biomaterials and other calcium phosphate materials, Dent. Mater. J. 39 (2020) 187–199, doi:10.4012/dmj.2020-001.
[137] A. Dey, P.H.H. Bomans, F.A. Müller, J. Will, P.M. Frederik, G. De With, N.A.J.M. Sommerdijk, The role of prenucleation clusters in surface-induced calcium phosphate crystallization, Nat. Mater. 9 (2010) 1010–1014, doi:10.1038/nmat2900.
[138] F. Nudelman, K. Pieterse, A. George, P.H.H. Bomans, H. Friedrich, L.J. Brylka, P.A.J. Hilbers, G. De With, N.A.J.M. Sommerdijk, The role of collagen in bone apatite formation in the presence of hydroxyapatite nucleation inhibitors, Nat. Mater. 9 (2010) 1004–1009, doi:10.1038/NMAT2875.
[139] L. Wang, G.H. Nancollas, Pathways to biomineralization and biodemineralization of calcium phosphates : the thermodynamic and kinetic controls, Dalt. Trans. (2009) 2665–2672, doi:10.1039/b815887h.
[140] W.J.E.M. Habraken, J. Tao, L.J. Brylka, H. Friedrich, L. Bertinetti, A.S. Schenk, A. Verch, V. Dmitrovic, P.H.H. Bomans, P.M. Frederik, J. Laven, P. Van Der Schoot, B. Aichmayer, G. De With, J.J. DeYoreo, N.A.J.M. Sommerdijk, Ion-association complexes unite classical and non-classical theories for the biomimetic nucleation of calcium phosphate, Nat. Commun. 4 (2013) 1507–1512, doi:10.1038/ncomms2490.
[141] K. Kobayashi, T. Anada, T. Handa, N. Kanda, M. Yoshinari, T. Takahashi, O. Suzuki, Osteoconductive property of a mechanical mixture of octacalcium phosphate and amorphous calcium phosphate, ACS Appl. Mater. Interfaces 6 (2014) 22602–22611, doi:10.1021/am5067139.
[142] S. Sakai, T. Anada, K. Tsuchiya, H. Yamazaki, H.C. Margolis, O. Suzuki, Comparative study on the resorbability and dissolution behavior of octacalcium phosphate, β-tricalcium phosphate, and hydroxyapatite under physiological conditions, Dent. Mater. J. 35 (2016) 216–224, doi:10.4012/dmj.2015-255.
[143] J.C. Heughebaert, G.H. Nancollas, Kinetics of crystallization of octacalcium phosphate, J. Phys. Chem. 88 (1984) 2478–2481, doi:10.1021/j150656a012.
[144] A. Vyalikh, C. Elschner, M. Schulz, R. Mai, U. Scheler, Early stages of biomineral formation—a solid-state NMR investigation of the mandibles of minipigs, Magnetochemistry 3 (2017) 39, doi:10.3390/magnetochemistry3040039.
[145] Y. Ezoe, T. Anada, H. Yamazaki, T. Handa, K. Kobayashi, T. Takahashi, O. Suzuki, Characterization of partially hydrolyzed OCP crystals deposited in a gelatin matrix as a scaffold for bone tissue engineering, J. Nanoparticle Res. 17 (2015), doi:10.1007/s11051-015-2864-1.
[146] X. Lu, Y. Leng, Theoretical analysis of calcium phosphate precipitation in simulated body fluid, Biomaterials 26 (2005) 1097–1108, doi:10.1016/j.biomaterials.2004.05.034.
[147] O. Suzuki, S. Kamakura, T. Katagiri, M. Nakamura, B. Zhao, Y. Honda, R. Kamijo, Bone formation enhanced by implanted octacalcium phosphate involving conversion into Ca-deficient hydroxyapatite, Biomaterials 27 (2006) 2671–2681, doi:10.1016/j.biomaterials.2005.12.004.
[148] N.V Petrakova, A.Y. Teterina, P.V Mikheeva, S.A. Akhmedova, E.A. Kuvshinova, I.K. Sviridova, N.S. Sergeeva, I.V Smirnov, A.Y. Fedotov, Y.F. Kargin, S.M. Barinov, V.S. Komlev, In vitro study of octacalcium phosphate behavior in different model solutions, ACS Omega (2021) 7487–7498, doi:10.1021/acsomega.0c06016.
[149] T. Yokoi, I.Y. Kim, C. Ohtsuki, Mineralization of calcium phosphate on octacalcium phosphate in a solution mimicking in vivo conditions, Phosphorus Res. Bull. 26 (2012) 71–76, doi:10.3363/prb.26.71.
[150] T. Fuji, T. Anada, Y. Honda, Y. Shiwaku, H. Koike, S. Kamakura, K. Sasaki, O. Suzuki, Octacalcium phosphate-precipitated alginate scaffold for bone regeneration, Tissue Eng. - Part A. 15 (2009) 3525–3535, doi:10.1089/ten.tea.2009.0048.
[151] T. Handa, T. Anada, Y. Honda, H. Yamazaki, K. Kobayashi, N. Kanda, S. Kamakura, S. Echigo, O. Suzuki, The effect of an octacalcium phosphate co-precipitated gelatin composite on the repair of critical-sized rat calvarial defects, Acta Biomater. 8 (2012) 1190–1200, doi:10.1016/j.actbio.2011.12.002.
[152] S. Morimoto, T. Anada, Y. Honda, O. Suzuki, Comparative study on in vitro biocompatibility of synthetic octacalcium phosphate and calcium phosphate ceramics used clinically, Biomed. Mater. 7 (2012), doi:10.1088/1748-6041/7/4/045020.
[153] R. Nishikawa, T. Anada, R. Ishiko-Uzuka, O. Suzuki, Osteoblastic differentiation of stromal ST-2 cells from octacalcium phosphate exposure via p38 signaling pathway, Dent. Mater. J. 33 (2014) 242–251, doi:10.4012/dmj.2013-226.
[154] O. Suzuki, T. Anada, Octacalcium phosphate: a potential scaffold material for controlling activity of bone-related cells in vitro, Mater. Sci. Forum. 783–786 (2014) 1366–1371, doi:10.4028/www.scientific.net/msf.783-786.1366.
[155] S. Saito, R. Hamai, Y. Shiwaku, T. Hasegawa, S. Sakai, K. Tsuchiya, Y. Sai, R. Iwama, N. Amizuka, T. Takahashi, O. Suzuki, Involvement of distant octacalcium phosphate scaffolds in enhancing early differentiation of osteocytes during bone regeneration, Acta Biomater (2021), doi:10.1016/j.actbio.2021.05.017.
[156] T. Kurobane, Y. Shiwaku, T. Anada, R. Hamai, K. Tsuchiya, K. Baba, M. Iikubo, T. Takahashi, O. Suzuki, Angiogenesis involvement by octacalcium phosphate-gelatin composite-driven bone regeneration in rat calvaria critical-sized defect, Acta Biomater 88 (2019) 514–526, doi:10.1016/j.actbio.2019.02.021.
[157] K. Suzuki, T. Anada, T. Miyazaki, N. Miyatake, Y. Honda, K.N. Kishimoto, M. Hosaka, H. Imaizumi, E. Itoi, O. Suzuki, Effect of addition of hyaluronic acids on the osteoconductivity and biodegradability of synthetic octacalcium phosphate, Acta Biomater. 10 (2014) 531–543, doi:10.1016/j.actbio.2013.09.005.
[158] G. Fuentes, E. Peón, Y. Campos, N. López, C.X. Resende, G.D.A. Soares, Application of new statistical approach to study drug release from OCP coating on titanium sheets, Key Eng. Mater. 398 (2009) 511–514, doi:10.4028/www.scientific.net/KEM.396-398.511.
[159] S. Hiromoto, M. Inoue, T. Taguchi, M. Yamane, N. Ohtsu, In vitro and in vivo biocompatibility and corrosion behaviour of a bioabsorbable magnesium alloy coated with octacalcium phosphate and hydroxyapatite, Acta Biomater. (2014), doi:10.1016/j.actbio.2014.09.026.
[160] F. Barrère, C.M. Van Der Valk, R.A.J. Dalmeijer, G. Meijer, C.A. Van Blitterswijk, K. De Groot, P. Layrolle, Osteogenecity of octacalcium phosphate coatings applied on porous metal implants, J. Biomed. Mater. Res. - Part A 66 (2003) 779–788, doi:10.1002/jbm.a.10454.
[161] P. Habibovic, C.M. Van Der Valk, C.A. Van Blitterswijk, K. De Groot, G. Meijer, Influence of octacalcium phosphate coating on osteoinductive properties of biomaterials, J. Mater. Sci. Mater. Med. 15 (2004) 373–380, doi:10.1023/B:JMSM.0000021104.42685.9f.
[162] Y. Sugiura, M.L. Munar, K. Ishikawa, Fabrication of octacalcium phosphate block through a dissolution-precipitation reaction using a calcium sulphate hemihydrate block as a precursor, J. Mater. Sci. Mater. Med. 29 (2018) 1–8, doi:10.1007/s10856-018-6162-1.
[163] Y. Sugiura, M.L. Munar, K. Ishikawa, Fabrication of octacalcium phosphate foam through phase conversion and its histological evaluation, Mater. Lett. 212 (2018) 28–31, doi:10.1016/j.matlet.2017.10.051.
[164] E.E. Golub, K. Boesze-Battaglia, The role of alkaline phosphatase in osteogenesis, Curr. Opin. Orthop. (2007) 444–448, doi:10.1084/jem.93.5.415.
[165] S. Yamada, D. Heymann, J.M. Bouler, G. Daculsi, Osteoclastic resorption of calcium phosphate ceramics with different hydroxyapatite/β-tricalcium phosphate ratios, Biomaterials 18 (1997) 1037–1041, doi:10.1016/S0142-9612(97)00036-7.
[166] M.S. Tung, N. Eidelman, B. Sieck, W.E. Brown, Octacalcium phosphate solubility product from 4 to 37°C, J. Res. Natl. Bur. Stand. (1934) 93 (1988) 613–624, doi:10.6028/jres.093.153.
[167] S. Kamakura, Y. Sasano, T. Shimizu, K. Hatori, O. Suzuki, M. Kagayama, K. Motegi, Implanted octacalcium phosphate is more resorbable than β-tricalcium phosphate and hydroxyapatite, J. Biomed. Mater. Res. 59 (2002) 29–34, doi:10.1002/jbm.1213.
[168] Y. Shiwaku, K. Tsuchiya, L. Xiao, O. Suzuki, Effect of calcium phosphate phases affecting the crosstalk between osteoblasts and osteoclasts in vitro, J. Biomed. Mater. Res. - Part A 107 (2019) 1001–1013, doi:10.1002/jbm.a.36626.
[169] S. Kamakura, Y. Sasano, O. Suzuki, Synthetic octacalcium phosphate (OCP) is an effective scaffold to regenerate bone, Int. Congr. Ser. 1284 (2005) 290–295, doi:10.1016/j.ics.2005.06.035.
[170] S. Kamakura, S. Nakajo, O. Suzuki, Y. Sasano, New scaffold for recombinant human bone morphogenetic protein-2, J. Biomed. Mater. Res. - Part A 71 (2004) 299–307, doi:10.1002/jbm.a.30157.

[171] M. Ramazanoglu, R. Lutz, C. Ergun, C. von Wilmowsky, E. Nkenke, K.A. Schlegel, The effect of combined delivery of recombinant human bone morphogenetic protein-2 and recombinant human vascular endothelial growth factor 165 from biomimetic calcium-phosphate-coated implants on osseointegration, Clin. Oral Implants Res. 22 (2011) 1433–1439, doi:10.1111/j.1600-0501.2010.02133.x.
[172] R. Dimitriou, E. Jones, D. Mcgonagle, P.V Giannoudis, Bone regeneration : current concepts and future directions, BMC Med. 66 (2011).
[173] J. Henkel, M.A. Woodruff, D.R. Epari, R. Steck, V. Glatt, I.C. Dickinson, F.M. Choong, M.A. Schuetz, D.W. Hutmacher, Bone regeneration based on tissue engineering conceptions—a 21st century perspective, Nat. Publ. Gr. (2013) 216–248, doi:10.4248/BR201303002.
[174] M.R. Newman, D.S.W. Benoit, Local and targeted drug delivery for bone regeneration, Curr. Opin. Biotechnol. 40 (2016) 125–132, doi:10.1016/j.copbio.2016.02.029.
[175] E. Sarigol-Calamak, C. Hascicek, Tissue Scaffolds as a local drug delivery system for bone regeneration, Cutting-Edge Enabling Technol. Regen. Med. (2018) 475–493.
[176] S. Anil, A.F. Al-sulaimani, A.E. Beeran, E.P. Chalisserry, H.P.R. Varma, M.D. Al Amri, Drug delivery systems in bone regeneration and implant dentistry, Curr. Concepts Dent. Implantol. (2015).
[177] A. Shuid, N. Ibrahim, M. Amin, I. Mohamed, Drug delivery systems for prevention and treatment of osteoporotic fracture, Curr. Drug Targets 14 (2013) 1558–1564, doi:10.2174/13894501146661311085390 5.
[178] D. Bhowmik, H. Gopinath, B.P. Kumar, S. Duraivel, K.P.S. Kumar, Controlled release drug delivery systems, Pharma Innov. 1 (2012) 24–32.
[179] K. Park, The controlled drug delivery systems: past forward and future back, J. Control. Release (2014), doi:10.1016/j.jconrel.2014.03.054.
[180] Uskokovic Vuk, T.A. Desai, Phase composition control of calcium phosphate nanoparticles for tunable drug delivery kinetics and treatment of osteomyelitis. I. Preparation and drug release, J. Biomed. Mater. Res. - Part A 101 A (2013) 1416–1426, doi:10.1002/jbm.a.34426.
[181] C. Li, X. Ge, G. Li, Q. Gao, R. Ding, A facile hydrothermal method for synthesis of submillimeter-long octacalcium phosphate and hydroxyapatite as drug carriers with sustained release behaviors, Adv. Powder Technol. 25 (2014) 1661–1666, doi:10.1016/j.apt.2014.06.001.
[182] N.S. Chickerur, M.S. Tung, W.E. Brown, A mechanism for incorporation of carbonate into apatite, Calcif. Tissue Int. 32 (1980) 55–62, doi:10.1007/BF02408521.
[183] B.B. Tomazic, I. Mayer, W.E. Brown, Ion incorporation into octacalcium phosphate hydrolyzates, J. Cryst. Growth 108 (1991) 670–682, doi:10.1016/0022-0248(91)90247-3.
[184] D. Shen, N. Horiuchi, S. Nozaki, M. Miyashin, K. Yamashita, A. Nagai, Synthesis and enhanced bone regeneration of carbonate substituted octacalcium phosphate, Biomed. Mater. Eng. 28 (2017) 9–21, doi:10.3233/BME-171651.
[185] C.G. Bellows, J.N.M. Heersche, J.E. Aubin, Inorganic phosphate added exogenously or released from β-glycerophosphate initiates mineralization of osteoid nodules in vitro, Bone Miner. 17 (1992) 15–29, doi:10.1016/0169-6009(92)90707-K.
[186] T. Yokoi, T. Goto, M. Hara, T. Sekino, T. Seki, M. Kamitakahara, C. Ohtsuki, S. Kitaoka, S. Takahashi, M. Kawashita, Incorporation of tetracarboxylate ions into octacalcium phosphate for the development of next-generation biofriendly materials, Commun. Chem. 4 (2021) 2–10, doi:10.1038/s42004-020-00443-5.
[187] H. Shi, X. Ye, J. Zhang, T. Wu, T. Yu, C. Zhou, J. Ye, A thermostability perspective on enhancing physicochemical and cytological characteristics of octacalcium phosphate by doping iron and strontium, Bioact. Mater. 6 (2020) 1267–1282, doi:10.1016/j.bioactmat.2020.10.025.
[188] Y. Shiwaku, T. Anada, H. Yamazaki, Y. Honda, S. Morimoto, K. Sasaki, O. Suzuki, Structural, morphological and surface characteristics of two types of octacalcium phosphate-derived fluoride-containing apatitic calcium phosphates, Acta Biomater. 8 (2012) 4417–4425, doi:10.1016/j.actbio.2012.07.041.
[189] E. Boanini, P. Torricelli, M. Gazzano, M. Fini, A. Bigi, The effect of alendronate doped calcium phosphates on bone cells activity, Bone 51 (2012) 944–952, doi:10.1016/j.bone.2012.07.020.
[190] N. Ito, M. Kamitakahara, K. Ioku, Preparation and evaluation of spherical porous granules of octacalcium phosphate/hydroxyapatite as drug carriers in bone cancer treatment, Mater. Lett. 120 (2014) 94–96, doi:10.1016/j.matlet.2014.01.040.
[191] M. Kamitakahara, A. Ishii, H. Matsubara, M. Kawashita, M. Furuya, H. Kanetaka, Fabrication and evaluation of ascorbic acid phosphate-loaded spherical porous hydroxyapatite/octacalcium phosphate granules, J. Ceram. Soc. Jpn. 129 (2021) 60–65, doi:10.2109/jcersj2.20170.
[192] L. Forte, P. Torricelli, F. Bonvicini, E. Boanini, G.A. Gentilomi, G. Lusvardi, E.Della Bella, M. Fini, E. Vecchio Nepita, A. Bigi, Biomimetic fabrication of antibacterial calcium phosphates mediated by polydopamine, J. Inorg. Biochem. 178 (2018) 43–53, doi:10.1016/j.jinorgbio.2017.10.004.
[193] E. Boanini, M. Gazzano, A. Bigi, Ionic substitutions in calcium phosphates synthesized at low temperature, Acta Biomater. 6 (2010) 1882–1894, doi:10.1016/j.actbio.2009.12.041.
[194] M.E. Fleet, Infrared spectra of carbonate apatites: evidence for a connection between bone mineral and body fluids, Am. Min. 102 (2017) 149–157, doi:10.2138/am-2017-5704.
[195] C. Rey, C. Combes, C. Drouet, M.J. Glimcher, Bone mineral: update on chemical composition and structure, Osteoporos. Int. 20 (2009) 1013–1021, doi:10.1007/s00198-009-0860-y.
[196] J. Kolmas, A. Jaklewicz, A. Zima, M. Bućko, Z. Paszkiewicz, J. Lis, A. Ślósarczyk, W. Kolodziejski, Incorporation of carbonate and magnesium ions into synthetic hydroxyapatite: the effect on physicochemical properties, J. Mol. Struct. 987 (2011) 40–50, doi:10.1016/j.molstruc.2010.11.058.
[197] M. Vignoles, G. Bonel, D.W. Holcomb, R.A. Young, Influence of preparation conditions on the composition of type B carbonated hydroxyapatite and on the localization of the carbonate ions, Calcif. Tissue Int. 43 (1988) 33–40, doi:10.1007/BF02555165.
[198] N. Strutynska, O. Livitska, S. Prylutska, Y. Yumyna, P. Zelena, L. Skivka, A. Malyshenko, L. Vovchenko, V. Strelchuk, Y. Prylutskyy, N. Slobodyanik, U. Ritter, New nanostructured apatite-type (Na+,Zn2+,CO32−)-doped calcium phosphates: preparation, mechanical properties and antibacterial activity, J. Mol. Struct. 1222 (2020) 128932, doi:10.1016/j.molstruc.2020.128932.
[199] A.H.K. Chou, R.Z. LeGeros, Z. Chen, Y. Li, Antibacterial effect of zinc phosphate mineralized guided bone regeneration membranes, Implant Dent. 16 (2007) 89–100, doi:10.1097/ID.0b013e318031224a.
[200] M. Frasnelli, F. Cristofaro, V.M. Sglavo, S. Dirè, E. Callone, R. Ceccato, G. Bruni, A.I. Cornaglia, L. Visai, Synthesis and characterization of strontium-substituted hydroxyapatite nanoparticles for bone regeneration, Mater. Sci. Eng. C 71 (2017) 653–662, doi:10.1016/j.msec.2016.10.047.
[201] H. Shi, S. Yang, S. Zeng, X. Liu, J. Zhang, T. Wu, X. Ye, T. Yu, C. Zhou, J. Ye, Enhanced angiogenesis of biodegradable iron-doped octacalcium phosphate/poly(lactic-co-glycolic acid) scaffold for potential cancerous bone regeneration, Appl. Mater. Today 15 (2019) 100–114, doi:10.1016/j.apmt.2019.01.002.
[202] M.J. Mura-Galelli, H. Narusawa, T. Shimada, M. Iijima, T. Aoba, Effects of fluoride on precipitation and hydrolysis of octacalcium phosphate in an experimental model simulating enamel mineralization during amelogenesis, Cells Mater. 2 (1992).
[203] Y. Fan, J.R. Nelson, J.R. Alvarez, J. Hagan, A. Berrier, X. Xu, Amelogenin-assisted ex vivo remineralization of human enamel : effects of supersaturation degree and fluoride concentration, Acta Biomater. 7 (2011) 2293–2302, doi:10.1016/j.actbio.2011.01.028.
[204] M. Iijima, K. Onuma, Roles of fluoride on octacalcium phosphate and apatite formation on amorphous calcium phosphate substrate, Cryst. Growth Des. 18 (2018) 2279–2288, doi:10.1021/acs.cgd.7b01717.
[205] A. Bigi, E. Boanini, D. Walsh, S. Mann, Morphosynthesis of octacalcium phosphate hollow microspheres by polyelectrolyte- mediated crystallization, Angew. Chem. Int. Ed. 41 (2002) 2163–2166.
[206] M. Marković, B.O. Fowler, W.E. Brown, Octacalcium phosphate carboxylates. 1. Preparation and identification, Chem. Mater. 5 (1993) 1401–1405, doi:10.1021/cm00034a007.
[207] M. Markovic, B.O. Fowler, W.E. Brown, Octacalcium phosphate carboxylates. 2. Characterization and structural considerations, Chem. Mater. (1993) 1406–1416.
[208] H. Monma, M. Goto, Succinate-complexed octacalcium phosphate, Bull. Chem. Soc. Jpn. 56 (1983) 3843–3844, doi:10.1246/bcsj.56.3843.
[209] T. Yokoi, H. Kato, I.Y. Kim, K. Kikuta, M. Kawashita, C. Ohtsuki, Synthesis of octacalcium phosphate with incorporated succinate and suberate ions, Ceram. Int. 38 (2012) 3815–3820, doi:10.1016/j.ceramint.2012.01.030.
[210] T. Yokoi, H. Kato, I.Y. Kim, K. Kikuta, M. Kamitakahara, M. Kawashita, C. Ohtsuki, Formation of octacalcium phosphates with co-incorporated succinate and suberate ions, Dalt. Trans. 41 (2012) 2732–2737, doi:10.1039/c2dt11580h.
[211] S. Aoki, A. Nakahira, H. Nakayama, K. Sakamoto, S. Yamaguchi, K. Suganuma, Synthesis and aldehyde absorption properties of aspartate-octacalcium phosphate inclusion compound, J. Phys. Chem. Solids 65 (2004) 465–470, doi:10.1016/j.jpcs.2003.10.030.
[212] S.K. Boda, Y. Almoshari, H. Wang, X. Wang, R.A. Reinhardt, B. Duan, D. Wang, J. Xie, Mineralized nanofiber segments coupled with calcium-binding BMP-2 peptides for alveolar bone regeneration, Acta Biomater. 85 (2019) 282–293, doi:10.1016/j.actbio.2018.12.051.
[213] S.K. Boda, H. Wang, J. V John, R.A. Reinhardt, J. Xie, Dual delivery of alendronate and E7-BMP – 2 peptide via calcium chelation to mineralized nano fiber fragments for alveolar bone regeneration, (2020). https://doi.org/10.1021/acsbiomaterials.0c00145.
[214] K. Wei, C. Lai, Y. Wang, Formation of monetite nanoparticles and nanofibers in reverse micelles, J. Mater. Sci. 42 (2007) 5340–5346, doi:10.1007/s10853-006-0902-1.
[215] Y. Wang, C. Lai, K. Wei, S. Tang, Influence of temperature, ripening time, and cosurfactant on solvothermal synthesis of calcium phosphate nanobelts, Mater. Lett. 59 (2005) 1098–1104, doi:10.1016/j.matlet.2004.12.016.
[216] A. Lebugle, A. Rodrigues, P. Bonnevialle, J.J. Voigt, P. Canal, F. Rodriguez, Study of implantable calcium phosphate systems for the slow release of methotrexate, Biomaterials 23 (2002) 3517–3522.
[217] Y. Sugiura, H. Obika, M. Horie, K. Niitsu, Y. Makita, Aesthetic silver-doped octacalcium phosphate powders exhibiting both contact antibacterial ability and low cytotoxicity, ACS Omega 5 (2020) 24434–24444, doi:10.1021/acsomega.0c02868.
[218] M.D.S. Tea Mihelj Josipovic, Monika Kovacevic, Sarah Matesa, Marina Kostesic, Nives Matijakovic, Borna Radatovic, Daniel M. Lyons, Damir Kralj, The influence of different classes of amino acids on calcium phosphates seeded growth, (2020) 8–12.
[219] L.S. Costanzo, Regulation of calcium and phosphate homeostasis, Adv. Physiol. Educ. 20 (1998) 206–216.
[220] J.G. Taylor, D.A. Bushinsky, Calcium and phosphate homeostasis, Blood Purif. 27 (2009) 387–394, doi:10.1159/000209740.

Appendix 2
2. pielikums

Exploring the Formation Kinetics of Octacalcium Phosphate from Alpha-Tricalcium Phosphate: Synthesis Scale-Up, Determination of Transient Phases, Their Morphology and Biocompatibility

Ilijana Kovrlija, Ksenia Menshikh, Olivier Marsan, Christian Rey, Christèle Combes, Janis Locs, Dagnija Loca

Biomolecules, 13 (2023), 462. DOI:10.3390/biom13030462

I.K. input: **w**riting – original draft and review & editing, conceptualization, visualization, formal analysis, investigation.

biomolecules

MDPI

Article

Exploring the Formation Kinetics of Octacalcium Phosphate from Alpha-Tricalcium Phosphate: Synthesis Scale-Up, Determination of Transient Phases, Their Morphology and Biocompatibility

Ilijana Kovrlija [1], Ksenia Menshikh [2], Olivier Marsan [3], Christian Rey [3], Christèle Combes [3], Janis Locs [1,4] and Dagnija Loca [1,4,*]

[1] Rudolfs Cimdins Riga Biomaterials Innovation and Development Centre, Faculty of Materials Science and Applied Chemistry, Institute of General Chemical Engineering, Riga Technical University, Pulka 3, LV-1007 Riga, Latvia
[2] Center for Translational Research on Autoimmune and Allergic Disease—CAAD, Department of Health Sciences, Università del Piemonte Orientale, 28100 Novara, Italy
[3] CIRIMAT, Université de Toulouse, CNRS, Toulouse INP—ENSIACET, 4 Allée Emile Monso, CEDEX 4, 31030 Toulouse, France
[4] Baltic Biomaterials Centre of Excellence, Headquarters at Riga Technical University, LV-1007 Riga, Latvia
* Correspondence: dagnija.loca@rtu.lv; Tel.: +371-67089628; Fax: +371-67089619

Abstract: Even with decades of research studies behind octacalcium phosphate (OCP), determination of OCP phase formation has proved to be a cumbersome challenge. Even though obtaining a large quantity of OCP is important for potential clinical uses, it still remains a hindrance to obtain high yields of pure OCP. Taking that into consideration, the purpose of this study was to scale-up OCP synthesis for the first time and to use a multi-technique approach to follow the phase transformation pathway at multiple time points. In the present study, OCP has been synthesized from α-tricalcium phosphate (α-TCP), and subsequently scaled-up tenfold and hundredfold (100 mg → 10 g). The hydrolysis mechanism has been followed and described by using XRD and FTIR spectroscopy, as well as Raman and SEM. Gradual transformation into the OCP phase transpired through dicalcium phosphate dihydrate (brushite, DCPD, up to ~36%) as an intermediary phase. Furthermore, the obtained transitional phases and final OCP phases (across all scale-up levels) were tested with human bone marrow-derived mesenchymal stem cells (hBMSCs), in order to see how different phase mixtures affect the cell viability, and also to corroborate the safety of the scaled-up product. Twelve out of seventeen specimens showed satisfactory percentages of cell viability and confirmed the prospective use of scaled-up OCP in further in vitro studies. The present study, therefore, provides the first scale-up process of OCP synthesis, an in depth understanding of the formation pathway, and investigation of the parameters able to contribute in the OCP phase formation.

Keywords: octacalcium phosphate; α-TCP; DCPD; calcium phosphate; hydrolysis; scale-up; mesenchymal stem cells; FTIR; XRD; Raman

Citation: Kovrlija, I.; Menshikh, K.; Marsan, O.; Rey, C.; Combes, C.; Locs, J.; Loca, D. Exploring the Formation Kinetics of Octacalcium Phosphate from Alpha-Tricalcium Phosphate: Synthesis Scale-Up, Determination of Transient Phases, Their Morphology and Biocompatibility. *Biomolecules* **2023**, *13*, 462. https://doi.org/10.3390/biom13030462

Academic Editors: Bahman Anvari and Letizia Sambri

Received: 9 January 2023
Revised: 17 February 2023
Accepted: 28 February 2023
Published: 2 March 2023

1. Introduction

Ever since calcium phosphate (CaP) started to gain scientific interest in 1770 [1], a revolution has taken place across several fields, ranging from chemistry and material science to biomedical applications. Many synthetic bone substitutes have been developed, but the limitation of the natural material, with its complex and non-stoichiometric calcium phosphate apatite structure, means they are still far out of reach from achieving the optimum goal. The main reasons being that the natural material contains many substitutes for calcium and phosphate ions and a great number of heterogeneities corresponding to the type of bone can influence it (trabecular or compact [2], biological diversity, remodelling rate, living

style, etc [3–6]). However, the formation of non-stoichiometric apatites has emerged as a potential solution. One of the calcium phosphates that has been pushing itself to the forefront of material science and has also been considered as a bone mineral precursor [7–9] is octacalcium phosphate ($Ca_8(HPO_4)_2(PO_4)_4 \cdot 5H_2O$; OCP). Its similarity to apatite stems from the characteristic apatite layers parallel to the (100) plane, with interlaying hydrated layers that are comprised of an alterable number of water molecules, which are found between more spatially spread out phosphate and calcium ions [10]. In addition, OCP can explain the existence of non-stoichiometry in apatites [3] through its ability to interlay with apatite domains [3]. Moreover, OCP has a plethora of other benefits such as solubility in close equilibrium with blood serum [11,12], substantial affinity towards organic molecules (helpful in biological mineralization, drug delivery platforms) [13], the tendency to convert to the thermodynamically more stable apatite [14], and the potential to promote osteoblastic cell differentiation [15].

Several improvements of OCP with different ions and drugs have been published [16,17]. There has also been evidence that an ultrahigh drug loading capacity can be accomplished if the drug loading is implemented in situ during the primary stages of CaP synthesis [18]. Conversely, if OCP is to be used as a drug delivery vehicle, the complexity of the formation pathway needs to be identified and substantiated. For that reason, significant efforts have been taken to develop the OCP synthesis processes. The precipitation route has been heavily employed and examined in more detail than the older, original hydrolysis route [19,20]. However, synthesis via precipitation has its own limitations, and with the already complicated chemistry of CaP formation, it can bring undesired outcomes. Several aspects ranging from the preparation of precursor solutions (e.g., calcium sources), incomplete reactions involving metastable phases, and even the impact of incomplete washing can have a negative effect on the precipitated product [21]. The excessive number of parameters (dose rate, stirring, purity of precursor salts) can trigger an already highly sensitive mechanism and cause an even greater inconvenience in establishing the phase purity. If the utilization of the CaP is being aimed at creating a drug delivery system, one must be careful of the synthesis environment due to the sensitivity of the chosen drug. All of the aforementioned reasons have pushed the decision to select the hydrolysis pathway of obtaining OCP as a preferential method [22–24]. Even though hydrolysis is a complex process [25], involving not only a precipitation control, but also a dissolution control, the existence of only one precursor could make the repeatability of the synthesis with different incorporated drugs more secure. As examples of precursors, α-tricalcium phosphate (α–TCP) and dicalcium phosphate dihydrate ($CaHPO_4 \cdot 2H_2O$, DCPD or brushite) have been used in the literature [24,26–28]. The first experiments with α–TCP have been performed by Monma et al. [28], where they have tested different approaches to optimize the new (at that time) and simple innovative method of obtaining OCP. To our knowledge Monma, Graham, and Bigi were the only ones to study the effects of different synthesis parameters on the α–TCP transformation kinetic in more detail [24,28,29]. Utilization of a precursor such as α–TCP limits the pool of unwanted external ion incorporation (e.g., chloride ion (Cl^-)), and if chosen, it could be performed at room temperature, which would also enable the easy in situ incorporation of ions and drugs [30,31]. However, the study of Graham and Brown was performed a while ago and the reaction process was determined only via the X-ray diffraction technique (XRD) and not by using a multiple technique approach to further check the composition of the formed OCP. Other obstacles that have been noticed throughout the literature review is the relatively small amount of the obtained product or no information on how much was obtained, as well as whether the synthesis yield is uniform across the performed characterization techniques.

Having in mind the present limits, the main goal of the manuscript is to shed light on the chemical processes occurring during the α-TCP hydrolysis route towards obtaining OCP as a final product. The subsequent step that we tried to embark on was to perform a tenfold and a hundredfold scale-up of the reaction. Herein, we present a series of experiments displaying the kinetic transformation and a potential pathway of OCP formation from

α-TCP as the initial raw material. Encouraged by the satisfactory preliminary agreement in all the experiments and throughout all the scale-up platforms, we have confirmed the results with a set of preselected characterization methods able to deliver the data on different levels (XRD, Fourier transform infrared (FTIR), Raman spectroscopy, and scanning electron microscopy (SEM)). As no research team has been able to deliver the quantifiable data of the OCP phase purity due to the strong resemblance with apatite, and as many of them do not present an entire picture, in the present manuscript we have assembled the data from the aforementioned techniques and created one joint thread among them. Determining the quantities of present phases with different techniques is still a big challenge, but providing a semi-quantitative approach with combining all the complementary methods is to be of significant value for the scientific community. Additionally, as the end goal of each biomaterial (used for bone tissue engineering) is to enhance the bone reconstruction/neoformation [32], attained final OCPs and the mix of phases from observed kinetic time points have undergone cytocompatibility tests with human bone marrow-derived mesenchymal stem cells (hBMSCs).

Within the current manuscript we have, for the first time, successfully performed a scale-up of the OCP synthesis process and proven the biocompatibility of the hundredfold scaled-up intermediate and final products. Furthermore, as OCP has great potential as a drug delivery vehicle, and as its mechanism of the formation pathway is of utmost importance for the in situ drug loading, we have provided a comprehensive physico-chemical overview of the phase interchange that transpire in the four described steps of the hydrolysis process of α-TCP to OCP. The data have been backed up with XRD, FTIR and Raman spectroscopy, BET, laser granulometry, and SEM in order to create a common thread of information that is usually found in scarce detail.

2. Materials and Methods

2.1. Materials

The following reagents have been used throughout the experiments: diammonium hydrogen phosphate ($(NH_4)_2HPO_4$, ACS, M = 132.05 g/mol, Lot A1015407 628), calcium nitrate tetrahydrate ($Ca(NO_3)_2 \cdot 4H_2O$, ACS, M = 236.15 g/mol, Lot AM1339021 840), and sodium hydroxide (NaOH, ISO, M = 40.00 g/mol, Lot B1289298 624) were purchased from Emsure® (Darmstadt, Germany). Orthophosphoric acid (H_3PO_4, 75%) was purchased from Latvijas Ķīmija, Riga, Latvia. Potassium bromide (KBr for IR spectroscopy, Uvasol®) was purchased from Merck KGaA, Darmstadt, Germany. Low-glucose as well as high-glucose Dulbecco's modified Eagle's medium (DMEM), fetal bovine serum (FBS), and Trypsin EDTA 1X were purchased from Sigma-Aldrich (St. Louis, MO, USA) while penicillin–streptomycin was purchased from Invitrogen (Waltham, MA, USA). Ethanol (EtOH, BioUltra, ≥99.8%, molecular biology grade, CAS: 64-17-5) was purchased from Sigma-Aldrich, USA. The 24-well plates (Ref. N. 30024) were purchased from SPL Life Sciences (Pochon, Republic of Korea). Resazurin sodium salt (Ref. N. R7017-5G, CAS: 62758-13-8) was purchased from Sigma-Aldrich, USA. 4′,6-Diamidino-2-phenylindole dihydrochloride (DAPI, Ref. N. 90229, CAS: 28718-90-3) was purchased from Millipore (St. Louis, MO, USA) and Alexa Flour 594-conjugated phalloidin (Ref. N. A12381) was purchased from Invitrogen. Tween®-20 detergent (Molecular biology grade, CAS: 9005-64-5) and paraformaldehyde (Reagent grade, crystalline, Ref. N. P6148-1KG, CAS: 30525-89-4) were purchased from Sigma-Aldrich, USA. Phosphate buffered saline (PBS) (N.P4417, Lot SLCH0989) was purchased from Sigma-Aldrich, USA. The cell line used for the research has the following specifications: human bone marrow-derived stem cells (hBMSCs, hTERT-BMSC clone Y201bMSCs), isolated previously by James et al. [33] from bone marrow and immortalized through hTERT lentiviral vectors.

2.2. Synthesis Methodology

2.2.1. Synthesis of Amorphous Calcium Phosphate

To prepare α–TCP, later used for OCP formation, amorphous calcium phosphate (ACP) was heat treated. Hence, the synthesis of ACP is first presented. The wet precipitation method was used to synthesize the ACP powder with a Ca/P molar ratio of 1.5. Both 0.29 M $(NH_4)_2HPO_4$ and 0.43 M $Ca(NO_3)_2{\cdot}4H_2O$ were used for this purpose. The pH of prepared solutions was adjusted using 7 M NaOH. The solutions were poured into the beaker at the same time at room temperature and stirred with a magnetic stirrer. Upon the end of the synthesis, the suspension had a pH value of 9.1–9.4. To obtain the product, the suspension was filtered, rinsed, and frozen in liquid nitrogen. Prepared samples were lyophilized (BETA 2-8 LSCplus, Martin Christ Freeze Dryers, Osterode, Germany) for 72 h (1 mbar for primary drying stage and 0.0010 mbar for secondary drying stage).

2.2.2. α-Tricalcium Phosphate Synthesis and Hydrolysis to Octacalcium Phosphate

To obtain α-TCP, the ACP was heat treated at 650 °C (heating rate 5 °C/min, holding time one hour) [34,35]. Prior to continuing with OCP synthesis, α-TCP was fully analyzed and its phase composition was confirmed with XRD. A total of 100 mg of α-TCP were immersed into 50 mL of 0.0016 M H_3PO_4 solution at room temperature, under unremitting stirring (300 rpm), during the 24 h period. pH was monitored throughout the entire time frame. After each selected time point (1 h, 3 h, 6 h, 10 h, 12 h, and 24 h), the collected suspension was centrifuged at 3000 rpm for 2 min, washed several times with deionized water, and dried overnight at 37 °C (Figure S1 in Supplementary Material (SM)). The same α-TCP used for the synthesis was operated as a reference for α-TCP in all measurements. The above described synthesis (100 mg) is further referred as the initial synthesis (IS). The syntheses have been performed more than five times in order to claim the repetitive formation pattern.

2.2.3. Tenfold and Hundredfold Scale-Up

An identical preparation procedure of α-TCP powder was performed for both scale-up levels. The stirring rate for each level of synthesis was increased due to the increased volume. Based on the preliminary findings, after the preparatory tests, the time points for observation have been chosen. An amount of 1.0 g of α-TCP raw material was immersed into 500 mL of 0.0016 M H_3PO_4 (tenfold scale-up, referred to further on as the 10 × SC; 1 g yield). The suspension was under continuous stirring (400 rpm), during the 72-h period. Due to the geometric and volume limitations of the reactor, a used amount of α-TCP powder for the hundredfold scale-up (referred to further on as the 100 × SC; 10 g amount) was recalculated to the total volume of 4.5 L. Stirring was supplied through the overhead mixer (500 rpm) during the course of 180 h. For both set ups, pH was monitored throughout the entire duration of the synthesis. After each selected time point, the collected suspensions were centrifuged at 3000 rpm, for 2 min, washed with deionized water, and dried at 37 °C. The syntheses have been performed more than five times in order to claim the repetitive formation pattern.

2.2.4. Octacalcium Phosphate Formation Pathway

The kinetic transformation and mechanism of OCP formation were followed on each level (IS, 10 × SC and 100 × SC). For IS, samples have been taken at 1 h, 3 h, 6 h, 10 h, 12 h, and 24 h. For 10 × SC, samples have been taken at 24 h, 48 h, and 72 h. For 100 × SC, samples have been taken at multiple time points out of which 1 h, 24 h, 30 h, 48 h, 78 h, 96 h, 144 h, and 180 h have been focused on in the main manuscript, as they exhibited the important changes. The list of all analyzed samples at different time points and their presentation within the manuscript and SM have been described in Table S1. Because of the small initial amount of the α-TCP powder used, IS was performed individually for each time point. The amount of 50 mL of samples from tenfold and hundred-fold scale-ups was collected from a 600 mL and five L reactor, respectively. Each sample taken was operated

according to the steps described in Sections 2.2.2 and 2.2.3. Figure S1 in Supplementary Material summarizes the experiment methodology.

2.3. Phase and Composition Characterization

2.3.1. X-ray Diffraction

The presence of crystalline phases in all obtained samples was examined by using X-ray powder diffractometry (XRD). XRD was performed using PANalytical Aeris diffractometer (The Netherlands) and accompanying analyses were performed with suitable software (X'Pert Data Collector, X'Pert Data Viewer, X'PertHighScore and the International Centre for Diffraction Data PDF-2 (ICDD) database). To obtain the XRD pattern, the following parameters were used: 40 kV and 15 mA, step size 0.0435°, within 2θ range from 3° to 60°, time per step 299.575 s. The quantitative amount of the observed phases was determined with the Rietveld refinement procedure by using Profex software [36]. For crystalline phase identification following, ICDD entries were used—#026-1056 for OCP, #01-072-1243 for hydroxyapatite (HAp), #009-0077 for DCPD, and #009-0348 for α-TCP. The analysis was also conducted on the performed preliminary synthesis in order to claim the repetitive formation pattern, and the final one was presented in the manuscript.

2.3.2. Fourier-Transform Infrared Spectroscopy

The Fourier-transform infrared spectrometer Nicolet iS 50 (Thermo Scientific, Waltham, MA, USA) was used in transmission mode with the potassium bromide (KBr) pellet method, which was employed to characterize functional groups of powders at the molecular level. The FTIR spectra were recorded in the range of 4000–400 cm^{-1}, with 64 scans at a resolution of 4 cm^{-1}. The processing software was OMNIC 9.6.251. The shape of the bands was considered to be Gaussian and/or Lorentzian. Spectral subtractions have been performed with the OMNIC software. The analysis was also conducted on the performed preliminary synthesis in order to claim the repetitive formation pattern, and the final one was presented in the manuscript. The measurements were reproducible, with an approximate error of ±0.3 absorbance units due to both signal noise and variability in the sample preparation.

2.3.3. Raman Spectroscopy

Powders were analyzed by using a confocal RAMAN LabRAM HR 800 microscope (Horiba Jobin Yvon, Japan). The samples were subjected to continuous laser radiation stemming from a diode laser at 532 nm (power: 12 mW) under an Olympus BX 41 microscope. Focus was achieved by an objective ×100 with a numerical aperture of 0.9 that provided the system with a lateral resolution of 0.72 μm and an axial resolution of 2.61 μm. Spectra were acquired using 600 and 1800 lines/mm grating, with a spectral resolution of 2 and 0.6 cm^{-1}, respectively. The spectra were evaluated and decomposed with LabSpec 6 software. Additionally, spectral decompositions were performed, following the subtraction of a linear baseline, in the 1200–800 cm^{-1} domain corresponding to the ν_1 and ν_3 vibrational domains of phosphate species. Furthermore, to confirm the homogeneity of each sample, a DuoScanTM imaging system was applied to perform the macro-scale mapping (50 μm × 50 μm size) of the samples. The measurements were reproducible with an approximate error of 1–2 wavenumber units due to the machine signal noise and calibration preparation.

2.4. Physical Characterization of the Powders

2.4.1. Brunnauer–Emmet–Teller Method

Specific surface area (SSA) of the powders was determined by using the Brunnauer–Emmet–Teller method (BET) (ISO 9277:2010, QUADRASORB SI and Quadra Win) on a nitrogen adsorption–desorption isotherm obtained at −196 °C. Prior to applying the method, samples were degassed for 24 h at 25 °C (Autosorb Degasser Model AD-9) to remove any excess of moisture and vapors. The results were shown as an average value ± standard deviation from three replicates.

2.4.2. Laser Granulometry

The particle size distribution of the starting α-TCP powder, 10 × SC and 100 × SC, was determined using laser diffraction granulometer (Malvern Mastersizer 3000) in dry mode. Additionally, the median size $d_{0.5}$ of α-TCP, analogous to a volume cumulative percentage of 50%, was determined. The results were shown as an average value ± standard deviation from three replicates.

2.4.3. Scanning Electron Microscopy

The surface morphology of the final OCP particles/phases and other key transient steps/phases was visualized using a scanning electron microscope (SEM, Tescan Mira\LMU, Tescan, Czech Republic). Sample image generation was performed with secondary electrons, created at an acceleration voltage of 30 kV. Samples were secured with an electrically conductive double-sided adhesive carbon tape on a standard aluminium pin stub. Prior to the SEM measurement, samples were sputter coated with gold, using Emitech K550X (Quorum Technologies, Lewes, UK) sputter coater.

2.5. In Vitro Biological Studies

2.5.1. In Vitro Cytocompatibility Evaluation

Human bone marrow-derived mesenchymal stem cells were employed to estimate the preliminary cytocompatibility of transient phases that were obtained during the synthesis. The cells were cultivated in low-glucose Dulbecco's modified Eagle's medium, supplemented with 15% fetal bovine serum and 1% penicillin -streptomycin at 37 °C in an incubator with a 5% CO_2 and humidified atmosphere. The prepared samples were sterilized for three hours in 70% ethanol, washed two times with PBS, and soaked in the complete culture medium overnight. After overnight incubation, the conditioned medium was exchanged with the fresh culture medium.

The in vitro cytocompatibility evaluation of the powders was performed in direct contact with hBMSCs. The 24-well plates were used for seeding the cells in a defined concentration (2×10^4 cells/well). Seeding was completed four hours before the addition of the samples. The powders were suspended in the culture medium in the concentration of 0.5 mg/mL. The in vitro set up was cultivated for three days with a daily change of the culture medium. Morphology of the cells was monitored throughout the experiment via light microscopy. During three days, the metabolic activity of the hBMSCs was assessed every 24 h, using the fluorimetric resazurin reduction assay in accordance with the manufacturer's instructions. The samples were incubated for four hours and successively evaluated with a spectrofluorometer (Spark, Tecan Trading AG, Mannedorf, Switzerland), using an excitation wavelength of 530 nm and an emission reading of 590 nm.

2.5.2. Cell Phenotype Morphology

Morphology of the cells, after the three-day direct contact with the powder specimens, was evaluated via immunofluorescent imaging (IF). DAPI was used to label the cell nuclei, while Alexa Fluor 594-conjugated phalloidin was used to visualize cytoskeleton f-actin filaments. Briefly, samples were washed with PBS and fixed for 20 min with 4% paraformaldehyde. Subsequently, they were washed twice with PBS to elute the fixative and sample powder residues, and then stained with a mixture of DAPI and phalloidin in 0.5% Tween®-20 for one hour. Stained samples were checked using the digital light microscope (Invitrogen EVOS Floid, from Thermo Scientific, Waltham, MA, USA).

2.5.3. Statistical Analysis

In all of the experiments, if applicable, each group of samples was represented by three or six replicates. Results were shown as the mean value ± standard deviation. When comparing groups of samples, analysis was performed in Prism (v8, GraphPad Software, San Diego, CA, USA), using the one-way ANOVA, Tukey's post hoc analysis, and normal

distribution Shapiro–Wilk's test. For every comparison performed, the difference was considered as significant for $p < 0.05$.

3. Results

To be as certain as possible in the phase determination of the presented CaP phases, a detailed description of each characterization technique has been reported in the following sections. As the task of determining quantitatively the crystalline phase content has proven to be a tremendous challenge, the semi-quantitative analysis has been presented. The importance of a whole picture gained from multiple methods underlines the fact that assessing the phase identity (or alterations of chemical compositions—non-stoichiometry, variable hydration level, etc.) based on one single technique is not possible.

3.1. Phase and Composition Characterization

Prior to starting the OCP synthesis, thermal transformation of ACP (SSA 72 ± 14 m^2/g, $d_{0.5}$ = 75 ± 5 µm) to α-TCP was confirmed using XRD analysis (Figure S2). Characteristic maxima of α-TCP were in accordance with the reference XRD pattern provided by the ICDD (Figure S2a). FTIR and Raman spectroscopy analyses efficiently followed the XRD data, with specific α-TCP bands clearly discernible in the spectrum (Figure S2d,e). The median particle size ($d_{0.5}$) determined by the laser diffraction granulometry was 37 ± 3 µm (Figure S2f), while the specific surface area was 8.8 ± 0.2 m^2/g. SEM micrographs displayed the morphology of α-TCP aggregates (Figure S2b,c). The starting precursor for OCP was quantified and the powder was composed of 99% α-TCP (based on the Rietveld calculation, Profex software). Additionally, the as-synthesized low temperature α-TCP exhibits a higher SSA than the previously synthesized high temperature α-TCP [37]. Moreover, it was also higher than the α–TCP used previously for OCP formation. Indeed, the α-TCP used in the study of Bigi et al. [29] was milled and, according to the literature, SSA increases with milling, which still remained relatively low [38]. Furthermore, α-TCP production process in this study was characterized by the lower energy consumption coupled with a lower CO_2 footprint [34,35].

3.1.1. X-ray Diffraction

The XRD pattern allows for the identification of the three main crystalline phases, with variable ratios according to the hydrolysis time: α-TCP, DCPD, and OCP. No halo or background irregularity, suggestive of an amorphous phase, were detected. The data obtained reveal that despite a constant liquid to solid ratio of the precursors, the time of the OCP synthesis has increased with the amount of the initial α-TCP used. Hence, the end of the synthesis increased with the scale-up level. The final OCP phase was attained after 24 h, 72 h, and 180 h for IS, 10 × SC and 100 × SC, respectively (Figure 1). All the X-ray diffraction peaks observed at low angles are characteristic of the OCP triclinic structure. A low angle (100) maximum at 2θ = 4.7 degrees and a doublet at 9.4 and 9.7 (200 and 010) 2θ degrees, respectively, were clearly seen (Figure 1). However, the 25–35° 2θ maxima present in the OCP structure are not very well resolved and they are also overlapping with the XRD maxima of apatite, the main impurity often reported in OCP preparation (Figures S3–S6). In reference to the intensity of the maximum at 4.7 degrees, IS (Figure S3) and 10 × SC have exhibited a higher intensity, while the overall crystallinity (observed from the peak height and resolution) appears to be the highest in 10 × SC (Figure S4).

A detailed progression of the OCP phase formation has been followed as a function of time. Due to the great number of samples (Table S1), analysis of the vital time points of the 100 × SC synthesis (1 h, 24 h, 48 h, 78 h, 96 h, 144 h, and 180 h) and final OCP phases will be shown in the main manuscript, while other time points can be found in the SM, as indicated in Table S1. XRD patterns have shown the gradual transition from the α-TCP phase via DCPD to the OCP phase, while their presence was shifting in dependence to the observed time point (Figure 2). Visually noticed changes were accompanied by the fluctuation in pH values (Figure 2). The same phase transformation pattern has been

observed across all scale-up levels, and evolution of the crystalline phase went from the α-TCP as a starting point to the mix of α-TCP, DCPD, and OCP and finally to the OCP phase. As it was mentioned, the apatite phase has a strong resemblance to OCP, thus the corresponding reference patterns have been added throughout the graphs.

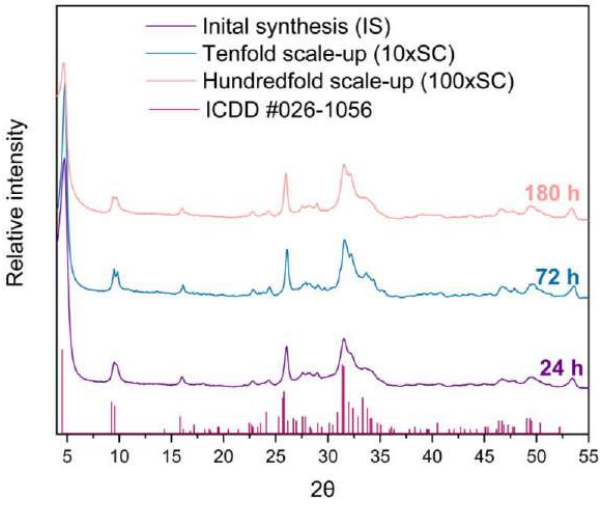

Figure 1. XRD patterns of final OCP powders obtained in three levels of scale-up. The reference simulated pattern (ICDD entry #026-1056) corresponds to the main maxima of the OCP triclinic phase.

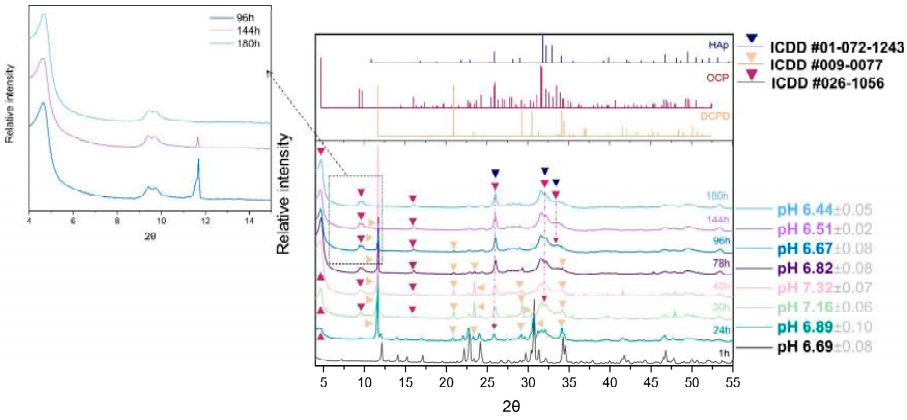

Figure 2. Hundredfold scale-up (100 × SC): sequence of XRD patterns illustrating the gradual transition from α-TCP phase via DCPD to OCP phase at pivotal time points chosen due to the prevalent, visually noticed change, accompanied by the fluctuation in pH values.

By using the Rietveld refinement, the progression of the 100 × SC phases formation based on the XRD method has been quantified and displayed in Figure 3 and in Section 3.2 (together with SEM micrographs in the Section 3.2). The progression of the time of the CaP phase interchange was an evolution from ~100% of α-TCP (in the first hour) to ~37% of DCPD and ~63% of OCP (at 27 h) and ended with ~100% of OCP. The OCP ratio versus the reaction time of IS and 10 × SC, authenticated via XRD patterns, can be found in the Supplementary Materials (Figures S3 and S4, respectively). Moreover, additional kinetic time points of the 100 × SC OCP formation can be seen in Figures S5 and S6.

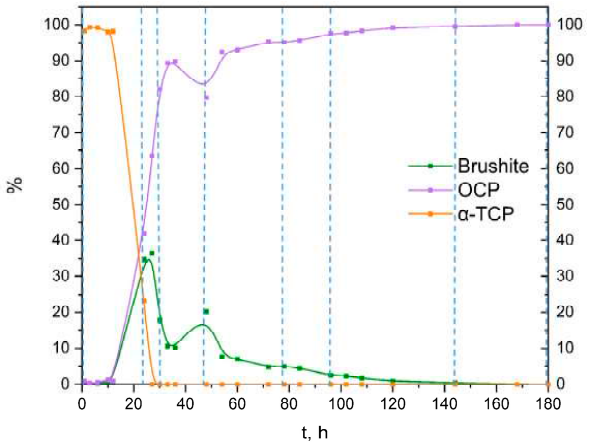

Figure 3. Quantitative analysis of the crystalline phases involved in the α-TCP transformation to OCP, based on XRD data from 100 × SC (after Rietveld refinement using Profex software [36]); vertical lines present the time points analyzed in detail in the main manuscript.

3.1.2. Fourier-Transform Infrared Spectroscopy and Raman Spectroscopy

The ν_1 P–O stretching mode clearly displayed the strongest lines expected for the OCP phase in Raman (Figure 4B), whereas in FTIR it was the ν_3 P–O stretching mode at 1300–1000 cm^{-1} (Figure 4A). In addition, characteristic vibrations of HPO_4^{2-}, which despite being weak, differentiate the OCP from stoichiometric HAp and were clearly seen at 917, 875, 1007, and 1295 cm^{-1} (blue and green shading, Figure 4A). The OCP samples often show unexpected OH^- vibration modes at 3570 cm^{-1} (stretching mode) and 633 cm^{-1} (libration mode) related to the evolution of the structure towards the more stable HAp [39]. The assignment of the line at 633 cm^{-1} to HAp impurities in OCP has been discussed and, according to Fowler, could correspond also to the water libration line of OCP [40]. A very faint OH^- stretching line can be distinguished as a shoulder on the strong H_2O stretching line in the long lasting 10 × SC and 100 × SC syntheses (orange shading in Figure 4A). Furthermore, it can be noticed that 100 × SC absorbance bands (Figures 4A and 5B1,B2), in the region from 1130–1020 cm^{-1} (blue shading Figure 4A), seem to be somewhat less resolved, which could signal a lower crystallinity of OCP in comparison to lower scale-ups (IS and 10 × SC) [41].

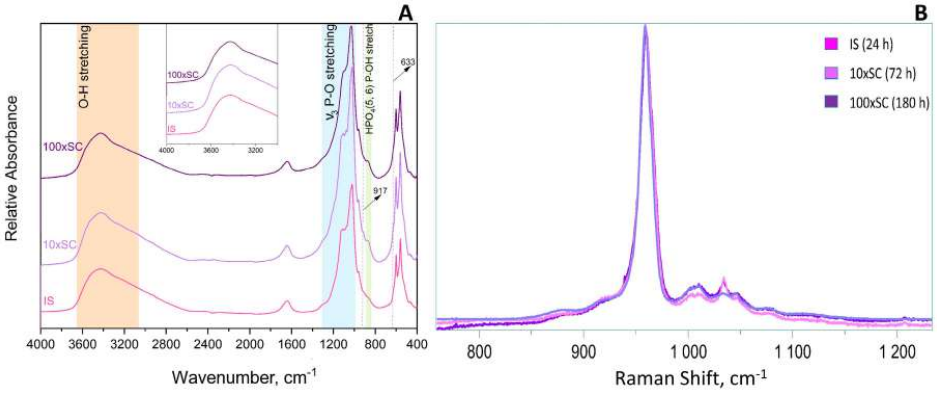

Figure 4. FTIR (**A**) and Raman (**B**) spectra of final OCP phases obtained in three levels of scale-up.

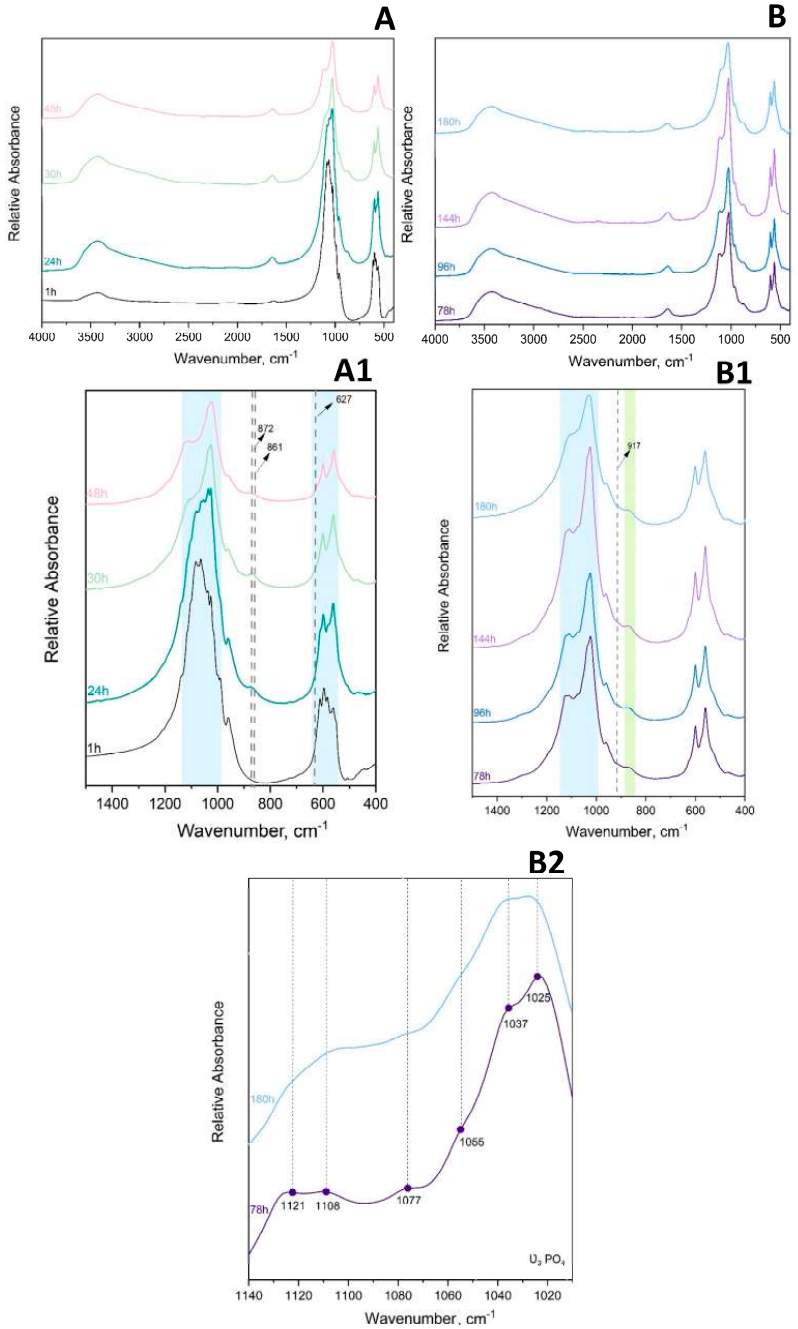

Figure 5. FTIR (**A**,**A1**) absorbance spectrum of 1 h–48 h 100 × SC and (**B**,**B1**,**B2**) of 78 h–180 h 100 × SC. Green shadowed area is marking the narrow range of HPO_4 (5, 6) P–OH stretch and blue shadowed area corresponds to PO_4 stretching.

FTIR Spectroscopy

The main observations in the IR spectrum were as following: within the first 12 h of 100 × SC, the most intense bands of α-TCP in the PO_4 region are barely observed (1300–900 cm^{-1} domain and 700–500 cm^{-1} domain). Almost no spectra changes in the period between 33 h and 180 h period were noticed (Figure 5A–B1, Figures S10 and S11). The ν_3 stretching mode of PO_4^{3-} and HPO_4^{2-}, at 1077 cm^{-1}, 1093 cm^{-1}, and 1121 cm^{-1}, with the faint but characteristic line of OCP HPO_4(6) [P-(OH)], stretch at 917 cm^{-1} and O–H in-plane bending around 1295 cm^{-1} were clearly seen at the 78 h time point (Figure 5B2). The H_2O stretching mode of structural water, allocated to DCPD (~3500 cm^{-1}), was observed at 24 h of 10 × SC (Figure S9), as well as in the initial synthesis at 10 h and 12 h (Figure S8) [42,43]. The DCPD characteristic absorbance band at 790 cm^{-1}, which corresponds to a broad libration water line, has been noticed at 24 h 10 × SC (Figure S9).

To enhance the sensitivity of FTIR spectroscopy, spectral subtractions have been performed to remove overlapping absorbance, improve absorbance bands of interest, and/or to try to further discern the DCPD bands [44]. Following this approach, we have subtracted the absorbance bands of the final 100 × SC OCP phase 180 h and 100 × SC 78 h time point (Figure S12) and between the 78 h/48 h time point of 100 × SC (Figure S12). The main reasoning was due to the previously mentioned observation that even at the 78 h point, OCP was well transformed. Furthermore, the spectral subtraction has been additionally applied on the 10 × SC 72 h/24 h-time point (Figure S13) to enhance the DCPD band vibrations even more. The spectrum of the 100 × SC 180 h/78 h subtraction has not revealed a significant difference other than the more pronounced bands at 2900 cm^{-1} (connected with CH stretching of organic impurities possibly generated by wear particles resulting in a long stirring time) [43]. The subtraction result of 78 h/48 h and 10 × SC 72 h/24 h had substantially more DCPD bands within a very broad 3000 cm^{-1} region and was also masked in the $\nu_{1,3}$ PO_4 region. Moreover, for the 10 × SC 72 h/24 h, a very expressed broad band at 790 cm^{-1} corresponding to the out-of-plane bending of the HPO_4^{2-} in DCPD was revealed via subtraction.

Raman Spectroscopy

Analogous to FTIR, a clear transition from α-TCP powder to a sample where OCP is in majority was noticed in the first 24 h of 100 × SC (Figure 6). The bands with a strong intensity were mostly located in the region between 900–1000 cm^{-1}, which corresponds to the ν_3 triple-degenerate asymmetric P–O stretching mode and partly to the ν_1 symmetric P–O stretching vibration. After the 30 h time point, the presence of the characteristic α-TCP band arrangements evolved to OCP (Figure 6). The 964 cm^{-1}, 976 cm^{-1}, 984 cm^{-1}, and 998 cm^{-1} bands have vanished, and the most prominent band at 958 cm^{-1} also present in OCP has remained. Over the time period, this broad band evolved into a massif, composed of two more marked bands at 965 and 958 cm^{-1} that were characteristic of OCP (Figure S18). The low resolution of this massif could indicate a poorly crystallized OCP phase. Furthermore, the second derivative of the Raman spectra did not reveal the presence of the apatite phase, which could attest to OCP, although the detection of a poorly crystalline apatite would not be easy to detect in this system with broad lines.

In order to determine the homogeneity of the samples, Raman analyses carried out in micro spot were confronted with an analysis in macro spot (having a beam size of 50 × 50 μm (duoscan)) for each time point in 100 × SC. For the beginning time points of OCP formation (up to 12 h), the samples presented a homogeneous composition of α-TCP, but above this time point and up to 48 h, several signatures comprising different phase ratios were observed (Figure S16).

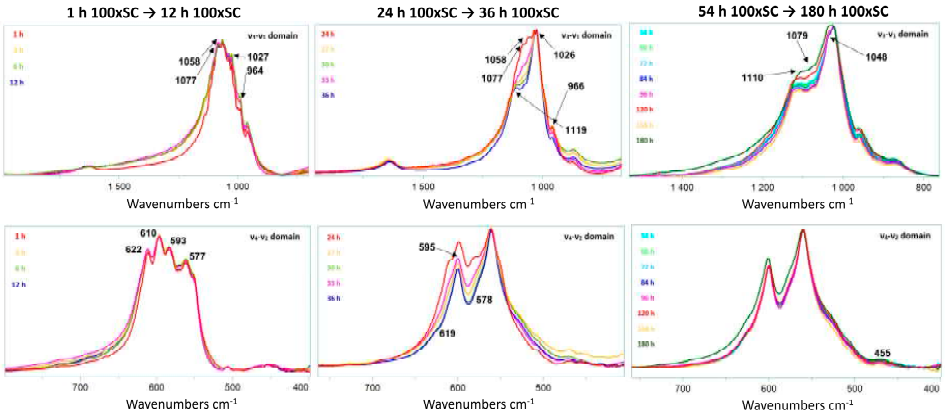

Figure 6. Raman spectra of the OCP formation as a function of time in 100 × SC. The graph displays a close up of ν_1–ν_4 stretching mode of the P–O vibration. Assignment of the highlighted bands can be found in Table S2.

3.1.3. Specific Surface Area and Particle Size

Specific surface area results have been reported in the Table 1. High SSA values of all the final OCP phases may have an impact on the physicochemical and biological reactivity of the material.

Table 1. Specific surface area of the starting precursor and the final OCP phases at all levels of scale-up.

	α-TCP	**OCP, IS**	**OCP, 10 × SC**	**OCP, 100 × SC**
SSA, m^2/g	9.0 ± 0.6	53 ± 6	66 ± 5	63 ± 8

Particle size distributions have been presented in Figure S21. The starting α-TCP precursor had a monomodal curve (Figure S2f), and every transformation time point analyzed exhibited bimodal curves. The final OCP phases in both scale-up levels had the smallest primary particle size in the range of 5–25 µm, equaling to a ~5% volume fraction. However, the presence of the secondary distribution in the range of 150–500 µm indicated that the primary particles were unevenly agglomerated. Considering that the measurement has been conducted on the dry powder samples, the release of pressure applied during the analysis might not have been strong enough to separate certain agglomerates. Since the size of the individual OCP crystals appears to be smaller than several µm (Figures 7, 8 and S21), small, loosely aggregated OCP plate-like particles could be denoted as nano-submicro OCP. Moreover, high SSA is a strong indicator of submicro size, at least in one dimension.

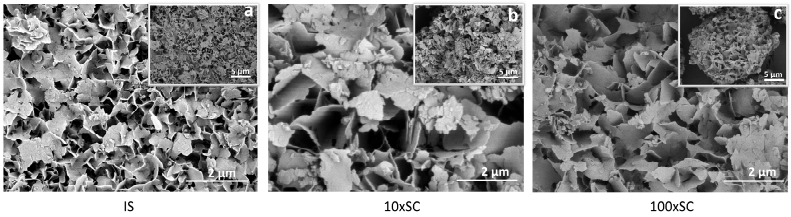

Figure 7. SEM micrographs of the final OCP phases (scale bar 5 µm (top right) and 2 µm (bottom right)): (**a**) initial synthesis (24 h time point), (**b**) tenfold scale-up (72 h time point), and (**c**) hundredfold scale-up (180 h time point).

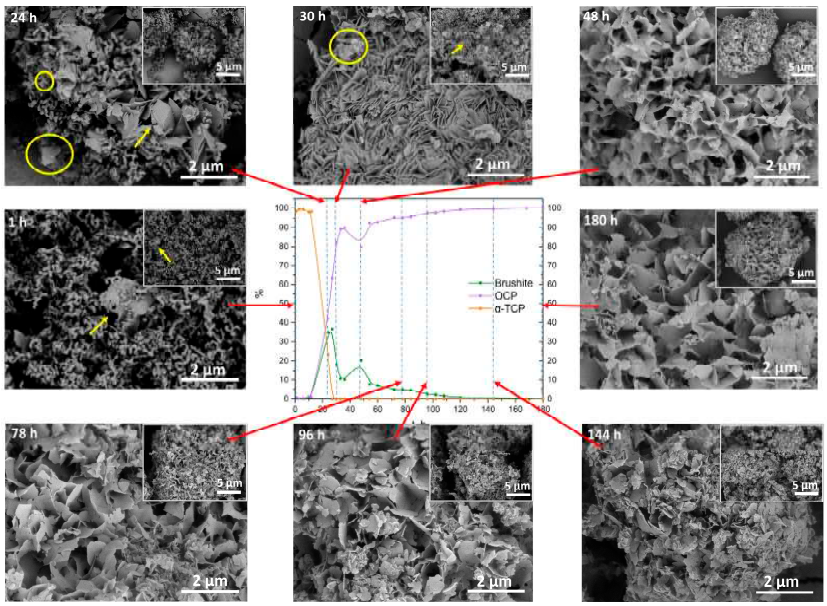

Figure 8. Scanning electron micrographs of α-TCP transformation to OCP (100 × SC), observed at specific time points (1 h–180 h) indicated on each SEM image (scale bar 5 µm and 2 µm) and connected (red arrow) to the according point (dashed line) in the phase content diagram based on the XRD quantitative data. Yellow arrow indicates possible DCPD crystals, while the yellow circle is marking the potential OCP plates.

3.2. Morphology Characterization

The final OCP phases exhibited plate-like morphology, with crystals having uneven edges and being approximately 100-nm thick (Figure 7). The plates seemed to be 1–3 µm in width, with smaller chipped plates being one over the other, indicating that OCP plates grew over the larger DCPD plates. In all scale-up levels, agglomeration took place and thin plate-like crystals formed loosely packed agglomerates (Figures 7, 8, S19 and S20).

When the individual follow-up time points were observed via SEM, a clear change in the phases could be seen. After 1 h of 100 × SC, the sample contained thin thread-like crystals of α-TCP, however, small needle- or plate-like crystals started to appear within the α-TCP aggregates (Figure 8, 1 h). As the synthesis progressed, at the 24 h and 30 h time points (Figure 8, 24 h, 30 h), a gradual increase to larger and thicker plate-like particles was observed. It could be concluded that the larger and substantially more massive plates at those time points were attributed to DCPD (marked with an arrow) and smaller thinner plate-like crystals of OCP started to form (marked with a circle). However, this is hard to differentiate due to the high morphological similarity of the two crystals/phases. The same trend was observed with the initial time points of IS (Figure S19) and 10 × SC (Figure S20). Throughout the rest of the synthesis, a roughly uniform appearance of the crystals remained. Crystals stayed in the same plate-like shape, with noticed fragmentation of the larger particles and continuous presence of the spherical aggregates.

3.3. In Vitro Biological Assays

3.3.1. Cell Viability Assessment

To evaluate the cytotoxicity of the final and the transient powders, samples were incubated in direct contact with hBMSCs for 3 days at the concentration of 0.5 mg/mL. Samples were considered non-compatible with hBMSCs, if the cell viability was lower than

70% following ISO 10993-5:2009(E) [45]. The resazurin reduction fluorimetric assay showed a decrease in the metabolic activity of cells in contact with powders in comparison to cells on polystyrene. However, on the third day of cultivation, only five types of seventeen tested samples—10 × SC 24 h, 10 × SC 72 h, IS 1 h, IS 3 h, and IS 10 h—resulted in the hBMSC metabolic activity being slightly lower than the 70% threshold, while the other time points of each scale-up were above the threshold and thus were considered cytocompatible (Figure 9). Compared to the control group, represented by the cells grown on polystyrene, three out of five non-cytocompatible samples led to a significant decrease in the metabolic activity of hBMSCs (10 × SC 24 h, IS 1 h, and IS 3 h).

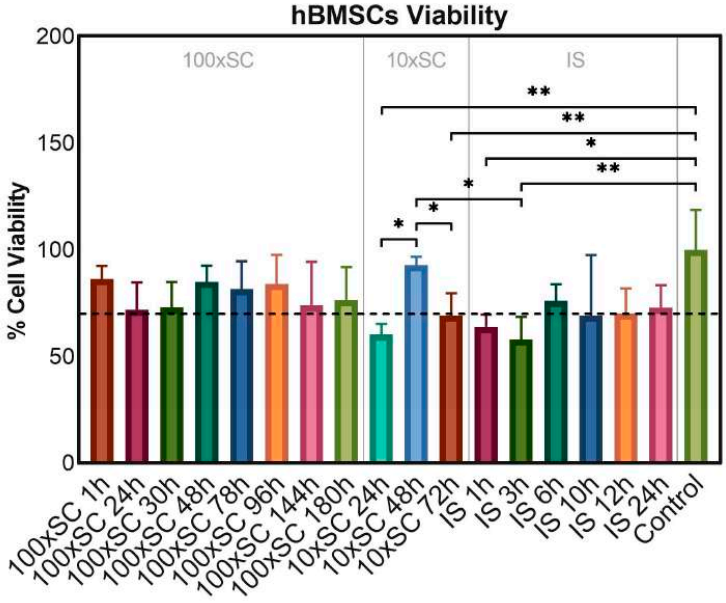

Figure 9. In vitro cell viability of the final and the transient powders after three days of incubation in direct contact with hBMSCs. 'Control' series represented cells cultivated on polystyrene without CaP samples. Error bars represent the mean ± standard deviation of three replicates. Multiple comparisons were performed on relative fluorescent units via one-way ANOVA with Tukey's correction; significant differences between groups of samples were indicated with asterisks (* for $p \leq 0.05$, ** for $p \leq 0.01$).

3.3.2. Cell Phenotype Morphology

Confirming the results obtained in the metabolic activity assay, microscopy revealed a normal spread, attachment, and morphology of the cells incubated in direct contact with the 100 × SC samples (Figures S22 and 10) when compared to cells cultivated on polystyrene (Figure S22, 'Control'). Samples from the group of tenfold synthesis (10 × SC) demonstrated an uneven spread and lower confluence of the cells in the observation area, and more importantly, the presence of a relatively large amount of powder particles (Figure S23). The most cytotoxic result within this scale-up, in terms of the resazurin reduction assay (IS 3 h sample series—58 ± 10.6% cell viability), demonstrated an even spread of slightly larger agglomerates, while in the comparably toxic series of IS 1 h (64 ± 5.7% cell viability) the agglomerates were smaller with a same even spread. The morphology of the cells in the group was not altered.

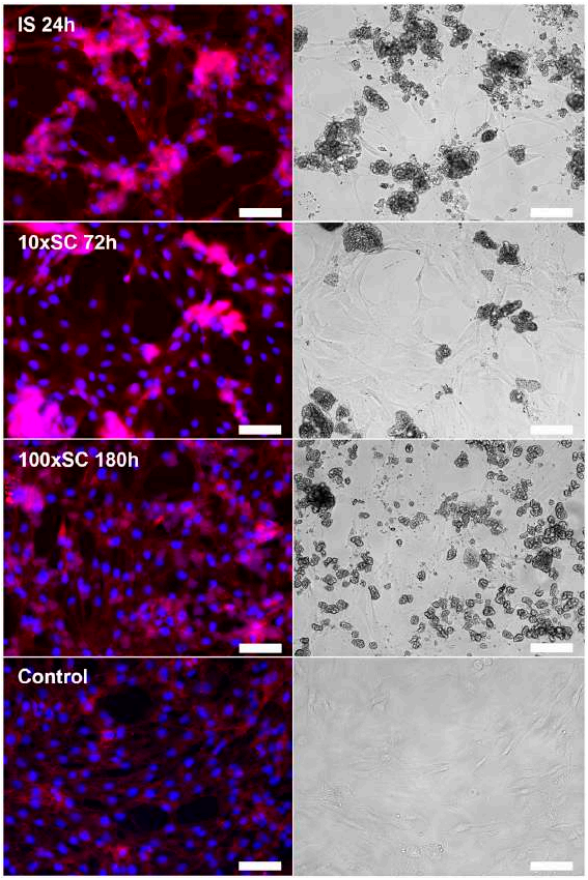

Figure 10. hBMSCs morphology on the third day of cultivation in direct contact with final OCP samples (IS, 10 × SC and 100 × SC) in the concentration of 0.5 mg/mL. Control represented cells on polystyrene. Immunofluorescent (**left** column) and bright-field (**right** column) microscopy. Image bar scale: 125 μm.

4. Discussion

4.1. Phase and Composition Characterization

4.1.1. X-ray Diffraction

In general, the OCP formation via the hydrolysis of α-TCP is represented by the following chemical equation [41].

$$3\,Ca_3(PO_4)_2 + 7\,H_2O \rightarrow Ca_8(HPO_4)_2(PO_4)_4{\cdot}5H_2O + Ca(OH)_2 \quad (1)$$

This global reaction induces an increase in the solution pH, related to the proton uptake by PO_4^{3-} groups in the OCP phase and a corresponding release of soluble $Ca(OH)_2$. As it was seen in Section 3.1.1, the time of the OCP synthesis has increased from the initial 24 h to 72 h and to 180 h for IS, 10 × SC and 100 × SC, respectively (Figure 1). The X-ray diffraction maximum that was observed at low angles is characteristic of the OCP triclinic structure (4.7 2θ degrees). However, this most intense and very specific peak of the OCP structure is superimposed to the X-ray diffusion background and not easily accessible. In addition, one must take into consideration that due to the plate-like morphology of

OCP, preferential orientations can appear, which strongly affect this peak's intensity. This is why different authors often consider the doublet at 9.4 and 9.7 2θ degrees as a factual representative of the OCP triclinic phase [9,28,46,47]. As it was mentioned before, the same crystalline phase evolution has been seen across all scale-up levels (α-TCP, mix of α-TCP, DCPD and OCP, and finally OCP). Thus, the XRD patterns of samples collected at different synthesis time points clearly show that global reaction one, describing the direct conversion of α-TCP into OCP, is inadequate, as the DCPD has been identified as an intermediary phase during this reaction (Figures 2 and S3–S6). Within the suspension medium, the pH variations are sensitive indicators of the chemical reactions involved, which allow us to clarify the different steps of this conversion. Hence, several steps were distinguished as follows.

Dissolution

At the beginning, the 0.0016 M phosphoric acid solution pH was 2.80 ± 0.15. At the addition of the α-TCP powder, a rapid increase in pH was observed, which stabilized at 6.69 ± 0.08 at 1 h. This first event corresponded to the fast dissolution of α-TCP according to reaction two (proposed for a 6.7 end pH):

$$Ca_3(PO_4)_2 + 3\,H_2O \rightarrow 3\,Ca^{2+} + H_2PO_4^{-} + HPO_4^{2-} + 3\,OH^{-} \quad (2)$$

This step, implying a release of OH^-, puts the reaction medium at a pH close to neutrality, thus corresponding to the buffering zone of orthophosphate anions (Figure S7).

Precipitation

Considering the solubility of α-TCP (and to some extent, the initial acidic dissolution, followed by a strong pH variation towards alkaline medium), the solution obtained is highly supersaturated with respect to OCP, DCPD, and also HAp. A strong advantage of OCP and DCPD is that they show a better ability to nucleate and grow (higher crystallization rates) than HAp [48–50]. The formation of these phases from the ions in the solution corresponds to the release of protons and the decrease in pH.

Growth Step of DCPD and OCP Phases

The α-TCP to DCPD conversion appeared to be much faster than that of α-TCP to OCP, which was in accordance with the crystal growth rate of these two compounds [10]. The reaction of DCPD growth from the α-TCP hydrolysis is as follows:

$$Ca_3(PO_4)_2 + 3\,H_2O \rightarrow 3\,Ca^{2+} + H_2PO_4^{-} + HPO_4^{2-} + 3\,OH^{-} \quad (3)$$

implying that, like for OCP formation (Equation (1)), an alkalinization of the solution and these two reactions (Equations (1) and (3)) raise the pH up to 7.32 ± 0.07 (Figure 2). At the onset of the highest pH value (48 h 100 × SC), the strongest X-ray diffraction peak of DCPD, the (020) reflection, becomes noticeably more intense than any other diffraction peak maximum (Figure 2).

DCPD to OCP Conversion Step

When α-TCP has been completely dissolved, DCPD became the most soluble phase of the system and also the precursor for the conversion into OCP, which corresponds to the historically most used preparation method of OCP (Equation (4)) [39]:

$$8\,CaHPO_4{\cdot}2H_2O \rightarrow Ca_8(PO_4)_4(HPO_4)_2{\cdot}5H_2O + 2\,H_3PO_4 + 11\,H_2O \quad (4)$$

This reaction results in a release of protons in the solution, which has been attenuated in the system due to the buffering properties of the present phosphate medium, resulting with the final pH of 6.44 ± 0.05.

4.1.2. Fourier-Transform Infrared Spectroscopy and Raman Spectroscopy

In order to delve deeper into the analysis of the α-TCP to OCP formation pathway and to get the information on the phases at the molecular level, FTIR and Raman spectroscopy have been employed as the chosen techniques. In addition, as the unit cell of OCP contains two HPO_4 crystallographic sites, labelled HPO_4(5) and HPO_4(6), their P–(OH) stretch and OH in-plane bend cannot be distinguished via the XRD method. Therefore, the IR and Raman spectra can help in discerning the progressive hydrolysis. The spectra of the final OCP phases (Figure 4) were in agreement with the XRD patterns and with the data provided in the literature (Table S2). By observing the analysis provided via the FTIR technique, it can be seen that the analysis of the phase transformation between the first occurrence of the OCP phase and the end of OCP formation does not fit well with the XRD results (24 h for 100 × SC and 10 × SC, 10 h for IS). The extreme anisotropy of the DCPD crystals or extreme ordering of them have resulted in a relatively high phase presence in XRD (up to ~36% at 27 h for 100 × SC), but in the FTIR and Raman spectra DCPD has been barely noticed. The α-TCP phase appears also difficult to detect in mixtures due to the profusion of expected lines associated with a dispersion of their intensities. As it is difficult to monitor the progression of OCP and its potential evolution with time via FT-IR spectroscopy, the main focus will be placed on the most important lines that separate it from both the transitional phases and from the possible presence of calcium-deficient apatite (CDHAp) (which can also be obtained after ageing). The spectral data throughout the literature have suggested that the main difference between the spectra of OCP and the apatite phase reside in HPO_4^{2-} vibration lines [3,40,51–53]. Thus, the assignment of HPO_4^{2-} lines bending and O–H stretching modes with bands connected with H_2O will be highlighted.

Assignment of HPO_4^{2-} Ion bonds

By observing a single OCP unit cell, six phosphate groups can be differentiated (P1–P6). P1–P4 can be found within the apatite-like layer, distributed on two triangular sets (two Ca^{2+} and two PO_4^{3-} per each set), while the remaining two (P5, P6) are serving as a connection bridge between the two asymmetrical cell units [52]. During the phase transformation from OCP into CDHAp, a decrease in HPO_4(6) happens first (in regard to HPO_4(5) which is close to the vibration line of an apatitic HPO_4). The most significant HPO_4 lines assigned to OCP are: 1295 cm^{-1} assigned to the OH in-plane deformation mode and 917 cm^{-1} to the P(6)–(OH) stretch of a strongly hydrogen-bonded HPO_4^{2-} ion [40,52,53]. For all the assignments see Figures 5 and S8–S11.

O–H Stretching Modes and Bands Connected with H_2O

Even though the OCP spectral range between 2500 and 3700 cm^{-1} has been portrayed by a very broad absorbance band (with an overtone and combination bands present), it shows an important distinction from apatite. The lack of a recognizable 3572 cm^{-1} OH^- band for HAp is one of the indicators of a pure unaltered OCP formation (or at least with minimum HAp presence) [40]. Another rather characteristic OH^- line at 633 cm^{-1} is assigned to the OH^- libration movement in HAp. A line is also found in this range (627 cm^{-1}) as a shoulder in OCP, which has been assigned by Fowler et al. to a libration movement of the H_2O(4) water molecule of OCP. Thus, only the OH^- stretching line at 3572 cm^{-1} is a marker of HAp formation, which has not been detected.

The small presence of DCPD noticed in the spectrum recorded for 100 × SC could be attributed to the heterogeneity of the sample. As DCPD crystals tend to be larger in size, even a small number of them in the whole batch could be recognized using the XRD method. Nevertheless, for FTIR analysis (Figures 5 and S8–S11), a considerably smaller amount of specimen is used, hence a probability of missing the crystals in the composition is possible.

Similar to FTIR, Raman band vibrations are also closely packed and most of the time are overlapping, hence all of them have been disclosed in Table S2, while the most important

ones were discussed in Section 3.1.2. After observing the attained bands from the micro and macro spot in Raman, the differences between these two measurement modes could indicate that the formation and/or dissolution of the phases were intimately linked to the size of the grains (or aggregates) of the starting powders. From 100 × SC 24 h, an increase in the band at 959 cm^{-1} and a widening of the main massif has been noted, authenticating the formation of OCP. However, a different proportion of the present phases was observed between the two measurement modes. Once the sample at 100 × SC 27 h has been analyzed with duoscan, a change in the band at 962 cm^{-1} was observed. This, together with the "red shift" of the massif, when compared to the spectrum obtained in micro spot mode, could attest to the presence of apatite or/and a greater proportion of α-TCP (Figure S17). For the analysis carried out in the micro spot mode, an additional band was observed at 949 cm^{-1} (for 27 h), which could be attributed to an amorphous TCP phase, as well as an additional band at 970 cm^{-1}, which has not been attributed. From 100 × SC 48 h until the end of the synthesis, a single profile has been observed between the micro spot and macro spot. A total absence of the band at 917 cm^{-1} can be noted, which has pointed to the end of α-TCP presence. In addition, the large mass may be associated to the amorphous phase(s) and/or related to the convolution of several crystalline phases composed of the main band at 959 cm^{-1} and the shoulder at 966 cm^{-1}, associated with ν_1PO_4 of OCP, but also to the HPO_4 environments at 870 and 917 cm^{-1}. Nevertheless, the uncertainty of containing characteristic bands of a more or less well-crystallized apatite or an amorphous phase (TCP) has to be thought of.

However, similar to the FTIR spectra, only a small number of vibration bands corresponding to DCPD were observed in the Raman spectra. In the spectrum of 10 × SC, the specific band at 986 cm^{-1} was noticed (Figure S15). At 24 h, the band's presence was pronounced, but still not as strong, whereas at 48 h the band in the PO_4 stretching region was significantly stronger and quite easily discernible. The same position of the band can be seen also in the IS 12 h time point (Figure S14). Alongside the aforementioned band, the intense vibration of the HPO_4 ion at 877 cm^{-1} in 10 × SC is indicative of the presence of DCPD in the phase mixture, but at the same time, the HPO_4 ion of OCP vibrates at the same frequency. Furthermore, it would seem that in the kinetics of the formation of the OCP, the time points of 10 h and 12 h of IS are opposite. This is, on one hand, due to the heterogeneity of the mixtures, but also due to the differences in the scan size of each entity (micro spot of the laser).

4.2. Morphology Characterization

OCP crystals grow along (010) and (100) faces, with [001] persisting as the dominant growth direction, commonly having the appearance of thin plate-like crystals [3,39,51]. DCPD has a similar morphology, but the crystals are bigger and heftier (width between 5 and 10 μm, with possible elongation to 70–80 μm) [26]. The formation of the specific OCP crystals is considered to be connected to the Hartman–Perdok theory of periodic bond chains [54]. The theory suggests that a continuous path of strong bonds within the crystal structure has a portion of the lattice which is cut by a certain face (hkl). In the case of OCP, the plates grow in the [001] direction, with the largest face, 100, while in width the predominant faces are 110 and 010. Numerous 100 interconnections, at low synthesis temperatures, lead to the formation of spherical aggregates looking like sand roses. At the same time, as we described in Section 3.1.1, while the dissolution of α-TCP is ongoing, it is being followed by the growth step of DCPD, and from DCPD, transformation to the OCP phase transpires. Hence, multiple factors influence the morphology of the particles.

4.3. In Vitro Biological Assays

The main goal behind doing the in vitro biological assay was to establish the cytocompatibility behind each mix of the CaP phases throughout the reaction scale-up. In other words, as there was no record of the OCP synthesis scale-up, it was highly necessary to check if the initial cytocompatibility of OCP remained. Furthermore, as it was possible

to scale up the initial synthesis from 100 mg to 10 g, the next step in the research would be to try to scale up even further. However, an additional scale-up would imply that in order to obtain OCP as a single phase, the reaction would last even longer. Thus, several questions need to be answered: firstly, if we scaled up the reaction 100 times, is the final product still as cytocompatible as the original synthesis product? What will be the cell response to the mixture of CaP phases during the transition? Finally, would a certain phase ratio demonstrate better cytocompatibility with cells than pure OCP itself? If a mix of OCP, DCPD, and/or α-TCP would show a desirable outcome when subjected to a direct contact with cells in vitro, would it be safe (or even more preferable) to stop the next level of scale-up at a specific time?

Presented results in Section 3.3 have confirmed that throughout the entire pathway of OCP formation (IS, 10 × SC and 100 × SC) the obtained products are safe to use in biological assays. Furthermore, if the time points between 48 h and 96 h of the 100 × SC scale-up were taken into consideration and the reaction was stopped at a point of having 80% of OCP, the results would still yield > 80% of cell metabolic activity. However, in order to be certain in such a claim more studies are needed, followed up with assessment of the pro-osteogenic efficacy at each time point. Based on the XRD quantitative data calculated with Profex, at IS 1 h and IS 3 h CaP the phase content was >92% α-TCP, <8% OCP, and for 10 × SC 24 h the phase content was ~25%, ~45% OCP, and ~29% DCPD. It is not completely sure why the starting time points of each scale-up exhibited the lowest cell viability. The authors believe it was connected with the pH change that would happen during the exposure of the powders to the cell medium. As eventually each phase is expected to transform to CDHAp or OCP (as an intermediate phase), the transformation from the starting mix of phases (α-TCP, DCPD present) would have created a more alkaline environment due to the release of OH^- ions (see Section 3.1.1). An additional factor that could influence the percentage of viable cells is the size of the agglomerate that is being formed in the direct contact with the cells.

To additionally corroborate the phase influence on the cells and to monitor the cell morphology throughout the incubation period, bright-field microscopy was used. On the third day of hBMSCs cultivation with the samples, visual analysis was complemented with immunofluorescent staining. All kinetic time points (IS, 10 × SC and 100 × SC) have been analyzed, and the cell morphology after the contact with final OCP phases has been shown in Figure 10. Considering the procedure of staining, which includes the multiple rinsing of cells with PBS, the observation of particles points to either a strong attachment of the material to the cell layer or to their internalization into hBMSCs. The presence of powder particles was also observed in the culture plate wells with the initial synthesis (Figure S24). However, the amount and size of the particles and/or agglomerates in the observation area were poorly correlated with the previously described viability rate. By following the cell morphology, within the scope of this research we found no clear connection between the amount and size of the CaP powder particles and the previously described cell viability rate. However, the morphology of the cells in all sample groups was not altered. Further studies are needed in order to assess whether there is a correlation between the tested powders and possible CaP particle internalization within the hBMSCs.

5. Conclusions

Within the present study, OCP was synthesized from α-TCP (prepared from ACP) at room temperature via the hydrolysis method and the process was for the first time successfully scaled-up (tenfold and hundredfold). By following the formation kinetics at multiple time points, the gradual transition from the α-TCP phase via DCPD to the OCP phase was established and characterized using a multi-technique approach.

The α-TCP–DCPD–OCP transformation chemistry encompassed the dissolution step, precipitation step, growth of DCPD/OCP, and the step of DCPD conversion into OCP. Previously well-recognized phase fingerprints confirmed the final OCP phases: maxima at 4.7 2θ degrees and the doublet at 9.4 and 9.7 2θ degrees; IR assignment of HPO_4^{2-}

ion at 524 cm^{-1}, 1295 cm^{-1}, and 917 cm^{-1}, together with the lack of a recognizable 3572 cm^{-1} O–H band for Hap and the ν_1 P–O stretching mode in Raman. Due to the phase interweaving (α-TCP–DCPD–OCP), the inhomogeneity of the samples was seen in Raman in the beginning stages of the synthesis when macro spot analysis was applied. The morphology of the OCP samples in all scale-up levels showed the characteristic plate-like structure. Moreover, in order to test the biocompatibility of not only final OCP phases, but also all the transient phases, in vitro cell toxicity analyses were performed and no cytotoxic effects were observed for 12 out of 17 tested samples. Cell phenotype morphology showed possible CaP particle internalization within the cells when hBMSCs were subjected to direct contact with the powders. This phenomenon, for the first time, indicated that the upscaling of the method did not negatively influence the cell viability. Furthermore, it could denote the proof of concept for the potential usage of the DCPD/OCP phase mixture (presented in the intermediary time points) for in vitro and in vivo purposes.

Supplementary Materials: The following supporting information can be downloaded at: https://www.mdpi.com/article/10.3390/biom13030462/s1. Figure S1. OCP formation from α-TCP suspension—follow-up methodology; Figure S2. Characterization of the starting α-TCP powder by (a) XRD, (b,c) SEM, (d) FTIR and (e) Raman spectroscopy, and (f) laser granulometry; Figure S3. XRD pattern of the specimens collected at different time points during 24 h of IS, with principal phase reference XRD patterns attained from ICDD; Figure S4. XRD pattern of the specimens collected at different time points during 72 h of 10 × SC, with principal phase reference XRD patterns attained from ICDD; Figure S5. XRD pattern of the specimens collected at different time points from 3 to 54 h during 100 × SC and principal phase reference XRD patterns attained from ICDD; Figure S6. XRD pattern of the specimens collected from 60 to 168 h during 100 × SC, and principal phase reference XRD patterns attained from ICDD; Figure S7. Speciation of orthophosphate species according to the pH. Drawing adopted from Wikipedia; Figure S8. FTIR absorbance spectrum of specimens collected at different time points during the 24 h of IS; Figure S9. FTIR absorbance spectrum of powders collected at 24, 48 and 72 h of 10 × SC; Figure S10. FTIR absorbance spectrum of powders collected at different time points during 36 h of 100 × SC; Figure S11. FTIR absorbance spectrum of specimens collected at different time points during the period from 54 h–168 h of 100 × SC; Figure S12. FTIR subtraction absorbance band between 100 × SC 78 h and 180 h samples (upper row) and FTIR subtraction absorbance band between 100 × SC 48 h and 78 h samples; Figure S13. FTIR subtraction absorbance band between 10 × SC 24 h and 72 h samples; Figure S14. Raman spectra of the powders collected at different time points during initial synthesis (IS); Figure S15. Raman spectra of the powder evolution as a function of time in 10 × SC synthesis; Figure S16. Raman spectra comparison between micro (light color) and macro spot (dark color) of the powders collected during 100 × SC; Figure S17. Raman spectra comparison between micro (light color) and macro spot (dark color) of the powders collected after 24 h and 27 h during 100 × SC; Figure S18. Raman spectra of final OCP phases obtained in three levels of scale-up and the representation of the second derivative of the most prominent band at 958 cm^{-1}; Figure S19. Scanning electron micrographs of α-TCP transformation to OCP (initial synthesis), observed at specific time points indicated below each SEM image; Figure S20. Scanning electron micrographs of α-TCP transformation to OCP (10 × SC), observed at specific time points indicated below each SEM image; Figure S21. Particle size distribution and SEM micrographs of powders collected at different time points during 10 × SC and 100 × SC, showing the presence of agglomerated crystals; Figure S22. hBMSCs morphology on the third day of cultivation in direct contact with hundredfold synthesis OCP samples in the concentration of 0.5 mg/mL; Figure S23. hBMSCs morphology on the third day of cultivation in direct contact with ten-fold synthesis OCP samples in the concentration of 0.5 mg/mL. *Control* represents cells on polystyrene. Immunofluorescent (DAPI—blue, phalloidin—red) and bright-field microscopy; Figure S24. hBMSCs morphology on the third day of cultivation in direct contact with initial synthesis OCP samples in the concentration of 0.5 mg/mL; Table S1. List of all the analyzed samples collected at different time points and their presentation within the main manuscript and the supplementary information (SI); Table S2. FTIR and Raman band assignments for OCP, α-TCP and DCPD.

Author Contributions: I.K.—writing—original draft, conceptualization, visualization, formal analysis, investigation; K.M.—writing—original draft, formal analysis, investigation; O.M.—writing—review and editing, formal analysis; C.R.—writing—review and editing, formal analysis; C.C.—writing—review and editing, resources; J.L.—funding acquisition, conceptualization, writing—review and editing, resources; D.L.—funding acquisition, supervision, conceptualization, writing—review and editing, resources. All authors have read and agreed to the published version of the manuscript.

Funding: The authors acknowledge financial support for granting Open Access from the European Union's Horizon 2020 research and innovation programme under the grant agreement [No. 952347 (RISEus2)], as well as the European Union's Horizon 2020 research and innovation programme under the Marie Skłodowska-Curie grant agreement [No 860462 (PREMUROSA)].

Institutional Review Board Statement: Not applicable.

Informed Consent Statement: Not applicable.

Data Availability Statement: The data presented in this study are available on request from the corresponding author. The data are not publicly available due to the connected study.

Conflicts of Interest: The authors declare no conflict of interest.

References

1. Dorozhkin, S.V. Calcium orthophosphates and human beings: A historical perspective from the 1770s until 1940. *Biomatter* **2012**, *2*, 53–70. [CrossRef]
2. Kuhn, L.T.; Grynpas, M.D.; Rey, C.C.; Wu, Y.; Ackerman, J.; Glimcher, M.J. A Comparison of the Physical and Chemical Differences Between Cancellous and Cortical Bovine Bone Mineral at Two Ages. *Calcif. Tissue Int.* **2008**, *83*, 146–154. [CrossRef]
3. Brown, W.E.; Chow, L.C. Chemical Properties of Bone Mineral. *Annu. Rev. Mater. Sci.* **1976**, *6*, 213–236. [CrossRef]
4. Rasmussen, K.L.; Milner, G.R.; Delbey, T.; Skytte, L.; Lynnerup, N.; Thomsen, J.L.; Schiavone, S.; Torino, M.; Larsen, L.A.; Boldsen, J.L. Trace element distribution in human cortical bone microstructure: The potential for unravelling diet and social status in archaeological bones. *Herit. Sci.* **2020**, *8*, 111. [CrossRef]
5. Erel, Y.; Pinhasi, R.; Coppa, A.; Ticher, A.; Tirosh, O.; Carmel, L. Lead in Archeological Human Bones Reflecting Historical Changes in Lead Production. *Environ. Sci. Technol.* **2021**, *55*, 14407–14413. [CrossRef]
6. Manea-Krichten, M.; Patterson, C.; Miller, G.; Settle, D.; Erel, Y. Comparative increases of lead and barium with age in human tooth enamel, rib and ulna. *Sci. Total Environ.* **1991**, *107*, 179–203. [CrossRef]
7. Suzuki, O. Octacalcium phosphate (OCP)-based bone substitute materials. *Jpn. Dent. Sci. Rev.* **2013**, *49*, 58–71. [CrossRef]
8. Suzuki, O.; Insley, G. *Octacalcium Phosphate Biomaterials*; Woodhead Publishing Series in Biomaterials: Sawston, UK, 2020.
9. Pompe, W.; Worch, H.; Habraken, W.J.E.M.; Simon, P.; Kniep, R.; Ehrlich, H.; Paufler, P. Octacalcium phosphate—A metastable mineral phase controls the evolution of scaffold forming proteins. *J. Mater. Chem. B* **2015**, *3*, 5318–5329. [CrossRef]
10. Elliott, J.C. Structure and Chemistry of the Apatites and Other Calcium Orthophosphates. In *Studies in Inorganic Chemistry*; Elsevier Science: Amsterdam, The Netherlands, 1994; Volume 18, pp. 1–389. [CrossRef]
11. Brown, W.; Eidelman, N.; Tomazic, B. Octacalcium Phosphate as a Precursor in Biomineral Formation. *Adv. Dent. Res.* **1987**, *1*, 306–313. [CrossRef]
12. Tung, M.; Eidelman, N.; Sieck, B.; Brown, W. Octacalcium Phosphate Solubility Product from 4 to 37 °C. *J. Res. Natl. Bur. Stand.* **1934**, *93*, 613–624. [CrossRef]
13. Yang, X.; Gao, X.; Gan, Y.; Gao, C.; Zhang, X.; Ting, K.; Wu, B.M.; Gou, Z. Facile Synthesis of Octacalcium Phosphate Nanobelts: Growth Mechanism and Surface Adsorption Properties. *J. Phys. Chem. C* **2010**, *114*, 6265–6271. [CrossRef]
14. Miyatake, N.; Kishimoto, K.N.; Anada, T.; Imaizumi, H.; Itoi, E.; Suzuki, O. Effect of partial hydrolysis of octacalcium phosphate on its osteoconductive characteristics. *Biomaterials* **2009**, *30*, 1005–1014. [CrossRef]
15. Suzuki, O.; Anada, T. Octacalcium Phosphate: A Potential Scaffold Material for Controlling Activity of Bone-Related Cells In Vitro. *Mater. Sci. Forum* **2014**, *783–786*, 1366–1371. [CrossRef]
16. Boanini, E.; Gazzano, M.; Bigi, A. Ionic substitutions in calcium phosphates synthesized at low temperature. *Acta Biomater.* **2010**, *6*, 1882–1894. [CrossRef]
17. Kovrlija, I.; Locs, J.; Loca, D. Octacalcium phosphate: Innovative vehicle for the local biologically active substance delivery in bone regeneration. *Acta Biomater.* **2021**, *135*, 27–47. [CrossRef]
18. Tang, Q.-L.; Zhu, Y.-J.; Wu, J.; Chen, F.; Cao, S.-W. Calcium phosphate drug nanocarriers with ultrahigh and adjustable drug-loading capacity: One-step synthesis, in situ drug loading and prolonged drug release. *Nanomed. Nanotechnol. Biol. Med.* **2011**, *7*, 428–434. [CrossRef]
19. Pan, H.; Jiang, S.; Zhang, T.; Tang, R. *In Situ Solution Study of Calcium Phosphate Crystallization Kinetics*, 1st ed.; Elsevier Inc.: Amsterdam, The Netherlands, 2013. [CrossRef]
20. Carino, A.; Ludwig, C.; Cervellino, A.; Müller, E.; Testino, A. Formation and transformation of calcium phosphate phases under biologically relevant conditions: Experiments and modelling. *Acta Biomater.* **2018**, *74*, 478–488. [CrossRef]

21. Drouet, C. Apatite Formation: Why It May Not Work as Planned, and How to Conclusively Identify Apatite Compounds. *BioMed Res. Int.* **2013**, *2013*, 490946. [CrossRef]
22. Temizel, N.; Girisken, G.; Tas, A.C. Accelerated transformation of brushite to octacalcium phosphate in new biomineralization media between 36.5 °C and 80 °C. *Mater. Sci. Eng. C* **2011**, *31*, 1136–1143. [CrossRef]
23. Tripathi, G.; Miyazaki, T. Synthesis and in vitro biodegradation of pure octacalcium phosphate spheres. *Int. J. Appl. Ceram. Technol.* **2020**, *17*, 372–379. [CrossRef]
24. Graham, S.; Brown, P.W. The low temperature formation of octacalcium phosphate. *J. Cryst. Growth* **1993**, *132*, 215–225. [CrossRef]
25. Hamai, R.; Sakai, S.; Shiwaku, Y.; Anada, T.; Tsuchiya, K.; Ishimoto, T.; Nakano, T.; Suzuki, O. Octacalcium phosphate crystals including a higher density dislocation improve its materials osteogenecity. *Appl. Mater. Today* **2022**, *26*, 101279. [CrossRef]
26. Mandel, S.; Tas, A.C. Brushite ($CaHPO_4{\cdot}2H_2O$) to octacalcium phosphate ($Ca_8(HPO_4)_2(PO_4)_4{\cdot}5H_2O$) transformation in DMEM solutions at 36.5 °C. *Mater. Sci. Eng. C* **2010**, *30*, 245–254. [CrossRef]
27. Kukueva, E.V.; Putlyaev, V.I.; Tikhonov, A.; Safronova, T.V. Octacalcium phosphate as a precursor for the fabrication of composite bioceramics. *Inorg. Mater.* **2017**, *53*, 212–219. [CrossRef]
28. Monma, H. Preparation of octacalcium phosphate by the hydrolysis of α-tricalcium phosphate. *J. Mater. Sci.* **1980**, *15*, 2428–2434. [CrossRef]
29. Bigi, A.; Boanini, E.; Botter, R.; Panzavolta, S.; Rubini, K. α-Tricalcium phosphate hydrolysis to octacalcium phosphate: Effect of sodium polyacrylate. *Biomaterials* **2002**, *23*, 1849–1854. [CrossRef]
30. Ressler, A.; Ivanišević, I.; Žužić, A.; Somers, N. The ionic substituted octacalcium phosphate for biomedical applications: A new pathway to follow? *Ceram. Int.* **2022**, *48*, 8838–8851. [CrossRef]
31. Sugiura, Y. Ionic insertion fabrication of novel octacalcium phosphate block materials exhibiting antibacterial ability and biocompatibility. *J. Ceram. Soc. Jpn.* **2022**, *130*, 639–647. [CrossRef]
32. Suzuki, O.; Hamai, R.; Sakai, S. The material design of octacalcium phosphate bone substitute: Increased dissolution and osteogenecity. *Acta Biomater.* **2022**, *158*, 1–11. [CrossRef]
33. James, S.; Fox, J.; Afsari, F.; Lee, J.; Clough, S.; Knight, C.; Ashmore, J.; Ashton, P.; Preham, O.; Hoogduijn, M.; et al. Multiparameter Analysis of Human Bone Marrow Stromal Cells Identifies Distinct Immunomodulatory and Differentiation-Competent Subtypes. *Stem Cell Rep.* **2015**, *4*, 1004–1015. [CrossRef]
34. Irbe, Z.; Buss, A.; Loca, D.; Malniece, L. Synthesis of Amorphous Calcium Phosphate as a Starting Material for α-Tricalcium Phosphate. *Solid State Phenom.* **2017**, *267*, 119–123. [CrossRef]
35. Irbe, Z.; Loca, D.; Pura, A.; Berzina-Cimdina, L. Synthesis and Properties of α-Tricalcium Phosphate from Amorphous Calcium Phosphate as Component for Bone Cements. *Key Eng. Mater.* **2017**, *721*, 182–186. [CrossRef]
36. Döbelin, N. Validation of XRD phase quantification using semi-synthetic data. *Powder Diffr.* **2020**, *35*, 262–275. [CrossRef]
37. Kolmas, J.; Kaflak, A.; Zima, A.; Ślósarczyk, A. Alpha-tricalcium phosphate synthesized by two different routes: Structural and spectroscopic characterization. *Ceram. Int.* **2015**, *41*, 5727–5733. [CrossRef]
38. Camiré, C.; Gbureck, U.; Hirsiger, W.; Bohner, M. Correlating crystallinity and reactivity in an α-tricalcium phosphate. *Biomaterials* **2005**, *26*, 2787–2794. [CrossRef]
39. Brown, W.E.; Lehr, J.R.; Smith, J.P.; Frazier, A.W. Crystallography of Octacalcium Phosphate. *J. Am. Chem. Soc.* **1957**, *79*, 5318–5319. [CrossRef]
40. Fowler, B.O.; Markovic, M.; Brown, W.E. Octacalcium phosphate. 3. Infrared and Raman vibrational spectra. *Chem. Mater.* **1993**, *5*, 1417–1423. [CrossRef]
41. Rey, C.C.; Combes, C.; Drouet, C. Synthesis and physical chemical characterizations of octacalcium phosphate–based biomaterials for hard-tissue regeneration. In *Octacalcium Phosphate Biomaterials*; Woodhead Publishing: Sawston, UK, 2019. [CrossRef]
42. Sayahi, M.; Santos, J.; El-feki, H.; Charvillat, C.; Karacan, I.; Milthorpe, B.; Drouet, C.; Sayahi, M.; Santos, J.; El-Feki, H.; et al. Brushite (Ca, M) HPO_4, $2H_2O$ doping with bioactive ions (M = Mg^{2+}, Sr^{2+}, Zn^{2+}, Cu^{2+} and Ag^{+}):new path to functional biomaterials? *Mater. Today Chem.* **2020**, *16*, 100230. [CrossRef]
43. Hirsch, A.; Azuri, I.; Addadi, L.; Weiner, S.; Yang, K.; Curtarolo, S.; Kronik, L. Infrared Absorption Spectrum of Brushite from First Principles. *Chem. Mater.* **2014**, *26*, 2934–2942. [CrossRef]
44. Margenot, A.J.; Calderón, F.J.; Parikh, S.J. Limitations and Potential of Spectral Subtractions in Fourier-Transform Infrared Spectroscopy of Soil Samples. *Soil Sci. Soc. Am. J.* **2016**, *80*, 10–26. [CrossRef]
45. *ISO, 10993–10995*; Biological Evaluation of Medical Devices—Part 5: Tests for In Vitro Cytotoxicity, Third Edit. International Organization for Standardization: Geneva, Switzerland, 2009.
46. Habraken, W.J.E.M.; Tao, J.; Brylka, L.J.; Friedrich, H.; Bertinetti, L.; Schenk, A.S.; Verch, A.; Dmitrovic, V.; Bomans, P.H.H.; Frederik, P.M.; et al. Ion-association complexes unite classical and non-classical theories for the biomimetic nucleation of calcium phosphate. *Nat. Commun.* **2013**, *4*, 1507. [CrossRef] [PubMed]
47. Monma, H.; Nishimura, Y.; Okura, T. Characterization of layer-structured octacalcium phosphate/dicarboxylate com-posite. *Phosphorus Res. Bull.* **2005**, *18*, 127–134. [CrossRef] [PubMed]
48. Heughebaert, J.C.; Nancollas, G.H. Kinetics of crystallization of octacalcium phosphate. *J. Phys. Chem.* **1984**, *88*, 2478–2481. [CrossRef]
49. Barone, J.P.; Nancollas, G.H. The Seeded Growth of Calcium Phosphates. The Kinetics of Growth of Dicalcium Phosphate Dihydrate on Enamel, Dentin, and Calculus. *J. Dent. Res.* **1978**, *57*, 153–161. [CrossRef]

50. Wang, L.; Nancollas, G.H. Pathways to biomineralization and biodemineralization of calcium phosphates: The thermodynamic and kinetic controls. *Dalton Trans.* **2009**, *15*, 2665–2672. [CrossRef]
51. Chow, L.C.; Eanes, E.D. Octacalcium phosphate. *Acta Biomater.* **2011**, *135*, 653. [CrossRef]
52. Berry, E.E.; Baddiel, C.B. Some assignments in the infra-red spectrum of octacalcium phosphate. *Spectrochim. Acta Part A Mol. Spectrosc.* **1967**, *23*, 1781–1792. [CrossRef]
53. Rey, C.; Marsan, O.; Combes, C.; Drouet, C.; Grossin, D.; Sarda, S. Characterization of Calcium Phosphates Using Vibrational Spectroscopies. *Adv. Calcium Phosphate Biomater.* **2014**, *2*, 229–266. [CrossRef]
54. Terpstra, R.; Bennema, P. Crystal morphology of octacalcium phosphate: Theory and observation. *J. Cryst. Growth* **1987**, *82*, 416–426. [CrossRef]

Appendix 3
3. pielikums

Fusion and classification algorithm of octacalcium phosphate production based on XRD and FTIR data

Mauro Nascimben, Ilijana Kovrlija, Janis Locs, Dagnija Loca, Lia Rimondini
Scientific Reports, 14:1489 (2024), 1–11, DOI: 10.1038/s41598-024-51795-0

I.K. input: laboratory experiments, data collection and organization, results discussion, manuscript draft writing, manuscript editing and revision.

scientific reports

Check for updates

OPEN

Fusion and classification algorithm of octacalcium phosphate production based on XRD and FTIR data

Mauro Nascimben[1,2]✉, Ilijana Kovrlija[3], Janis Locs[3,4], Dagnija Loca[3,4] & Lia Rimondini[1]

The present manuscript tested an automated analysis sequence to provide a decision support system to track the OCP synthesis from α-TCP over time. Initially, the XRD and FTIR signals from a hundredfold scaled-up hydrolysis of OCP from α-TCP were fused and modeled by the curve fitting based on the significantly established maxima from the literature and nine features extracted from the fitted shapes. Afterward, the analysis sequence enclosed the machine learning techniques for feature ranking, spatial filtering, and dimensionality reduction to support the automatic recognition of the synthesis stages. The proposed analysis pipeline for OCP identification might be the foundation for a decision support system explicitly targeting OCP synthesis. Future projects will exploit the suggested methodology for pinpointing the OCP production over time (including the intermediary phases present in the OCP formation) and for evaluating whether biological variables might be merged with biomaterial properties to build a unified model of tissue response to the implant.

Bone regeneration is crucial in multiple healthcare sectors, such as dentistry and orthopedics, where bone replacement and healing are fundamental for a patient's well-being and quality of life. Regenerative medicine's primary strive is osteogenesis, the bone formation and growth process. Osteogenesis is stimulated by osteoinduction, which involves recruiting and stimulating stem cells to promote their differentiation into preosteoblasts[1]. On the contrary, osteoconduction is the ability of bone-forming cells to advance across a matrix and partly replace it with the new bone over a certain period[2]. However, when it comes to implants, osteoconduction is also dependent on the conditions within the setup and the reactions to the used biomaterial. As the final goal is to have a material that shows osteoinductive properties (e.g., calcium phosphates, CaPs), it is essential to steer the research toward finding the best candidates[3]. Besides having the properties mentioned above (biocompatibility, osteoconductivity, osteoinductivity), CaPs have structural and compositional features similar to native bone and are abundantly present in the human body. The spectra of present CaP compositions are very diverse[4], with plentiful potential phases (alongside apatite) able to form depending on experimental conditions, experimental mistakes (approximations), reactions with the immersion solutions, etc.[5].

One of the CaPs that stood out, based on its structural similarity to hydroxyapatite and extraordinary biological attributes, is octacalcium phosphate (OCP)[6]. An additional advantage of OCP is its ability to convert to the thermodynamically more stable phase (hydroxyapatite), both in vitro and in vivo[7]. It is generally synthesized through the precipitation of various aqueous solutions containing calcium and phosphate ion source or via the hydrolysis of α-tricalcium phosphate (α-TCP)[8,9] or brushite (dicalcium phosphate dihydrate, DCPD)[10,11]. Moreover, OCP can stimulate bone formation by osteoblast differentiation and osteoclast formation. However, the stability of the pure OCP phase formation depends on a narrow region of pH and temperature of the reaction. At the same time, those parameters can influence the crystallinity, size, and morphology of the crystals, as well as possible conversion to a different CaP phase upon the end of the synthesis[12–14]. Consequently, synthesizing and characterizing the properties of engineered biomaterials require extensive laboratory experiments not only for manufacturing but also to study the biocompatibility between the physicochemical properties of the surface with the surrounding biological microenvironment[15]. Development procedures should establish and encompass

[1]Center for Translational Research on Autoimmune and Allergic Diseases-CAAD, Department of Health Sciences, Università del Piemonte Orientale UPO, 28100 Novara, Italy. [2]Enginsoft SpA, 35129 Padua, Italy. [3]Institute of Biomaterials and Bioengineering, Faculty of Natural Sciences and Technology, Riga Technical University, Riga, Pulka 3, LV-1007, Latvia. [4]Baltic Biomaterials Centre of Excellence, Headquarters at Riga Technical University, Riga, Latvia. ✉email: mauro.nascimben@uniupo.it

protocols that could assess at what stage the synthesis is or what could be the potential end product, without the experimental guidelines relying primarily on empirical methods or researchers' intuition (e.g., trial-and-error). One potential solution could be that the exploitable data from the pre-clinical phase is used for building computational models able to support decision-making during biomaterials design[16]. In the early stages of materials synthesis for tissue engineering, data from in vitro assays analyzed with advanced data mining methods could provide innovative information for optimizing the composition of the biomaterials[17–19]. For example, the bacterial proliferation on polymeric material was determined through machine learning (ML)[20], or Wang et al. studied fatigue cracks on metallic implants[21] through automated algorithms. Another advantage could be the application of predictive techniques on multi-dimensional data to automate or bolster peculiar phases of the manufacturing process. ML processes are automated compared to the classic design of experiments (DoE) optimization in bioengineering, where an operator has to decide on a limited set of input parameters for the model. The ML algorithms disclose relevant patterns in the data providing high-accuracy prediction or categorization[22]. They are preferred over DoE when datasets are not small or not composed of pure numerical values, given the ability of ML to handle different data formats such as images, spectra, numerical datasets, categorical variables, etc. Indeed, biomedical implant production evaluated through data analytics could overcome the limitations of physics modeling, commonly applied to simulate an output given input and standard pre-selected environmental parameters, offering effective surrogate methods for materials chemistry[23].

In the present research, data collected from the synthesis of octacalcium phosphate from α-tricalcium phosphate (α-TCP) based on the X-ray diffractometry (XRD) and Fourier transform infrared spectroscopy (FTIR) has been merged and analyzed by using a novel computational model. The paucity of data on how to obtain a pure OCP phase while at the same time maintaining the successful scale-ups of the synthesis or time alterations shows a dire need for help that artificial intelligence can provide. This multi-source approach that integrates data from different laboratory techniques and computational modeling might help characterize OCP formation more extensively. Other authors already tried to merge data, for example, to enhance comprehension of crystallized membrane proteins; however, their approach fused 2D crystal images from the same source[24]. The current investigation aims at proposing a data mining methodology or analysis sequence whose main aspects are outlined as follows:

- explore the possibility of merging the information extracted from heterogeneous data sources recorded during the scaled-up OCP synthesis.
- evaluate the most relevant features derived from the peak modeling of the recorded XRD and FTIR signals through machine learning.
- facilitate the interpretation of the outcomes during OCP manufacturing by proposing an algorithm able to define OCP formation phases automatically. Actual implementation represents the foundation for a more complex system based on the same logic that can potentially track all intermediary phases that may occur during the OCP formation.

The final goal is to support researchers' decision-making by offering supplementary analysis to existing laboratory practice.

Results

The analysis sequence considered the features derived from modeling the peaks belonging to the scaled-up XRD and FTIR signals. The scaled-up synthesis (10 g final product amount) was selected as the small-scale one (e.g., 100 mg, which was the target of previous research[9]) resulted in quite a small yield of the final product; thus, the reproducibility and uniformity between different batches was not ensured. Moreover, to accomplish a multi-technique characterization across various platforms and to later use considerable amounts of the product for in vitro and in vivo tests, high yield and scale-up of the technology are of utmost importance.

After the XRD and FTIR shapes were processed to compatible signals, nine features were derived from the modeled peaks through Gaussian or Lorentzian shapes. Recursive feature elimination determined a subset of relevant attributes from the nine collected descriptors. This subset of seven attributes of each signal peak was the dataset employed to recognize OCP production phases. A low-dimensional embedding of each peak's seven most significant descriptors was computed for visualization purposes through Kernel Principal component analysis (k-PCA) employing a cosine template (Fig. 1): the two classes representing the time evolution of OCP production overlap, making it challenging to identify the different production stages.

Undeniably, an algorithm working as an automatic scorer might need further data processing to learn how to associate an XRD or FTIR value to one of the two classes representing OCP (analogous to "F" class) or α -TCP (corresponding to "I" class). A solution could be transforming the values to facilitate the automatic identification of OCP formation's initial and final stages. For example, each class could be rotated concerning the other to occupy different portions of the Cartesian plane; in this way, the classes could create a non-overlapping map with well-defined point clouds. One approach for reducing data structure dependence could be applying spatial filters[25–28] paired with a transformation highlighting the presence of clusters. These two methods applied in sequence to the data might facilitate the identification of a decision boundary for scoring OCP production phases. Spatial filters are commonly used for noise reduction on images[29,30] or as part of the first layers of convolutional neural networks or other machine learning analysis sequences[31,32]. Other applications include improving Gaussian peak shape determination in optics[33]. The spatial filter enhanced class separability by uncorrelating the one-versus-other class configurations. In Fig. 2, kernel principal component analysis reduced the seven spatially filtered features to highlight the patterns useful for automatic OCP phase prediction. Indeed k-PCA can mimic the behavior of spatial clustering algorithms[34], ameliorating the separability between classes' instances.

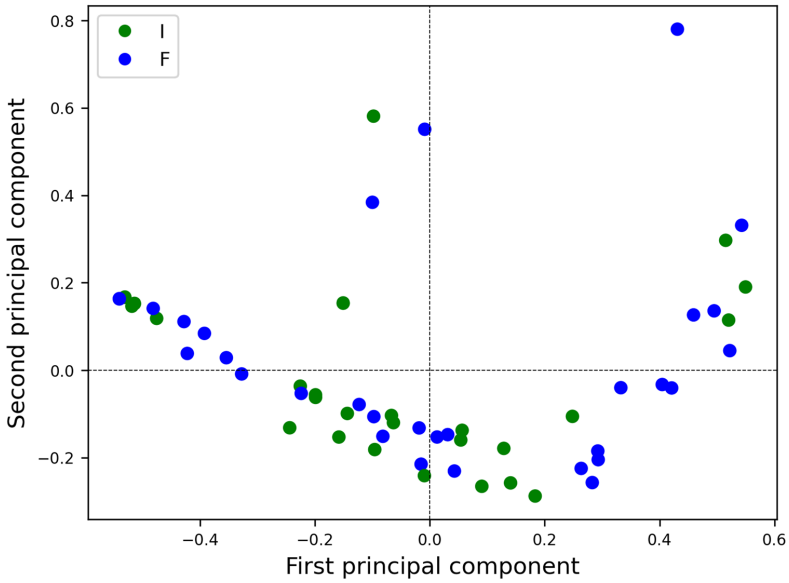

Figure 1. Low dimensional representation through kernel principal component analysis of the seven most important features ("I" are green points depicting "Initial" phase, whereas "F" are blue features of "Final" stage).

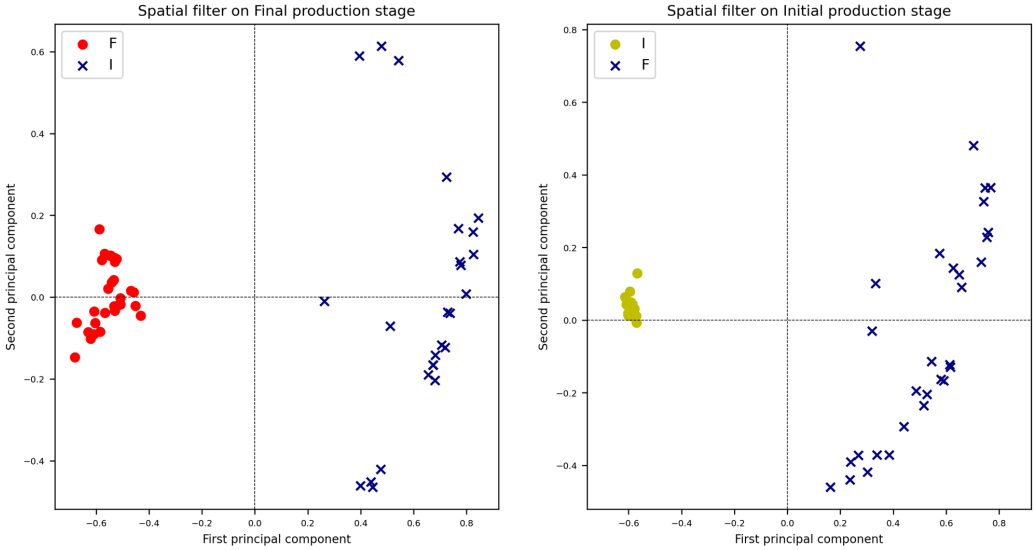

Figure 2. Kernel principal component analysis of the spatially filtered classes in the one-vs-other configurations. On the left, the "Final" spatially filtered and k-PCA embedded class is shown in red versus the class I. On the right, the "Initial" spatially filtered and k-PCA reduced samples are in yellow.

The final map of one spatially filtered class (e.g., I) versus the other is shown in Fig. 3a; the two clusters produced by k-PCA were also associated with each theta or wavenumber to link XRD and FTIR signal characteristics. By applying this computational strategy, the production phases could be represented as two-dimensional embeddings, easily interpretable by a human operator for quality control. Furthermore, presenting two distinct point clouds is crucial to draw a decision boundary exploitable for building a support decision system to categorize

	Variance of k-PCA components	
	First component	Second component
Class I	0.0902	0.0421
Class F	0.1138	0.0573
Class I (spatially filtered)	0.0002	0.0008
Class F (spatially filtered)	0.0036	0.006

Table 1. Variance modifications in the low dimensional embedding by k-PCA with or without spatial filtering.

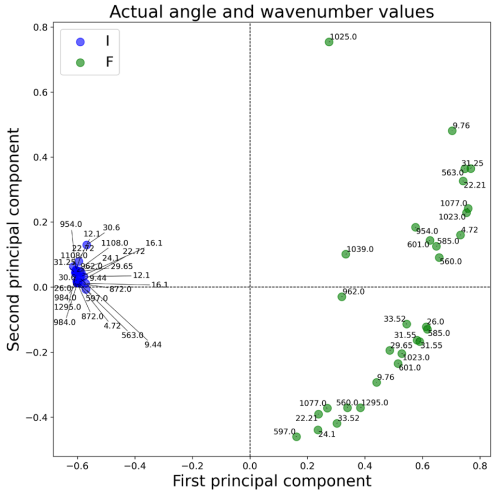

(a) Bi-dimensional representation by kernel PCA of the spatially filtered class "I" versus "F" and the corresponding angle or wavenumber values.

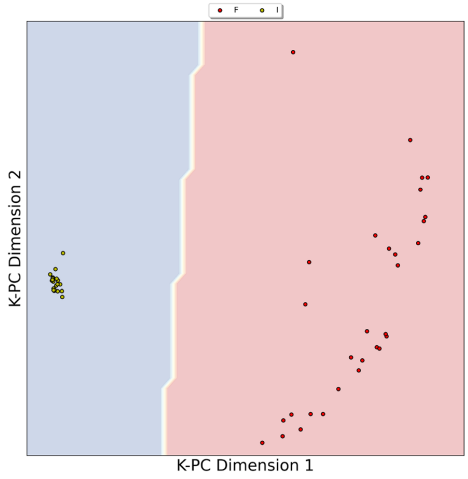

(b) The white edge is a possible decision boundary to automatically score future data by building a decision system for OCP phase synthesis detection over Figure 3a representation.

Figure 3. Application of the spatial filter followed by dimensionality reduction using k-PCA highlighting model usage and its interpretability.

the OCP production phases. After applying the spatial filter and reducing the dimensionality by k-PCA, a linear boundary could be sufficient to classify the dataset instances automatically, as demonstrated graphically in Fig. 3b. According to the example, points falling on the right side of the edge could be classified as "F", whereas those laying on the left of the white boundary are marked as the "I" OCP phase. Table 1 reports the modifications of the variance found in the First and Second k-PCA components when the data is spatially filtered (e.g., Fig. 2) or not (e.g., Fig. 1).

Understanding and accounting for the common spatial patterns in the fused data makes it possible to reduce the overall variance, leading to more accurate and reliable analyses and predictions. The peak shape descriptors composing the dataset analyzed through the proposed procedure were transformed to enhance specific features of the signals, making it easier to detect data patterns or structures. In conclusion, the research objective of obtaining two separable point clouds representing the distinct production phases of OCP synthesis was reached by applying spatial filtering paired with k-PCA dimensionality reduction to XRD and FTIR peaks descriptors. An automated decision support system might exploit the current analysis sequence to track OCP production phases consistently.

Discussion

Machine learning-based procedures can support materials science, offering techniques to accelerate innovation and the return on investment (laboratory and experimental costs). In the current investigation, we proposed merging heterogeneous data sources from XRD patterns and FTIR spectra to augment the information available for accurate and automatic identification of octacalcium phosphate production phases. The innovation resides in the possibility of tracking the different stages of biomaterial synthesis by fusing standard laboratory tests. For the development of biomaterials, multiple steps to determine the physicochemical characteristics accurately and comprehensively are needed. Thus, combining various sources in a unique algorithm might propose a different approach than analyzing the physicochemical properties of each laboratory test separately. The complicated interaction between structures, composition, and hands-on experience is a significant step to overcome in clinical

biomaterials design. Fusing sources of information to define these aspects might improve the understanding of biomaterials production.

In addition to proposing a way to merge signals from different sources (XRD and FTIR), this study introduced a novel analysis sequence to extract and evaluate features characterizing the initial and final stages of octacalcium phosphate synthesis. The analysis pipeline included a spatial filter followed by dimensionality reduction with k-PCA, demonstrating how this combination of techniques could produce unique patterns describing biomaterial production. It could constitute the foundation for a more sophisticated methodology that could be developed to track the kinetics of OCP phase formation, including the intermediate states. As proven in[35], the middle stages of α-TCP to OCP conversion contain the brushite phase (dicalcium phosphate dihydrate, DCPD), a precursor to obtaining pure octacalcium phosphate. Unfortunately, even though DCPD is clearly seen in XRD patterns, FTIR showed trace instability and is more subtle to recognize without supervision[36,37]. Even though the XRD patterns are the primary way to identify the crystalline phase (in conjunction with the International Centre for Diffraction Data PDF-2 (ICDD) database), due to the specific crystal structure of OCP that is very similar to hydroxyapatite, certain parts of the pattern overlap and it is not possible (yet) to differentiate OCP from HAp with certainty from using only XRD patterns. In order to finalize the structural identification, FTIR spectroscopy was conducted on all samples. From the point of view of materials science, the advantage of the proposed methodology for OCP production tracking (as it is a metastable phase with high similarity to HAp) is the possibility of showing the chemical composition into a well-defined spatially 2D embedding of the original features representing the detection of a specific vibration of hydrogen phosphate (HPO_4^{2-}) ion. Pinpointing the presence of HPO_4^{2-} and phosphate (PO_4^{3-}) groups is paramount in determining OCP phase purity. OCP's characteristic vibrations at 917, 875, 1007, and 1295 cm^{-1} show the presence of hydrogen phosphate, and they differentiate the OCP from stoichiometric HAp. Thus, combining XRD and FTIR is crucial for OCP production tracking, as demonstrated in the proposed analysis pipeline. Indeed, only peaks for OCP and α-TCP were included during the current investigation. In the future, the algorithm developed within this study will be fine-tuned to follow all relevant kinetic steps of CaP transformation.

Additionally, fusing different data sources can significantly enhance the predictive capabilities of machine learning models for several reasons. One is that by integrating multiple data sources, researchers can access a more comprehensive view of the problem or phenomenon they are trying to model. This broader perspective can provide more context, enabling a more accurate understanding of the underlying patterns and relationships within the data. Different data sources may offer diverse sets of features that can complement each other. Combining these features allows researchers to create a more robust and informative feature set for training the machine-learning model; this leads to improved feature representation and a better understanding of the underlying data structure. Another advantage is connected with a reduced bias and variance. Incorporating data from various sources can help mitigate the biases and variances in individual data sets. By leveraging diverse data, a researcher can balance out any tendencies that might be present in one data source, leading to a more balanced and accurate model. Moreover, an improved generalization ability could arise from merged datasets. Fusing data from multiple sources can enhance the generalization capabilities of a machine-learning model. By training on diverse data, the model can learn more generalized patterns and relationships, making it more robust and capable of making accurate predictions on unseen data.

Another relevant aspect of the current work is the application of spatial filtering techniques on peak descriptors to ease the automatic scoring of the initial and final phases of OCP synthesis from α-TCP. This addition, together with k-PCA dimensionality reduction, improves the algorithm's ability to detect the production stages without supervision by creating well-defined clusters, consequently improving the accuracy of a classifier trained to label the merged data. Through spatial filtering, similarities or shared characteristics existing within neighboring data points are recognized: for example, trends, clusters, autocorrelation, and other forms of interdependence. Identifying common patterns can reduce variance in the data, leading to more robust and insightful predictive analyses. Modifying the spatial filter formulation to work in a one-versus-rest configuration could make scoring more than two OCP production phases possible.

Even if the procedure looks promising, a limitation of the current study is connected with the ability to test it on other bioengineered materials. Although the analysis pipeline at the end could identify suitable clusters tracking biomaterial compositional modifications, as shown in Fig. 3b, the procedure might be evaluated in synthesizing other compounds to test its effectiveness.

A final remark and a possible research direction for furtherly expanding current results could be the inclusion of biological variables. The microenvironment enclosing cells and biomaterials implanted in the human body requires the control of cell function by manipulating surface properties to shape the biological responses (e.g., cell phenotypes). The proposed technique could incorporate material properties with biological information to tune cell behavior in response to modifications in the materials' biophysical properties. For example, the biomaterial's mechanical properties influence the development of fibrosis; thus, linking the material's properties to cell activity might be another advancement in biomaterials research. Future research will explore the possibility of merging biological and material compositional variables.

Methods

The analysis pipeline tested in the current investigation is summarized in Fig. 4. The initial analysis steps focused on merging XRD patterns and FTIR spectra to enlarge the dataset's size and test if these joint attributes might reveal critical aspects of OCP synthesis. Afterward, the signals' peaks were modeled as Gaussian or Lorentzian shapes, and a set of features or ratios was calculated, acting as α-TCP or OCP descriptors.

Once the most important and descriptive features were obtained by recursive feature elimination, they were related to OCP synthesis stages ("Initial" or "Final") to verify if the current methodology could automatically

highlight characteristics of OCP production. The proposed solution exploited a spatial filter paired with dimensionality reduction, demonstrating that it can automate the OCP or α-TCP discrimination.

Octacalcium phosphate synthesis and characterization: laboratory data

OCP was obtained from low temperature α-tricalcium phosphate (α-TCP) via hydrolysis method. The scaled-up synthesis (100 times) was used to evaluate the quality of the product. Briefly, 10 g of α-TCP were placed in 5 L of 0.0016 M orthophosphoric acid (H_3PO_4, 75% Latvijas Kımija, Riga, Latvia) and stirred with an overhead mixer (500 rpm) during the course of 180 h. The pH was monitored throughout the entire duration of the synthesis. The collected suspensions were centrifuged at 3000 rpm for 2 min, washed with deionized water, and dried at 37 °C. During the experiment, multiple samples from the reactor were collected to follow the compositional changes after 1 h, 24 h, 30 h, 48 h, 78 h, 96 h, 144 h, and 180 h. In the present analysis, the first two (i.e., 1 h and 24 h) and the last two (144 h and 180 h) XRD and FTIR signals were included in the numerical experiments.

The presence of crystalline phases was examined by using X-ray powder diffractometry (XRD) and Fourier-transform infrared spectroscopy (FTIR). XRD was performed using PANalytical Aeris diffractometer (The Netherlands) and accompanying analyses were performed with suitable software (X'Pert Data Collector, X'Pert Data Viewer, X'PertHighScore and the International Centre for Diffraction Data PDF-2 (ICDD) database). During the XRD measurement, the following parameters were used: 40 kV and 15 mA, step size 0.0435°, 2θ range from 3 to 60, time per step 299.575 s. For crystalline phase identification following, ICDD entries were used-#026-1056 for OCP and #009-0348 for α-TCP. The Fourier-transform infrared spectrometer Nicolet iS 50 (Thermo Scientific, Waltham, MA, USA) was used in transmission mode with the potassium bromide (KBr) pellet method. The FTIR spectra were recorded in the range of 4000–400 cm^{-1}, with 64 scans at a resolution of 4 cm^{-1}.

The XRD pattern served as a tool for identifying the three primary crystalline phases, their ratios varying with hydrolysis time: α-TCP, DCPD, and OCP. The analysis pipeline will focus on the initial and final time points of the scaled-up synthesis (1 h, 24 h, 144 h, and 180 h), while additional specifics can be found in[9]. The XRD patterns gradually transition from the α-TCP phase through DCPD to the OCP phase. Initially, only α-TCP was observed, consistent with the ICDD pattern (#009-0348) of α-TCP. The most prominent peaks were located at 12.1 and 30.7 2θ degrees, with double peaks around 22.8 2θ degrees and approximately 34 2θ degrees. After completion of the synthesis, the prominent peaks for OCP remained. While the overlap in the XRD pattern between 25–35 2θ degrees poses a challenge in distinguishing between HAp and OCP, peculiar reflections at lower angles confirmed the OCP phase. Specifically, the XRD pattern of OCP (seen in the final stages of the synthesis at 144 h and 180 h) exhibits a unique low angle (100) peak at 2θ 4.72°, along with a doublet at 2θ 9.44° (200) and 9.77° (010). The key observations in the IR spectrum were the following: within the initial 24 h of synthesis, the most prominent bands of α-TCP were prevalent. The most intense bands in the α-TCP spectrum were identified in the ranges of 1300–900 cm^{-1} and 700–500 cm^{-1}, associated with the vibrations of PO_4^{3-}. The concentrated peaks within these domains facilitated the easier distinction of α-TCP from other calcium phosphates. As the synthesis

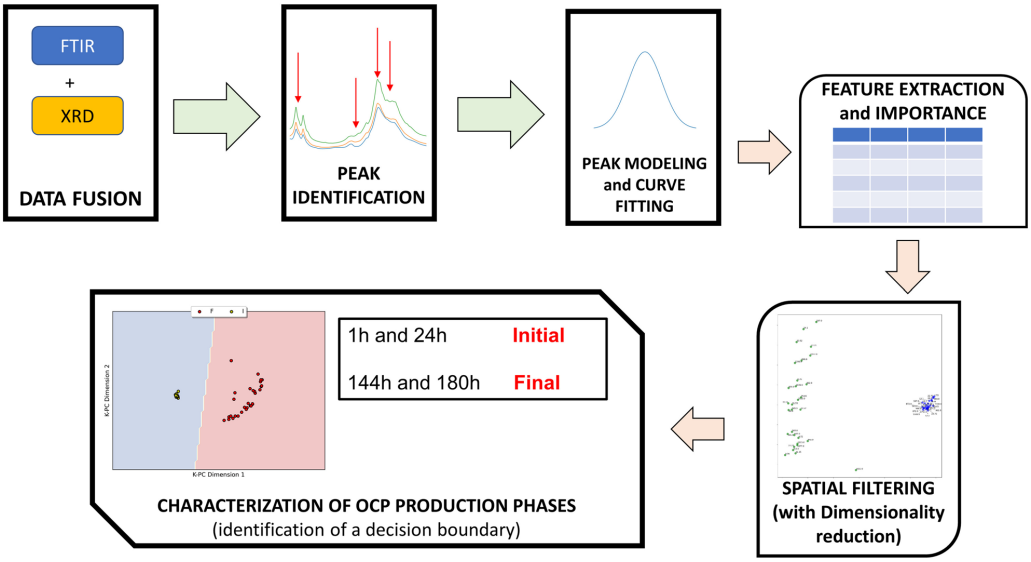

Figure 4. Green arrows: initial sequence of the proposed analysis pipeline with pre-processing of the FTIR and XRD signals and their fusion, automatic peak detection, modeling of the peaks. Orange arrows: feature extraction and feature importance evaluation by machine learning, application of a spatial filter paired with kernel principal component analysis on the the reduced dataset, theoretical decisin boundary to distinguish between the stages of OCP synthesis.

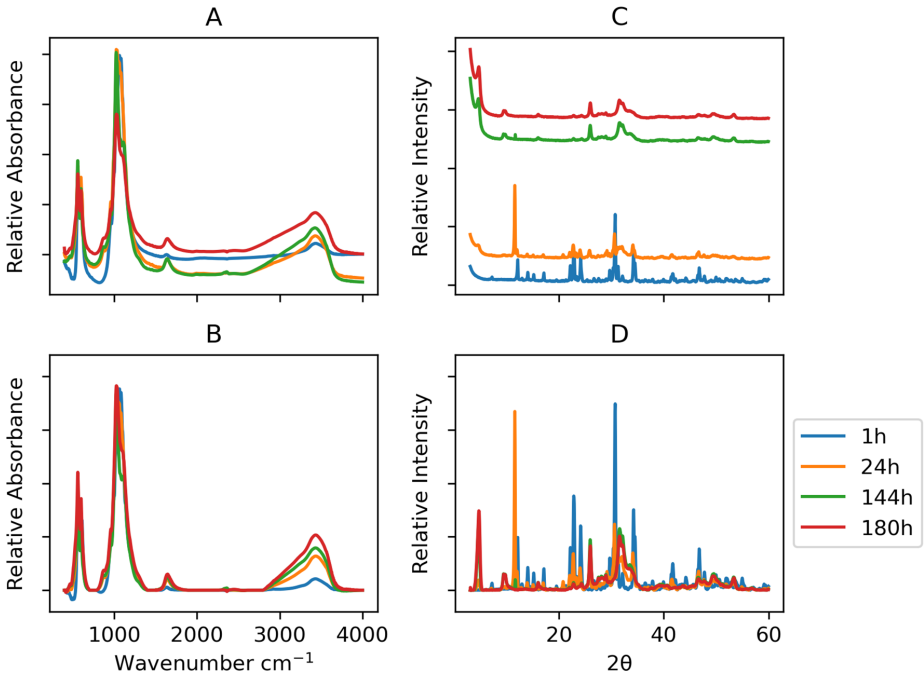

Figure 5. Effect of standardization and baseline correction on XRD and FTIR signals: (**A**) raw FTIR signals, (**B**) FTIR post-processed signals, (**C**) raw XRD signals, (**D**) XRD post-processed signals. The x-axes between vertical plots are shared.

progressed towards its final stages (at 144 h and 180 h), distinct features emerged. The $\nu 3$ stretching mode of PO_4^{3-} and HPO_4^{2-}, detected at 1077 cm^{-1}, 1093 cm^{-1}, and 1121 cm^{-1}, along with the subtle but characteristic line of OCP HPO_4 (6) [P − (OH)] stretching at 917 cm^{-1}, and O–H in-plane bending at approximately 1295 cm^{-1}, became discernible. The PO_4^{3-} $\nu 4$ domain in the FTIR spectrum of OCP encompassed absorbance bands at 524, 560, 601, and 627 cm^{-1}.

Computational resources

All numerical experiments of the proposed analysis pipeline were demonstrated on commodity hardware (a laptop computer equipped with Intel i5 CPU and 16 Gb RAM). This choice ensured the reproducibility of the current analysis sequence by other groups or researchers because it does not require cloud or cluster computing resources. Custom Python functions processed and analyzed the data upon importing the spectra as CSV files.

XRD and FTIR signals pre-processing

Several techniques could be applied to spectroscopic spectra to adjust deviations from the ordinate axis[38]. In the current study, the FTIR baseline correction was performed by preselecting a few wavenumber ranges supposed to pertain to the baseline and to model the signals inside these regions with principal component analysis, then interpolating the first component's loadings over the spectra and finally adapting the baseline of the spectra by the multiplication between principal component scores and first component's interpolated loadings[39]. Afterward, signals were standardized, centering the point values on the median (rather than the mean) and the distances divided by the interquartile range (rather than standard deviation). This standardization methodology should keep the same degree of values between peaks and baseline values as found in the original input. Indeed, peaks could be interpreted as "outliers" compared to baseline points if standardized by the mean and standard deviation that might shrink the data range. As reported in other literature manuscripts, the data bounds were preserved using the median and interquartile range[40–42]. Furthermore, the data range was normalized between zero and one. For XRD, the signals were smoothed by a Hamming window of five points[43] and baseline corrected with rubberband fitting[44]. Standardization and normalization were the same as applied to FTIR signals (Fig. 5). After processing, both XRD and FTIR signals resulted in a compatible range; thus, features extracted from the peaks could be aggregated and do not require further manipulation.

XRD and FTIR peak identification and modeling

The primary XRD maxima and FTIR absorbance bands were corroborated according to the literature data: articles attributing FTIR wavenumbers relevant for OCP or α-TCP determination were[13,14,45–47], and for XRD phase composition, the maxima were selected according to angles suggested following the previous body of knowledge in the field[45,48–53]. All parameters from the literature were marked as vertical lines in the Figures SM1 and SM2, and peak identification on actual signals was adjusted according to a tolerance margin accounting for peak shifts[54,55]. The values found in the literature matched the signals, as detailed in[9].

The specific vibrations of absorbance bands extracted from the literature are reported in Figure SM1. Valleys were searched in the points surrounding the peaks by inspecting the sign change in the first derivative (from negative to positive), and checking if the second-order derivative was negative. The noise level was estimated as the average of the baseline signal and used to exclude any peak-to-valley distance below the noise threshold. Each peak was modeled according to Gaussian, Lorentzian, or Voigt shapes; however, no Voigt shapes were observed. To design appropriate curves, the valleys of each fitted shape were lengthened from the edges using the tangent line upon reaching the zero absorption height.

Each XRD pattern was linearly detrended to remove any spurious deviation from the x axis. Figure SM2 displays the maxima detected from the current literature for possible initial and final phases. Then each peak was associated with the corresponding valley with the same procedure applied to FTIR, measuring the local minima preceding and coming after the peak.

The signals at 1 h and 24 h were labeled as the "Initial phase", abbreviated as "I", whereas signals at 144 h and 180 h were the latter synthesis phases, called the "Final stage", and abbreviated as "F". Initial phase wavenumbers identifying absorbance bands from FTIR spectra analysis were 563, 585, 597, 954, 984, 1025, and 1039 cm^{-1}; those for XRD were at 12.10, 22.21, 22.72, 24.10, 29.65, 30.6, 31.25 2θ angles. Final phase wavenumbers characterizing FTIR absorbance bands were 560, 601, 872, 962, 1023, 1077, 1108, and 1295 cm^{-1}; the angles for XRD were 4.72, 9.44, 9.76, 16.10, 26, 31.55, 32.59, 33.52. The angles and wavenumber values of each peak were illustrated in Figures SM3a and SM3b, in relation to class membership. Using these strip plots, one could note the shifts in XRD or FTIR associated with each class; despite a few peculiar patterns, most data points only fluctuate a few values along the x-axis.

XRD and FTIR peak modeling

Utilizing the peak height and distance from the valley, each peak was represented by a Gaussian, Lorentzian, or Voigt shape. The best matching curve fitting was selected to minimize the variance error. Tables SM1 and SM2 collect information about each peak fitted shape ("G" stands for Gaussian or "L" is for Lorentzian) .

From each fitted curve, nine features were computed:

- Normalized absorbance or intensity at the peak (also known as height of the peak) from zero
- Dispersion of the fitted distribution measured at 2 and 3 standard deviations
- Area under the fitted curve
- Kurtosis (descriptor of tailedness of the fitted shape)
- Skewness (descriptor of asymmetry of the fitted shape)
- Ratio between the normalized absorbance or intensity of a peak and a valley
- Ratio between peak height and width
- Amplitude at half width

All nine features from XRD and FTIR were merged in a unique dataset of 56 rows, shuffling the entries row-wise. At the same time, the two mentioned above class labels were associated with each instance: "I" meant the early stages of OCP production (present phase: α-TCP at 1 h and 24 h), and "F", the latter phases of the OCP transformation enclosing 144 h and 180 h time points. In this way, each row of the joint dataset was linked to a class summarizing the phase of the OCP synthesis (Table 2). Moreover, each row representing the features extracted from the fitted models of the XRD and FTIR peaks had a corresponding theta or wavenumber value.

Feature selection

Not all nine features derived from the XRD and FTIR peak fitting might be meaningful in establishing peculiar characteristics of the time evolution during OCP production. For example, a few of them could be redundant or less informative than others. For this reason, a machine learning methodology has been employed to score each feature and retain only those most important in determining the time frame of OCP phase shifts. In other terms, features were scored in their ability to distinguish the class labels. With the recursive feature elimination procedure, a classifier is continuously trained on all features removing the one that contributes less than others to the classification results, as shown for nanomaterials toxicity prediction[56]. At the end of the procedure,

Time	Class label	Class instances	XRD instances	FTIR instances
1 h and 24 h	Initial	26	14	12
144 h and 180 h	Final	30	14	16

Table 2. Class labels associated to each time point of OCP production.

each feature is ranked by the times it contributes to the best outcomes using a Random Forest classifier coded to account for class imbalances[57]. Additionally, cross-validation was chosen as the training method to provide a complete evaluation of all instances and enhance generalization (3-fold stratified cross-validation)[58]. The less essential dataset attributes for phase discrimination were the peak's kurtosis and the height/width ratio.

Spatial filtering

In current implementation the reduced dataset containing the seven most significant attributes was inputted to a custom Python function acting as spatial filter. The spatially filtered data matrix to discriminate the two classes could be written as

$$F = W^T E \tag{1}$$

with F the surrogate, spatially filtered points, E the original signal feature array of N samples, and W the spatial filters. The matrix W contains the eigenvectors corresponding to the first eigenvalue and the last one: through general eigen-decomposition it could be possible to maximize the ratio of the projected covariance of one condition compared to the other, highlighting the discriminative patterns optimized on the variance of the classes. In the proposed approach, the covariance matrices for the two classes C_{class1} and C_{class2} could be computed by simultaneous diagonalization

$$C_{class1} = \frac{E_{class1}\, E_{class1}^T}{N_{class1}} \tag{2}$$

$$C_{class2} = \frac{E_{class2}\, E_{class2}^T}{N_{class2}} \tag{3}$$

$$C = C_{class1} + C_{class2} = P_0 + D + P_0^T \tag{4}$$

with P_0 the matrix of eigenvectors, whereas D represents the diagonal matrix of eigenvalues of C. In D the eigenvalues are sorted in descending order to facilitate the identification of the first and the last one. Solving by applying the generalized eigenvalue problem, and considering that the eigenvectors are the same for both classes

$$C_{class2}^{-1}\, C_{class1} = P\, D\, P^{-1} \tag{5}$$

which is equivalent to

$$D = P\, C_{class1}\, P^T \tag{6}$$

$$I = P\, C_{class2}\, P^T \tag{7}$$

with I the identity matrix such that $I = D_{class1} + D_{class2}$.

The first and last eigenvectors of P according to the eigenvalues could be selected as spatial filters. Similar method based on eigenvectors was applied on other disciplines to evaluate spatial dependence[26,28,59–61].

k-PCA

Kernel principal component analysis (k-PCA) is an extension of the classical principal component analysis technique[62]; in many real-world applications, data may not be linearly separable, and conventional PCA may not capture the underlying structure effectively. Kernel PCA addresses this limitation by implicitly mapping the input data into a high-dimensional feature space, where it becomes linearly separable. The key idea behind Kernel PCA is to use a kernel function to implicitly transform the input data into a higher-dimensional space, where linear techniques can be applied more effectively[63]. The "kernel trick" captures complex, nonlinear relationships in the data. The most commonly used kernel functions include the polynomial kernel, radial basis function kernel, and sigmoid kernel. The k-PCA procedure initially calculates the similarity or distance between each pair of data points based on the chosen kernel function. Afterward, the kernel matrix is transformed to ensure the data is centered in the feature space. It is performed by subtracting the mean of each column and each row of the kernel matrix from the corresponding elements; this operation centers the data around zero in the feature space. Then, the eigenvectors and eigenvalues of the centered kernel matrix are computed. These eigenvectors represent the directions in the high-dimensional space that capture the most variance in the data. Finally, the data is projected onto the principal components obtained from the eigenvectors. In kernel principal component analysis, the data's measurement unit remains unchanged as the kernel trick is implicitly applied to map the data into a higher-dimensional space. In Figs. 1, 2, and 3, the two-component k-PCA was applied, with the axes representing the directions in the high-dimensional feature space that capture the most variance after the data has been implicitly mapped using a chosen kernel function. Unlike standard PCA, where the axes represent the principal components that are linear combinations of the original features, the axes in k-PCA represent nonlinear combinations of the original features.

Data availibility

The datasets generated and/or analysed during the current study are available from the corresponding author on reasonable request.

Received: 23 June 2023; Accepted: 8 January 2024
Published online: 17 January 2024

References

1. Albrektsson, T. & Johansson, C. Osteoinduction, osteoconduction and osseointegration. *Eur. Spine J.* **10**, S96–S101 (2001).
2. Jayesh, R. S. & Dhinakarsamy, V. Osseointegration. *J. Pharm. Bioallied Sci.* **7**, S226 (2015).
3. Dorozhkin, S. V. Multiphasic calcium orthophosphate (capo4) bioceramics and their biomedical applications. *Ceram. Int.* **42**, 6529–6554 (2016).
4. Drouet, C. Apatite formation: Why it may not work as planned, and how to conclusively identify apatite compounds. *BioMed Res. Int.* **2013**, 25 (2013).
5. Kovrlija, I., Locs, J. & Loca, D. Octacalcium phosphate: Innovative vehicle for the local biologically active substance delivery in bone regeneration. *Acta Biomater.* **135**, 27–47 (2021).
6. Suzuki, O., Shiwaku, Y. & Hamai, R. Octacalcium phosphate bone substitute materials: Comparison between properties of biomaterials and other calcium phosphate materials. *Dent. Mater. J.* **39**, 187–199 (2020).
7. Deguchi, K., Nomura, S., Tsuchiya, A., Takahashi, I. & Ishikawa, K. Effects of the carbonate content in carbonate apatite on bone replacement. *J. Tissue Eng. Regen. Med.* **16**, 200–206 (2022).
8. Suzuki, O. Octacalcium phosphate: Osteoconductivity and crystal chemistry. *Acta Biomater.* **6**, 3379–3387 (2010).
9. Kovrlija, I. *et al.* Exploring the formation kinetics of octacalcium phosphate from alpha-tricalcium phosphate: Synthesis scale-up, determination of transient phases, their morphology and biocompatibility. *Biomolecules* **13**, 462 (2023).
10. Suzuki, O., Hamai, R. & Sakai, S. The material design of octacalcium phosphate bone substitute: Increased dissolution and osteogenecity. *Acta Biomater.* **20**, 20 (2022).
11. Fedotov, A. Y. *et al.* Preparation of octacalcium phosphate from calcium carbonate powder. *Inorg. Mater.* **49**, 1148–1151 (2013).
12. Chow, L. C. & Eanes, E. D. *Octacalcium Phosphate* Vol. 18 (Karger Medical and Scientific Publishers, 2001).
13. Fowler, B. O., Markovic, M. & Brown, W. E. Octacalcium phosphate. 3. Infrared and Raman vibrational spectra. *Chem. Mater.* **5**, 1417–1423 (1993).
14. Markovic, M., Fowler, B. O. & Brown, W. E. Octacalcium phosphate carboxylates. 2. characterization and structural considerations. *Chem. Mater.* **5**, 1406–1416 (1993).
15. di Giacomo, V., Cataldi, A. & Sancilio, S. Biological factors, metals, and biomaterials regulating osteogenesis through autophagy. *Int. J. Mol. Sci.* **21**, 2789 (2020).
16. Suwardi, A. *et al.* Machine learning-driven biomaterials evolution. *Adv. Mater.* **34**, 2102703 (2022).
17. Al-Kharusi, G., Dunne, N. J., Little, S. & Levingstone, T. J. The role of machine learning and design of experiments in the advancement of biomaterial and tissue engineering research. *Bioengineering* **9**, 561 (2022).
18. Meyer, T. A., Ramirez, C., Tamasi, M. J. & Gormley, A. J. A user's guide to machine learning for polymeric biomaterials. *ACS Polym. Au* **3**, 141–157 (2022).
19. Guo, J. L., Januszyk, M. & Longaker, M. T. Machine learning in tissue engineering. *Tissue Eng. Part A* **29**, 2–19 (2023).
20. Hook, A. L. *et al.* Combinatorial discovery of polymers resistant to bacterial attachment. *Nat. Biotechnol.* **30**, 868–875 (2012).
21. Wang, H., Zhang, W., Sun, F. & Zhang, W. A comparison study of machine learning based algorithms for fatigue crack growth calculation. *Materials*https://doi.org/10.3390/ma10050543 *(2017).*
22. Kerner, J., Dogan, A. & von Recum, H. Machine learning and big data provide crucial insight for future biomaterials discovery and research. *Acta Biomater.* **130**, 54–65 (2021).
23. Kalidindi, S. R. Feature engineering of material structure for ai-based materials knowledge systems. *J. Appl. Phys.* **128**, 041103 (2020).
24. Gipson, B., Zeng, X. & Stahlberg, H. 2dx_merge: Data management and merging for 2d crystal images. *J. Struct. Biol.* **160**, 375–384 (2007).
25. Griffith, D. A. & Griffith, D. A. *Spatial Filtering* (Springer, 2003).
26. Liu, X., Kounadi, O. & Zurita-Milla, R. Incorporating spatial autocorrelation in machine learning models using spatial lag and eigenvector spatial filtering features. *ISPRS Int. J. Geo Inf.* **11**, 242 (2022).
27. McCORD, M., Davis, P., Bidanset, P. & Hermans, L. Prediction accuracy for property tax mass appraisal: A comparison between regularized machine learning and the eigenvector spatial filter approach. *J. Prop. Tax Assess. Admin.* **19**, 2 (2022).
28. Islam, M. D., Li, B., Lee, C. & Wang, X. Incorporating spatial information in machine learning: The Moran eigenvector spatial filter approach. *Trans. GIS* **26**, 902–922 (2022).
29. Fan, L., Zhang, F., Fan, H. & Zhang, C. Brief review of image denoising techniques. *Vis. Comput. Ind. Biomed. Art* **2**, 1–12 (2019).
30. Hou, Y. *et al.* The state-of-the-art review on applications of intrusive sensing, image processing techniques, and machine learning methods in pavement monitoring and analysis. *Engineering* **7**, 845–856 (2021).
31. Du, P. *et al.* Advances of four machine learning methods for spatial data handling: A review. *J. Geovisual. Spat. Anal.* **4**, 1–25 (2020).
32. Mathew, A., Amudha, P. & Sivakumari, S. Deep learning techniques: An overview. *Adv. Mach. Learn. Technol. Appl. Proc.* **2020**, 599–608 (2021).
33. Maigyte, L. & Staliunas, K. Spatial filtering with photonic crystals. *Appl. Phys. Rev.* **2**, 25 (2015).
34. Jade, A. *et al.* Feature extraction and denoising using kernel PCA. *Chem. Eng. Sci.* **58**, 4441–4448 (2003).
35. Bannerman, A., Williams, R., Cox, S. & Grover, L. Visualising phase change in a brushite-based calcium phosphate ceramic. *Sci. Rep.* **6**, 32671 (2016).
36. Lee, D. & Kumta, P. N. Chemical synthesis and stabilization of magnesium substituted brushite. *Mater. Sci. Eng., C* **30**, 934–943 (2010).
37. Sánchez-Enríquez, J. & Reyes-Gasga, J. Obtaining ca (h2po4) 2· h2o, monocalcium phosphate monohydrate, via monetite from brushite by using sonication. *Ultrason. Sonochem.* **20**, 948–954 (2013).
38. Liu, Y. & Yu, Y. A survey of the baseline correction algorithms for real-time spectroscopy processing. In *Real-time Photonic Measurements, Data Management, and Processing II*, vol. 10026, 79–85 (SPIE, 2016).
39. Gemperline, P. J. Principal component analysis. *Pract. Guide Chemom.* **2**, 69–104 (2006).
40. Coopman, R. *et al.* Glycation in human fingernail clippings using atr-ftir spectrometry, a new marker for the diagnosis and monitoring of diabetes mellitus. *Clin. Biochem.* **50**, 62–67 (2017).
41. Zhang, L., Small, G. W. & Arnold, M. A. Multivariate calibration standardization across instruments for the determination of glucose by Fourier transform near-infrared spectrometry. *Anal. Chem.* **75**, 5905–5915 (2003).
42. Van der Drift, S., Jorritsma, R., Schonewille, J., Knijn, H. & Stegeman, J. Routine detection of hyperketonemia in dairy cows using Fourier transform infrared spectroscopy analysis of β-hydroxybutyrate and acetone in milk in combination with test-day information. *J. Dairy Sci.* **95**, 4886–4898 (2012).
43. Eilers, P. H. A perfect smoother. *Anal. Chem.* **75**, 3631–3636 (2003).
44. Rowlands, C. & Elliott, S. Automated algorithm for baseline subtraction in spectra. *J. Raman Spectrosc.* **42**, 363–369 (2011).
45. Rey, C. *et al.* Characterization of calcium phosphates using vibrational spectroscopies. *Adv. Calc. Phosphate Biomater.* **20**, 229–266 (2014).

46. Rey, C. C., Combes, C. & Drouet, C. Synthesis and physical chemical characterizations of octacalcium phosphate-based biomaterials for hard-tissue regeneration. In *Octacalcium Phosphate Biomaterials* 177–212 (Elsevier, 2020).
47. Sayahi, M. *et al.* Brushite (ca, m) hpo4, 2h2o doping with bioactive ions (m= mg2+, sr2+, zn2+, cu2+, and ag+): A new path to functional biomaterials?. *Materi. Today Chem.* **16**, 100230 (2020).
48. Irbe, Z., Buss, A., Loca, D. & Malniece, L. Synthesis of amorphous calcium phosphate as a starting material for α-tricalcium phosphate. In *Solid State Phenomena* Vol. 267 119–123 (Trans Tech Publ, 2017).
49. Miyatake, N. *et al.* Effect of partial hydrolysis of octacalcium phosphate on its osteoconductive characteristics. *Biomaterials* **30**, 1005–1014 (2009).
50. Arellano-Jiménez, M., García-García, R. & Reyes-Gasga, J. Synthesis and hydrolysis of octacalcium phosphate and its characterization by electron microscopy and x-ray diffraction. *J. Phys. Chem. Solids* **70**, 390–395 (2009).
51. Döbelin, N. Interlaboratory study on the quantification of calcium phosphate phases by rietveld refinement. *Powder Diffr.* **30**, 231–241 (2015).
52. Ding, X., Li, A., Yang, F., Sun, K. & Sun, X. β-tricalcium phosphate and octacalcium phosphate composite bioceramic material for bone tissue engineering. *J. Biomater. Appl.* **34**, 1294–1299 (2020).
53. Shiwaku, Y. *et al.* Analysis of physicochemical properties of octacalcium phosphate prepared by hydrolysis and co-precipitation with fluoride ions. *J. Ceram. Soc. Jpn.* **118**, 402–405 (2010).
54. Buhrke, V. E., Jenkins, R. & Smith, D. K. *Practical Guide for the Preparation of Specimens for X-Ray Fluorescence and X-Ray Diffraction Analysis* (Wiley-VCH, 1998).
55. Mayerhofer, T. & Krafft, C. Five reasons why not every peak shift in infrared (ir) spectra indicates a chemical structure change. *IR Spectrosc. Today's Spectrosc.* **36**, 25 (2021).
56. Bahl, A. *et al.* Recursive feature elimination in random forest classification supports nanomaterial grouping. *NanoImpact* **15**, 100179 (2019).
57. Wei, J. *et al.* Machine learning in materials science. *InfoMat* **1**, 338–358 (2019).
58. Sha, W. *et al.* Artificial intelligence to power the future of materials science and engineering. *Adv. Intell. Syst.* **2**, 1900143 (2020).
59. Zhang, Y., Brooks, D. H., Franceschini, M. A. & Boas, D. A. Eigenvector-based spatial filtering for reduction of physiological interference in diffuse optical imaging. *J. Biomed. Opt.* **10**, 011014–011014 (2005).
60. Murakami, D. & Griffith, D. A. Random effects specifications in eigenvector spatial filtering: A simulation study. *J. Geogr. Syst.* **17**, 311–331 (2015).
61. Chen, M., Wakai, R. T. & Veen, B. V. Eigenvector based spatial filtering of fetal biomagnetic signals. *J. Perinat. Med.* **29**, 486–496. https://doi.org/10.1515/JPM.2001.068 (2001).
62. Schölkopf, B., Smola, A. & Müller, K.-R. Kernel principal component analysis. In *International Conference on Artificial Neural Networks*, 583–588 (Springer, 1997).
63. Blanchard, G., Bousquet, O. & Zwald, L. Statistical properties of kernel principal component analysis. *Mach. Learn.* **66**, 259–294 (2007).

Acknowledgements

This project has received funding from the European Union's Horizon 2020 research and innovation program under the Marie Sklodowska Curie Grant agreement No 860462. The authors acknowledge the access to the infrastructure and expertise of the BBCE—Baltic Biomaterials Centre of Excellence (European Union's Horizon 2020 research and innovation programme under Grant agreement No. 857287).

Author contributions

M.N. (conceptualization, methodology, numerical experiments, analysis, results discussion, manuscript draft writing, manuscript editing and revision), I.K. (laboratory experiments, data collection and organization, results discussion, manuscript draft writing, manuscript editing and revision), J.L. (project supervision, results discussion, manuscript revision), D.L. (project supervision, results discussion, manuscript revision), L.R. (funding, project administration, project supervision, manuscript revision).

Competing interests

The authors declare no competing interests.

Additional information

Supplementary Information The online version contains supplementary material available at https://doi.org/10.1038/s41598-024-51795-0.

Correspondence and requests for materials should be addressed to M.N.

Appendix 4
4. pielikums

Doxorubicin loaded octacalcium phosphate particles as controlled release drug delivery systems: physico-chemical characterization, *in vitro* drug release and evaluation of cell death pathway

Ilijana Kovrlija, Elżbieta Pańczyszyn, Oznur Demir, Marta Laizane, Marco Corazzari, Janis Locs, Dagnija Loca

International Journal of Pharmaceutics, 653, 2024, 123932, DOI: 10.1016/j.ijpharm.2024.123932

I.K. input: **w**riting – original draft and review & editing, conceptualization, visualization, formal analysis, investigation.

International Journal of Pharmaceutics 653 (2024) 123932

Contents lists available at ScienceDirect

International Journal of Pharmaceutics

journal homepage: www.elsevier.com/locate/ijpharm

Doxorubicin loaded octacalcium phosphate particles as controlled release drug delivery systems: Physico-chemical characterization, *in vitro* drug release and evaluation of cell death pathway

Ilijana Kovrlija [a,b], Elżbieta Pańczyszyn [c,1], Oznur Demir [a,b,1], Marta Laizane [a,b], Marco Corazzari [c,d], Janis Locs [a,b], Dagnija Loca [a,b,*]

[a] Institute of Biomaterials and Bioengineering, Faculty of Natural Sciences and Technology, Riga Technical University, Pulka 3, Riga LV-1007, Latvia
[b] Baltic Biomaterials Centre of Excellence, Headquarters at Riga Technical University, Riga, Latvia
[c] Department of Health Science & Center for Translational Research on Autoimmune and Allergic Disease (CAAD), University of Piemonte Orientale, 28100 Novara, Italy
[d] Interdisciplinary Research Center of Autoimmune Diseases (IRCAD), University of Piemonte Orientale, Novara, Italy

ARTICLE INFO

Keywords:
Octacalcium phosphate
Doxorubicin
Drug delivery
Apoptosis
Osteosarcoma cells
MC3T3-E1

ABSTRACT

Mastering new and efficient ways to obtain successful drug delivery systems (DDS) with controlled release became a paramount quest in the scientific community. Increase of malignant bone tumors and the necessity to optimize an approach of localized drug delivery require research to be even more intensified. Octacalcium phosphate (OCP), with a number of advantages over current counterparts is extensively used in bone engineering. The aim of the present research was to synthesize bioactive and biocompatible doxorubicin (DOX) containing OCP particles. DOX-OCP was successfully obtained *in situ* in an exhaustive range of added drug (1–20 wt%, theoretical loading). Based on XRD, above 10 wt% of DOX, OCP formation was inhibited and the obtained product was low crystalline α-TCP. *In-vitro* drug release was performed in pH 7.4 and 6.0. In both pH environments DOX had a continuous release over six weeks. However, the initial drug burst for pH 7.4, in the first 24 h, ranged from 15.9 ± 1.3 % to 33.5 ± 12 % and for pH 6.0 23.7 ± 1.5 % to 36.2 ± 12 %.The DOX-OCP exhibited an inhibitory effect on viability of osteosarcoma cell lines MG63, U2OS and HOS. In contrast, MC3T3-E1 cells (IC50 > 0.062 μM) displayed increased viability and proliferation from 3rd to 7th day. Testing of the DDS on ferroptotic markers (CHAC1, ACSL4 and PTGS2) showed that OCP-DOX does not induce ferroptotic cell death. Moreover, the evaluation of protein levels of cleaved PARP, by western blotting analysis, corroborated that apoptosis is the main pathway of programmed cell death in osteosarcoma cells induced by DOX-OCP.

1. Introduction

One of the frontline difficulties of today's society is a myriad of different types of cancer. It has been projected that by the onset of 2040, global cancer cases will reach staggering 26 million, with 15 million people standing in need of chemotherapy (Wilson et al., 2019). According to the publicly available data, bone tumours comprise roughly 3–5 % of juvenile cancers and less than 1 % of cancers in adults. Osteosarcoma (OS) is one of the main representatives of malignant skeletal tumour (accounting to ~ 40 % of bone tumours), most commonly diagnosed as the primary malignant bone tumour. Treatment of OS is essentially based on various chemotherapies, followed by surgical resection, while only a scarce number of alternatives are present (vaccines, immune checkpoint inhibitors, monoclonal antibodies) (Martinez et al., 2021). Even though chemotherapy is extremely important as adjuvant therapy, significant data suggests that osteoporosis is an unwanted side effect, resulted from accelerated loss of bone mineral density due to the treatment (Guise, 2006; Siebler et al., 2002). Recent study has demonstrated that senescence (loss of a cell's power of division and growth) propels age-related bone loss contributing to an already dangerous chemotherapy-induced bone loss (Yao et al., 2020).

Doxorubicin hydrochloride (DOX, Doxorubicin, Adriamycin) is a photosensitive, water-soluble chemotherapeutic drug, derived from *Streptomyces peucetius* var. *caesius*. It is being extensively used as the

* Corresponding author at: Institute of Biomaterials and Bioengineering, Riga Technical University, Pulka Street 3, LV-1007, Riga, Latvia.
E-mail address: dagnija.loca@rtu.lv (D. Loca).
[1] Equal input from both Authors.

https://doi.org/10.1016/j.ijpharm.2024.123932
Received 7 November 2023; Received in revised form 16 February 2024; Accepted 19 February 2024
Available online 21 February 2024

first-line therapy for a variety of cancers, among which are osteogenic bone cancers (Sritharan & Sivalingam, 2021). Even though DOX has a reputation as a well-established and highly effective anti-neoplastic agent (Sritharan & Sivalingam, 2021; Tacar et al., 2012; van der Zanden et al., 2021), the successful use of it has been hampered by toxicities ranging from nausea and hematopoietic suppression, to an increased risk of doxorubicin-induced cardiomyopathy (Olson & Mushlin, 1990; van der Zanden et al., 2021; Yin et al., 2018). DOX toxicity is connected with intravenous administration of the drug and its initial half-life of eight minutes and a terminal half-life of 30 h (40 % of the administered dosage gets metabolized by other organs) (Sritharan & Sivalingam, 2021). This initial drug burst (large amounts of the drug are being released before the release rate reaches a stable profile) can have a less negative effect if the delivery of DOX is targeted. Research has shown that the lower initial burst and slower *in vitro* release of doxorubicin loaded microparticles resulted in a lower short term cytotoxicity to Glioma C6 cells when compared to the free drug (Lin et al., 2005). Additional hindrance to the treatment of OS is chemoresistance, usually triggered by the cells poor reaction to the initial therapy or the acquired resistance developed over time. Chemoresistance of osteosarcoma cells to DOX is found to be coupled with the increased drug efflux via p-glycoprotein, mutations in topoisomerase II enzyme, DNA damage repair and surge of detoxification. To increase its widespread applicability and to limit the development of chemoresistance and dosage-dependent toxicity, it is of paramount importance to design a drug delivery system (DDS) that will regulate the localized administration and short/long-term effects of doxorubicin. For that reason, several research groups have investigated the combination of DOX with nanoparticles, liposomal formulations or polymers (Elbayoumi & Torchilin, 2009; Gautier et al., 2012; Modh et al., 2021; A. Z. Wang et al., 2012). Following these benchmarks, calcium phosphates (CaPs), functionalized with drugs/ions for biological or therapeutical applications, have been occupying the scientific headlines in the field of bone therapy (Lebugle et al., 2002; Loca et al., 2015; Mosina et al., 2022).

One of the most important members of CaPs, octacalcium phosphate (OCP, $Ca_8(HPO_4)_2(PO_4)_4x5H_2O$), has been postulated to be a precursor of biological apatite crystals due to its intrinsic structure (Kovrlija et al., 2021; L.C.Chow & Eanes, 2001; Mathew et al., 1988). Next to the abundant accounts of OCP enhancing the bone formation (Anada et al., 2008; Saito et al., 2021; Suzuki & Insley, 2020), as of recently it is being reported as a potent drug delivery vehicle for the incorporation of different therapeutical agents (Kovrlija et al., 2021). OCP has several advantages over other calcium phosphates in terms of a possible drug carrier. The peculiar arrangement of the structure, crystallographic planes resembling the ones from apatite, and a relatively empty water layer (approximately 0.8 nm in thickness), enables the incorporation of distinct ions and molecules inside and not only by adsorption (L.C.Chow & Eanes, 2001). OCP has the ability to readily convert to a thermodynamically more stable phase, calcium deficient hydroxyapatite (CDHAp), demonstrating an ameliorated effect on the bone formation (Honda et al., 2007). Furthermore, the fact that it has higher solubility than the stoichiometric hydroxyapatite (0.0081 g/L at 25 °C for OCP, and 0.0003 g/L for HAp) can directly influence the drug release kinetics and the overall release profile (Dorozhkin, 2016). With this OCP has the potential of a triple effect on sustained delivery of DOX: initial burst release from the DOX molecules adsorbed on the surface of OCP, release of DOX incorporated inside of the OCP's water layer caused by the gradual transformation to apatite and if OCP was combined with a polymer (e.g. alginate) it would allow an even more prolonged drug release as the construct would degrade. As envisioned DDS would be implemented locally in the tumour site and the form of the end application can vary. OCP has been used as a composite coating on titanium alloys (Bordbar-Khiabani et al., 2023), as an injectable cement paste (Demir et al., 2023) or in the form of pellets (Lebugle et al., 2002). Together with the local distribution of the drug, such OCP construct could later on mimic the formation of biomimetic apatite and boost the healing and regeneration processes.

As a drug delivery system, OCP has been previously used in the cancer research and it showed promising results. Main findings have focused on the combined effect with an antineoplastic agent, methotrexate (MTX). Lebugle et al. (Lebugle et al., 2002) have used implants, made mostly from partly hydrolysed OCP and dextran, which were doped with 2, 4 and 6 % of MTX and subsequently tested for *in vitro* and *in vivo* pharmacokinetics and biocompatibility. In vitro release profile resulted in 95.2 %, 68.3 % and 71.9 % of released MTX for granules containing 2 %, 4 % or 6 % of drug, respectively. In *in vivo* environment, 75 % of 2 % MTX remained in the doped implants after 24 h, and 25 % after a week. Ito's research group (Ito et al., 2014), observed the behaviour of a mixture of OCP and HAp as a new potential drug carrier for MTX. Here, the specific characteristic of OCP to hydrolyse into CDHAp were postulated to be the assisting mechanism of the drug release. Tested DDS was capable of retaining the drug, while the release profile was continuous for 48 h and the proliferation of human osteosarcoma cell line was considerably inhibited ($1x10^5$ cells, while the control had $4x10^5$ cells, approximately). Another interesting approach was the functionalization of OCP with extrinsic iron ions and their combination into a scaffold with poly(lactic-co-glycolic acid) for chemotherapy and bone repair after surgery (Shi et al., 2019). Presented DDS sustained human umbilical vein endothelial cell (HUVECs) adhesion and spreading *in vitro* and prompted improved angiogenesis *in vivo*. Model proteins (bovine serum albumin and lysozyme) were significantly greater than on the control without doping (~8.5 and 9.5 mg/g, respectively), neovascularization was higher (after 4 weeks implantation from 71.7 ± 6.6 to 99.8 ± 9.8 per mm^2, depending on the concentration of ion), and DDS had higher stimulatory effects on potential vascularization (~0.25 IOD/area).

Several inorganic CaP biomaterials have been combined with DOX. DOX-loaded apatite particles have shown the cytotoxic behaviour toward human SAOS-2 osteosarcoma cells *in vitro* (~0.2 absorbance, while control had ~ 0.6) (Iafisco et al., 2016). Furthermore, a self-setting paste – combining amorphous calcium phosphate and doxorubicin loaded particles of bone-like carbonated nanocrystalline apatite, have been tested and the *in vivo* implantation was carried out (Martinez et al., 2021). Average number of metastatic pits was 2.0 for the DDS, versus 3.3 for the control, which represented a decrease of nearly 40 %. DOX was also combined with nano and micro HAp by immersing them in dissolved DOX in phosphate-buffered saline (PBS) at different pH (Y. Liu et al., 2022b). At pH 2.5, 81 % DOX was released from nano HAp during 72 h. 46 % DOX was released at pH 5 and at pH 7.4 16 % of the drug was released. For the complex with micro HAp at pH 5.6–6.8, 8–16 % of the drug was released extracellularly compared to pH 7.4. Overall, in *in vivo* setting, micro HAp complex and nano HAp complex had the same antitumor efficacy, whereas micro HAp-DOX was less cytotoxic to MC3T3 cell line compared to nano HAp alone within the 50–100 μg/mL concentration range. When HAp was combined with alfa hemihydrate calcium sulfate (40 to 60 ratio), the biphasic material released 28 % DOX *in vitro* during the first week and at pH 5, 36 % was released, with a strong cytotoxic effect on both MG-63 cells (75 %) and 143B cells (98 %) (Y. Liu et al., 2021). The aforementioned combination of the anticancer drugs and different OCPs could also be the potential strategy to reduce presence of osteosarcoma drug-resistant phenotype, as well as to treat the disease after the therapeutic effect has gone (with the bone regenerative properties of CaPs) (Cree & Charlton, 2017; Nussinov et al., 2021; Pisa & Kapoor, 2020). Moreover, the usage of the local drug delivery systems eliminates the systemic toxicity and lowers the needed amount of the drug. However, to our knowledge, when it came to functionalizing OCP with doxorubicin, DDS that preserves the unique OCP phase and shows anti-osteosarcoma properties has not yet been developed.

Hence, in order to go one step further with the design of a suitable drug delivery vehicle for the bone cancers, a novel, *in situ* synthesis of doxorubicin doped octacalcium phosphate (DOX-OCP) via the

hydrolysis of α-tricalcium phosphate (α-TCP), has been performed. OCP has been functionalized with DOX in a large doping range (from 1 wt% to 20 wt% of theoretical DOX loading). Products were analyzed by an extensive multi-technique characterization approach with X-ray diffractometry (XRD), to certify the existence of OCP phase, and Fourier-transform infrared spectroscopy (FTIR) to show hydrogen phosphate (HPO_4(5) and HPO_4(6)) group P-(OH) stretch and OH in-plane bend. Furthermore, scanning electron microscopy (SEM) was performed to show the morphology of the novel DDS. After establishing the physicochemical characteristics of the materials, the *in vitro* release kinetics of doxorubicin in phosphate-buffered saline (PBS) at pH 7.4 and pH 6.0 were assessed over a six-week period using ultraviolet–visible spectrometry (UV–Vis). Furthermore, as prepared local drug delivery systems (DOX-OCP) were subjected to the cytocompatibility evaluation with human osteosarcoma cell lines, MG-63 and murine calvarial cell line, MC3T3-E1. The cytotoxicity of the DOX towards MG63 and MC3T3-E1 cells was also assessed by determining the IC50 values. The choice of using both MG63 and MC3T3-E1 cell lines enables a comparative analysis of the response between cancer cells (MG63) and normal cells (MC3T3-E1), when exposed to the DOX-OCP drug delivery system. By studying the impact of DOX loaded OCP powders on MG63 cells, valuable insights can be gained regarding the development of effective *in vivo* drug delivery systems for bone cancer treatment (Banerjee & Bose, 2019). Additionally, assessing the effects on MC3T3-E1 cell line, provides important information on the system's efficacy in post-tumor excision treatments and its potential to reduce metastases (Pinski et al., 2001).

Apoptosis has long been considered a deliberate mechanism of programmed cell death (PCD) and the pathways involved in this process have been extensively studied in various types of tumour cells (X. Wang et al., 2022). Moreover, the induction of apoptosis was recognized as a prominent therapeutic approach for eliminating cancer cells (Ji et al., 2015; J. Li et al., 2016; Pfeffer & Singh, 2018; Singh et al., 2022). However, recent increasing evidence has proven that an anti-tumour strategy based on the induction of non-apoptotic cell death is a promising direction for addressing certain challenges (e.g., poor chemotherapy efficacy, genomic alterations, low tumour cellularity) in the cancer therapy (X. Wang et al., 2022). Ferroptosis is a newly discovered form of PCD that differs from apoptosis, necrosis, and autophagy at both morphological and biochemical levels (Xuejun Jiang et al., 2021). Ferroptosis characteristics, identified by iron-dependent accumulation of lipid peroxides and inhibition of GPX4, highlight new treatment opportunities for cancers that are resistant to conventional therapies, including osteosarcoma (S. Li et al., 2023; X. Liu et al., 2022b; Qiu et al., 2022). Furthermore, the recently developed therapeutic agent for osteosarcoma by Fu et al., was observed to impede tumour growth through the induction and synergistic interaction of ferroptosis and apoptosis (Fu et al., 2021). Osteosarcoma exhibits high genetic heterogeneity, leading to variations in genomic and proteomic profiles among cell lines. Consequently, these cells may display diverse differentiation capacities, ranging from osteoblastic to other phenotypes resembling neoplasms *in vivo*. Moreover, differences in tumor formation capacity, influenced by the composition of the extracellular matrix (ECM), and metastatic potential, determined by the expression of specific markers, contribute to their aggressiveness. These variations can significantly impact tumor response to treatment and overall therapy outcomes. Hence, employing a variety of cell lines is essential when screening for PCD. Therefore, in order to test which pathway of cell death is undergoing when exposed to OCP-DOX DDS, we evaluated the induction and execution of both apoptosis and ferroptosis with a panel of OS cells – U2OS, MG63 and HOS.

Through this comprehensive evaluation, our study aims to enhance the understanding of the effects DOX-OCP drug delivery system has on bone cancer cells, leading to the development of improved treatment strategies to minimize metastasis after tumour excision. Furthermore, present research helps to understand the role OCP could have in the incorporation of a known chemotherapeutic drug, and the synergy effects the presented construct could have on the biological response. This would provide a new, alternate, functionalized bone material for therapeutic applications.

2. Materials and methods

2.1. Materials

The following reagents have been used throughout the experiments: orthophosphoric acid (H_3PO_4, 75 %) was purchased from Latvijas Ķimija, Latvia. Doxorubicin hydrochloride (DOX, Lot 20120715) was purchased from CHEMOS Gmbh Germany and from Merck, Milan, IT, hydrochloric acid (HCl, 37 %, Lot Z0720617 111) was purchased from Emsure®, Germany and phosphate buffered saline (PBS, Lot SLCH0989) from Sigma Aldrich, USA. Dulbecco's phosphate buffered saline (DPBS) was purchased from Sigma Aldrich (Darmstadt, Germany) and Gibco™ and Thermo Fisher, USA. Dimethyl sulfoxide (DMSO) was purchased from Sigma Aldrich, USA. 24-well plates with insert purchased from VMR, USA. Minimum essential medium α (MEM-α), penicillin–streptomycin (pen-strep), fetal bovine serum (FBS) and Trypsin EDTA 1X were acquired from Gibco™, Thermo Fisher, USA and from EuroClone, Pero, IT. MG63 and MC3T3-E1 cells (LOT:7009744) were purchased from ATCC, USA. Cell counting kit-8 (CCK-8) and CellTiter Blue assay kit were purchased from Sigma Aldrich, USA. U2OS, MG63 and HOS osteosarcoma cell lines (used to test cell death with 1DOX-OCP) were purchased from 'Biological Resource Center ICLC Cell bank, Core facility IRCCS Ospedale Policlinico San Martino, Genova (IT). Dulbecco's modified Eagle's medium – DMEM, EuroClone; Pero, IT. L-glutamine was from Sigma-Aldrich; Milan, IT and Ferrostatin-1 (Fer1) from Merck, Milan, IT. AlamarBlue™ reagent (Bio-Rad; Berkeley, CA, US) and multiwell inserts (0.4 μm pore size; Sarstedt, Germany). TripleXtractor reagent (Grisp; Porto, PT); ExcelRT™ Reverse Transcription Kit (SMOBIO, Bio-Cell; Rome, IT) and RIPA Buffer supplemented with a protease inhibitor cocktail (Merck, Milan, IT). Non-fat dry milk (Merck, Milan, IT), and Tween20 (Merck, Milan, IT). Primary antibodies: anti-cleaved PARP (1:1000, Cell Signaling Technology: Danvers, US); anti-Tubulin (1:1000, Santa Cruz Biotechnology, Dallas, US), secondary antibodies (1:5000; Bio-Rad) and SuperSignal West Pico Plus (ThermoFisher).

2.2. Synthesis methodology

2.2.1. Synthesis of octacalcium phosphate

To obtain α-TCP, amorphous calcium phosphate (ACP) was synthesized and heated for one hour at 650 °C (5 °C/min) (Kovrlija et al., 2023). Prior to OCP synthesis, α-TCP was fully analyzed and its phase composition was corroborated with XRD. 100 mg of α-TCP were immersed into 50 mL of 0.0016 M H_3PO_4 solution at room temperature, under unremitting stirring (300 rpm), during the 24 h period. pH was monitored throughout the entire time frame. Obtained sample was washed with deionized water and left to dry at 37 °C. The obtained octacalcium phosphate is further referred to as the OCP. The synthesis have been performed more than five times in order to claim the formation of OCP.

2.2.2. Incorporation of doxorubicin in octacalcium phosphate

Same procedure of α-TCP hydrolysis towards OCP was used for the drug incorporation. 100 mg of α-TCP and corresponding amount of theoretical DOX load (1, 3, 5, 7, 8, 9, 10 and 20 wt%) were simultaneously immersed into 50 mL of 0.0016 M H_3PO_4 solution at room temperature for 24 h, with constant stirring (300 rpm). Obtained samples were left to dry at 37 °C. The obtained doxorubicin loaded octacalcium phosphate is named depending on the theoretical loading amount of DOX that was added (see Table 1). Additional samples were synthesized in the same manner with 12, 15 and 18 wt% of DOX to

Table 1
Identification of obtained doxorubicin loaded calcium phosphates.

Sample name	Precursor	Theoretical amount of DOX used (wt%)
OCP	α-TCP	0
1DOX-OCP		1
3DOX-OCP		3
5DOX-OCP		5
7DOX-OCP		7
8DOX-OCP		8
9DOX-OCP		9
10DOX-OCP		10
12DOX-CaP		12
15DOX-CaP		15
18DOX-CaP		18
20DOX-CaP		20

ascertain the CaP phase that is being formed between the further tested 10 wt% and 20 wt% of DOX. However, they were not used in the *in vitro* drug release and cytotoxicity assessments. The synthesis have been performed more than five times in order to claim the formation or inhibition of OCP phase.

2.2.2.1. Assessment of doxorubicin adsorption on octacalcium phosphate. In order to test whether the *in situ* methodology of adding doxorubicin to OCP results in the drug being incorporated into OCP, an adsorption test was carried out in the following manner. 100 mg of OCP and 9 mg of DOX (corresponding to the 9DOX-OCP from the *in situ* loading) were added in 50 mL of PBS and stirred continuously for 24 h (300 rpm). Obtained samples were left to dry at 37 °C. As obtained product (referred further as 9DOX-OCP ads.) was tested with XRD and subjected to *in vitro* drug release test for 48 h in PBS pH 7.4.

2.3. Phase and composition characterization

2.3.1. X-ray diffraction

Presence of OCP phase was examined by using X-ray powder diffractometry. XRD was completed using PANalytical Aeris diffractometer (The Netherlands) and complementary analysis were done with X'PertHighScore and the International Centre for Diffraction Data PDF-2 (ICDD) database. To obtain XRD pattern the following parameters were used: 40 kV and 15 mA, step size 0.0435°, from 3° to 60° 2θ degrees and time per step 299.575 s. For crystalline phase identification ICDD entries were used – #026–1056 for OCP and #009–0348 for α-TCP.

2.3.2. Fourier-transform infrared spectroscopy

Fourier transform infrared spectrometer Thermo Scientific Nicolet™ iS^{TM}50 (Waltham, MA, USA), used in Attenuated Total Reflectance (ATR) mode, was employed to characterize functional groups of powders at the molecular level. The FTIR spectra were recorded in the range 4000–400 cm^{-1}, with the number of scans 64, at a resolution of 4 cm^{-1}. The processing software was OMNIC.

2.3.3. Scanning electron microscopy

The surface morphology of the OCP and DOX-OCP was visualized by scanning electron microscope (Tescan Mira\LMU, Tescan, Czech Republic). Sample image generation was performed with combination of secondary electrons and back-scattered electrons, created at an acceleration voltage of 5 kV. Samples were secured with an electrically conductive double-sided adhesive carbon tape, on a standard aluminium pin stubs. Prior to the SEM measurement, samples were sputter coated with gold, using Emitech K550X (Quorum Technologies, United Kingdom) sputter coater.

2.4. Determination of drug release profiles in vitro

2.4.1. Drug content and drug release in physiological and tumour mimetic pH

To evaluate *in vitro* DOX release from the prepared DOX-OCP powders, 15 mg of three replicate samples from each DOX-OCP batch were immersed in 4 mL of PBS (pH 7.4 and pH 6.0) and incubated at 37 °C ± 0.5 °C and 100 rpm (Environmental Shaker – incubator ES-20, Biosan, Riga, Latvia). The pH of PBS was adjusted with HCl. 2 mL aliquots of the solutions were taken directly from the vessels after 40 min, 2 h, 4 h, 6 h, 24 h, 48 h and 72 h and, finally, every seven days for a period of 42 days for pH 7.4 and for pH 6.0. The volume taken in both experiments was replaced with 2 mL of fresh corresponding solution, keeping the total dissolution medium volume constant. To determine the drug content in DOX-OCP, all samples were dissolved in the acidic water (pH 1.5 ± 0.05, adjusted with HCl), at a solid to liquid ratio of 1 mg/1 mL and mixed with a vortex. DOX content in dissolution medium was determined using Ultra Violet-Visible spectrometry (UV–Vis, Evolution 300, Thermo Scientific, Waltham, MA, analysis software: VISION pro) at λ = 480 nm and expressed as the cumulative DOX release from the DOX-OCP powders.

2.4.2. Drug adsorption on octacalcium phosphate

DOX adsorption experiments on OCP were carried out using a single DOX to OCP ratio corresponding to the 9 wt% for 9DOX-OCP in the *in situ* methodology (100 mg of OCP, 9 mg of DOX). In order to compare 9DOX-OCP and 9DOX-OCP ads, total drug content was determined, and DOX release was tested for 48 h. The total amount of DOX (DOXads) was determined by dissolving it in the acidic water (pH 1.5 ± 0.05, adjusted with HCl), at a solid to liquid ratio of 1 mg/1 mL and testing with UV–VIS at λ = 480 nm. The drug release of 9DOX-OCP ads was tested at pH 7.4, by following the same procedure described in the previous paragraph.

2.5. In vitro biological studies

2.5.1. Determination of IC50 and cytocompatibility

2.5.1.1. Cell culture. Cytotoxicity of 1DOX-OCP, 5DOX-OCP and 10DOX-OCP was tested on human-derived osteosarcoma cell line MG63 and mouse-derived preosteoblast cell line MC3T3-E1. Prior to the experiments, both cell lines were continuously cultured as described in ATCC product sheet. Briefly, MG63 cells were expanded in α-MEM medium supplemented with 10 % FBS and 1 % pen-strep. Similarly, MC3T3-E1 cells were cultivated in α-MEM medium supplemented with 10 % FBS and 1 % pen-strep. All cell lines were maintained at 37°C in a humidified atmosphere – 5 % CO_2.

2.5.1.2. Drug cytotoxicity. DOX stock solution was prepared by dissolving it in a dimethyl sulfoxide to achieve a high concentration (10 mM). Then, a series of DOX dilutions were prepared by diluting the stock solution with culture medium to obtain a range of concentration (0.1 nM to 1 μM). The stock solution was sterilized through filtering by using 0.22 μm syringe filter.

Each cell line was plated at a concentration of 1x10^4 cells/well in 96-well plate, respectively. The plates were incubated in the incubator for 24 h to allow cell attachment and growth. After 24 h incubation period, the culture media was removed and the DOX dilutions were added by following the serial dilution protocol. The culture medium only (no DOX) was used as a control. Cells were treated with DOX dilutions for 24 h. After 24 h incubation, cell viability was assessed using cell-counting kit-8 (CCK-8). Absorbance was measured by using microplate reader (Infinite® 200 PRO, Tecan, USA) at 450 nm. The percentage of cell viability was calculated for each DOX concentration and for the control wells. A dose–response curve using the log-transformed DOX concentrations was plotted to calculate the IC50 level of DOX (DOX

concentration that causes 50 % inhibition of cell viability) on MG63 and MC3T3-E1 cell lines.

2.5.1.3. Cell viability assays. MG63 and MC3T3-E1 cells were cultured as described above. The cytotoxicity of DOX-loaded OCP powders (1DOX-OCP, 5DOX-OCP, and 10DOX-OCP) was assessed using indirect methods. Prior to cell seeding, DOX-loaded OCP powders were sterilized with 70 % ethanol for 40 min. $5x10^4$ cells were seeded per well in a 24-well plate. Then, a cell strainer (VMR, USA) with a pore size of 0.4 μm, containing 3.75 mg DOX-loaded OCP powder, was placed in each well and incubated for 7 days. The powder/medium ratio (3.75 mg/mL) was maintained, as in the DOX release measurement experiment. Cell viability (%) was determined using the CellTiter-Blue™ assay, following the manufacturer's instructions. Briefly, CellTiter-Blue reagent was added to each well on day 1, 2, 3, 5, and 7, and incubated for two hours. After incubation, the CellTiter-Blue™ containing medium was transferred to a 96-well plate, and the absorbance was measured at 570 nm using a microplate reader (Infinite® 200 PRO, Tecan, USA), with 600 nm as the reference wavelength. Additionally, optical images of the cells were captured after 7 days of incubation to assess their morphology and overall growth.

2.5.2. Determination of cell death pathway

2.5.2.1. Cell culture and treatment. U2OS, MG63 and HOS osteosarcoma cell lines were maintained in DMEM supplemented with 10 % FBS, 2 mM L-glutamine and 1 % penicillin/streptomycin, and cultured at 37 °C in humidified incubator with 5 % CO_2. Cells were exposed to 3.75 mg/mL of 1DOX-OCP, 5.4 μM doxorubicin and 10 μm Ferrostatin-1.

2.5.2.2. Cell viability assays. Cell viability was measured using AlamarBlue™ reagent according to the manufacturer's instructions. Briefly, cells were plated in 24-well plates at a density of $15x10^3$ cells/well. Cells were exposed for 48 – 72 h to 3.75 mg/mL of 1DOX-OCP or OCP alone in indirect contact, by using multiwell inserts. After treatments, the cell medium was discarded and an appropriate volume of AlamarBlue® reagent was added and incubated for up to 4 h. Fluorescence was monitored at 530–560 nm excitation wavelength and 590 nm emission wavelength, using a TECAN microplate reader (TECAN, Switzerland).

2.5.2.3. qRT-PCR. TripleXtractor reagent was used to isolate total RNA, as indicated by the supplier. The ExcelRT™ Reverse Transcription Kit was used to synthesize cDNA, following the manufacturer's instructions, by using 2 mg of total RNA. Quantitative PCR reactions were performed by using a CFX96 thermocycler. Primer sequences are reported in Table 2 and were designed by using the online IDT PrimerQuest Tool software (IDT; https://eu.idtdna.com/Primerquest/Home/Index). The L34 mRNA level was used as an internal control, and the comparative Ct method (DDCt) was used for the relative quantification of gene expression (Gagliardi et al., 2023).

2.5.2.4. Western Blotting analysis. Proteins were isolated by using a RIPA Buffer supplemented with a protease inhibitor cocktail. An equal amount of proteins (20 μg) were subjected to an SDS-PAGE and electroblotted onto nitrocellulose membranes (Bio-Rad). Membranes were blocked for 1 h by using 5 % non-fat dry milk in PBS plus 0.1 % Tween20 and incubated with indicated primary antibodies in a blocking solution, overnight at 4 °C. Primary antibodies were: anti-cleaved PARP (1:1000); anti-Tubulin (1:1000). Detection was achieved using HRP-conjugated secondary antibodies (1:5000) and visualized by SuperSignal West Pico Plus (ThermoFisher). Images were acquired by using a ChemiDoc Touch Imaging System (Bio-Rad) and analyzed by Image Lab software (Bio-Rad).

Table 2
Primer sequences.

Target	*Sequence: Forward/Reverse*
CHAC1	CTCAAGCGCTGTGGATTT/TGTCTCCCTGCCAGAAA
ACSL4	CCTGCAGCCATAGGTAAAG/CAGGCCAGTGTGAAAGAATA
PTGS2	GCCTGGTCTGATGATGTATG/GTATTAGCCTGCTTGTCTGG
L34	GTCCCGAACCCCTGGTAATAGA/GGCCCTGCTGACATGTTTCTT

2.6. Statistical analysis

Each group of samples was represented by three or six replicates. All the synthesis have been done more than five times to show the repetitive formation pathway. Where applicable, results were presented as mean value ± standard deviation.

When comparing groups of samples, analysis was performed in Prism (v8, GraphPad Software, USA), using the one-way ANOVA, Tukey's post hoc analysis and normal distribution Shapiro–Wilk's test. The difference was considered significant for $p < 0.05$. All the experiments were performed in triplicate, and date values were presented as means ± standard deviations. Viability data were analysed using the two-way ANOVA and then Tukey's multiple comparison test. P-values of < 0.05 were considered to indicate statistical significance.

3. Results and discussion

With their exceptional bioactivity and tailorable biodegradability, calcium phosphates have been standing out from other biomaterials, which made them an excellent choice for drug delivery in biomedical applications, orthopaedics and dentistry. OCP is reckoned to possess a higher affinity towards organic molecules than other CaPs (Yang et al., 2010). This is owing to the particular arrangement of the structure, crystallographic planes and a relatively empty water layer, where the incorporation of distinct ions and molecules is much more achievable. The interchangeably arranged structure made of an apatite layer of 1.1 nm– resembling the main attributes of HAp, and a water layer, comprised of ten water molecules (H_2O) in the unit cell of 0.8 nm, mimic a channel going lengthways with the c-axis (Kovrlija et al., 2021). Furthermore, it has been hypothesized that, if the drug loading is implemented *in situ* in the first steps of the OCP synthesis, it can lead to ultrahigh drug loading capacity, ensuring a prolonged drug release (Tang et al., 2011). This is mainly because of the numerous binding sites that are resulting from CaP clusters, which have an ultrahigh specific surface area, giving the possibility for the drug molecules to be adsorbed on the surface. In our previous work (Kovrlija et al., 2023) we have shown that during the hydrolysis process, α-TCP transforms to OCP through several steps: dissolution, precipitation and the growth step of OCP phase. As these steps in the mechanism imply a release of hydroxyl ions (OH^-) and orthophosphate anions (HPO_4^{2-}), their subsequent role in the formation of the hydrated layer in the OCP led us to assume that incorporating the DOX during the *in situ* OCP synthesis process, could potentially lead to the drug loading in the hydrated layer itself.

3.1. Synthesis and characterization of doxorubicin loaded octacalcium phosphate

Being a metastable phase, OCP formation depends on multiple factors and it is not easy to obtain a final pure product without impurities (e.g., brushite) that are present in its transformation process (Kovrlija et al., 2023). Due to this, the first step was to establish the thermal transformation of ACP to α-TCP to be certain that the sintering has yielded pure α-TCP (Fig. 1A in supplementary file (Fig. 1A S)). Subsequently, pure OCP has been synthesized from the low temperature α-TCP and used as a reference material for the final step of creating the DDS with OCP and varying contents of doxorubicin.

3.1.1. Formation of α-TCP and pure OCP

Thermal transformation of ACP to α-TCP was confirmed using XRD

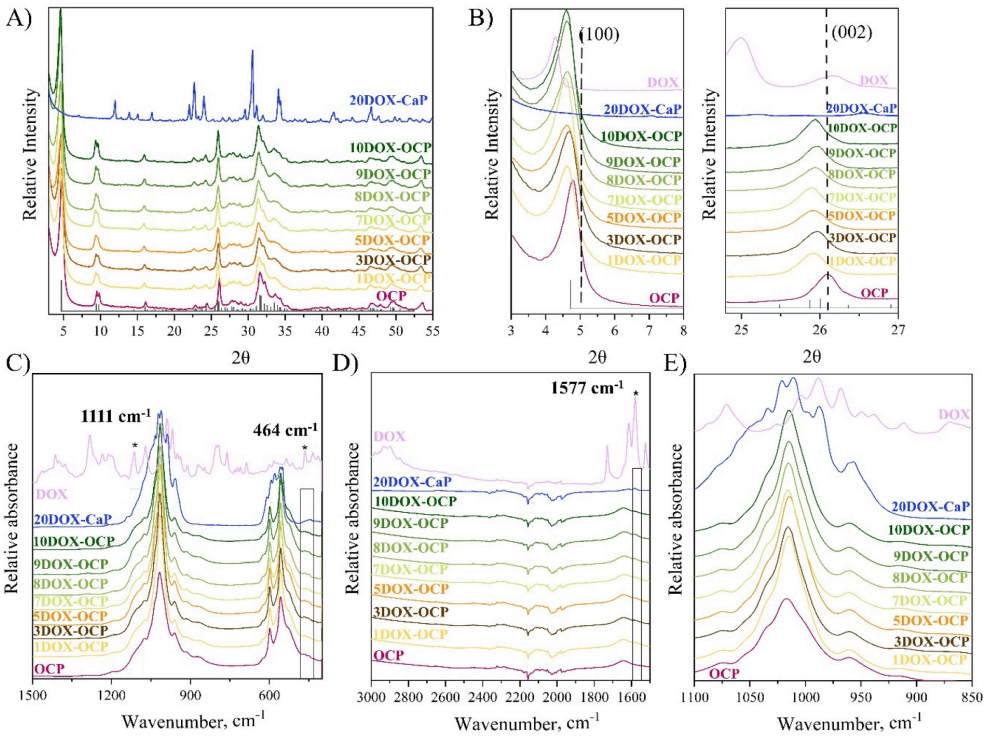

Fig. 1. Characterization of OCP and DOX-OCP (1 – 20 wt%): A) XRD patterns; the reference simulated pattern (ICDD entry #026–1056) corresponds to OCP triclinic phase. B) XRD patterns of OCP and DOX-OCPs. Maxima at 4.7 and 26.1 2θ degrees are respectively attributed to the planes (100) and (002) of OCP crystal. C, D, E) FTIR spectra of DOX-OCP. Star and the combining brackets mark the bands that have changes due to DOX incorporation.

analysis (Fig. 1A in supplementary file (Fig. 1A S)). Representative maxima of α-TCP were in agreement with the reference XRD pattern provided by the ICDD, while FTIR spectroscopy analyses clearly showed the specific α-TCP bands (1300–900 cm^{-1} domain and 700–500 cm^{-1} domain, attributed to the vibrations of PO_4^{3-}) found in the spectra (Fig. 1B S). SEM micrographs (Fig. 1C S) displayed the morphology of α-TCP agglomerates with elongated grain like particles (sizes below 500 nm).

Using α-TCP as the only precursor, OCP was synthesized via hydrolysis process, within 24 h. The XRD pattern, FTIR spectra and SEM corroborated the formation of pure OCP from α-TCP (Fig. 1D S, 1E S, 1F S, respectively).

3.1.2. Doxorubicin loaded OCP

In order to attain the highest possible drug loading, doxorubicin was added *in situ*, at the beginning of the α-TCP hydrolysis. However, as it was shown before with other ions/drugs added to OCP (Kovrlija et al., 2021), loading can be done up to a certain extent, after which the formation of OCP can be inhibited. With this limitation, two questions have been acknowledged: can DOX be loaded into OCP and how much of it can be added to have the OCP phase?

3.1.3. X-Ray Diffraction

DOX was added in the range from 1 wt% to 20 wt% of the total starting amount (Table 1). DOX-OCP phases were attained after 24 h (Fig. 1 A)). Once the syntheses have been performed successfully and OCP particles with 1, 3, 5, 7, 8, 9 and 10 wt% (theoretical loading) of doxorubicin were obtained, XRD analysis have confirmed the characteristic OCP fingerprints, proving that the mechanism of α-TCP conversion was still possible (Fig. 1 A). All X-ray diffraction peaks observed at low angles are characteristic to the OCP triclinic structure. Low angle (100) maximum, at 2θ = 4.7 degrees and a doublet (200) and (010) at 9.4 and 9.7 degrees, respectively, were clearly seen (Fig. 1 A))(Kovrlija et al., 2023). If compared with pure OCP, DOX-OCP diffractograms exhibited a slight shift towards the lower 2θ degrees (Fig. 1B). Slight shift of the 4.7 and 26.1 2θ degrees maxima, respectively, attributed to the planes (100) and (002) of OCP crystal, indicated the lattice expansion in the DOX-OCP system (Fig. 1 B). Moreover, obtained results revealed, that the crystal structure of OCPs was slightly altered with the increasing DOX content, according to the changes of diffraction angle and peak intensity (Fig. 1B). While not a definitive confirmation of DOX integration into the OCP structure, the shifted main maxima observed at 4.3, peaks at 10.1, 16.5, 26.20, and a pattern spanning from 30.1 to 36.5 2θ degrees, suggest a potential for significant influence. It was also shown that the stabilization of the OCP structure was dependent on the amount of DOX used for the OCP-DOX synthesis. If the amount was above 10 wt% (theoretical loading), it led to the inhibition of the c-axis growth and the destabilization of the overall transformation mechanism, leaving the drug adsorbed on the α-TCP phase (Fig. 2 S and Fig. 1 A and B). The concentrations of DOX between 10 and 20 wt% (12, 15 and 18 wt%) have all inhibited the OCP formation (Fig. 2 S), and for further *in vitro* analysis 20DOX-OCP has been chosen as a representative of them. The most significant maxima for α-TCP remained in 20DOX-OCP (12.1, 30.7 2θ degrees, with double maxima ~ 22.8 and ~ 34 2θ degrees) (Fig. 1 A and B).

To test the difference between the synthesis methodologies and to

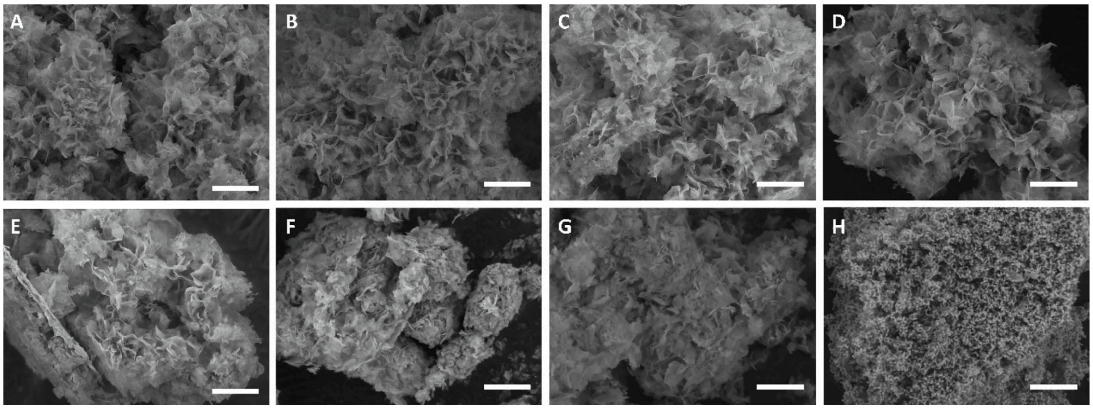

Fig. 2. Characterization of OCP and DOX-OCP (1 – 10 wt%) and DOX-TCP (20 wt%): SEM micrographs (a – 1 wt%, b – 3 wt%, c – 5 wt%, d – 7 wt%, e – 8 wt%, f – 9 wt%, g – 10 wt% and h – 20 wt%); scale bar 5 μm bottom right.

confirm whether the *in situ* strategy resulted in DOX being incorporated in OCP, adsorption experiment has been done. By mixing OCP with the DOX solution, no significant changes have been noticed in the crystallographic pattern of OCP (Fig. 3 S). Previously observed peak shift of the characteristic maxima in 9DOX-OCP synthesized *in situ* (4.7 and 9.4 and 9.7 2θ degrees), which was an indication of DOX incorporation within the water layer, has not been seen in 9DOX-OCP ads. That suggested that DOX was solely adsorbed on the material's surface. The most noticeable change within 9DOX-OCP ads was pronounced maxima at ~ 31 and 45 2θ degrees, which have been assigned to the sodium chloride (NaCl) that was present in the PBS (Fig. 3 S).

3.1.4. Fourier Transform Infrared Spectroscopy

To corroborate the structural identification, FT-IR spectroscopy has been completed on all of the samples. Assignment of the presence of the hydrogen phosphate (HPO_4^{2-}) and phosphate (PO_4^{3-}) groups is of crucial value when establishing the OCP phase. All of the samples, except 20DOX-CaP, have representative markings of the OCP phase (Fig. 1C). The PO_4^{3-} ν_3 stretching mode encompassing the bands at 1077 cm^{-1}, 1296 cm^{-1} and 1120 cm^{-1} has been accentuated. Additionally, PO_4^{3-} ν_4 domain of the OCP spectrum showed the characteristic absorbance bands at 524, 560, 601 and 627 cm^{-1}. More importantly, P-OH stretching at 917 cm^{-1} and 861 cm^{-1}, connected with the HPO_4^{2-} ion has been prominently distinguished. Same as in XRD data, 20DOX-CaP exhibited clearly the markings of α-TCP with strongest bands found in 1300–900 cm^{-1} and 700–500 cm^{-1} domain, attributed to the vibrations of PO_4^{3-}. To some extent, the influence of strong DOX absorbance bands can be seen in DOX-OCP systems. Increasing intensity of the band in the region 1570 cm^{-1} indicates an antisymmetric COO stretch. DOX prominent peak at ~ 1111 cm^{-1} led to the broadening of the PO_4^{3-} ν_3 stretching domain when compared to OCP and as a result, slight shoulder band can be distinguished in DOX-OCP systems (Fig. 1C). The band at 464 cm^{-1} (Fig. 1C) from DOX could indicate the traces in the composition of all the DOX-OCP samples, as the increase in the intensity of the band is gradually higher with the increase of the drug load. The bands assigned to HPO_4(5) at 1193 cm^{-1} in OCP were reduced to a weak band at DOX-OCPs, indicating that the HPO_4(5) group is substantially reduced. However, most of the bands only had a slight broadening, with a high possibility of auxiliary convoluted bands underneath the main ones, hindering the possibility of clearly marking the peaks of DOX (Fig. 1C). Another possible explanation to the changes in the chemical structure could be the formation of DOX/Ca^{2+} complexes. The oscillation of the aromatic ring (C–H oscillations derived from aliphatic groups (e.g., methoxy groups)) occurs throughout the spectral range and also in the areas where slight changes have been noticed in DOX-OCPs (~1580–1600 cm^{-1}). Moreover, the divalent metal-DOX complexes showed the ring breathing and bending vibrations of C(16)-C(18) = O, C (30)–H3 at ~ 1000 cm^{-1} (Jabłonska-Trypuc et al., 2017).

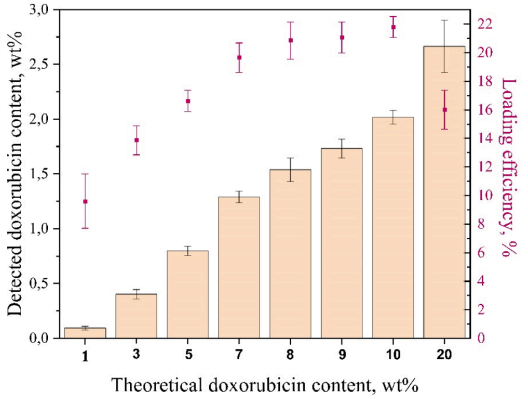

Fig. 3. Total DOX content and DOX loading efficiency in OCP-DOX samples (1 – 10 wt%), and in DOX-TCP sample (20 wt%).

3.1.5. Surface morphology

Particular OCP plate-like morphology makes it easy to distinguish between HAp and α-TCP. Plate crystals usually have a strong tendency to assemble into a rose-like form; however, the size of such an agglomerate varies among different samples, where OCP thin plates did not exceed 2 μm (Fig. 2). During the *in situ* incorporation of DOX, plate-like particles seemed to be more overlapping and entwining with the increase of DOX amount in samples, subsequently leading them to form agglomerates from 1 to 20 μm (Fig. 2 A-G). However, there is no definite indication that this is due to the DOX presence within the system. The highest wt% of incorporated DOX (20 wt%) led to the inhibition of OCP plate like structure and preservation of elongated grain-like particles typical for α-TCP (Fig. 2 H).

3.2. Evaluation of DOX release kinetics from DOX loaded OCP particles

Ever since it was approved by the Food and Drug Administration

(FDA) in 1974 (Sritharan & Sivalingam, 2021), DOX was used in many combinations with multiple intracellular targets. When intravenously administered DOX had an initial half-life of 8 min and a terminal half-life of 30 h, while plasma clearance of doxorubicin was 324–809 mL/min/m^2, and the effect on DNA has been seen in concentrations as low as 10 nM. Nevertheless, the dosage amounts vary depending on the site of usage and overall conditions (e.g., *in vitro*: 2 μM/5 μM for 24 h, *in vivo*: 5 mg/kg/dose, every 15 days (Sritharan & Sivalingam, 2021)). Due to these limitations of short half-life and systemic poisoning, local drug delivery vehicles are highly sought after. CaP therapeutic functionalisation to treat bone diseases became very attractive because of its ability to incorporate and retain the active substance while providing a way to deliver it locally in a controlled manner. DOX adsorption experiments on apatite substrates showed that DOX molecules did not have a high affinity for the surface of apatite and the amount of DOX adsorbed was 8 μmol DOX m^{-2} apatite (Iafisco et al., 2016). When DOX was incorporated into bone cements, contradictory data was seen. One group observed a sustained and controlled release (Tani et al., 2006), while Genin et al. recorded a burst release for the first 40 h that continued to a prolonged release up to 240 h (25 % DOX after 40 h and 35 % after 240 h) (Génin et al., 2004; Pylostomou et al., 2023).

The effect of the *in situ* incorporation of doxorubicin into OCP had a detrimental impact on the amount of the incorporated DOX, as well as on the cumulative drug release. As expected, the obtained results showed that with an increase of theoretical DOX content in the OCP, the detected incorporated drug content and the loading efficiency increased gradually (Fig. 3). In the case of DOX content of 1, 5 and 10 wt% (theoretical loading), the amount of detected incorporated DOX was 0.093 ± 0.01 wt% with the loading efficiency 9.6 ± 1.9 %, 1.54 ± 0.1 wt% with the loading efficiency 20.85 ± 1.29 % and 2.02 ± 0.06 wt% with the loading efficiency 21.8 ± 0.73 %, respectively.

However, with DOX loading of 20 wt%, which did not yield the OCP phase, the highest incorporated DOX amount was observed (2.66 ± 0.24 wt%), but the loading efficiency was quite low (15.99 ± 1.36 %). A possible reason could be that DOX was adsorbed on the surface of α-TCP, thus at the same time inhibited the OCP formation and showed a higher detected drug content.

The *in vitro* release of doxorubicin from the DOX-OCP system in pH 7.4 and pH 6.0 is shown in the Fig. 4. Early DOX burst release, observed initially in the first 24 h up to three days for pH 7.4, ranged from approximately 17 % to 75 % (Fig. 4A), while the continued and uniform release was monitored up to six weeks (Fig. 4B). The plateau of the cumulative release percentage was inversely proportional to the theoretical content of doxorubicin. For example, for 5DOX-OCP, 23.6 ± 1.6 % (28.0 ± 3.7 μg) was released after two hours, 38.9 ± 1.3 % (46.3 ± 4.2 μg) after 72 h and 52.5 ± 2.3 % (62.3 ± 5.8 μg) after 42 days. While, the 10DOX-OCP reached 15.9 ± 1.3 % after two hours, 27.7 ± 1.7 % after 72 h and 38.3 ± 2.0 % after 42 days. It was noticed that the lower the amount of the incorporated doxorubicin, the higher the release rate. This observation could be caused by the phase transformation of OCP to calcium deficient hydroxyapatite. Lower amounts of drug may result in faster transformation, which could consequently lead to a faster release (Ito et al., 2014). Except for 1DOX-OCP, all other tested samples have not completely released the active substance, indicating that the drug release period can be substantially longer. In general, increasing the concentration of the drug loading increased the adsorbed amount of

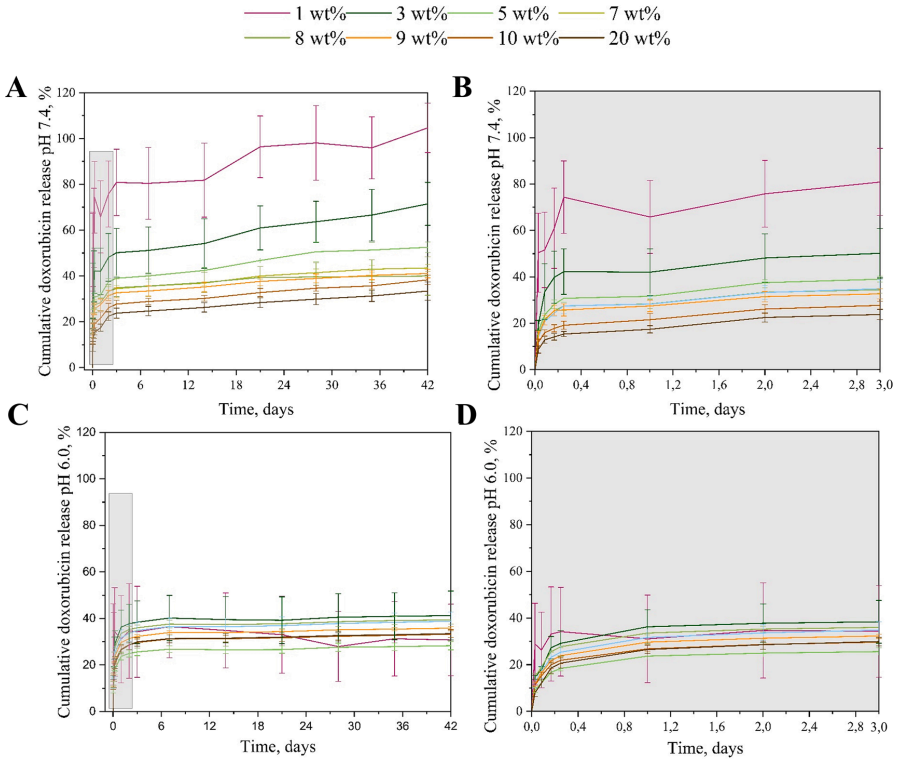

Fig. 4. Doxorubicin doped OCP: A) total doxorubicin release during six weeks (%) pH 7.4 and B) doxorubicin initial burst release in the first 72 h (%) pH 7.4C) total doxorubicin release during six weeks (%) pH 6.0 and D) doxorubicin initial burst release in the first 72 h (%) pH 6.0.

drug until a certain threshold. In our case, even though the amount of the detected incorporated DOX content increased with the addition of 20 wt% of the drug (Fig. 3), the obtained DDS was not considered successful as it prevented the formation of OCP.

The *in vitro* release of doxorubicin from the DOX-OCP system in the tumour mimetic environment (PBS pH 6.0) showed a similar trend for the higher amounts of loaded doxorubicin (7, 8, 9, 10 and 20 wt%), whereas for the lower amounts the release was slower (1, 3 and 5 wt%). Early DOX burst release, observed initially in the first 24 h up to three days, ranged from approximately 23 % to 39 % (Fig. 4D), while the continued and uniform release was monitored up to six weeks (Fig. 4C). For example, 5DOX-OCP released 12.1 ± 0.9 % (20.4 ± 1.6 μg) of DOX after two hours, 25.6 ± 1.6 % (42.9 ± 3.2 μg) after 72 h and 52.5 ± 2.3 % (47.4 ± 4.0 μg) after 42 days. While, the 10DOX-OCP had almost the same release, reaching 15.3 ± 1.3 % after two hours, 29.6 ± 1.5 % after 72 h and 33.1 ± 1.4 % after 42 days. The slower release (and similar release) trend of DOX-OCPs in pH 6.0, could be connected with the stability of OCP in the acidic solutions. OCP's transformation to apatite is solution mediated and guided by factors such as pH, temperature, ionic concentration, time etc. In acidic pH, OCP is stable, except when the solution contains fluoride ions (LeGeros et al., 1989). As we assume the partial release of the drug from DOX-OCP DDS is due to the gradual transition of OCP to apatite, if that transition is hindered the release would be either similar or slower (in case of the small amounts of the drug being incorporated).

In the literature, the mechanism of adsorption and parameters of several models are being attuned to fit the experimental curves, i.e. isotherms of drug adsorption, out of which the most common ones are Langmuir's and Freundlich's (Parent et al., 2017). If the detected quantity of the drug increases gradually with the drug concentration, which was the case in our DDS, it follows Freundlich's isotherm. This potentially indicates that the prospective carrier sites of adsorption stay unsaturated. The initial burst release of DOX within the first six hours continued until day three in a decreased trend, and then it stabilized and continued for the following 39 days. One way to control the initial drug release would be to incorporate the DOX carrier into a polymer, thus creating a more complex DDS (Pelss et al., 2011). Physical adsorption of the doxorubicin molecules to the surface of OCP, through electrostatic forces or hydrogen bonding, between the positively charged DOX molecules and negatively charged OCP could explain the initial burst release. Whereas, the sustained DOX release afterwards could be clarified through strong chemical interaction (Ca–O) that can hamper the escape of the drug from the DOX-OCP drug delivery system. Similar behaviour was noticed by Zhu et al (Qi et al., 2015) when they loaded amorphous calcium phosphate (ACP) with doxorubicin and tested the ACP/Dox DDS in PBS solution, at different pH values. Doxorubicin release was found to be low and they reached a plateau (1.7 %) over a period of 13 h. Jiang et al. (Xiaodan Jiang et al., 2022) tested the release of DOX from hydroxyapatite and also confirmed a quick release during the initial immersion period, followed by the slowly sustained release during the later immersion period (36.5 % at pH 7.4 after 100 h). To test the difference in release between the incorporated doxorubicin via the *in situ* method and doxorubicin adsorbed onto the OCP, 9DOX-OCP ads was immersed in PBS pH 7.4 and observed for 48 h. The initial detected amount of DOX was higher in 9DOX-OCP ads (3.07 ± 0.4 %) than in 9DOX-OCP (1.7 ± 0.1 %). In the first 6 h, 48.3 ± 2.2 % of DOX was released, while at 48 h the detected amount was 51.1 ± 2.8 % (Fig. 4 S). In comparison to the 9DOX-OCP, where DOX was integrated through *in situ* synthesis, only 25.7 ± 2.6 % of DOX was released at the 6th hour, with the total release reaching only 31.5 ± 2.2 % on the second day. This clearly confirmed the effectiveness of the *in situ* method.In *vitro* release evaluations are not envisioned to predict the *in vivo* release, but they rather aim to advance the overall knowledge regarding the parameters inducing the DDS comportment and to give an indication of the set-up of the initial *in vitro* biological screenings.

3.3. In vitro cell studies

3.3.0.1. IC50 and Cellular Response

The IC_{50} values were drawn from the DOX dose–response curve of each cell line (Fig. 5). Accordingly, more than 0.85 ng (0.016 μM) and 3.397 ng (0.062 μM) of DOX is having an inhibitory effect for MG63 and MC3T3-E1 cells, respectively.

The influence of DOX release on the viability of MG63 and MC3T3-E1 cells was tested by placing OCP and DOX-loaded OCP powders in contact with cells by using inserts (Fig. 6). The culture medium incubated with DOX loaded OCPs (5DOX-OCP and 10DOX-OCP) suppressed MG63 and MC3T3-E1 cells in the period of 7 days. However, from day 3 to day 7 of culturing, the pure OCP showed a proliferative effect on both cell lines, resulting in increased cell viability (from 72.70 % to 84.89 % for MG63 cells and from 62.34 % to 96.84 % for MC3T3-E1 cells). The inhibition rate of 10DOX-OCP on the cell viability was significantly higher than that of the 5DOX-OCP and 1DOX-OCP, providing the additional evidence of their pronounced inhibitory effect on MG63 cells (Fig. 6 (a)). These *in vitro* cell studies also demonstrated that a time and concentration-dependent decreasing proliferation rate of MG63 and MC3T3-E1 cells was more evident with 5DOX-OCP and 10DOX-OCP (Fig. 6). With both formulations, the rate of viable cells after 72 h was dramatically low (30.81 ± 0.34 and 17.84 ± 0.09 for MG63 cells and 36.93 ± 1.27 and 24.19 ± 3.22 for MC3T3-E1 cells, respectively). MG63 viability decrease, when exposed to DOX-OCPs, could be solely attributed to the cytotoxic effects of DOX. DOX is known to interfere with DNA replication and induce cell death in various cancer cell lines (Akutsu et al., 1995; Roncuzzi et al., 2014; Wen et al., 2018). In this case, the DOX-loaded OCP powders likely released DOX molecules into the surrounding culture medium, which then interacted with the MG63 cells and caused a decrease in their viability. On the other hand, the increase in viability of MC3T3-E1 cells after 72 h could be due to several factors. MC3T3-E1 cells may have different characteristics or mechanisms that make them more resistant to the cytotoxic effects of DOX compared to the MG63 cells (Fig. 5). It is known that different cell lines can vary in their sensitivity or resistance to chemotherapy drugs, including DOX. Factors such as variations in drug uptake, efflux pumps, DNA repair mechanisms, cell cycle regulation, and apoptotic pathways can influence a cell line's response to cytotoxic agents (J. Wang et al., 2009). Furthermore, the presence of elevated Ca^{2+} ions in the medium could potentially activate the extracellular calcium-sensing receptor (Thorn et al., 2011). This activation, in turn, may enhance the proliferation of the cells. If the DOX created a Ca-complex with the CaP in the proposed DDS, the literature data have shown that the complexation of doxorubicin with metal ions has the ability to increase the cytotoxic properties of the drug (Jabłonska-Trypuc et al., 2017). It has been shown that complexes with Fe^{3+} and Cu^{2+} ions facilitate the binding of doxorubicin to DNA and increase the production of reactive oxygen species, which aids in the cytotoxic effect. However studies also have shown that doxorubicin can form DNA double-stranded breaks in human cells enabling the calcium channel blocker to sensitize cells to doxorubicin and dampen the doxorubicin efficacy (Thuy et al., 2016). Moreover, the observation of comparable or increased viability levels of the OCP powder in comparison to the control group indicated that the uptake of Ca^{2+} ions, which play a crucial role in osteointegration, positively influenced cell proliferation.

Phase-contrast micrographs showed that after 7 days of incubation, the majority of MG-63 cells on the plate incubated with DOX-OCPs were dead, remaining rounded and small in size, indicating an inhibitory effect of DOX (Fig. 6 (c)). In comparison, the control group and OCP powders appeared to result in more spread-out cell lines. The introduction of OCP powders into the cell medium significantly improved cell adhesion, as seen from the polygonal morphology of the cells. The largest cells were observed in the control group.

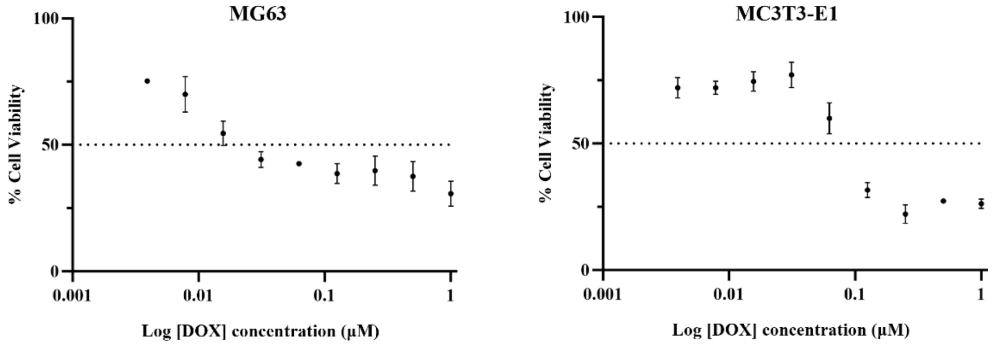

Fig. 5. Comparison of the sensitivity to doxorubicin of the MG63 and MC3T3-E1 cell lines. Cell viability was measured using CCK-8 assay to determine the IC_{50} (μM) of doxorubicin in MG63 (a) and MC3T3-E1 (b) cells after treatment with different concentrations of doxorubicin for 24 h. Error bars indicate the standard deviations (n = 3).

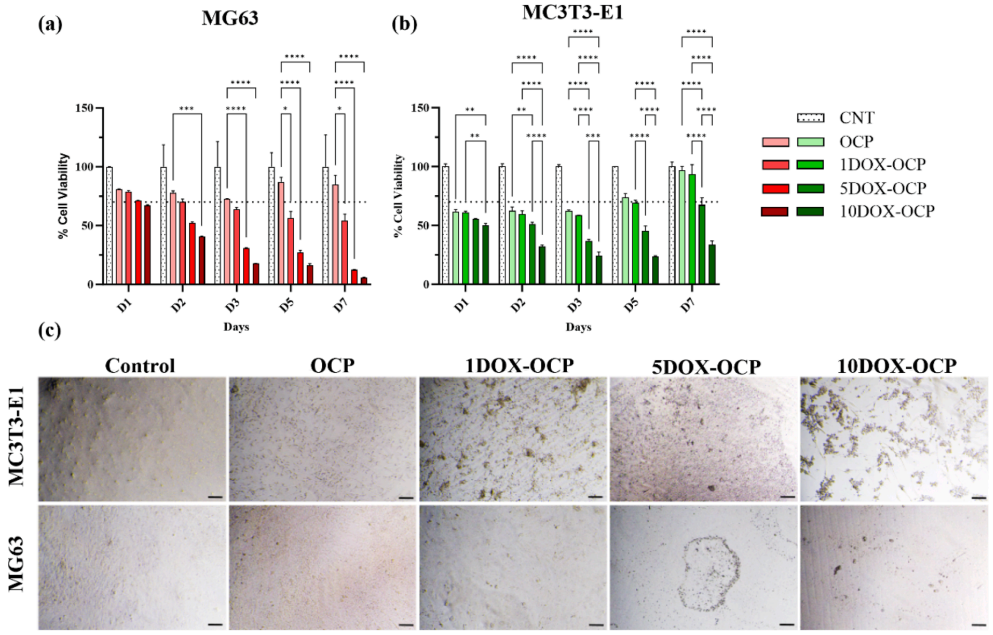

Fig. 6. Cell viability studies of DOX-loaded OCP powders. (a) Cell viability assay of MG63 cells and (b) MC3T3-E1 cells with OCP, 1DOX-OCP, 5DOX-OCP and 10DOX-OCP powders. The dotted line in (a) and (b) represents the viability limit at 70 %. This means that if the viability of cells falls below 70 %, the released drugs or ions are considered toxic. Error bars indicate the standard deviations (n = 3). Statistically significant differences: * for < 0.05 ** for $p < 0.005$, *** for $p < 0.001$, **** for $p < 0.0001$. (c) Phase-contrast images of cell morphology after 7 days of cultivation in different powders. Scale bar indicates 10 μm.

3.3.0.2. Pathway of cell death

To evaluate the anticancer properties and the pathway of cell death induced by 1DOX-OCP, a panel of three human osteosarcoma (OS) cell lines was used. U2OS, HOS, and MG-63 cells were exposed to 3.75 mg/mL 1DOX-OCP or 3.75 mg/mL OCP. 5.4 μM of doxorubicin (DOX), corresponding to the estimated drug released by 1DOX-OCP within 72 h, were used as a positive control. Firstly, cell viability was evaluated after 72 h, in cells stained with AlamarBlue. As in the previous cytocompatibility tests, results indicated a significant decrease in the viability of all tested osteosarcoma cells upon exposure to 1DOX-OCP (Fig. 7). The observed differences in cell viability between 1DOX-OCP and DOX could result from the immediate availability of the drug at the final concentration in the positive control group (DOX), whereas doxorubicin from 1 wt% of OCP-DOX was released gradually in a time-dependent manner, which corresponded to the *in vitro* drug release study (Fig. 4).

In the second stage, the three cell lines were exposed to 3.75 mg/mL of 1OCP-DOX, 3.75 mg/mL of pure OCP, or 5.4 μM doxorubicin (DOX), and the expression of the three well-known ferroptotic markers, such as CHAC1, ACSL4 and PTGS2 (Chen et al., 2021) was evaluated after 48 h by qPCR. Results indicated significant upregulation of all three genes only in HOS cells exposed to 1DOX-OCP (Fig. 5 S). Then, in order to verify if OCP-DOX induces ferroptotic cell death, OS cells were exposed for 72 h to 3.75 mg/mL of 1DOX-OCP and 5.4 μM DOX alone or in combination with the ferroptosis inhibitor Ferrostatin-1 (Fer-1) (Miotto

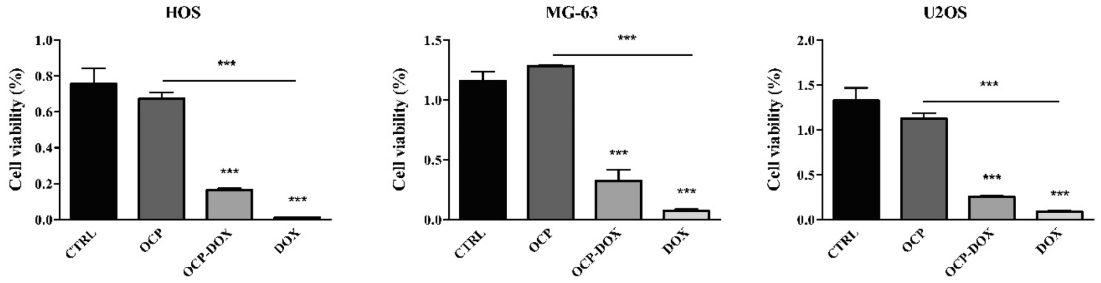

Fig. 7. Sensitivity of OS cells to DOX-loaded OCP powder. The indicated OS cell lines were exposed 72 h to 1DOX-OCP, pure OCP and doxorubicin (positive control). Cell viability was evaluated in AlamarBlue-stained cells. Histograms represent mean ± s.d.; n = 3; ***p < 0.001.

et al., 2020). Cell viability evaluated in AlamarBlue-stained cells revealed no significant changes in OS cell survival in the presence of 1OCP-DOX + Fer1 compared to 1OCP-DOX alone (Fig. 8 A). These results indicated that ferroptosis is not involved in OCP-DOX-induced cell death in OS cells.

Next, we investigated the involvement of the conventional pathway of doxorubicin-induced PCD, apoptosis (S. Wang et al., 2004). To this aim, U2OS, HOS, and MG-63 cells were exposed to 1DOX-OCP, and levels of cleaved PARP, considered as a hallmark of apoptosis (Chaitanya et al., 2010), were evaluated after 48 h of treatment, by western blotting analysis. Results shown in Fig. 8 B indicate increased expression of cleaved PARP in HOS and MG-63 cells exposed to 1OCP-DOX, confirming the induction of apoptotic cell death.

Collectively, our results confirmed the anticancer effects of OCP-DOX, indicating that apoptosis is the main pathway of programmed cell death responsible for its cytotoxic effect on osteosarcoma cells.

4. Conclusions

Even though functionalized OCP crystals revealed a high potential and are assumed to be the future of tailored DDSs, the paucity of evidence on the comprehensive release profile *in vitro*, the aftermath of the *in vivo* settings and their relationship and implications is evident. The presented findings offer new insights into the design of DOX-loaded OCP, and their usage as potential drug vehicles, with satisfying drug loading capacity and sustained release behavior.

In situ loading of DOX-OCP has shown that for the first time it was possible to incorporate the doxorubicin into octacalcium phosphate, while maintaining its characteristic crystal structure. The maximum possible loading that was achieved was 10 wt%, theoretical drug load and the detected DOX content was 2.02 ± 0.06 wt% with the loading efficiency 21.8 ± 0.73 %. Furthermore, it was proven that everything above 10 wt% inhibited the OCP formation. With the developed DOX-OCP systems, the two out of three benefits of OCP's triple effect (discussed in the Introduction section) have been seen: 1) the initial drug that was adsorbed on the surface of OCP was released at first and is

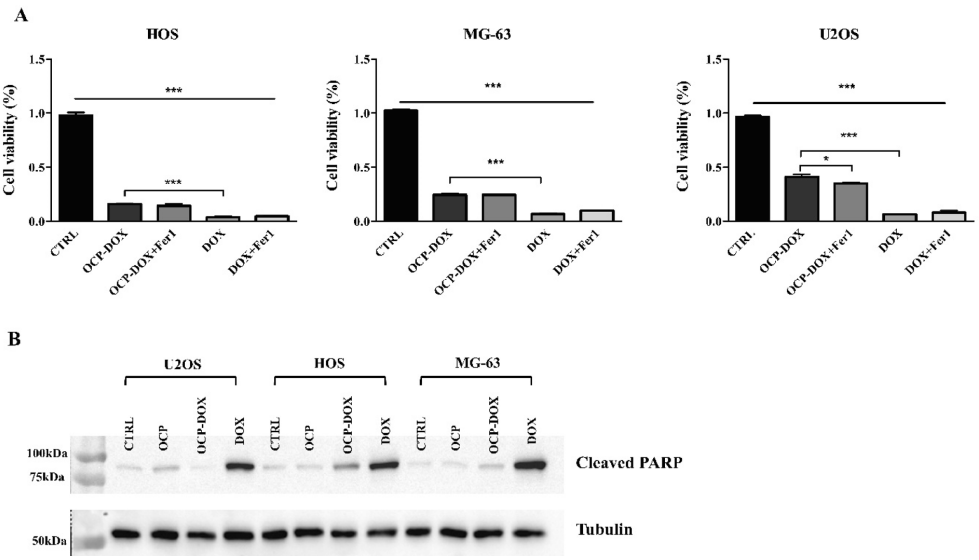

Fig. 8. Characterization of cell death induced by DOX-loaded OCP powder in osteosarcoma cells. (A) U2OS, HOS, and MG63 cells were exposed for 72 h to 1DOX-OCP, pure OCP or doxorubicin alone or in combination with 10 μM of Fer1 (OCP-DOX + Fer1, DOX + Fer1) and cell viability was evaluated in AlamarBlue-stained cells. (B) Protein levels of cleaved PARP were evaluated in osteosarcoma cells exposed as in (A), by western blotting analysis. GAPDH was used as a loading control. Histograms represent mean ± s.d.; n = 3; *p < 0.05, ***p < 0.001.

characterized as an initial burst release of DOX (Fig. 4A) and 2) the drug was also incorporated inside the OCP's water layer (seen through the shifts of characteristic OCP peaks in XRD, Fig. 1 A,B) that helped with the prolonged drug release as the OCP construct slowly transformed to a more stable phase. As a corroboration that the release was slower if the drug loading was done at the same time as the OCP was forming (*in situ* method), the adsorption experiment was also performed, DOX release was tested for 48 h and obtained results clearly evidenced that the initial burst release in this case is drastically higher (up to 50 % compared to *in situ*) and no changes in the crystal structure of OCP were noticed. Due to the other advantages of this methodology, for instance, low cost, facile preparation method, presence of a single precursor and the environmentally friendly approach, DOX-OCP application in drug delivery has shown high potential.

The *in vitro* cell studies exhibited time and concentration-dependent decrease in the proliferation rate of MG63 and MC3T3 cells, when they were exposed to the DOX-loaded OCP powders. Complex formulation between DOX and CaP in the proposed DDS potentially enhances the cytotoxic properties of the drug, as seen in previous studies. This additional effect of complexation could contribute to increased cytotoxicity against cancer cells. However, the potential of OCP powders to enhance cell proliferation through the presence of elevated Ca^{2+} ions in the surrounding medium has also been recorded throughout different studies. This additional data demonstrated that the interaction between calcium and doxorubicin, instead of a synergistic effect, reduced the efficacy of doxorubicin and led to a recovery in cell viability. Once the pathway of programmed cell death responsible for the aforementioned cytotoxic effect was tested, it showed that apoptosis is the main pathway.

As the DOX-OCP drug delivery system would be administered locally in the cancer site, aside of the therapeutic effect the drug would offer, OCP could have an ameliorating outcome on the bone regeneration process. DOX-OCP application would potentially be interchangeable and could range from the composite scaffolds or protective coatings (e.g., with alginate) to injectable bone cements and even the granular shape of the powders themselves. However, even if the DOX-OCP drug delivery system has already shown a prolonged drug release in PBS (7.4 and 6.0 pH), additional improvements in terms of the *in vitro* drug release and the control of the initial burst release (e.g., addition of the polymer) are still needed. Thus, testing of such advanced constructs, followed by a wider scope of *in vitro* conditions, as well as additional biological tests, will be worth investigating in future studies.

5. Data availability statement

The datasets used and/or analysed during the current study are available from the corresponding author on reasonable request.

CRediT authorship contribution statement

Ilijana Kovrlija: Writing – review & editing, Writing – original draft, Visualization, Investigation, Formal analysis, Conceptualization. **Elżbieta Pańczyszyn:** Writing – original draft, Investigation, Formal analysis. **Oznur Demir:** Writing – review & editing, Writing – original draft, Investigation, Formal analysis. **Marta Laizane:** Formal analysis. **Marco Corazzari:** Supervision. **Janis Locs:** Writing – review & editing, Resources, Funding acquisition, Conceptualization. **Dagnija Loca:** Writing – review & editing, Supervision, Resources, Funding acquisition, Conceptualization.

Declaration of competing interest

The authors declare that they have no known competing financial interests or personal relationships that could have appeared to influence the work reported in this paper.

Data availability

Data will be made available on request.

Acknowledgement

The authors acknowledge the financial support for granting Open Access and access to the infrastructure and expertise from the European Union's Horizon 2020 Research and Innovation programme under grant agreement [No. 857287 (BBCE)], as well as the European Union's Horizon 2020 Research and Innovation programme under the Marie Skłodowska-Curie grant agreement [No. 860462 (PREMUROSA)].

Appendix A. Supplementary data

Supplementary data to this article can be found online at https://doi.org/10.1016/j.ijpharm.2024.123932.

References

Akutsu, M., Kano, Y., Tsunoda, S., Suzuki, K., Yazawa, Y., Miura, Y., 1995. Schedule-dependent interaction between paclitaxel and doxorubicin in human cancer cell lines in vitro. European Journal of Cancer 31 (13–14), 2341–2346. https://doi.org/10.1016/0959-8049(95)00448-3.

Anada, T., Araseki, A., Matsukawa, S., Yamasaki, T., Kamakura, S., & Suzuki, O. (2008). Effect of octacalcium phosphate ionic dissolution products on osteoblastic cell differentiation. *Key Engineering Materials*, *361-363 I*, 31–34. Doi: 10.4028/www.scientific.net/kem.361-363.31.

Banerjee, D., Bose, S., 2019. Comparative effects of controlled release of sodium bicarbonate and doxorubicin on osteoblast and osteosarcoma cell viability. Materials Today Chemistry 12, 200–208. https://doi.org/10.1016/j.mtchem.2018.11.008.

Bordbar-Khiabani, A., Kovrlija, I., Locs, J., Loca, D., Gasik, M., 2023. Octacalcium Phosphate-Laden Hydrogels on 3D-Printed Titanium Biomaterials Improve Corrosion Resistance in Simulated Biological Media. International Journal of Molecular Sciences 24 (17). https://doi.org/10.3390/ijms241713135.

Chaitanya, G.V., Alexander, J.S., Babu, P.P., 2010. PARP-1 cleavage fragments: Signatures of cell-death proteases in neurodegeneration. Cell Communication and Signaling 8, 1–11. https://doi.org/10.1186/1478-811X-8-31.

Chen, X., Comish, P.B., Tang, D., Kang, R., 2021. Characteristics and Biomarkers of Ferroptosis. Frontiers in Cell and Developmental Biology 9 (January), 1–9. https://doi.org/10.3389/fcell.2021.637162.

Chow, L.C., Eanes, E.D., 2001. Octacalcium phosphate. In. Monographs in Oral Science Vol. 18. https://doi.org/10.1007/springerreference_39293.

Cree, I.A., Charlton, P., 2017. Molecular chess ? Hallmarks of anti-cancer drug resistance. BMC Cancer 1–8. https://doi.org/10.1186/s12885-016-2999-1.

Demir, O., Pylostomou, A., Loca, D., 2023. Octacalcium phosphate phase forming cements as an injectable bone substitute materials: Preparation and in vitro structural study. Biomaterials Advances 107386. https://doi.org/10.1016/j.bioadv.2023.213731.

Dorozhkin, S.V., 2016. Multiphasic calcium orthophosphate (CaPO4) bioceramics and their biomedical applications. Ceramics International 42 (6), 6529–6554. https://doi.org/10.1016/j.ceramint.2016.01.062.

Elbayoumi, T.A., Torchilin, V.P., 2009. Tumor-targeted nanomedicines: Enhanced antitumor efficacy in vivo of doxorubicin-loaded, long-circulating liposomes modified with cancer-specific monoclonal antibody. Clinical Cancer Research 15 (6), 1973–1980. https://doi.org/10.1158/1078-0432.CCR-08-2392.

Fu, J., Li, T., Yang, Y., Jiang, L., Wang, W., Fu, L., Zhu, Y., Hao, Y., 2021. Activatable nanomedicine for overcoming hypoxia-induced resistance to chemotherapy and inhibiting tumor growth by inducing collaborative apoptosis and ferroptosis in solid tumors. Biomaterials 268, 120537. https://doi.org/10.1016/j.biomaterials.2020.120537.

Gagliardi, M., Saverio, V., Rossin, F., D'Eletto, M., Corazzari, M., 2023. Transglutaminase 2 and Ferroptosis: a new liaison? Cell Death Discovery 9 (1), 7–9. https://doi.org/10.1038/s41420-023-01394-1.

Gautier, J., Munnier, E., Paillard, A., Hervé, K., Douziech-Eyrolles, L., Soucé, M., Dubois, P., Chourpa, I., 2012. A pharmaceutical study of doxorubicin-loaded PEGylated nanoparticles for magnetic drug targeting. International Journal of Pharmaceutics 423 (1), 16–25. https://doi.org/10.1016/j.ijpharm.2011.06.010.

Génin, F.Y., Luo, P., Dash, K., 2004. Hydroxyapatite based drug delivery implant for cancer treatment. United States Patent 1 (12).

Guise, T.A., 2006. Bone Loss and Fracture Risk Associated with Cancer Therapy. The Oncologist 11 (10), 1121–1131. https://doi.org/10.1634/theoncologist.11-10-1121.

Honda, Y., Kamakura, S., Sasaki, K., Suzuki, O., 2007. Formation of bone-like apatite enhanced by hydrolysis of octacalcium phosphate crystals deposited in collagen matrix. Journal of Biomedical Materials Research - Part B Applied Biomaterials 80 (2), 281–289. https://doi.org/10.1002/jbm.b.30595.

Iafisco, M., Drouet, C., Adamiano, A., Pascaud, P., Montesi, M., Panseri, S., Sarda, S., Tampieri, A., 2016. Superparamagnetic iron-doped nanocrystalline apatite as a delivery system for doxorubicin. J. Mater. Chem. B 4, 57–70. https://doi.org/10.1039/c5tb01524c.

Ito, N., Kamitakahara, M., Ioku, K., 2014. Preparation and evaluation of spherical porous granules of octacalcium phosphate/hydroxyapatite as drug carriers in bone cancer treatment. Materials Letters 120, 94–96. https://doi.org/10.1016/j.matlet.2014.01.040.

Jabłonska-Trypuc, A., Swiderski, G., Kretowski, R., Lewandowski, W., 2017. Newly Synthesized Doxorubicin Complexes with Selected Metals — Synthesis. Structure and Anti-Breast Cancer Activity. *Molecules* 22, 1106. https://doi.org/10.3390/molecules22071106.

Ji, P., Yu, L., Guo, W.C., Mei, H.J., Wang, X.J., Chen, H., Fang, S., Yang, J., 2015. Doxorubicin inhibits proliferation of osteosarcoma cells through upregulation of the Notch signaling pathway. Oncology Research 22 (4), 185–191. https://doi.org/10.3727/096504015X14343704124340.

Jiang, Xiaodan, Zhao, Y., Wang, C., Sun, R., & Tang, Y. (2022). Effects of physico-chemical properties of ions-doped hydroxyapatite on adsorption and release performance of doxorubicin as a model anticancer drug. *Materials Chemistry and Physics*, *276*(August 2021), 125440. Doi: 10.1016/j.matchemphys.2021.125440.

Jiang, X., Stockwell, B.R., Conrad, M., 2021. Ferroptosis: mechanisms, biology and role in disease. Nature Reviews Molecular Cell Biology 22 (4), 266–282. https://doi.org/10.1038/s41580-020-00324-8.

Kovrlija, I., Locs, J., Loca, D., 2021. Octacalcium phosphate: Innovative vehicle for the local biologically active substance delivery in bone regeneration. Acta Biomaterialia 135, 27–47. https://doi.org/10.1016/j.actbio.2021.08.021.

Kovrlija, I., Menshikh, K., Marsan, O., Rey, C., Combes, C., Locs, J., Loca, D., 2023. Exploring the Formation Kinetics of Octacalcium Phosphate from Alpha-Tricalcium Phosphate : Synthesis Scale-Up, Determination of Transient Phases. Their Morphology and Biocompatibility, Biomolecules, p. 13.

Lebugle, A., Rodrigues, A., Bonnevialle, P., Voigt, J.J., Canal, P., Rodriguez, F., 2002. Study of implantable calcium phosphate systems for the slow release of methotrexate. Biomaterials 23, 3517–3522.

LeGeros, R.Z., Daculsi, G., Orly, I., Abergas, T., Torres, W., 1989. Solution-mediated transformation of octacalcium phosphate (OCP) to apatite. Scanning Microscopy 3 (1), 129–138.

Li, J., Yang, Z., Li, Y., Xia, J., Li, D., Li, H., Ren, M., Liao, Y., Yu, S., Chen, Y., Yang, Y., Zhang, Y., 2016. Cell apoptosis, autophagy and necroptosis in osteosarcoma treatment. Oncotarget 7 (28), 44763–44778. https://doi.org/10.18632/oncotarget.8206.

Li, S., Zhang, H., Liu, J., Shang, G., 2023. Targeted therapy for osteosarcoma: a review. Journal of Cancer Research and Clinical Oncology 149 (9), 6785–6797. https://doi.org/10.1007/s00432-023-04614-4.

Lin, R., Shi, L., Wang, C., 2005. In vitro study of anticancer drug doxorubicin in PLGA-based microparticles. Biomaterials 26, 4476–4485. https://doi.org/10.1016/j.biomaterials.2004.11.014.

Liu, X., Du, S., Wang, S., Ye, K., 2022a. Ferroptosis in osteosarcoma: A promising future. Frontiers in Oncology 12 (November), 1–9. https://doi.org/10.3389/fonc.2022.1031779.

Liu, Y., Raina, D.B., Sebastian, S., Nagesh, H., Isaksson, H., Engellau, J., Lidgren, L., Tägil, M., 2021. Sustained and controlled delivery of doxorubicin from an in-situ setting biphasic hydroxyapatite carrier for local treatment of a highly proliferative human osteosarcoma. Acta Biomaterialia 131, 555–571. https://doi.org/10.1016/j.actbio.2021.07.016.

Liu, Y., Nadeem, A., Sebastian, S., Olsson, M.A., Wai, S.N., Lidgren, L., Styring, E., Engellau, J., Isaksson, H., Magnus, T., Raina, D.B., 2022b. Bone mineral: A trojan horse for bone cancers. Efficient mitochondria targeted delivery and tumor eradication with nano hydroxyapatite containing doxorubicin. Materials Today Bio 14 (December 2021). https://doi.org/10.1016/j.mtbio.2022.100227.

Loca, D., Sokolova, M., Locs, J., Smirnova, A., Irbe, Z., 2015. Calcium phosphate bone cements for local vancomycin delivery. Materials Science and Engineering C 49 (1), 106–113. https://doi.org/10.1016/j.msec.2014.12.075.

Martinez, T., Sarda, S., Dupret-Bories, A., Charvillat, C., Projetti, F., Drouet, C., 2021. Toward a doxorubicin-loaded bioinspired bone cement for the localized treatment of osteosarcoma. Future Oncology 17 (26), 3511–3528. https://doi.org/10.2217/fon-2021-0128.

Mathew, M., Brown, W.E., Schroeder, L.W., Dickens, B., 1988. Crystal structure of octacalcium bis(hydrogenphosphate) tetrakis(phosphate)pentahydrate, Ca8(HP04)2(PO4)4·5H2O. Journal of Crystallographic and Spectroscopic Research 18 (3), 235–250. https://doi.org/10.1007/BF01194315.

Miotto, G., Rossetto, M., Di Paolo, M.L., Orian, L., Venerando, R., Roveri, A., Vučković, A. M., Bosello Travain, V., Zaccarin, M., Zennaro, L., Maiorino, M., Toppo, S., Ursini, F., Cozza, G., 2020. Insight into the mechanism of ferroptosis inhibition by ferrostatin-1. Redox Biology 28 (September 2019), 101328. https://doi.org/10.1016/j.redox.2019.101328.

Modh, H., Fang, D.J., Ou, Y.H., Yau, J.N.N., Kovshova, T., Nagpal, S., Knoll, J., Wallenwein, C.M., Maiti, K., Bhowmick, S., Gelperina, S., Pastorin, G., Wacker, M.G., 2021. Injectable drug delivery systems of doxorubicin revisited: In vitro-in vivo relationships using human clinical data. International Journal of Pharmaceutics 608 (April), 121073. https://doi.org/10.1016/j.ijpharm.2021.121073.

Mosina, M., Kovrlija, I., Stipniece, L., Locs, J., 2022. Gallium containing calcium phosphates: Potential antibacterial agents or fictitious truth. Acta Biomaterialia 150, 48–57. https://doi.org/10.1016/j.actbio.2022.07.063.

Nussinov, R., Tsai, C., Jang, H., 2021. Anticancer drug resistance : An update and perspective. Drug Resistance Updates 59, 100796. https://doi.org/10.1016/j.drup.2021.100796.

Olson, R.D., Mushlin, P.S., 1990. Doxorubicin cardiotoxicity: analysis of prevailing hypotheses. The FASEB Journal 4.

Parent, M., Baradari, H., Champion, E., Damia, C., Viana-trecant, M., 2017. Design of calcium phosphate ceramics for drug delivery applications in bone diseases : A review of the parameters affecting the loading and release of the therapeutic substance. Journal of Controlled Release 252, 1–17. https://doi.org/10.1016/j.jconrel.2017.02.012.

Pelss, J., Loca, D., Berzina-Cimdina, L., Locs, J., Lakevics, V., 2011. Release of anticancer drug doxorubicin from biodegradable polymer coated porous hydroxyapatite scaffolds. Advanced Materials Research 284–286, 1770–1773. https://doi.org/10.4028/www.scientific.net/AMR.284-286.1770.

Pfeffer, C.M., Singh, A.T.K., 2018. Apoptosis: A target for anticancer therapy. International Journal of Molecular Sciences 19 (2). https://doi.org/10.3390/ijms19020448.

Pinski, J., Parikh, A., Bova, G.S., Isaacs, J.T., 2001. Therapeutic Implications of Enhanced G0/G1 Checkpoint Control Induced by Coculture of Prostate Cancer Cells with Osteoblasts. Cancer Research 61 (9), 6372–6376.

Pisa, R., Kapoor, T.M., 2020. Chemical strategies to overcome resistance against targeted anticancer therapeutics. Nature Chemical Biology 16 (August), 817–825. https://doi.org/10.1038/s41589-020-0596-8.

Pylostomou, A., Oznur, D., Loca, D., 2023. Calcium phosphate bone cements as local drug delivery systems for bone cancer treatment. *Biomaterials*. Advances 148 (February). https://doi.org/10.1016/j.bioadv.2023.213367.

Qi, C., Zhu, Y.J., Sun, T.W., Wu, J., Chen, F., 2015. Microwave-Assisted Hydrothermal Rapid Synthesis of Amorphous Calcium Phosphate Mesoporous Microspheres Using Adenosine 5′-Diphosphate and Application in pH-Responsive Drug Delivery. Chemistry - an Asian Journal 10 (11), 2503–2511. https://doi.org/10.1002/asia.201500667.

Qiu, C., Liu, T., Luo, D., Luan, D., Cheng, L., Wang, S., 2022. Novel Therapeutic Savior for Osteosarcoma: The Endorsement of Ferroptosis. Frontiers in Oncology 12 (March), 1–7. https://doi.org/10.3389/fonc.2022.746030.

Roncuzzi, L., Pancotti, F., Baldini, N., 2014. Involvement of HIF-1α activation in the doxorubicin resistance of human osteosarcoma cells. Oncology Reports 32 (1), 389–394. https://doi.org/10.3892/or.2014.3181.

Saito, S., Hamai, R., Shiwaku, Y., Hasegawa, T., Sakai, S., Tsuchiya, K., Sai, Y., Iwama, R., Amizuka, N., Takahashi, T., Suzuki, O., 2021. Involvement of distant octacalcium phosphate scaffolds in enhancing early differentiation of osteocytes during bone regeneration. Acta Biomaterialia 129, 309–322. https://doi.org/10.1016/j.actbio.2021.05.017.

Shi, H., Yang, S., Zeng, S., Liu, X., Zhang, J., Zhang, J., Wu, T., Ye, X., Yu, T., Zhou, C., Ye, J., 2019. Enhanced angiogenesis of biodegradable iron-doped octacalcium phosphate/poly (lactic-co-glycolic acid) scaffold for potential cancerous bone regeneration. Applied Materials Today 15, 100–114. https://doi.org/10.1016/j.apmt.2019.01.002.

Siebler, T., Shalet, S.M., Robson, H., 2002. Effects of chemotherapy on bone metabolism and skeletal growth. Hormone Research 58 (SUPPL. 1), 80–85. https://doi.org/10.1159/000064769.

Singh, V., Khurana, A., Navik, U., Allawadhi, P., Bharani, K.K., Weiskirchen, R., 2022. Apoptosis and Pharmacological Therapies for Targeting Thereof for Cancer Therapeutics. Sci 4 (2). https://doi.org/10.3390/sci4020015.

Sritharan, S., Sivalingam, N., 2021. A comprehensive review on time-tested anticancer drug doxorubicin. Life Sciences 278, 119527. https://doi.org/10.1016/j.lfs.2021.119527.

Suzuki, O., Insley, G., 2020. Octacalcium Phosphate Biomaterials. Woodhead Publishing Series in. Biomaterials.

Tacar, O., Sriamornsak, P., Dass, C.R., 2012. Doxorubicin: an update on anticancer molecular action, toxicity and novel drug delivery systems. Journal of Pharmacy and Pharmacology 65, 157–170. https://doi.org/10.1111/j.2042-7158.2012.01567.x.

Tang, Q., Zhu, Y., Wu, J., Chen, F., Cao, S.-W., 2011. Calcium phosphate drug nanocarriers with ultrahigh and adjustable drug-loading capacity: One-step synthesis, in situ drug loading and prolonged drug release. Nanomedicine: Nanotechnology, Biology, and Medicine 7 (4), 428–434. https://doi.org/10.1016/j.nano.2010.12.005.

Tani, T., Okada, K., Takahashi, S., Suzuki, N., Shimada, Y., Itoi, E., 2006. Doxorubicin-loaded Calcium Phosphate Cement in the Management of Bone and Soft Tissue Tumors. In Vivo 60, 55–60.

Thorn, C.F., Oshiro, C., Marsh, S., Hernandez-Boussard, T., McLeod, H., Klein, T.E., Altman, R.B., 2011. Doxorubicin pathways: Pharmacodynamics and adverse effects. Pharmacogenetics and Genomics 21 (7), 440–446. https://doi.org/10.1097/FPC.0b013e32833ffb56.

Thuy, T., Nguyen, T., Lim, Y.J., Hui, M., Fan, M., Jackson, R.A., Lim, K.K., Ang, W.H., Hon, K., Ban, K., Chen, E.S., 2016. Calcium modulation of doxorubicin cytotoxicity in yeast and human cells. Genes to Cells 226–240. https://doi.org/10.1111/gtc.12346.

van der Zanden, S.Y., Qiao, X., Neefjes, J., 2021. New insights into the activities and toxicities of the old anticancer drug doxorubicin. The FEBS Journal 288, 6095–6111. https://doi.org/10.1111/febs.15583.

Wang, J., de Boer, J., de Groot, K., 2009. Proliferation and differentiation of osteoblast-like MC3T3-E1 cells on biomimetically and electrolytically deposited calcium phosphate coatings. Journal of Biomedical Materials Research. Part A 90 (3), 664–670. https://doi.org/10.1002/jbm.a.32128.

Wang, X., Hua, P., He, C., Chen, M., 2022. Non-apoptotic cell death-based cancer therapy: Molecular mechanism, pharmacological modulators, and nanomedicine. Acta Pharmaceutica Sinica B 12 (9), 3567–3593. https://doi.org/10.1016/j.apsb.2022.03.020.

Wang, S., Konorev, E.A., Kotamraju, S., Joseph, J., Kalivendi, S., Kalyanaraman, B., 2004. Doxorubicin induces apoptosis in normal and tumor cells via distinctly different mechanisms: Intermediacy of H2O2- and p53-dependent pathways. Journal of Biological Chemistry 279 (24), 25535–25543. https://doi.org/10.1074/jbc.M400944200.

Wang, A.Z., Langer, R., Farokhzad, O.C., 2012. Nanoparticle delivery of cancer drugs. Annual Review of Medicine 63, 185–198. https://doi.org/10.1146/annurev-med-040210-162544.

Wen, S.h., Su, S.C., Liou, B.H., Lin, C.H., Lee, K.R., 2018. Sulbactam-enhanced cytotoxicity of doxorubicin in breast cancer cells. Cancer Cell International 18 (1), 1–18. https://doi.org/10.1186/s12935-018-0625-9.

Wilson, B.E., Jacob, S., Yap, M.L., Ferlay, J., Bray, F., Barton, M.B., 2019. Estimates of global chemotherapy demands and corresponding physician workforce requirements for 2018 and 2040: a population-based study. Lancet Oncology 20 (6), 769–780. https://doi.org/10.1016/S1470-2045(19)30163-9.

Yang, X., Gao, X., Gan, Y., Gao, C., Zhang, X., Ting, K., Wu, B.M., Gou, Z., 2010. Facile synthesis of octacalcium phosphate nanobelts: Growth mechanism and surface adsorption properties. Journal of Physical Chemistry C 114 (14), 6265–6271. https://doi.org/10.1021/jp911576f.

Yao, Z., Murali, B., Ren, Q., Luo, X., Faget, D.V., Cole, T., Ricci, B., Thotala, D., Monahan, J., Van Deursen, J.M., Baker, D., Faccio, R., Schwarz, J.K., Stewart, S.A., 2020. Therapy-induced senescence drives bone loss. Cancer Research 80 (5), 1171–1182. https://doi.org/10.1158/0008-5472.CAN-19-2348.

Yin, J., Guo, J., Zhang, Q., Cui, L., Zhang, L., Zhang, T., Zhao, J., Li, J., Middleton, A., Carmichael, P.L., Peng, S., 2018. Toxicology in Vitro Doxorubicin-induced mitophagy and mitochondrial damage is associated with dysregulation of the PINK1 / parkin pathway. Toxicology in Vitro 51 (April), 1–10. https://doi.org/10.1016/j.tiv.2018.05.001.

Appendix 5
5. pielikums

Octacalcium Phosphate-Laden Hydrogels on 3D-Printed Titanium Biomaterials Improve Corrosion Resistance in Simulated Biological Media

Aydin Bordbar-Khiabani, Ilijana Kovrlija, Janis Locs, Dagnija Loca, Michael Gasik

International Journal of Molecular Sciences, 24 (2023), 13135, DOI: 10.3390/ijms241713135.

I.K. input: writing – original draft preparation, visualization, formal analysis, and investigation.

International Journal of
Molecular Sciences

MDPI

Article

Octacalcium Phosphate-Laden Hydrogels on 3D-Printed Titanium Biomaterials Improve Corrosion Resistance in Simulated Biological Media

Aydin Bordbar-Khiabani [1,*], Ilijana Kovrlija [2,3], Janis Locs [2,3], Dagnija Loca [2,3] and Michael Gasik [1]

[1] Department of Chemical and Metallurgical Engineering, School of Chemical Engineering, Aalto University Foundation, 02150 Espoo, Finland
[2] Rudolfs Cimdins Riga Biomaterials Innovation and Development Centre, Faculty of Materials Science and Applied Chemistry, Institute of General Chemical Engineering, Riga Technical University, Pulka 3, LV-1007 Riga, Latvia
[3] Baltic Biomaterials Centre of Excellence, Headquarters at Riga Technical University, LV-1007 Riga, Latvia
* Correspondence: aydin.bordbarkhiabani@aalto.fi; Tel.: +358-505677245

Abstract: The inflammatory-associated corrosion of metallic dental and orthopedic implants causes significant complications, which may result in the implant's failure. The corrosion resistance can be improved with coatings and surface treatments, but at the same time, it might affect the ability of metallic implants to undergo proper osteointegration. In this work, alginate hydrogels with and without octacalcium phosphate (OCP) were made on 3D-printed (patterned) titanium alloys (Ti Group 2 and Ti-Al-V Group 23) to enhance their anticorrosion properties in simulated normal, inflammatory, and severe inflammatory conditions in vitro. Alginate (Alg) and OCP-laden alginate (Alg/OCP) hydrogels were manufactured on the surface of 3D-printed Ti substrates and were characterized with wettability analysis, XRD, and FTIR. The electrochemical characterization of the samples was carried out with open circuit potential, potentiodynamic polarization, and electrochemical impedance spectroscopy (EIS). It was observed that the hydrophilicity of Alg/OCP coatings was higher than that of pure Alg and that OCP phase crystallinity was increased when samples were subjected to simulated biological media. The corrosion resistance of uncoated and coated samples was lower in inflammatory and severe inflammatory environments vs. normal media, but the hydrogel coatings on 3D-printed Ti layers moved the corrosion potential towards more nobler values, reducing the corrosion current density in all simulated solutions. These measurements revealed that OCP particles in the Alg hydrogel matrix noticeably increased the electrical charge transfer resistance at the substrate and coating interface more than with Alg hydrogel alone.

Keywords: titanium; implants; octacalcium phosphate; alginate; hydrogel; electrochemical behavior; simulated inflammatory conditions

Citation: Bordbar-Khiabani, A.; Kovrlija, I.; Locs, J.; Loca, D.; Gasik, M. Octacalcium Phosphate-Laden Hydrogels on 3D-Printed Titanium Biomaterials Improve Corrosion Resistance in Simulated Biological Media. *Int. J. Mol. Sci.* **2023**, *24*, 13135. https://doi.org/10.3390/ijms241713135

Academic Editor: Axel T. Neffe

Received: 21 July 2023
Revised: 17 August 2023
Accepted: 18 August 2023
Published: 24 August 2023

1. Introduction

Titanium alloys are the most widely used biomaterials for the manufacturing of dental and orthopedic implants mostly due to their outstanding mechanical properties and desired biocompatibility in the human body environment [1–3]. They have reasonable corrosion resistance under normal physiological conditions (pH ≈ 7) as their surfaces are intrinsically covered with dense protective oxide layers [4,5]. However, at inflammatory conditions, reactive oxygen species (ROS), lactic acid, hydroperoxyl radicals (HO_2), and hypochlorous acid (HOCl, expressed by leukocytes to the extracellular environment) interact with metal surfaces affecting corrosion resistance [6–8]. The extracellular medium becomes more acidic (pH ≈ 4–5) when osteoclasts release hydrochloric acid [6], and, subsequently, due to the reactions of neutrophils, microorganisms, and macrophages around an implant affected

by the severe inflammation, the environment may become even more oxidative and acidic (pH ≈ 2–3) [9,10].

One approach to address the aforementioned issue is the surface modification of the implants, which is a reasonably powerful strategy to enhance corrosion resistance [11,12]. For example, hydrogels have been extensively proven as excellent surface coatings for Ti implants due to their chemical stability, viscoelasticity, hydrophilicity, and biocompatibility [13,14]. Among them, sodium alginate (Alg) biopolymer coatings with high bioactivity, good biocompatibility, and cost-effectiveness has been broadly studied [15,16]. However, pure alginate exhibited poor mechanical properties and low activity towards the cells [17,18], and in addition, the adhesion of hydrogel and biopolymer coatings on flat metallic implants is reported to be weak [19]. Therefore, an intermediate surface modification using 3D techniques is usually needed for the better adhesion of these layers to metallic implants [20,21]. Additive manufacturing techniques can be an effective method to 3D print specific patterns on the implant surface [22]. In recent years, 3D-printed Ti biomaterials also showed great potential in promoting bioactivity and osseointegration on their surface, and such techniques have been employed to boost the corrosion resistance of Ti biomaterials in biological media [23]. Implants with rough or patterned surfaces may enhance the interlock between the hydrogel and the substrate [13,19], and as known, the implant surface roughness plays a crucial role in cellular and simultaneous bacterial colonization [24,25].

In general, there is a need for a suitable surface modification and/or a coating that will provide enhanced biocompatibility and osteointegration, being well adhered, and might offer potential for the ameliorated antibacterial properties or delivery of drugs or ions [26,27]. For this reason, titanium implants covered with a polymer can also be modified with bioactive inorganic materials such as calcium phosphates (CaPs) to improve the implant's biological function [28–30], while the environmental conditions on the implant surface with the presence of PO_4^{3-}, Ca^{2+} ions, and biomolecules in a wet environment are similar to those that are physiologically required for osteogenesis and osteoblast activities [31,32].

Octacalcium phosphate (OCP) has consistently ranked as one of the most promising calcium phosphates for the regeneration of bone tissue [26,33]. In vitro and in vivo studies demonstrated that OCP could be used as a material that improves the osteogenic condition of non-cell-interactive polymeric scaffolds, such as Alg [34–36]. However, synthesizing OCP depends on several factors (e.g., pH, temperature, precursors, duration, etc.), which can be the cause of phase impurities such as a mix of two or more CaPs or can lead to a premature transition into non-active apatite [37,38]. Due to its unique structure that has high similarities to hydroxyapatite (HAp) and the presence of a water layer, OCP has great potential for incorporating different drugs or ions, ensuring local drug release, and providing the antibacterial effect. On the other hand, its sensitive structure and readiness to convert to a more stable hydroxyapatite, when in contact with biological fluids, is what limits the use of OCP [39].

A titanium surface with hydrogels becomes hydrophilic and, hence, more capable of accumulating corrosive ions at the gel and substrate interface, changing the electrochemical corrosion behavior. Recent studies have shown that the presence of a layer of hydrogel on magnesium and nitinol implants significantly increases their corrosion resistance [40,41]. When a mixture of ACP and chitosan hydrogels has been used on the Ti, it exhibited a high corrosion resistance [42], but when porous calcium carbonate ($CaCO_3$) was mixed with alginate, the corrosion resistance was decreased [43]. Authors are not aware of systematic quantitative studies on the corrosion resistance of OCP-laden Alg hydrogels, especially when they are used as coatings on 3D-patterned titanium alloys. Therefore, the aim of this work is to study and compare the corrosion behavior of 3D-patterned Ti surfaces coated with Alg and a 3 wt% Alg:crystalline OCP phase (70:30 wt% inorganic:organic ratio) upon immersion in the media for simulated normal, inflammatory, and severe inflammatory conditions.

2. Results and Discussion

2.1. Coating Morphology and Wettability

The morphology of the Alg and Alg/OCP coatings on the 3D-printed Ti Gr2 and Gr23 substrates are shown in Figure 1, in two different magnifications. It was found that different 3D-printed Ti substrates had no noticeable effect on the morphologies of the hydrogel coatings, which were qualitatively quite similar. Low-magnification images also demonstrated uniform distribution and the complete covering of the square patterns by both hydrogels.

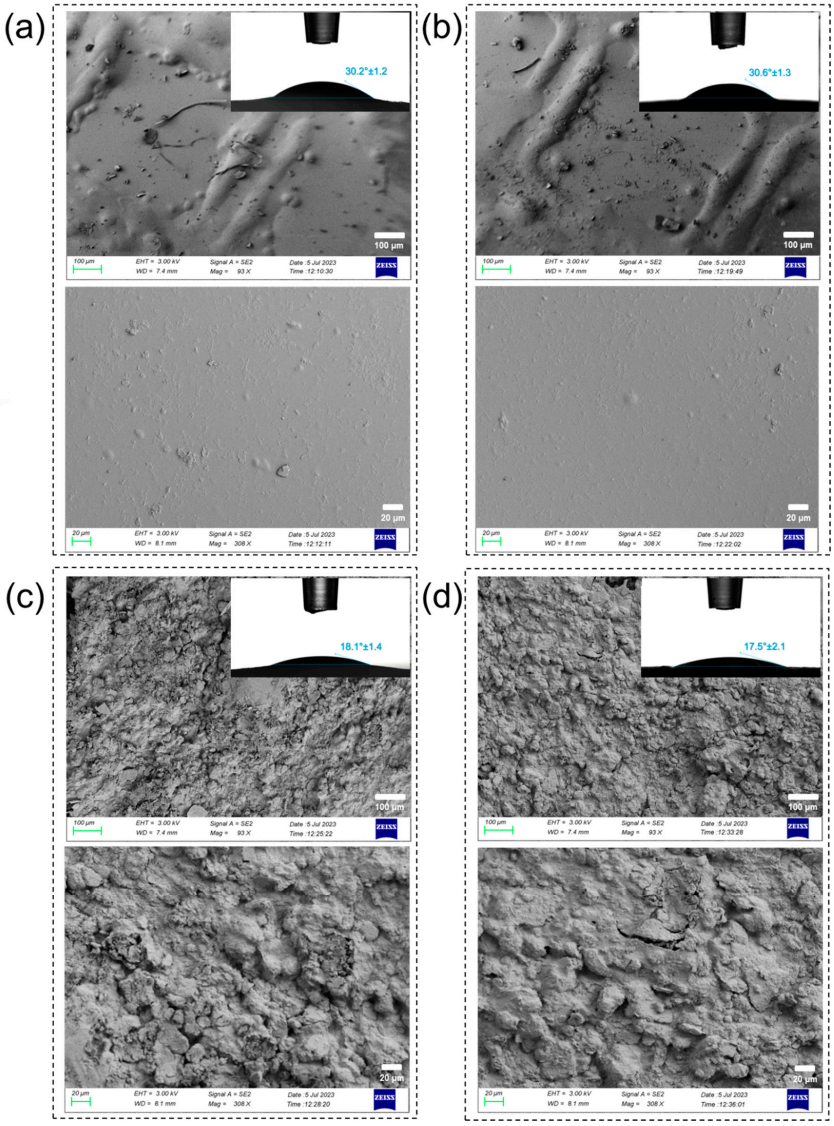

Figure 1. FESEM micrographs of Alg coating on 3D-printed (**a**) Ti Gr2 and (**b**) Ti Gr23 and Alg/OCP coatings on (**c**) Ti Gr2 and (**d**) Ti Gr23. The PBS solution droplet contact angle for hydrogel coatings on 3D-printed substrates are shown in insert images.

The inserted images in Figure 1 show the effect of hydrogel coatings on the surface wettability of patterned Ti groups. It can be seen that the contact angles on the hydrogel-coated samples were lower than those on the patterned Ti group [23], which indicates that these hydrogel coatings improved the wettability. The main reason for this might be the presence of hydrophilic functional groups such as carboxyl and hydroxyl in Alg [44]. It was also found that the introduction of OCP into Alg coatings reduced the contact angles. This might be mainly attributed to the increase in surface free energy due to the presence of OCP. Moreover, the presence of OCP particles in the form of agglomerates further increases the wettability of composite coatings. The space between the agglomerated OCP particles is larger than that of the smaller particles in the accumulation process because they cause a larger equivalent capillary radius, thus increasing the wetting rate [45].

2.2. Physicochemical Characterization of Alg/OCP Coatings

The OCP powder, synthesized from low-temperature α-TCP, used in the present study was physicochemically well characterized in our previous report [37]. A low-angle (100) maximum at 2θ = 4.7 degrees and a doublet at 9.4 and 9.7 (200 and 010) 2θ degrees, which are the characteristic X-ray diffraction fingerprints of OCP, were observed (Figure 2a). The FTIR spectrum showed the vibrations of HPO_4^{2-} at 917, 875, 1007, and 1295 cm^{-1}, which differentiate the OCP from stoichiometric hydroxyapatite (Figure 2b) [46,47]. The specific amorphous broad halo that was seen in the XRD pattern was specific to sodium-alginate biopolymer, and it aligned with the results from the FTIR spectra that showed a broad band centered at approximately 3500 cm^{-1} from the stretching of hydroxyl groups. The crystalline peaks correspond to calcium chloride, which was present in the crosslinking process (Figure 2a—star symbol). Once the composite was analyzed by FTIR, a set of several vibrations in the range of 1100–1000 cm^{-1}, connected to the glycoside bonds in the polysaccharide (C-O-C stretching), was seen [48].

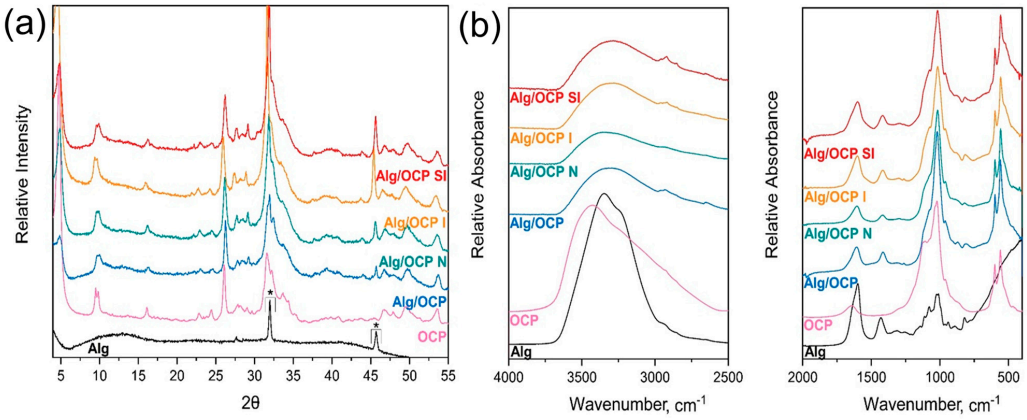

Figure 2. Physicochemical characterization of alginate, OCP, and the coating prior to the immersion (Alg/OCP) and after 1 h immersion in simulated normal (Alg/OCP N), inflammatory (Alg/OCP I), and severe inflammatory (Alg/OCP SI) conditions. (**a**) X-ray diffractograms; (**b**) FTIR spectra.

Due to its specific structure that comprises a water channel in between apatite layers, OCP is unable to be sintered or morphed in any way with the help of high temperatures [39]. On the other hand, combining it with polymers that require a more complex crosslinking process (e.g., a pH change or the addition of more components) could potentially cause the OCP phase to transform to hydroxyapatite. A combination of 3 wt% Alg solution and OCP, in the used ratio, was intended to preserve the crystalline form of OCP and provide a strong protective coating on the titanium alloys. In both XRD and FTIR data, the characteristic maxima of OCP were maintained after the Alg/OCPcoating preparation,

confirming that the Alg did not cause subsequent modifications in the crystal structure of OCP. The decrease in intensity and the broadening of the 25–35° 2θ area indicate the decrease in the crystallinity in Alg/OCP. However, once the coatings have been immersed into the respective solutions, CaP crystallinity intensifies again, and the OCP phase remains stable. This could potentially be because of the presence of different salts and ions in the media (i.e., BSA) that are beneficial towards the OCP as they slow down the hydrolysis via the absorption onto the OCP surface [49]. In FTIR spectra, the absorbance bands at 1620 and 1416 cm^{-1}, which were seen in pure Alg and in all tested coatings, corresponded to the antisymmetric and symmetric COO stretching vibration of the salified carboxyl group of alginic acid [50–52]. As it was seen also in the XRD patterns, the broadening of the ν_3PO_4 region (900–1200 cm^{-1}) is consistent with the reduction in OCP crystallinity when combined with Alg.

2.3. Electrochemical Studies

2.3.1. Open Circuit Potential

The changes in open circuit potential values as a function of time for the bare 3D-printed Ti groups and those coated with Alg and Alg/OCP hydrogels coatings in simulated media at 37 °C are shown in Figure 3. During electrochemical oxidation, the open circuit potential represents the thermodynamic tendency of the material. Both the Alg and Alg/OCP coatings on the Ti Gr2 and Ti Gr23 substrates showed higher values of potential at the end of 600 s in all simulated media than the bare samples, confirming the favorable effect of the coatings [53]. However, a small difference in the final recorded potential in the Alg-coated Ti Gr2 and Ti Gr23 samples in the severe inflammatory solution can be seen, which could be related to its low stability in low pH solutions. The obtained results revealed that the Alg/OCP coatings exhibited a higher potential than Alg on both substrates, indicating the positive role of OCP particles in the electrochemical performance of Alg.

By comparing Alg- and Alg/OCP-coated samples, it has been determined that the distribution of OCP particles in the Alg matrix creates a greater open circuit potential difference in the inflammatory medium than in the severe inflammatory medium, suggesting that these particles are capable of effective action in pH 5 and in the absence of BSA and lactate. Another noticeable variation is about the open circuit potential of hydrogel-coated Ti Gr2 in a normal medium. The potential of Alg-coated Ti Gr2 (red line) initially decreased over time during the 300 s, then increased slightly, and stabilized at −330 $mV_{Ag/AgCl}$. This indicates the dissolution of the developed oxide film during the 300 s and its subsequent growth at 600 s [54]. The Alg/OCP-coated Ti Gr2 (purple line) showed different behavior. The open circuit potential fluctuated during the first 50 s and then increased to positive values continuously. It shows the dissolution and growth of oxide film simultaneously in the first 50 s of immersion and then the subsequent growth by the end of the test. The results also showed that regardless of the type of hydrogel on the 3D-printed Ti substrates, Ti Gr23 has a more electropositive potential than Ti Gr2, which is likely to be due to the formation of dense composite oxide layers on Ti Gr23 [55]. During simulated inflammatory and severe inflammatory conditions, open circuit potential values moved toward electropositive potentials. The decomposition of H_2O_2 into H_2 and O_2 may explain this phenomenon, adding to the sluggish oxygen reduction reaction by acting as an additional cathodic reaction [56]. The presence of BSA and CLH in the inflammatory solution resulted in a decrease in open circuit potential values in severe inflammatory conditions. Still, potential values remained high and more positive than those of normal conditions.

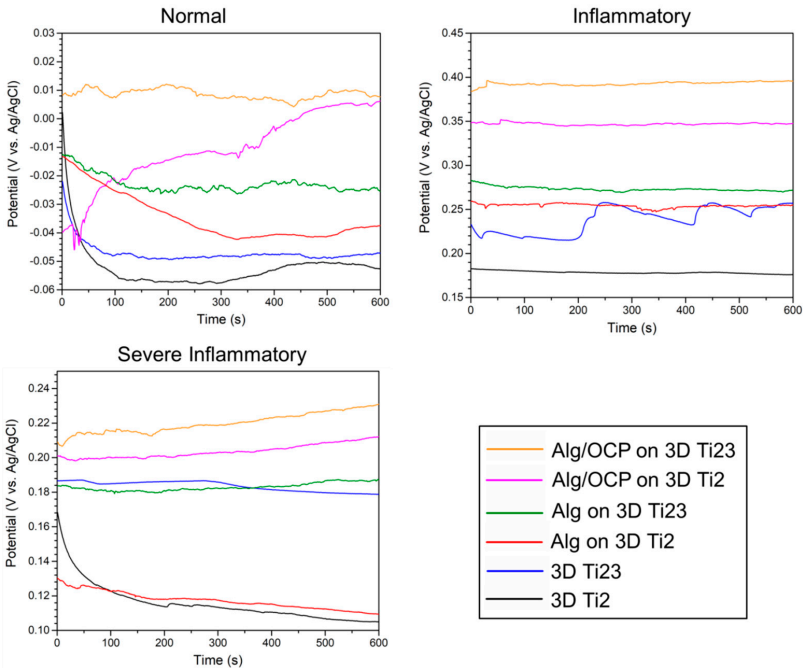

Figure 3. Open circuit potential monitoring of the prepared Alg and Alg/OCP coatings on 3D-printed Ti Gr2 and Ti Gr23 layers exposed in simulatednormal, inflammatory, and severe inflammatory conditions for 1 h.

2.3.2. Potentiodynamic Polarization

The potentiodynamic polarization curves of hydrogel coatings on 3D-printed Ti samples are presented in Figure 4. The obtained parameters from the Tafel extrapolation method, including corrosion potentials (E_{corr}), corrosion current densities (I_{corr}), and Tafel slopes of anodic (β_a) and cathodic (β_c) branches, as well as calculated polarization resistance using the Stern–Geary equation [57], are listed in Supplementary Table S1. The obtained results indicated that under inflammatory and severe inflammatory conditions, samples are incapable of exhibiting passive behavior due to the presence of H_2O_2 in their media [58]. It is noteworthy that anodic branches do not exhibit Tafel behavior under normal conditions, thus rendering the Stern–Geary analysis invalid [59]. Generally, excellent anticorrosion properties are largely dependent on an electropositive E_{corr}, low I_{corr}, and high R_p. It can be seen from Table S1 that the i_{corr} of the hydrogel-coated Ti Gr23 is lower than that of the coated Gr2 in all conditions, which confirms the fact that the corrosion resistance of the substrate affects the electrochemical performance of the coatings. By comparing the obtained parameters for uncoated and coated samples, it was found that a layer of hydrogel improves the corrosion resistance of 3D-printed Ti Gr2 and Gr23 in all media.

Enhanced corrosion resistance for coated surfaces may be related to the hydrogel layers' ability to protect the substrate both physically and chemically [60,61]. As seen in Table S1, Alg/OCP-coated Ti groups have nobler E_{corr}, lower I_{corr}, and higher R_p than Alg-coated samples in all simulated biological media. This is attributed to the fact that OCP inorganic particles with a low tendency for electrochemical reactions functioned as corrosion-inhibiting barriers and provided effective physical separation between the substrate and corrosive medium. The drastic decrease in the i_{corr} of hydrogel-coated samples immersed in the presence of the H_2O_2, BSA, and CLH compounds confirms, once

again, the increase in the reactivity of 3D-printed Ti substrates under these conditions [7,23]. Furthermore, it also confirms the decrease in corrosion resistance via the penetration of corrosive ions through hydrogel to the substrate.

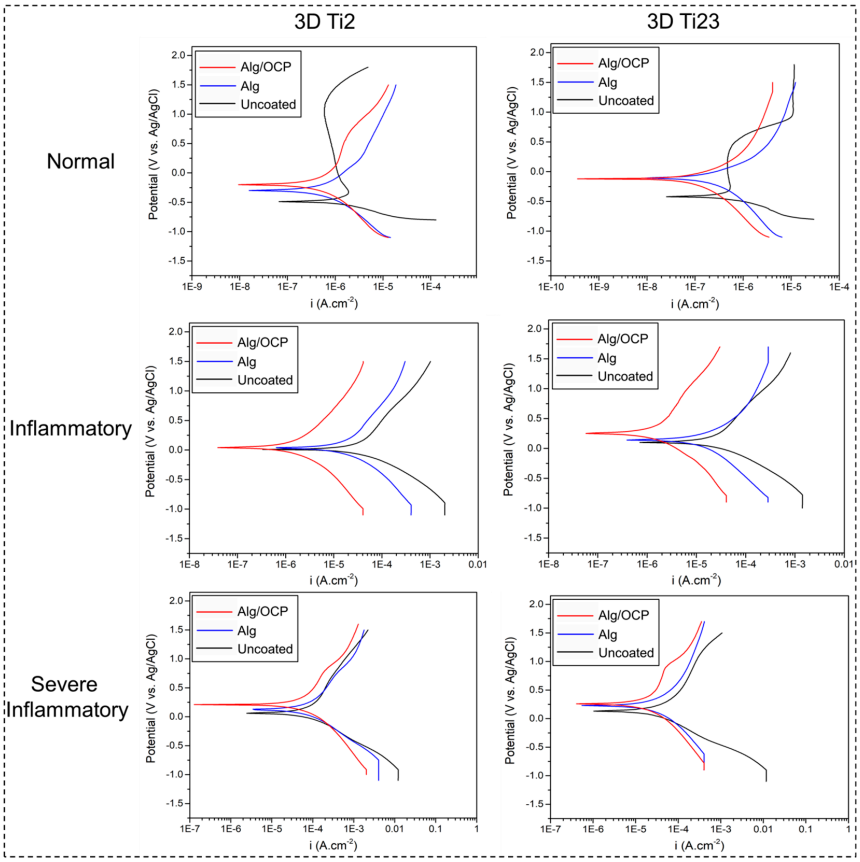

Figure 4. Potentiodynamic polarization curves of the prepared Alg and Alg/OCP coatings on 3D-printed Ti Gr2 and Ti Gr23 layers exposed in simulated normal, inflammatory, and severe inflammatory conditions for 1 h.

2.3.3. Electrochemical Impedance Spectroscopy

The Nyquist and the Bode amplitude/phase plots of the impedance data for bare and hydrogel-coated 3D-printed Ti groups in simulated media are presented in Figures 5 and 6, respectively. Figure 5 shows a decreasing trend in capacitive loop diameters of Nyquist plots for inflammatory and severe inflammatory conditions, suggesting a subsequent decrease in corrosion resistance with H_2O_2, BSA, and LCH added to PBS. The Bode amplitude plot also confirmed the same trend in the low-frequency range of the impedance modulus (Figure 6a–e). Under severe inflammatory conditions, phase angles of about 40° and 50° in Figure 6f suggest that there is a high corrosion rate for all samples. The equivalent circuit according to the fitted results of the plots is shown in Supplementary Figure S1 to quantitatively investigate the impedance values of the coated samples. Equivalent circuits for uncoated 3D-printed Ti groups have been shown in previous work [23]. In the proposed circuit in this study, R_s represents the solution's resistance between the R.E. and W.E. In

order to express the capacitive properties of coating surfaces due to the nonhomogeneous nature of the coatings, the constant phase element (CPE) is applied [62]:

$$Z_{CPE} = \frac{1}{Q(j\omega)^n} \quad (1)$$

where $j^2 = -1$, ω is an angular frequency (rad.s^{-1}), and n = 0. . .1 is the power coefficient (with n = 1, CPE behaves as a pure capacitance, and for n = 0, it behaves as a pure resistance). In the circuit, an electrical double layer's capacitance at the interface between a substrate and a solution is represented by CPE_{dl}, and its resistance to charge transfer is represented by R_{ct}. The R_c and CPE_c describe the resistance and capacitance of hydrogel coatings. Supplementary Table S2 summarizes the parameters that correspond to the fitted results. A hydrogel coatings' barrier property is evaluated by R_{ct} and R_c values. Greater R_{ct} implies a more difficult charge transfer and less dissolution of a substrate.

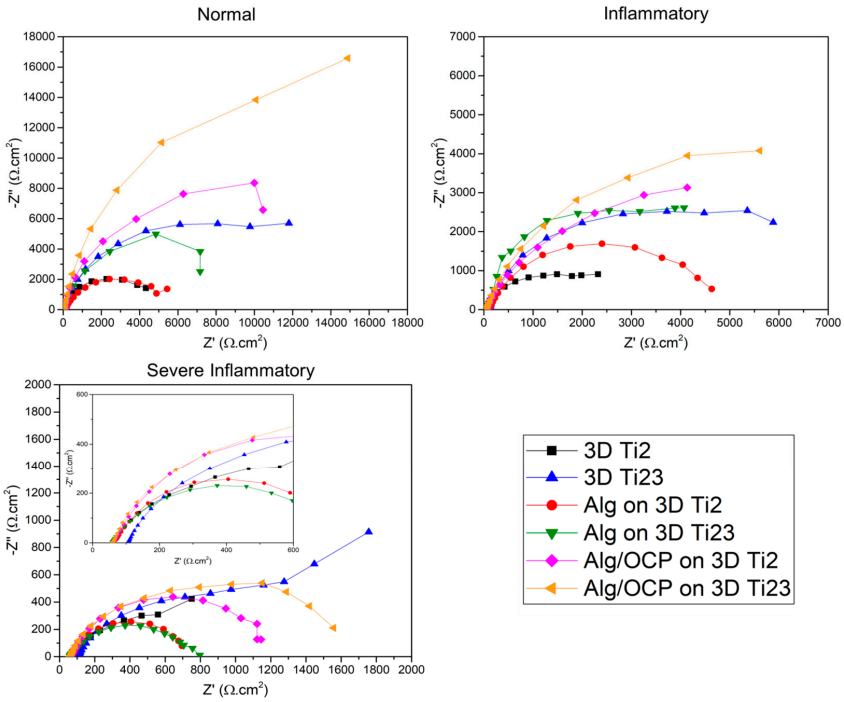

Figure 5. EIS plots of the prepared Alg and Alg/OCP coatings on 3D-printed Ti Gr2 and Ti Gr23 layers exposed in simulated normal, inflammatory, and severe inflammatory conditions for 1 h: Nyquist plots. Nyquist plots for the severe inflammatory condition have been enlarged for better display.

The obtained results showed that the R_{ct} values of hydrogel-coated samples were significantly higher than those of the 3D-printed Ti groups, indicating that the hydrogel coating creates a strong barrier that prevents corrosive ions' penetration to the substrate [63]. The hydrogel coatings had proper adhesion to substrates before and after electrochemical studies. For example, they were strong enough to withstand handling under flowing water jets. The R_{ct} of Alg/OCP-coated samples also increased as OCP particles were incorporated into Alg, suggesting that the OCP particles improved the barrier effect of coatings against electron transfer on the 3D-printed Ti surface. Furthermore, it was found that Alg hydrogel's R_c was further enhanced by the addition of OCP, suggesting that the OCP particles might strengthen the crosslinking degree of the Alg hydrogel coating and the

interfacial bonding force between the coating and the substrate, resulting in the increase in density of hydrogel coatings, and thus, the Alg/OCP-coated samples exhibited higher R_c than samples coated with pure Alg.

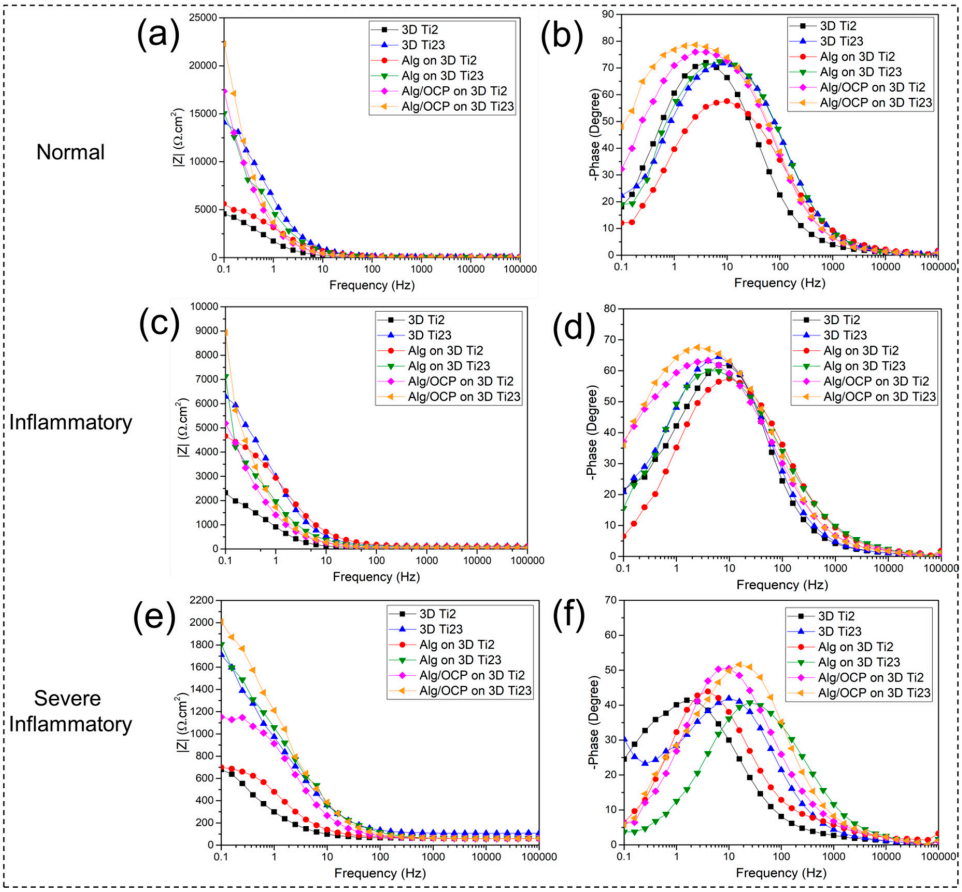

Figure 6. EIS plots of the prepared Alg and Alg/OCP coatings on 3D-printed Ti Gr2 and Ti Gr23 layers exposed in simulated (**a**) normal, (**b**) inflammatory, and (**c**) severe inflammatory conditions for 1 h: (**a**–**c**) Bode modulus and (**d**–**f**) Bode phase plots.

The decrease in the R_c values of coated samples in inflammatory and severe inflammatory conditions compared with normal conditions can be explained by the hydrogels becoming unstable following their dissolution by HCl and H_2O_2, which leads to a decrease in R_{ct} or an increase in substrate reactivity in these media. Usually, reduction and oxidation can cause the decomposition of disulfide bonds due to the presence of reductants, thus resulting in redox-responsive hydrogels [64]. In addition, by comparing R_c values in these conditions, it can be seen that hydrogel coatings in the inflammatory solution provide better protection of the substrate. In order to avoid the aforementioned issues, it is of paramount value to choose a polymer that can withstand the inflammatory and severe inflammatory conditions. In the literature, it has been shown that alginate exhibits relatively good resistance to degradation in moderate concentrations of H_2O_2 at 25 °C [65]. It has also been reported that Alg has a much lower degradation and polymerization rate in pH 5–9 compared to highly acidic solutions (pH < 3) [66]. In Alg, ionotropic gelation is induced by

bivalent (i.e., Ca^{2+}) or polyvalent cations that ionically crosslink carboxylate groups in the uronate blocks, leading to a gel with low solubility at low pH [67]. Therefore, the reduction in corrosion resistance of Alg-based hydrogel coatings in a severe inflammatory solution can be related to the presence of lactate and protein in this medium. Up to now, the effect of lactic acid on alginate has not been completely investigated. However, several models have been proposed regarding the interaction of proteins with Alg. In the most common of these models, the charged BSA in an acidic solution makes a connection between the positively charged parts of the protein and the carboxyl groups of Alg via electrostatic force [68]. On the other hand, the binding of corrosive ions to the protein branches and their pulling towards the substrate and increasing the corrosion rate have also been proven [69]. Thereby, proteins that act as connectors between corrosive ions and hydrogel coatings can be a good justification for reducing corrosion resistance in a severe inflammatory medium. An accurate elucidation of the effect of protein and organic acid on the structural change and corrosion behavior of the Alg-based composite should be suggested in future studies.

3. Materials and Method

3.1. Preparation of 3D-Printed Ti Alloys

The supplied Ti Gr2 (99.6% Ti) and Ti Gr23 alloy (Al 5.5. . .6.76%, V 3.5. . .4.5% wt., Ti—balance) plates by Goodfellow Cambridge Ltd. (Huntingdon, England) were cut into disks with 100 mm diameter and used as substrates. The Ti Gr2 (99.3% Ti), and Ti Gr23 (Al 5.4%, V 3.8%, Fe 0.2%, C 0.009% wt., balance Ti) powders (Merck, Germany) were used for laser-driven powder bed fusion (L-PBF) process. A 3D selective L-PBF printer (Mysint100, Sisma S.p.A., Vicenza, Italy) was used to overprint Ti Gr2 and Ti Gr23 layers in a square-patterned shape on their flat counterparts at Btech Innovation Ltd., Istanbul, Türkiye. After the 3D-printng process, the built parts were cut off into 15 mm diameter small disks (Supplementary Figure S2) with wire electrical discharge machining and washed with water and acetone. A scanning electron microscope (SEM, Hitachi TM-4000Plus-RAMI, Japan) was used to obtain images of 3D-printed TiGr2 and Ti Gr23 (Supplementary Figure S3a, respectively). A detailed description of the fabrication conditions and related parameters can be found in a previous study [23].

3.2. Synthesis of Octacalcium Phosphate

OCP was synthesized according to a previously published protocol [37]. Briefly, 1 g of in-house-synthesized α-tricalcium phosphate (α-TCP, 99% α-TCP) was mixed with 500 mL of 0.0016 M orthophosphoric acid (H_3PO_4, 75%, Latvijas Ķīmija) at room temperature and stirred (350 rpm) for 72 h with a monitored pH throughout the entire synthesis. The final product was washed with deionized water and left to freely dry overnight (37 °C). The syntheses were replicated more than three times to claim the repetitive formation of OCP.

3.3. Synthesis of Octacalcium-Phosphate-Laden Alginate Coatings

Sodium alginate (9005-38-3, Sigma Aldrich) was dissolved in the deionized water at 60 °C overnight to the final solution concentration of 3 wt% Alg. The Alg/OCP composites were prepared by intensively mixing the solid and liquid phases for 15 min, until a homogenous mass was formed. Up to 10 mg of Alg and Alg/OCP hydrogels were uniformly distributed over the 3D-printed Ti alloys, followed by immersion in 0.28 M $CaCl_2$ (A1308701911, Merck) for 15 min to crosslink (Supplementary Figure S4). Compared to Alg hydrogel coatings, which are transparent, the resulting Alg/OCP hydrogel displayed a white, opaque color. The prepared coatings were further used for electrochemical measurements, as shown in Figure 7.

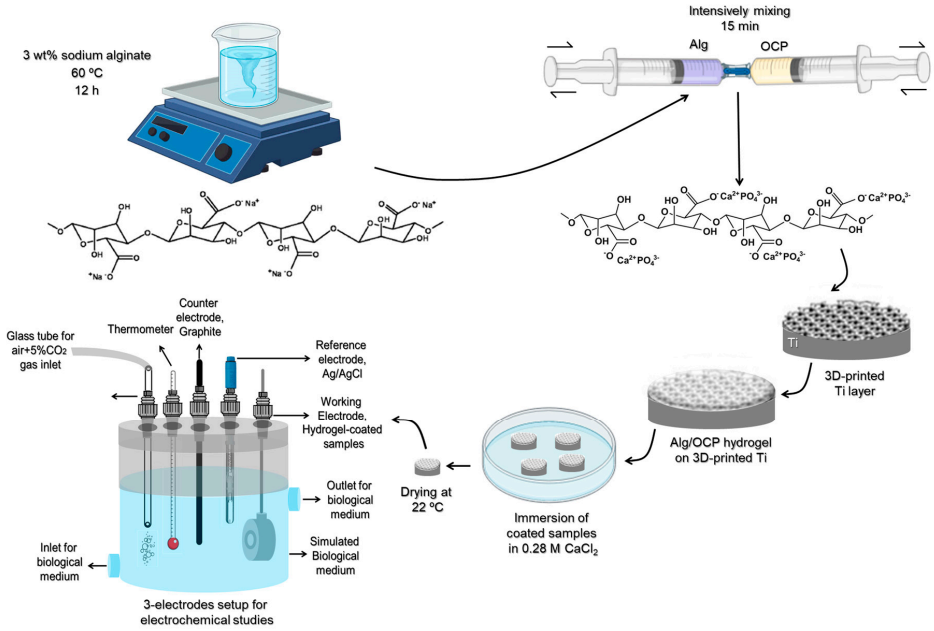

Figure 7. Schematic illustration of preparing Alg/OCP hydrogel coatings on 3D-printed Ti samples for electrochemical studies.

3.4. Physicochemical Characterization of the Alg/OCP Coatings

The presence of the OCP phase after the OCP synthesis and in Alg/OCP coatings was examined using X-ray powder diffractometry (XRD). XRD was performed with a PANalytical Aeris diffractometer (The Netherlands) with the following parameters: 40 kV, 15 mA, and a step size of 0.0435° from 3° to 60° (2θ degrees) with a time per step of 299.575 s. The International Centre for Diffraction Data PDF-2 (ICDD) database was used to corroborate the phase presence. For crystalline phase identification, ICDD#026-1056 has been used. Fourier-transform infrared spectroscopy (FTIR, Thermo Scientific Nicolet™ iSTM50 (Waltham, MA, USA)), used in Attenuated Total Reflectance (ATR) mode, was engaged to characterize functional groups of OCP and Alg/OCP at the molecular level with the spectra in the range of 4000–400 cm^{-1} (number of scans was 64 at a resolution of 4 cm^{-1}) and processed with the OMNIC software (Thermo Scientific). The Alg/OCP coatings have been tested prior to and after immersion in the relevant testing media.

3.5. Coating Characterization

The morphology of the Alg and Alg/OCP hydrogel coatings on 3D-printed Ti Gr2 and Gr23 was evaluated using field-emission scanning electron microscopy (FESEM, Zeiss Sigma VP, Germany). Samples were sputter-coated with Au/Pt prior to the FESEM observations. The FESEM observations were performed at different magnifications in secondary electron (SE) mode with the accelerating voltage of 3 kV. The wettability of hydrogel coatings was assessed using a Theta Flex optical tensiometer (Biolin Scientific, Finland) in sessile drop mode by measuring the contact angles of the 5 µL phosphate-buffered saline (PBS) solution's droplet. All wettability measurements were conducted under the same conditions of humidity (~60% RH) and temperature (24 °C).

3.6. Electrochemical Measurements

Electrochemical tests were performed with a potentiostat (IviumStat.h standard, The Netherlands) in a 3-electrode setup with a Ag/AgCl electrode as a reference elec-

trode (R.E.), a graphite rod as the counter electrode, and hydrogel-coated samples with an exposed area of 1 cm^2 in the Teflon holder as a working electrode (W.E.) (see Figure 7). The electrochemical response of the samples was evaluated in three different simulated biological media (see Table 1) at 37 ± 0.5 °C under slight anaerobic conditions by an aerating mixture of air + 5% CO_2 using solutions. The normal medium was made by dissolving PBS tablets (Sigma-Aldrich, USA) in l L of distilled water. For the simulation of the inflammatory conditions, hydrochloric acid (HCl; 37%, Merck, Germany) and H_2O_2 (30%, Merck, Germany) were added to the normal medium. For mimicking the severe inflammatory conditions, bovine serum albumin (BSA, Sigma-Aldrich, Germany) and calcium L-lactate hydrate (CLH, Sigma-Aldrich, Germany) were all added to the above inflammatory medium.

Table 1. Simulated biological media with their respective compositions, pH, and conductivity at 37 °C.

Simulated Biological Media	Reagents and Amounts					pH	Conductivity ($mS.cm^{-1}$)
	PBS	H_2O_2	HCl	BSA	CLH		
Normal (N)	Five standard tablets in 1 L of deionized water	-	-	-	-	7.4 ± 0.1	15.7 ± 0.5
Inflammatory (I)		150 mM	50 mM	-	-	5.2 ± 0.1	19.4 ± 0.3
Severe inflammatory (SI)				10 $g.L^{-1}$	10 $g.L^{-1}$	3.0 ± 0.2	16.1 ± 0.1

The conductivity and pH values of the simulated solutions were measured using a Mettler Toledo Inlab 730 probe and a Metrohm 691 pH meter, respectively. Considering H_2O_2 instability under light, all of the solutions were stored in dark bottles until tests.

The electrochemical response was analyzed based on open circuit potential, potentiodynamic polarization, and electrochemical impedance spectroscopy (EIS) tests. Before measurements, the samples were soaked in each medium for 1 h. The samples' open circuit potential was monitored during 600 s. Potentiodynamic polarization measurement was conducted under a constant sweep rate of 1 $mV.s^{-1}$ from −1.5 to 1.5 V. The EIS test was performed under an AC voltage of 10 mV in amplitude around open circuit potential in the frequency range of 100 kHz–0.010 Hz. The EIS plots were examined and fitted by the ZView software (version 3.1, Scribner Associates) to achieve a proper equivalent circuit. Chi-squared (χ^2) values in the order of 10^{-3} confirmed the quality of data fitting. All tests were conducted in triplicate to ensure reproducibility and reliability.

4. Conclusions

The inflammation process in the tissues surrounding Ti-based biomaterials can lead to increased acidity with the release of H_2O_2 and acids, weakening the corrosion resistance of these implanted devices. The results of this study showed that bare 3D-printed Ti substrates undergo electrochemical corrosion via chemical reactions between the Ti and the corrosive ions of inflammatory and severe inflammatory solutions and that hydrogel coatings might indeed act as a protective film for preventing the chloride and lactate ions in the simulated biological media from corroding the substrate, thereby improving the corrosion resistance of the Ti alloy. According to polarization and EIS study data, the introduction of OCP particles in the Alg hydrogel matrix decreases the corrosion current i_{corr}, leading to a notable improvement in the charge transfer resistance increase. The excellent corrosion protection of composite coatings eventually arises from blocking the transport pathway of corrosive ions with OCP particles in the hydrogel. These findings may open new opportunities for the surface engineering of Ti implants with the combination of additive manufacturing and modified hydrogel coatings, providing a potential method for the protection of metallic biomaterials during inflammatory processes.

Supplementary Materials: The following supporting information can be downloaded at https://www.mdpi.com/article/10.3390/ijms241713135/s1.

Author Contributions: A.B.-K.—writing—original draft preparation, conceptualization, visualization, formal analysis, and investigation; I.K.—writing—original draft preparation, visualization, formal analysis, and investigation; J.L.—funding acquisition, writing—review and editing, and resources; D.L.—funding acquisition, supervision, writing—review and editing, and resources; M.G.—funding acquisition, supervision, writing—review and editing, and resources. All authors have read and agreed to the published version of the manuscript.

Funding: Financial support from the European Union's Horizon 2020 research and innovation program under the Marie Skłodowska-Curie ITN "Premurosa" (GA 860462) is gratefully acknowledged. The authors also acknowledge the access to the infrastructure and expertise of the BBCE—the Baltic Biomaterials Centre of Excellence (European Union's Horizon 2020 research and innovation program under the grant agreement No. 857287).

Institutional Review Board Statement: Not applicable.

Informed Consent Statement: Not applicable.

Data Availability Statement: The data presented in this study are available on request from the corresponding author. The data are not publicly available due to the connected study.

Acknowledgments: The authors thankfully acknowledge the help and cooperation of Btech Innovations Ltd. in each stage of the production of the 3D-printed Ti layers.

Conflicts of Interest: The authors declare no conflict of interest.

References

1. Haugen, H.J.; Chen, H. Is There a Better Biomaterial for Dental Implants than Titanium?—A Review and Meta-Study Analysis. *J. Funct. Biomater.* **2022**, *13*, 46. [CrossRef] [PubMed]
2. Kaur, M.; Singh, K. Review on titanium and titanium based alloys as biomaterials for orthopaedic applications. *Mater. Sci. Eng. C* **2019**, *102*, 844–862. [CrossRef]
3. Sidhu, S.S.; Singh, H.; Gepreel, M.A. A review on alloy design, biological response, and strengthening of β-titanium alloys as bio-materials. *Mater. Sci. Eng. C* **2021**, *121*, 111661. [CrossRef] [PubMed]
4. Gurel, S.; Yagci, M.; Bal, B.; Canadinc, D. Corrosion behavior of novel Titanium-based high entropy alloys designed for medical implants. *Mater. Chem. Phys.* **2020**, *254*, 123377. [CrossRef]
5. Li, B.Q.; Xie, R.Z.; Lu, X. Microstructure, mechanical property and corrosion behavior of porous Ti–Ta–Nb–Zr. *Bioact. Mater.* **2020**, *5*, 564–568. [CrossRef] [PubMed]
6. Sadtler, K.; Singh, A.; Wolf, M.T.; Wang, X.; Pardoll, D.M.; Elisseeff, J.H. Design, clinical translation and immunological response of bio-materials in regenerative medicine. *Nat. Rev. Mater.* **2016**, *1*, 16040. [CrossRef]
7. Bordbar-Khiabani, A.; Gasik, M. Electrochemical and biological characterization of Ti–Nb–Zr–Si alloy for orthopedic applications. *Sci. Rep.* **2023**, *13*, 2312. [CrossRef]
8. Franz, S.; Rammelt, S.; Scharnweber, D.; Simon, J.C. Immune responses to implants—A review of the implications for the design of immunomodulatory biomaterials. *Biomaterials* **2011**, *32*, 6692–6709. [CrossRef]
9. Carlander, U.; Midander, K.; Hedberg, Y.S.; Johanson, G.; Bottai, M.; Karlsson, H.L. Macrophage-assisted dissolution of gold nanoparticles. *ACS Appl. Bio Mater.* **2019**, *2*, 1006–1016. [CrossRef]
10. Anderson, J.M.; Rodriguez, A.; Chang, D.T. Foreign body reaction to biomaterials. *Semin. Immunol.* **2008**, *20*, 86–100. [CrossRef]
11. Gasik, M.; Braem, A.; Chaudhari, A.; Duyck, J.; Vleugels, J. Titanium implants with modified surfaces: Meta-analysis of in vivo osteointegration. *Mater. Sci. Eng. C* **2015**, *49*, 152–158. [CrossRef] [PubMed]
12. Sasikumar, Y.; Indira, K.; Rajendran, N. Surface Modification Methods for Titanium and Its Alloys and Their Corrosion Behavior in Biological Environment: A Review. *J. Bio-Tribo-Corros.* **2019**, *5*, 36. [CrossRef]
13. Chen, H.; Feng, R.; Xia, T.; Wen, Z.; Li, Q.; Qiu, X.; Huang, B.; Li, Y. Progress in Surface Modification of Titanium Implants by Hydrogel Coatings. *Gels* **2023**, *9*, 423. [CrossRef]
14. Bordbar-Khiabani, A.; Gasik, M. Smart Hydrogels for Advanced Drug Delivery Systems. *Int. J. Mol. Sci.* **2022**, *23*, 3665. [CrossRef]
15. Yuan, N.; Jia, L.; Geng, Z.; Wang, R.; Li, Z.; Yang, X.; Cui, Z.; Zhu, S.; Liang, Y.; Liu, Y. The Incorporation of Strontium in a Sodium Alginate Coating on Titanium Surfaces for Improved Biological Properties. *BioMed Res. Int.* **2017**, *2017*, 9867819. [CrossRef]
16. Warcaba, M.; Kowalski, K.; Kopia, A.; Moskalewicz, T. Impact of Surface Topography, Chemistry and Properties on the Adhesion of Sodium Alginate Coatings Electrophoretically Deposited on Titanium Biomaterials. *Met. Mater. Trans. A* **2021**, *52*, 4454–4467. [CrossRef]
17. Sarker, B.; Singh, R.; Silva, R.; Roether, J.A.; Kaschta, J.; Detsch, R.; Schubert, D.W.; Cicha, I.; Boccaccini, A.R. Evaluation of Fibroblasts Adhesion and Proliferation on Alginate-Gelatin Crosslinked Hydrogel. *PLoS ONE* **2014**, *9*, e107952. [CrossRef]

18. Moskalewicz, T.; Warcaba, M.; Łukaszczyk, A.; Kot, M.; Kopia, A.; Hadzhieva, Z.; Boccaccini, A.R. Electrophoretic deposition, microstructure and properties of multicomponent sodium alginate-based coatings incorporated with graphite oxide and hydroxyapatite on titanium biomaterial substrates. *Appl. Surf. Sci.* **2022**, *575*, 151688. [CrossRef]
19. Li, W.; Liu, X.; Deng, Z.; Chen, Y.; Yu, Q.; Tang, W.; Sun, T.L.; Zhang, Y.S.; Yue, K. Tough Bonding, On-Demand Debonding, and Facile Rebonding between Hydrogels and Diverse Metal Surfaces. *Adv. Mater.* **2019**, *31*, e1904732. [CrossRef] [PubMed]
20. Yang, J.; Liu, F.; Zhou, C.; Li, H.; Yang, G.; Fang, S.; Lee, I.-S.; Liu, Y.; Bai, H.; Chen, C. 3D printed porous titanium filled with mineralized UV-responsive chitosan hydrogel promotes cell proliferation and osteogenesis in vitro. *J. Mater. Sci. Technol.* **2023**, *142*, 34–44. [CrossRef]
21. Che, Z.; Sun, Y.; Luo, W.; Zhu, L.; Li, Y.; Zhu, C.; Liu, T.; Huang, L. Bifunctionalized hydrogels promote angiogenesis and osseointegra-tion at the interface of three-dimensionally printed porous titanium scaffolds. *Mater. Des.* **2022**, *223*, 111118. [CrossRef]
22. Miranda, G.; Faria, S.; Bartolomeu, F.; Pinto, E.; Alves, N.; Peixinho, N.; Gasik, M.; Silva, F. A study on the production of thin-walled Ti6Al4V parts by selective laser melting. *J. Manuf. Process.* **2019**, *39*, 346–355. [CrossRef]
23. Bordbar-Khiabani, A.; Gasik, M. Electrochemical behavior of additively manufactured patterned titanium alloys under simulated normal, inflammatory, and severe inflammatory conditions. *J. Mater. Res. Technol.* **2023**, *26*, 356–370. [CrossRef]
24. Jing, D.; Zhai, M.; Tong, S.; Xu, F.; Cai, J.; Shen, G.; Wu, Y.; Li, X.; Xie, K.; Liu, J.; et al. Pulsed electromagnetic fields promote osteogenesis and osseointegration of porous titanium implants in bone defect repair through a Wnt/β-catenin signaling-associated mechanism. *Sci. Rep.* **2016**, *6*, 32045. [CrossRef] [PubMed]
25. Gasik, M.; Van Mellaert, L.; Pierron, D.; Braem, A.; Hofmans, D.; De Waelheyns, E.; Anné, J.; Harmand, M.-F.; Vleugels, J. Reduction of Biofilm Infection Risks and Promotion of Osteointegration for Optimized Surfaces of Titanium Implants. *Adv. Health Mater.* **2012**, *1*, 117–127. [CrossRef]
26. Kovrlija, I.; Locs, J.; Loca, D. Octacalcium phosphate: Innovative vehicle for the local biologically active substance delivery in bone regeneration. *Acta Biomater.* **2021**, *135*, 27–47. [CrossRef]
27. Mosina, M.; Kovrlija, I.; Stipniece, L.; Locs, J. Gallium containing calcium phosphates: Potential antibacterial agents or fictitious truth. *Acta Biomater.* **2022**, *150*, 48–57. [CrossRef]
28. Hurtado, A.; Aljabali, A.A.; Mishra, V.; Tambuwala, M.M.; Serrano-Aroca, Á. Alginate: Enhancement strategies for advanced applica-tions. *Int. J. Mol. Sci.* **2022**, *23*, 4486. [CrossRef]
29. Liang, B.; Zhao, H.; Zhang, Q.; Fan, Y.; Yue, Y.; Yin, P.; Guo, L. Ca^{2+} enhanced nacre-inspired montmorillonite–alginate film with supe-rior mechanical, transparent, fire retardancy, and shape memory properties. *ACS Appl. Mater. Interfaces* **2016**, *8*, 28816–28823. [CrossRef]
30. De Paula, F.L.; Barreto, I.C.; Rocha-Leão, M.H.; Borojevic, R.; Rossi, A.M.; Rosa, F.P.; Farina, M. Hydroxyapatite-alginate biocomposite promotes bone mineralization in different length scales in vivo. *Front. Mater. Sci. China* **2009**, *3*, 145–153. [CrossRef]
31. Douglas, T.E.L.; Schietse, J.; Zima, A.; Gorodzha, S.; Parakhonskiy, B.V.; KhaleNkow, D.; Shkarin, R.; Ivanova, A.; Baumbach, T.; Weinhardt, V.; et al. Novel self-gelling injectable hydrogel/alpha-tricalcium phosphate composites for bone regeneration: Physiochemical and microcomputer tomographical characterization. *J. Biomed. Mater. Res. Part A* **2018**, *106*, 822–828. [CrossRef] [PubMed]
32. Douglas, T.E.; Łapa, A.; Samal, S.K.; Declercq, H.A.; Schaubroeck, D.; Mendes, A.C.; der Voort, P.V.; Dokupil, A.; Plis, A.; De Schamphelaere, K.; et al. Enzymatic, urease-mediated mineralization of gellan gum hydrogel with calcium carbonate, magnesium-enriched calcium carbonate and magnesium carbonate for bone regeneration applications. *J. Tissue Eng. Regen. Med.* **2017**, *11*, 3556–3566. [CrossRef] [PubMed]
33. Fedotov, A.Y.; Komlev, V.S. Review of Octacalcium Phosphate Materials for Bone Tissue Engineering. *Inorg. Mater. Appl. Res.* **2022**, *13*, 985–1004. [CrossRef]
34. Fuji, T.; Anada, T.; Honda, Y.; Shiwaku, Y.; Koike, H.; Kamakura, S.; Sasaki, K.; Suzuki, O. Octacalcium phosphate–precipitated algi-nate scaffold for bone regeneration. *Tissue Eng. Part A* **2009**, *15*, 3525–3535. [CrossRef]
35. Suzuki, O. Octacalcium phosphate (OCP)-based bone substitute materials. *Jpn. Dent. Sci. Rev.* **2013**, *49*, 58–71. [CrossRef]
36. Suzuki, O.; Shiwaku, Y.; Hamai, R. Octacalcium phosphate bone substitute materials: Comparison between properties of bio-materials and other calcium phosphate materials. *Dent. Mater. J.* **2020**, *39*, 187–199. [CrossRef]
37. Kovrlija, I.; Menshikh, K.; Marsan, O.; Rey, C.; Combes, C.; Locs, J.; Loca, D. Exploring the Formation Kinetics of Octacalcium Phosphate from Alpha-Tricalcium Phosphate: Synthesis Scale-Up, Determination of Transient Phases, Their Morphology and Biocompatibility. *Biomolecules* **2023**, *13*, 462. [CrossRef]
38. Drouet, C. Apatite Formation: Why It May Not Work as Planned, and How to Conclusively Identify Apatite Compounds. *BioMed Res. Int.* **2013**, *2013*, 490946. [CrossRef]
39. Gasik, M.; Keski-Honkola, A.; Bilotsky, Y.; Friman, M. Development and optimisation of hydroxyapatite–ß-TCP functionally gra-dated biomaterial. *J. Mech. Behav. Biomed. Mater.* **2014**, *30*, 266–273. [CrossRef]
40. Du, M.; Huang, L.; Peng, M.; Hu, F.; Gao, Q.; Chen, Y.; Liu, P. Preparation of vancomycin-loaded alginate hydrogel coating on magne-sium alloy with enhanced anticorrosion and antibacterial properties. *Thin Solid Film.* **2020**, *693*, 137679. [CrossRef]
41. Simsek, G.M.; Barthes, J.; Muller, C.; McGuinness, G.B.; Vrana, N.E.; Yapici, G.G. PVA/gelatin-based hydrogel coating of nickel-titanium alloy for improved tissue-implant interface. *Appl. Phys. A* **2021**, *127*, 387. [CrossRef]

42. Pantović, M.R.; Stanojevic, B.P.; Pavlovic, M.M.; Mihailovic, M.D.; Stevanovic, J.S.; Panic, V.V.; Ignjatovic, N.L. Anodizing/anaphoretic electrodeposition of nano-calcium phosphate/chitosan lactate multifunctional coatings on Titanium with advanced corrosion resistance, bioactivity, and antibacterial properties. *ACS Biomater. Sci. Eng.* **2021**, *7*, 3088–3102. [CrossRef] [PubMed]
43. Saveleva, M.; Vladescu, A.; Cotrut, C.; Van der Meeren, L.; Surmeneva, M.; Surmenev, R.; Parakhonskiy, B.; Skirtach, A.G. The effect of hybrid coatings based on hydrogel, biopolymer and inorganic components on the corrosion behavior of titanium bone implants. *J. Mater. Chem. B* **2019**, *7*, 6778–6788. [CrossRef] [PubMed]
44. Hao, X.; Zhang, Z.; Liu, R. Study on Particles Wetted by the Calcium-Based Slurries and the Slurries Viscosity with the Wetting Agents. *Open Chem. Eng. J.* **2015**, *9*, 103–108. [CrossRef]
45. Deng, W.; Zheng, H.; Zhu, Z.; Deng, Y.; Shi, Y.; Wang, D.; Zhong, Y. Effect of Surfactant Formula on the Film Forming Capacity, Wettability, and Preservation Properties of Electrically Sprayed Sodium Alginate Coats. *Foods* **2023**, *12*, 2197. [CrossRef] [PubMed]
46. Fowler, B.O.; Markovic, M.; Brown, W.E. Octacalcium phosphate. 3. Infrared and Raman vibrational spectra. *Chem. Mater.* **1993**, *5*, 1417–1423. [CrossRef]
47. Ben-Nissan, B. Advances in calcium phosphate biomaterials preface. *Adv. Calcium Phosphate Biomater.* **2014**, *2*, 9–11.
48. Kuzmanović, M.; Božanić, D.K.; Milivojević, D.; Ćulafić, D.M.; Stanković, S.; Ballesteros, C.; Gonzalez-Benito, J. Sodium-alginate biopol-ymer as a template for the synthesis of nontoxic red emitting Mn^{2+}-doped CdS nanoparticles. *RSC Adv.* **2017**, *7*, 53422–53432. [CrossRef]
49. Shiraishi, N.; Anada, T.; Honda, Y.; Masuda, T.; Sasaki, K.; Suzuki, O. Preparation and characterization of porous alginate scaffolds containing various amounts of octacalcium phosphate (OCP) crystals. *J. Mater. Sci. Mater. Med.* **2009**, *21*, 907–914. [CrossRef]
50. Tsuchiya, K.; Hamai, R.; Sakai, S.; Suzuki, O. Comparative analysis of bovine serum albumin adsorption onto octacalcium phos-phate crystals prepared using different methods. *Dent. Mater. J.* **2020**, *39*, 883–891. [CrossRef] [PubMed]
51. Endo, K.; Anada, T.; Yamada, M.; Seki, M.; Sasaki, K.; Suzuki, O. Enhancement of osteoblastic differentiation in alginate gel beads with bioactive octacalcium phosphate particles. *Biomed. Mater.* **2015**, *10*, 065019. [CrossRef] [PubMed]
52. Sikkema, R.; Keohan, B.; Zhitomirsky, I. Alginic acid polymer-hydroxyapatite composites for bone tissue engineering. *Polymers* **2021**, *13*, 3070. [CrossRef] [PubMed]
53. England, A.H.; Clare, T.L. Synthesis and characterization of flexible hydrogel electrodes for electrochemical impedance measurements of protective coatings on metal sculptures. *Electroanalysis* **2014**, *26*, 1059–1067. [CrossRef]
54. Porcayo-Palafox, E.; Carrera-Chavez, S.I.; Casolco, S.R.; Porcayo-Calderon, J.; Salinas-Bravo, V.M. Electrochemical performance of Ti-based commercial biomaterials. *Adv. Mater. Sci. Eng.* **2019**, *2019*, 4352360. [CrossRef]
55. Shah, F.A.; Trobos, M.; Thomsen, P.; Palmquist, A. Commercially pure titanium (cp-Ti) versus titanium alloy (Ti_6Al_4V) materials as bone anchored implants—Is one truly better than the other? *Mater. Sci. Eng. C* **2016**, *62*, 960–966. [CrossRef]
56. Sotniczuk, A.; Kuczyńska-Zemła, D.; Kwaśniak, P.; Thomas, M.; Garbacz, H. Corrosion behavior of Ti-29Nb-13Ta-4.6Zr and commercially pure Ti under simulated inflammatory conditions–comparative effect of grain refinement and non-toxic β phase stabilizers. *Electrochim. Acta* **2019**, *312*, 369–379. [CrossRef]
57. Stern, M.; Geary, A.L. Electrochemical polarization: I. A theoretical analysis of the shape of polarization curves. *J. Electrochem. Soc.* **1957**, *104*, 56. [CrossRef]
58. Prestat, M.; Vucko, F.; Holzer, L.; Thierry, D. Microstructural aspects of Ti_6Al_4V degradation in H_2O_2-containing phosphate buff-ered saline. *Corros. Sci.* **2021**, *190*, 109640. [CrossRef]
59. Bai, Y.; Gai, X.; Li, S.; Zhang, L.-C.; Liu, Y.; Hao, Y.; Zhang, X.; Yang, R.; Gao, Y. Improved corrosion behaviour of electron beam melted Ti-6Al–4V alloy in phosphate buffered saline. *Corros. Sci.* **2017**, *123*, 289–296. [CrossRef]
60. Weng, W.; Wu, W.; Yu, X.; Sun, M.; Lin, Z.; Ibrahim, M.; Yang, H. Effect of GelMA hydrogel coatings on corrosion resistance and bio-compatibility of MAO-coated Mg alloys. *Materials* **2020**, *13*, 3834. [CrossRef]
61. Yang, Q.; Lin, B.; Tang, J.; Wang, Y.; Zheng, H.; Zhang, H.; Nie, Z.; Zhang, Y. A pH-Controlled Solid Inhibitor Based on *PAM* Hydrogel for Steel Corrosion Protection in Wide Range pH NaCl Medium. *Molecules* **2023**, *28*, 1314. [CrossRef] [PubMed]
62. Córdoba-Torres, P.; Mesquita, T.; Devos, O.; Tribollet, B.; Roche, V.; Nogueira, R. On the intrinsic coupling between constant-phase element parameters α and Q in electrochemical impedance spectroscopy. *Electrochim. Acta* **2012**, *72*, 172–178. [CrossRef]
63. Yoshimoto, N.; Fathona, I.W.; Yabuki, A. Self-healing polymer coating with efficient delivery for alginates and calcium nitrite to provide corrosion protection for carbon steel. *Colloids Surf. A Physicochem. Eng. Asp.* **2023**, *662*, 130970. [CrossRef]
64. Li, Z.; Lin, Z. Recent advances in polysaccharide-based hydrogels for synthesis and applications. *Aggregate* **2021**, *2*, e21. [CrossRef]
65. Mao, S.; Zhang, T.; Sun, W.; Ren, X. The depolymerization of sodium alginate by oxidative degradation. *Pharm. Dev. Technol.* **2011**, *17*, 763–769. [CrossRef] [PubMed]
66. Holme, H.K.; Lindmo, K.; Kristiansen, A.; Smidsrød, O. Thermal depolymerization of alginate in the solid state. *Carbohydr. Polym.* **2003**, *54*, 431–438. [CrossRef]
67. Le-Tien, C.; Millette, M.; Mateescu, M.-A.; Lacroix, M. Modified alginate and chitosan for lactic acid bacteria immobilization. *Biotechnol. Appl. Biochem.* **2004**, *39*, 347–354. [CrossRef]

68. Zhao, Y.; Li, F.; Carvajal, M.T.; Harris, M.T. Interactions between bovine serum albumin and alginate: An evaluation of alginate as protein carrier. *J. Colloid Interface Sci.* **2009**, *332*, 345–353. [CrossRef]
69. Talha, M.; Ma, Y.; Kumar, P.; Lin, Y.; Singh, A. Role of protein adsorption in the bio corrosion of metallic implants—A review. *Colloids Surf. B Biointerfaces* **2019**, *176*, 494–506. [CrossRef]

Ilijana Kovrlija was born in 1994 in Prijedor, Bosnia and Herzegovina. She obtained her Bachelor's degree in Biochemical Engineering and Biotechnology in 2017 and her Master's degree in the same field in 2018, both from the University of Belgrade. In 2020, Ilijana joined the Institute of Biomaterials and Bioengineering at Riga Technical University (RTU) as a PhD candidate within the Marie Skłodowska-Curie ITN programme – PREMUROSA, working on the Doctoral Thesis under the supervision of Professor Dagnija Loča and Professor Jānis Ločs. She is currently a scientific assistant at the RTU Institute of Biomaterials and Bioengineering. During her doctoral studies, Ilijana completed four scientific secondments at *CAAD* – University of Eastern Piedmont (Novara, Italy), *CIRIMAT* – University of Toulouse (Toulouse, France), and AALTO University (Helsinki, Finland). Her research interests include biomaterial synthesis, processing and characterization, as well as the development of drug delivery systems.

Ilijana Kovrlija dzimusi 1994. gadā Prijedorā (Bosnija un Hercegovina). Belgradas Universitātē ieguvusi bakalaura (2017) un maģistra (2018) grādu bioķīmijas inženierijā un biotehnoloģijā. 2020. gadā pievienojās Rīgas Tehniskās universitātes (RTU) Biomateriālu un bioinženierijas institūta komandai kā doktora grāda kandidāte Marijas Sklodovskas-Kirī ITN programmā *PREMUROSA*, promocijas darbu izstrādājot profesoru Dagnijas Ločas un Jāņa Loča vadībā. Patlaban ir RTU Biomateriālu un bioinženierijas institūta zinātniskā asistente. Doktora studiju laikā devās četrās zinātniskās vizītēs uz *CAAD* – Austrumpjemontas Universitāti (Novara, Itālija), *CIRIMAT* – Tulūzas Universitāti (Tulūza, Francija) un Ālto Universitāti (Helsinki, Somija), kur guva pieredzi *in vitro* pētījumu veikšanā, apguva kalciju fosfātu raksturošanas metodes un guva ieskatu kompozītmateriālu izveidē un analīzē. Zinātniskās intereses saistītas ar biomateriālu sintēzi, apstrādi un raksturošanu, kā arī zāļu piegādes sistēmu izstrādi.